

ELECTRON MICROSCOPE STUDIES OF COLLOIDAL METAL OXIDES

BY

ANNE M. GILDAWIE

DEPARTMENT OF CHEMISTRY

UNIVERSITY OF GLASGOW

THESIS SUBMITTED FOR THE DEGREE OF
DOCTOR OF PHILOSOPHY

AUGUST 1977

ProQuest Number: 13804134

All rights reserved

INFORMATION TO ALL USERS

The quality of this reproduction is dependent upon the quality of the copy submitted.

In the unlikely event that the author did not send a complete manuscript and there are missing pages, these will be noted. Also, if material had to be removed, a note will indicate the deletion.



ProQuest 13804134

Published by ProQuest LLC (2018). Copyright of the Dissertation is held by the Author.

All rights reserved.

This work is protected against unauthorized copying under Title 17, United States Code
Microform Edition © ProQuest LLC.

ProQuest LLC.
789 East Eisenhower Parkway
P.O. Box 1346
Ann Arbor, MI 48106 – 1346

CONTENTS

	page
<u>Summary</u>	1
<u>Introduction</u>	2
Hydrolyses of metal salts	3
Hydrolyses of iron(III) salts	8
The oxyhydroxides of iron	14
<u>Experimental</u>	19
Electron microscopy	19
pH measurement	39
X ray powder diffraction	39
Differential thermal analysis	39
Infra-red spectroscopy	39
Laser diffraction	40
Ultracentrifugation	41
Materials used	42
<u>Results</u>	
General survey	
Tin	45
Titanium	49
Uranium	53
Rare earths	55
Aluminium	57
Vanadium	61
Iron	72
Further work on the hydrolysis of iron(III) solutions.	83

CONTENTS (continued)

	page
<u>Discussion</u>	
General	114
Iron	117
Vanadium	127
Other systems	
Aluminium	133
Tin	135
Titanium	135
Rare earths	137
References	139

Acknowledgements

This work was carried out in the Inorganic Chemistry department under the direction of Prof. D.W.A. Sharp.

I would like to thank my supervisors Dr. J. R. Fryer and Dr. R. Paterson for their help and guidance throughout the course of this work.

I would like to thank Dr. Easson of the Biochemistry department of this University for help with the ultracentrifuge studies and Dr. T. Baird of the Electron Microscopy group for help with the X ray diffraction studies and for many useful discussions.

I would like to thank the technicians Helen Douglas, David Hendrie and Jim Walker for their assistance.

Finally I am very grateful to my husband Dr.D. Snell for all his help in writing this thesis.

Anne M. Gildawie

Summary.

The Electron Microscope was used to study metal salt hydrolyses and a survey of several systems was carried out. The iron and vanadium systems were chosen for more detailed examination.

The self hydrolysis of 0.01M VO_2SO_4 solution at various temperatures produced Bariandite and the stages in the hydrolysis were studied using the electron microscope. It is suggested that the final long 'needle' shaped crystals were formed by the rolling up of a thin film precursor.

The self hydrolysis of $\text{Fe}(\text{NO}_3)_3$, $\text{Fe}_2(\text{SO}_4)_3$ and $\text{Fe}(\text{ClO}_4)_3$ solutions at various temperatures gave $\alpha\text{-FeOOH}$ or $\alpha\text{-Fe}_2\text{O}_3$ depending upon the temperature of the hydrolysis, while FeCl_3 gave $\beta\text{-FeOOH}$. The anion not only affected the structure of the product but also the morphology; sulphate and chloride anions caused the oxide hydroxide precipitates to have a pod-like morphology, and this is explained in terms of a rolling up of the thin film precursors.

An overall mechanism is proposed for the precipitation of the iron oxide hydroxides and vanadium oxide in terms of a two-dimensional film which is formed by condensation of polynuclear species, and which then thickens in various ways (depending on the anion) to give the final crystalline product. This mechanism was formulated from the electron microscope evidence but is corroborated by ultracentrifuge studies in the iron system where stages corresponding to the thin films and the final product are also observed.

Of the other systems surveyed it seems probable that the oxide of Al and the hydroxides of Pr, Nd and Sm are also formed by this type of mechanism.

Introduction

The products of metal salt hydrolysis have many uses. The cationic complexes formed on hydrolysis of chromium salts are important in leather tanning. The gelatinous aluminium hydroxide formed by alkali hydrolysis of aluminium salts is used for water clarification and also as a mordant for dyeing cotton. Zirconia is used as a refractory in corrosion resistant furnace linings and hematite, $\alpha\text{Fe}_2\text{O}_3$, is used as an abrasive. Many metal oxides and hydroxyoxides are used for colouring pigments, for example, Cr_2O_3 (green), αFeOOH (yellow), βFeOOH (marigold), and γFeOOH (ochre). Anatase (TiO_2) gives a brilliant white pigment which is used in paints although it unfortunately accelerates the photoreduction of the polymer in which it is incorporated. Hydrous oxides, with large surface areas, may be used as catalyst supports and may also have ion exchange properties as shown for hydrous zirconia (Britz and Nancollas 1969).

To investigate the factors affecting the development of the structure and morphology of the final crystalline product of hydrolysis, it is necessary to obtain information about the species present in the solution before precipitation. The transmission electron microscope can image structures a few angströms in size and should enable pre-precipitation stages in the hydrolysis to be identified, provided that no fallacious evidence is introduced in preparing the specimen for microscopy. Hutchison (1970), working on the hydrolysis of zirconyl chloride, showed that the final product, monoclinic zirconia, had a 'pod' morphology. He suggested that a

probable mechanism for formation of the 'pods' was a rolling up of the intermediate 'sheet' material formed at an early stage. A similar pod morphology has been reported for βFeOOH (Gallacher 1970).

In this work two factors have been considered:

- (a) How general is this 'pod' like morphology, especially with a 'sheet' precursor;
- (b) How valid is the proposed mechanism, particularly in reference to the hydrolysis of iron (III) salts.

Hydrolysis of metal salts.

The hydrolysis of metal salt solutions has been studied for many years. As early as 1907 Werner and Pfeiffer recognised that the hydrolysis of metal ions was the result of deprotonation of the co-ordinated water molecules. The formation of the metal-oxygen bond weakens the oxygen-hydrogen bonds of the co-ordinated water molecule, so that, in aqueous solution, the co-ordinated water molecules are stronger acids than the free water molecules which behave as proton acceptors. The greater the strength of the metal-oxygen bond, which depends on the size and charge of the metal ion, the greater the extent of hydrolysis.

The product of hydrolysis may be a metal oxide, a hydrous oxide, an oxyhydroxide or an hydroxide depending on conditions of temperature and pH.

'Hydrous oxide' is the general term applied to precipitates with an indefinite amount of adsorbed water, usually formed as a gel by adding alkali to metal salt solutions. Hydrous oxide sols of Cr, Zr and Al,

consisting of spherical particles of narrow size distribution, have been prepared by controlled addition of alkali to the metal salt solution followed by aging (Bye and Sing 1972, Demchak and Matijevic 1969, Matijevic et al. 1971, Matijevic and Bell 1972, Brace and Matijevic 1973). A complexing solute particularly SO_4^{2-} seemed necessary for sol formation (Matijevic et al. 1973). A further study (Kennedy, Townsend and Emmerson 1973) on tin and iron hydrous oxide sols, in this case without the use of base, states that such sols may be prepared from the 'chlorides and sometimes the nitrates of at least 36 other elements'. Recent work (Matijevic et al. 1975) on the production of iron hydrous oxide sols from ferric sulphate solutions, identified the primary monodispersed particles as a basic ferric sulphate which on further aging underwent a secondary reaction producing 'spiky' growth. This secondary reaction was not further investigated.

An 'Oxyhydroxide' has the composition MOOH (where M stands for a ^{divalent} metal ion) intermediate between the oxide M_2O_3 and the hydroxide $\text{M}(\text{OH})_3$. Oxyhydroxides may be formed directly from hydrolysis of the metal salt or from the aging of an hydrous oxide. They were first thought to be hydrated oxides but later work (Kolthoff and Moskovitz 1936) has shown that they are 'oxide hydroxides'. The less cumbersome term 'oxyhydroxide' is generally used (Gallacher 1970).

Two general structures of MOOH occur (Wells 1962); diaspore (αAlOOH) structure, which includes goethite (αFeOOH) and groutite (αMnOOH); and the lepidocrocite (γFeOOH)

structure, which includes boehmite (γ -AlOOH), MnOOH (manganite) and γ -ScOOH (Milligan and MacAtee 1956).

Figure 1 shows the diasporite structure. Oxygen atoms are at the corners of each octahedron with the metal atom at the centre. The double lines indicate O-H-O bonds (Ewing 1935 a). The structure consists of close packed oxygen atoms with the metal atom in certain of the octahedral holes. All of the oxygen atoms are involved in hydrogen bonding and the O-H-O bond is fairly long. The octahedra share edges forming one-dimensionally infinite 'double rutile strings' (Ewing 1935 a) running parallel to the c axis, the strings being joined by sharing corners.

Figure 2 shows the structure of lepidocrocite (Ewing 1935 b). Oxygen atoms are at the corners of the octahedra with metal atoms in the centre and hydrogen bonds are indicated by the double lines. The octahedra are distorted with a flattening out of that portion of the octahedra in the interior of the double layer and a corresponding stretching of the edges away from the layers. The OH groups are on the outer surface of each layer and hydrogen bonding occurs between hydroxyl groups on different layers so holding the layers together. Only half the oxygen atoms are involved in hydrogen bonding. In this structure the layers are formed by the sharing of edges between the 'double rutile strings'.

The structures of two further modifications of FeOOH, β -FeOOH and δ -FeOOH, have been determined (MacKay 1960a) and will be discussed later.

Figure 1 The structure of Diaspore and Goethite.

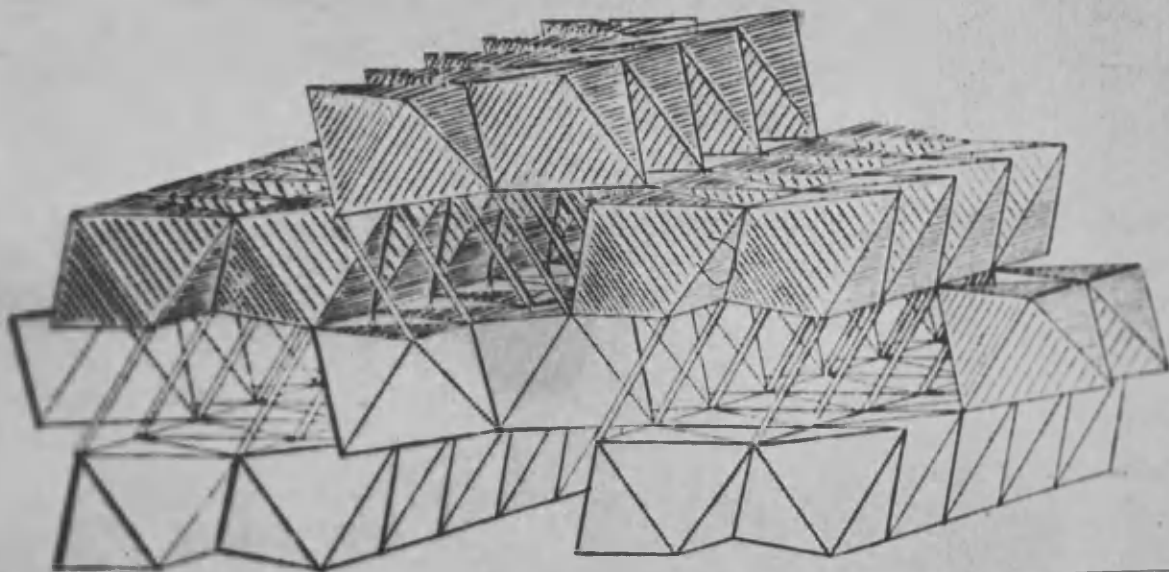
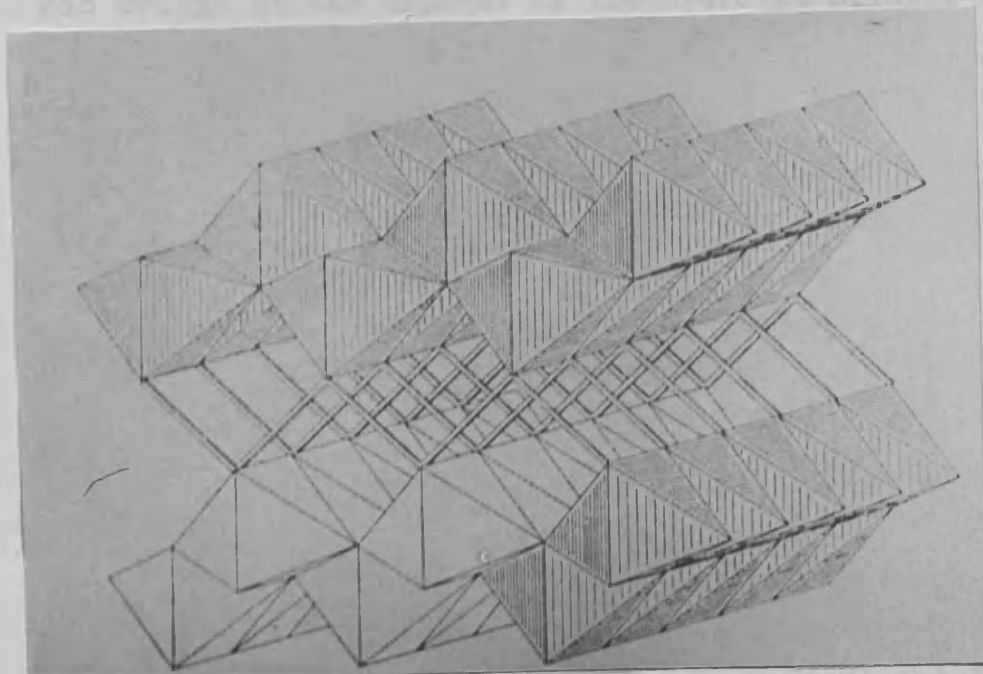
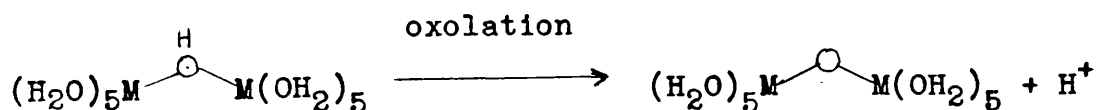
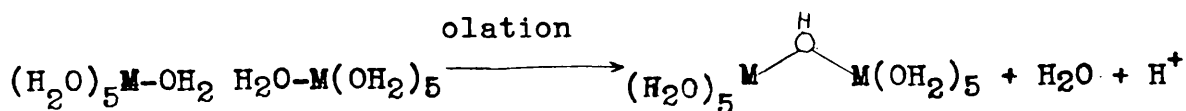


Figure 2 The structure of Lepidocrocite and Boehmite.



The precipitation of hydrous oxides and oxyhydroxides from metal salt solutions is more complex than most precipitation processes because nucleation and growth cannot be solely described by the deposition of ionic units upon a growing crystal nucleus. A variety of chemical reactions can occur, such as, condensation and polymerisation which involve the formation of polynuclear species via olation and oxolation reactions as shown below.



Olation is the formation of a hydroxyl bridge with the elimination of water. Oxolation is the formation of an oxo bridge at the expense of the hydroxyl bridge. Both processes produce H^+ (or H_3O^+) ions causing a decrease in the pH of the solution.

Polynuclear species are formed during the hydrolysis of many salts. The kinetics of many such reactions have been studied by Sillen and co-workers and the following species proposed (Sillen 1959), $(VO)_2(OH)_2^{2+}$; $Bi_6(OH)_{12}^{6+}$; $Sc((OH)_2Sc)_n^{(n+3)+}$; for $n=1, n=2$ and probably for higher values; $In((OH)_2In)_n^{(n+3)+}$; $UO_2((OH)_2UO_2)_n^{2+}$, a sheet-like structure with double OH bridges; $Th((OH)_3Th)_n^{(n+4)+}$, Th^{4+} ions linked by OH bridges forming chains; $Sn((OH)_2Sn)_2^{2+}$, a ring structure; and $Be_3(OH)_3^{3+}$, a six membered ring

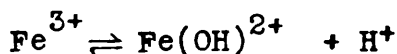
of three tetrahedra joined at the corners by hydroxyl groups. Other workers have proposed double hydroxyl bridged dimers of Fe^{3+} (Mulay and Selwood 1955), Cr^{3+} (Shuttleworth 1954), and Mo^{3+} (Jezowska-Trzebiatowska 1968), a tetrameric cation of Zr^{4+} , $(\text{Zr}(\text{OH})_2 \cdot 4\text{H}_2\text{O})_4^{8+}$ (Muha and Vaughan 1960), and a dimer of Al^{3+} , $\text{Al}_2(\text{OH})_5^+$ (Brosset 1952). The final precipitated oxyhydroxide appears to be based either on a chain-like or a sheet-like structure.

The hydrolysis of iron(III) salts.

An explanation of the slow hydrolysis of iron(III) salts was proposed by Goodwin in 1896. On the basis of conductivity measurements he proposed an instantaneous reversible hydrolysis forming $\text{Fe}(\text{OH})^{2+}$ and H^+ ions followed by a further hydrolysis caused by the slow polymerisation of the basic iron ions or ferric hydroxide molecules to form colloidal basic ferric oxide or hydroxide. A detailed study of this slow hydrolysis was reported in 1938 by Lamb and Jacques. They measured the conductivity, colour and pH of a series of iron(III) chloride, nitrate and sulphate solutions as a function of temperature, iron concentration and amount of free acid added to the system. Their results showed that all the solutions hydrolysed slowly (after an induction period of varying lengths) and in some cases steady state conditions were not obtained for many weeks, and that all the changes in properties observed were accelerated by increased temperatures. They interpreted these results in terms of the slow formation

of colloidal $\text{Fe}(\text{OH})_3$ from the rapidly produced species $\text{Fe}(\text{OH})^{2+}$, $\text{Fe}(\text{OH})_2^+$ and molecular $\text{Fe}(\text{OH})_3$.

The equilibria



(co-ordinated water molecules have been omitted)

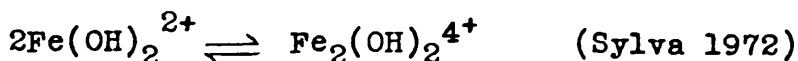
have been studied extensively (Sylva 1972) and the results indicate that true equilibrium is reached very rapidly. Therefore the changes in properties of the solutions studied by Lamb and Jacques are due to further polymerisation and condensation of these initial monomeric products to polynuclear species.

The formation of polynuclear species in hydrolysed iron(III) solutions was first indicated by Graham (1861) who detected particles of colloidal size in iron(III) chloride solutions alkalified by ammonium carbonate. There have been conflicting reports on whether discrete stable entities are formed or whether a continuous series of species exists. Jander et al (1930), from diffusion measurements on iron(III) perchlorate, suggested that a continuous series of polynuclear species containing from one to fifty iron atoms was present. Conductimetric studies (Arnek and Schlyter 1968) indicate the existence of the trimer $\text{Fe}_3(\text{OH})_4^{5+}$, and the compound $(\text{Fe}_4\text{O}_3(\text{OH})_5)\text{NO}_3$ has been isolated from hydrolysed iron(III) nitrate solutions (Zvyaginstev 1961). Spiro et al (1966) have isolated a high molecular weight polymer of approximate composition $(\text{Fe}_4\text{O}_3(\text{OH})_4(\text{NO}_3)_2(\text{H}_2\text{O})_{1.5})_{250}$ from the hydrolysis of iron(III) nitrate with potassium bicarbonate. The polymer has the structure of a flat ribbon almost 100 times as long

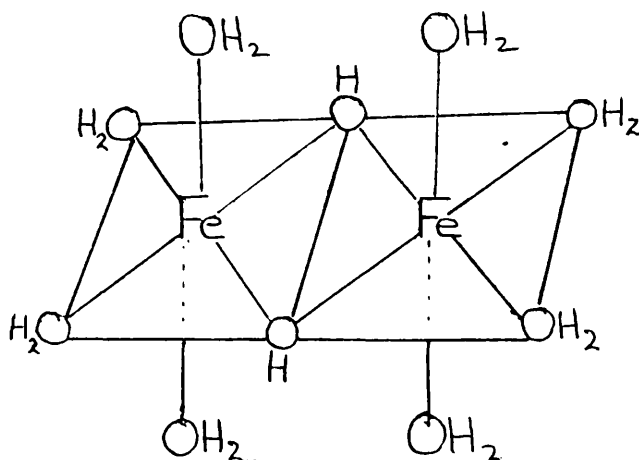
as wide with an overall spherical shape due to the gathering of the chains via bridged cross linkages (Brady 1968). Spiro suggests that the polymer particles grow rapidly until a stable structure is reached and that the series of stable polymers proposed by Jander does not exist.

Precipitation and polymerisation both occur by stepwise addition of low molecular weight species to the growing nuclei (Knight 1974). The processes are, however, different since in the polymer structure external iron atoms are tetrahedrally co-ordinated to oxo, hydroxo and water groups in a corner sharing bridged structure (Brady 1968); whereas, in the crystalline precipitates α , γ , and β FeOOH, the iron atoms are six co-ordinated in distorted octahedra (Bernal, Dasgupta and MacKay 1959). It has been shown (Sylva 1972) that the amount of iron present in the high molecular weight polymer increases linearly with the amount of base added to the system and that polymerisation and precipitation are competing processes with polymerisation being dominant in systems with a high concentration of added base (Spiro 1966, Knight 1974).

Potentiometric and magnetic studies on iron(III) perchlorate in 3 molar sodium perchlorate (Hedstrom 1953, Mulay and Selwood 1955) led to the proposal of the dimer $\text{Fe}_2(\text{OH})_2^{4+}$ as an hydrolysis product. Many kinetic studies have been carried out on the equilibrium



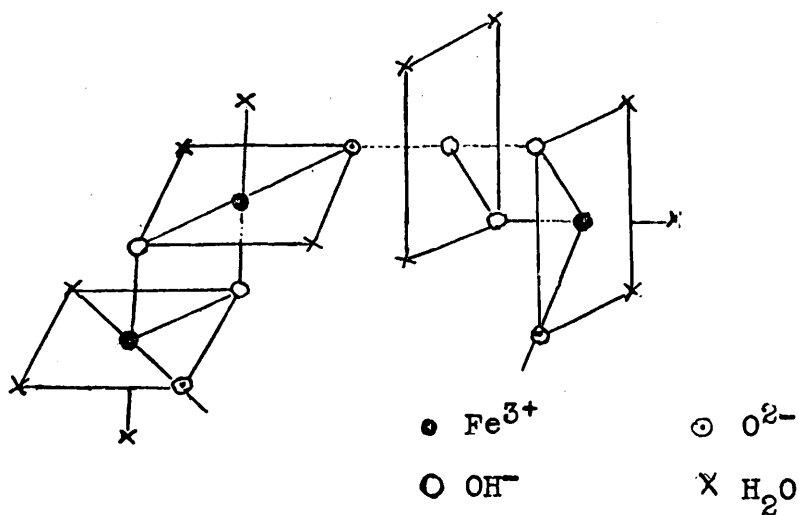
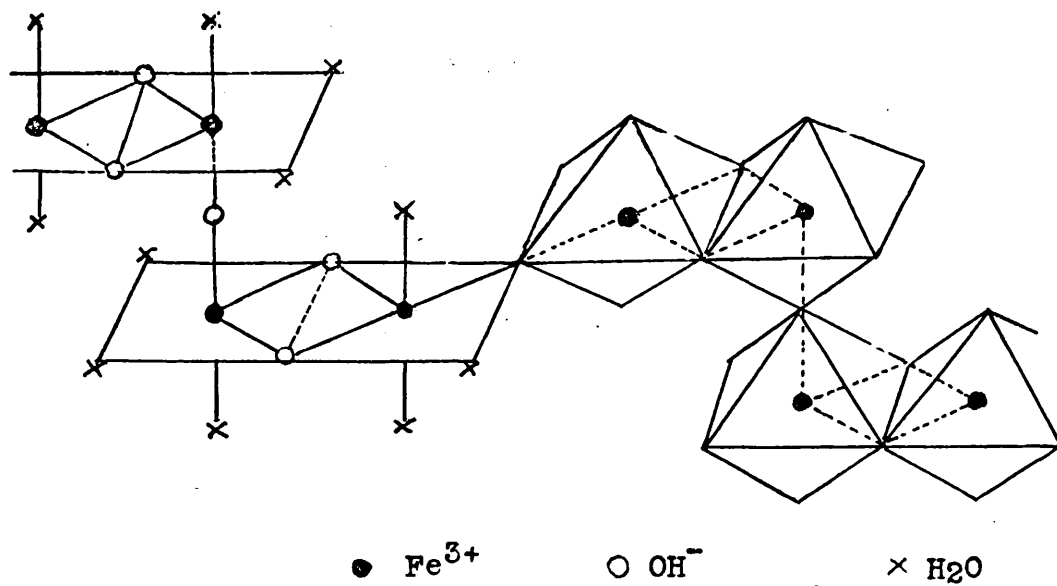
There are two possible forms of this dimer in aqueous solution, the dihydroxo form, $((\text{H}_2\text{O})_4\text{Fe}(\text{OH})_2\text{Fe}(\text{H}_2\text{O})_4)^{4+}$ or the oxo form, $((\text{H}_2\text{O})_5\text{Fe}-\text{O}-\text{Fe}(\text{H}_2\text{O})_5)^{4+}$. Kinetic studies using stopped flow techniques, on the dissociation of the aquo dimer (Lutz and Wendt 1970, Sommer 1970), indicate the presence of a diol bridge (two bridging OH units) but does not rule out the possibility of the equilibrium, $((\text{H}_2\text{O})_5\text{Fe}(\text{OH})\text{Fe}(\text{OH})(\text{H}_2\text{O})_4)^{4+} \rightleftharpoons ((\text{H}_2\text{O})_5\text{Fe}-\text{O}-\text{Fe}(\text{H}_2\text{O})_5)^{4+}$ (Wendt 1969). Schugar (1967) found no evidence for an Fe-O-Fe bridge in his infra red studies and the dihydroxo form of the dimer is normally used as shown below.



The formation of a crystalline precipitate involves elimination of co-ordinated water from this dimer and deprotonation of the OH groups.

The final form and structure of the crystalline precipitate are influenced by several factors. In aqueous media, at ambient temperatures α -FeOOH precipitates from iron(III) oxalate, acetate, nitrate and bromide (Weiser and Milligan 1935, Dasgupta and MacKay 1959). Sulphate solutions form α -FeOOH or a basic sulphate, depending on the concentration (Posnak 1922). β -FeOOH precipitates

from fluoride (MacKay 1960b) and chloride solutions (Wieser and Milligan 1935, MacKay 1960b, Soderquist 1966, Gallacher 1970). At reflux temperatures or above, $\alpha\text{Fe}_2\text{O}_3$ is formed from all of the above solutions (Weiser and Milligan 1935, Dasgupta and MacKay 1960). Excess base addition to iron(III) solutions produces an amorphous gel, which on slow aging, crystallises as αFeOOH or $\alpha\text{Fe}_2\text{O}_3$ depending on temperature and pH of aging (Atkinson, Posner and Quirk 1968, Schwertmann 1959, Knight 1974). The anion is important for solutions with low base additions. Perchlorate solutions form γFeOOH , chloride solutions form βFeOOH and nitrate solutions form αFeOOH with low base addition. All form αFeOOH under conditions of high base addition, OH/Fe ratio greater than 1.5 (Knight 1974). The compound formed on hydrolysis is related to the nature of the iron (III) complexes in the solution just before precipitation. Chloride, fluoride and sulphate anions have a high co-ordinating ability and iron-anion complexes are likely to occur with these anions. Perchlorate and nitrate have a much lower co-ordinating ability and therefore are less likely to form iron-anion complexes. An X-ray crystal structure of iron(III) chloride hexahydrate (Lind 1967a) shows a unit cell of $(\text{FeCl}_2(\text{OH}_2)_4)\text{Cl} \cdot 2\text{H}_2\text{O}$. The cation $(\text{FeCl}_2(\text{OH}_2)_4)^+$ persists in aqueous solution (Lind 1967b). A study by Kiyama (1974) shows that chloro and sulphato complexes are formed in acidic solutions of iron (III) chloride and sulphate whereas iron(III) nitrate forms aquo complexes. Further hydrolysis produces complexes with polynuclear cations and the chloride, sulphate or nitrate anion. The chloride

Figure 3a.A possible precursor for β FeOOH.Figure 3b.A possible precursor for α FeOOH.

(after Kiyama 1974)

and sulphate anions are bound to the iron cation as ligands. In the polycation the edge shared octahedral dimers $(\text{Fe}_2(\text{OH})_2(\text{H}_2\text{O})_8)^{4+}$ are antiferromagnetically bound together by monohydroxo bridges giving a zigzag structure, as shown in figure 3b, eventually producing αFeOOH , but in the chloride solution it is assumed that the dimers are bound by oxo bridges giving a ring-like structure, as shown in figure 3a, leading to βFeOOH . Mössbauer studies on iron (III) salt solutions (Vertes 1971) also indicate that in the sulphate and chloride solutions the anion is built into the dihydroxy dimer but in the perchlorate and nitrate case the dimers are free of anion.

The oxyhydroxides of iron

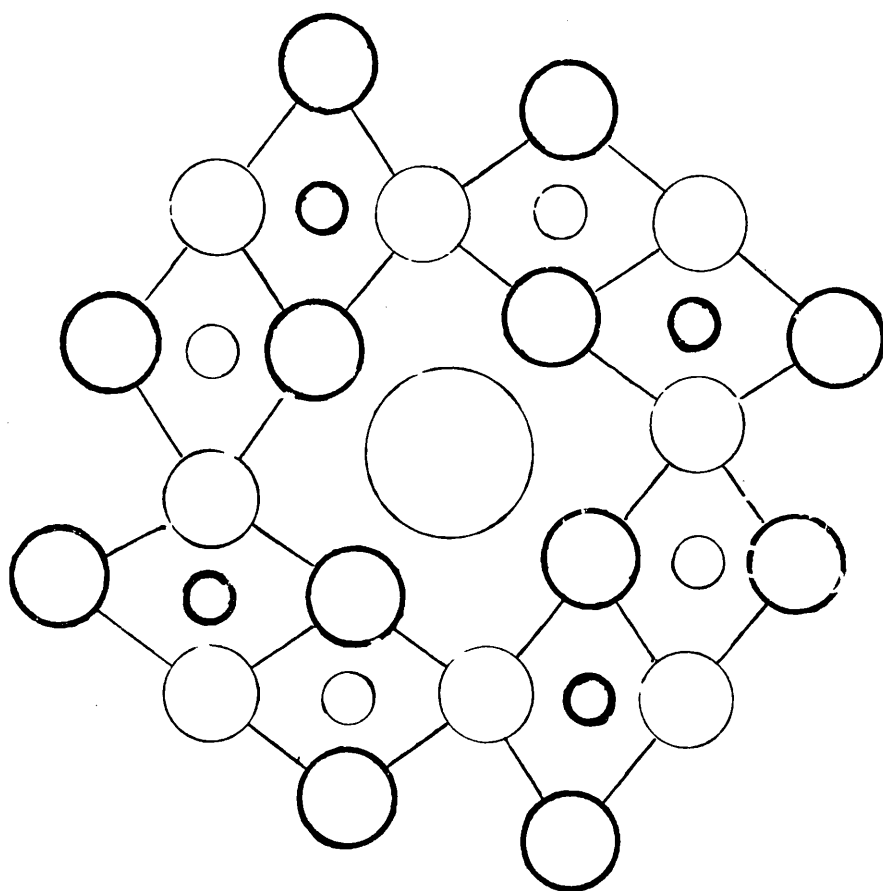
Four oxyhydroxides of iron have been characterised, and designated α , β , γ and δ . The crystal structure of γFeOOH (lepidocrocite) was determined by Ewing (1935b) and is shown in Figure 2. The Xray diffraction pattern was indexed on an orthorhombic unit cell with $a=3.87$, $b=12.51$, and $c=3.06\text{\AA}$. αFeOOH (goethite) is isostructural with diasporite (αAlOOH), which is shown in Figure 1. The crystal structure was determined by Goldsztaub (1932) and is based on an orthorhombic unit cell with dimensions, $a=4.64$, $b=10.0$, and $c=3.03\text{\AA}$. As prepared by Atkinson, Posner and Quirk (1968) αFeOOH was in the form of acicular and twinned crystals.

The existence and structure of δFeOOH , prepared from iron(II) sulphate, were discovered from Xray powder evidence by Bernal, Dasgupta and MacKay (1959). The

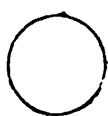
diffraction pattern was indexed on an hexagonal unit cell with $a=2.941$ and $c=4.49\text{\AA}$. The structure is an arrangement of hexagonally close packed oxygen/hydroxyl layers with Fe^{3+} ions between adjacent layers. About 20% of the Fe^{3+} ions are in tetrahedral sites (Francombe and Rooksby 1959).

β FeOOH (akaganeite) crystals were first isolated by Böhm (1925) from refluxing solutions of iron(III) chloride, and the mineral akaganeite was identified by MacKay (1962). When freshly precipitated, β FeOOH has a hollandite or BaMnO_2 structure with 5\AA square channels running parallel to the c axis (Bernal, Dasgupta and MacKay 1959), the sides being bounded by double rows of fused octahedra which contain Cl^- ions in an amount which corresponds to the formula " $\text{FeO}_{1-\frac{1}{4}}\text{OH}_{1+\frac{1}{4}}\text{Cl}$ " (Gallacher 1970). Washing removes most of the Cl^- ions. Figure 4 shows the structure of β FeOOH projected on the (001) face (MacKay 1960b). The Fe^{3+} ions are octahedrally surrounded by six oxygen or hydroxyl groups. The octahedra are linked to form double strings parallel to the c axis. The octahedra in each string share edges parallel to the a axis and each octahedron shares two edges with octahedra in the neighbouring string. The double strings are joined by sharing corners. The tetragonal unit cell dimensions have been given by MacKay (1960b) as $a=10.48\text{\AA}$ and $c=3.023\text{\AA}$. An unusual feature of β FeOOH is its morphology as revealed by electron microscopy. Feitknecht (1960) observed that the crystals had the appearance of bundles of parallel needles. Later investigations by Watson, Cardell and Heller (1962) provided more accurate information concerning the peculiar cigar shaped crystallites which they called 'somatoids'. A pattern of striations parallel

Figure 4. The structure of β FeOOH.
A projection on the (001) face.



O/OH $z = 0$



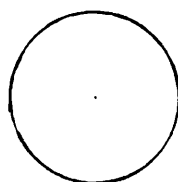
O/OH $z = \frac{1}{2}$



Fe $z = 0$



Fe $z = \frac{1}{2}$

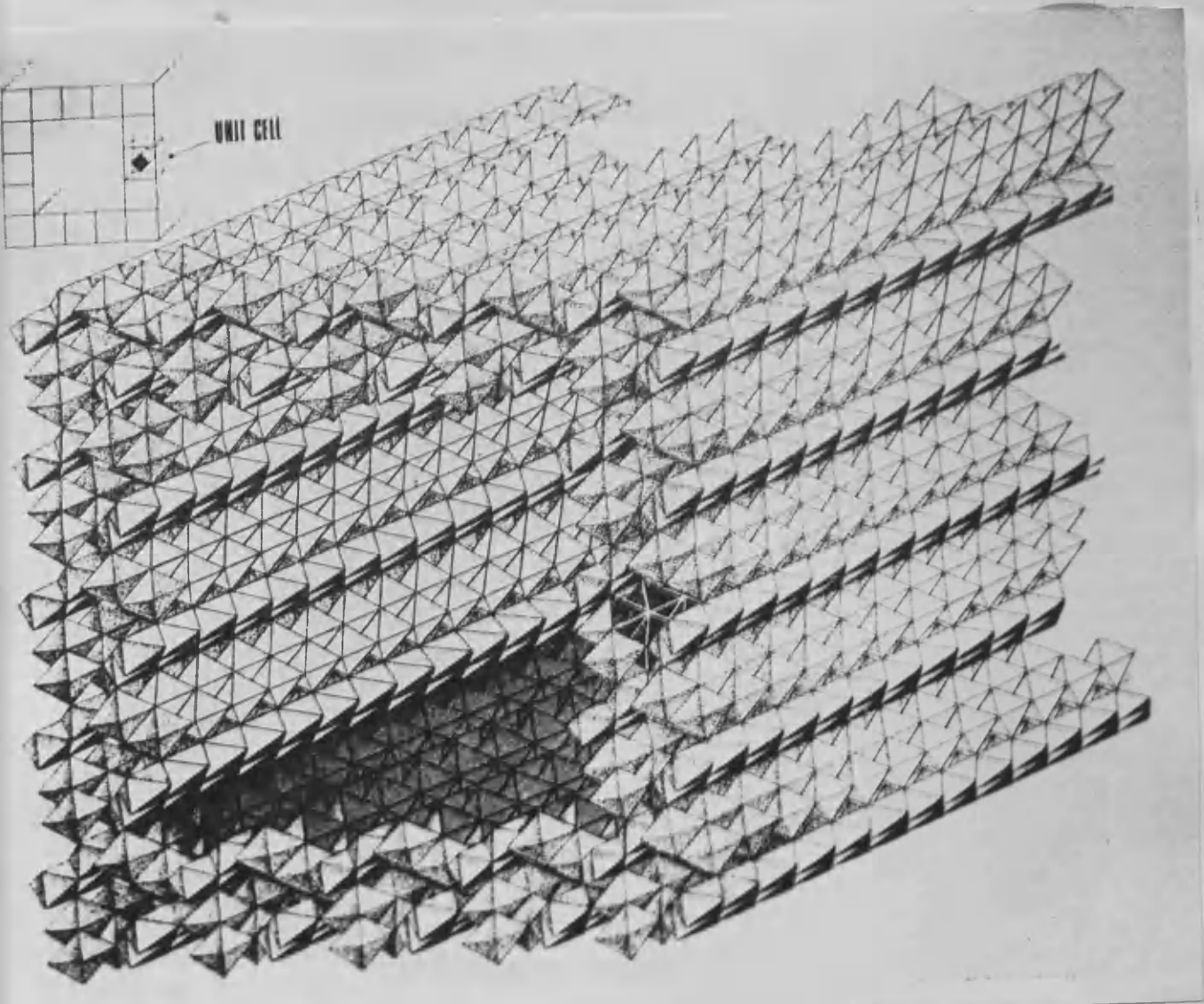


Cl/H₂O $z = \frac{1}{2}$

(after MacKay 1960)

to the main axis with a repeat distance of about 60\AA was accounted for using sectioning and shadow casting methods. The authors deduced that the crystals were square in cross section with a side length of about 500\AA , the crystals were up to 5000\AA in axial length, along what was shown to be the c axis (MacKay 1960a). Watson et al (1962) suggested that the structure within the crystals probably consisted of an oriented bundle of orthogonally packed rods, fairly loosely packed. The repeat distance was about 60\AA , the rods being about 30\AA thick and 30\AA apart. The rods were longer towards the centre of a crystal and were themselves crystals. There was some evidence from the cross sections that the rods were, in fact, hollow and an alternative model was proposed, taking this into account, in which the rods were packed more closely together. The not-infrequent star-shaped and Y-shaped crystals were regarded as twins. Gallacher (1970) using electron microscopy, Xray diffraction and gas absorption techniques extended this work and confirmed the presence of pores in βFeOOH . The mean pore diameter was found to be 28\AA . Figure 5 shows Gallacher's proposed atomic 'superstructure' of a single tubular crystal of βFeOOH . Each octahedron represents an Fe^{3+} ion octahedrally surrounded by oxygen or hydroxyl groups. Corner and edge sharing occurs. Walls one unit cell thick form large square channels of side 31.4\AA . The edge of the rod is built up of 5 unit cells giving an outer dimension of $5x_a$, 52.4\AA (Gallacher 1970). Infrared and Xray diffraction studies indicate free OH groups, that is, there is little or no hydrogen bonding. This is unusual for an oxyhydroxide, both αFeOOH and γFeOOH exhibit fairly strong hydrogen bonding.

Figure 5 An atomic superstructure of β -FeOOH



(from Gallagher 1970)

EXPERIMENTAL

Electron microscopy

The ability of a magnetic lens to focus an electron beam was demonstrated by Busch (1926) and a commercial model of an electron microscope was available in 1938 (Von Borries and Ruska). This instrument was capable of higher resolution than optical microscopes because of the short wavelength of an electron beam. In an electron microscope the electron beam is produced by a heated tungsten filament, accelerated by a potential usually between 40 and 100 kV, collimated and focused on the specimen by a condenser lens system. The electron image of the specimen is then magnified. The microscopes used in this work were a Siemens Elmiskop 1A, a Phillips 300 and a JEM 100c.

Image formation

The electron optical system

The design of modern electron microscopes and their operation has been recently described by Glauert (1974). The transmission mode of operation is shown schematically in Figure 6. The double condenser system has a strong first lens, to reduce the electron crossover to an image of about $1\frac{1}{4}$ μ m in diameter, and a weaker second lens to project this crossover onto the specimen plane. The second lens produces a slight magnification, giving a final focused beam diameter at the specimen of 2-3 μ m. The second condenser lens has a physical aperture which limits the beam striking the specimen and protects it from excessive heating. The diameter of the condenser aperture is variable from 50-200 μ m. An image is formed by the objective lens

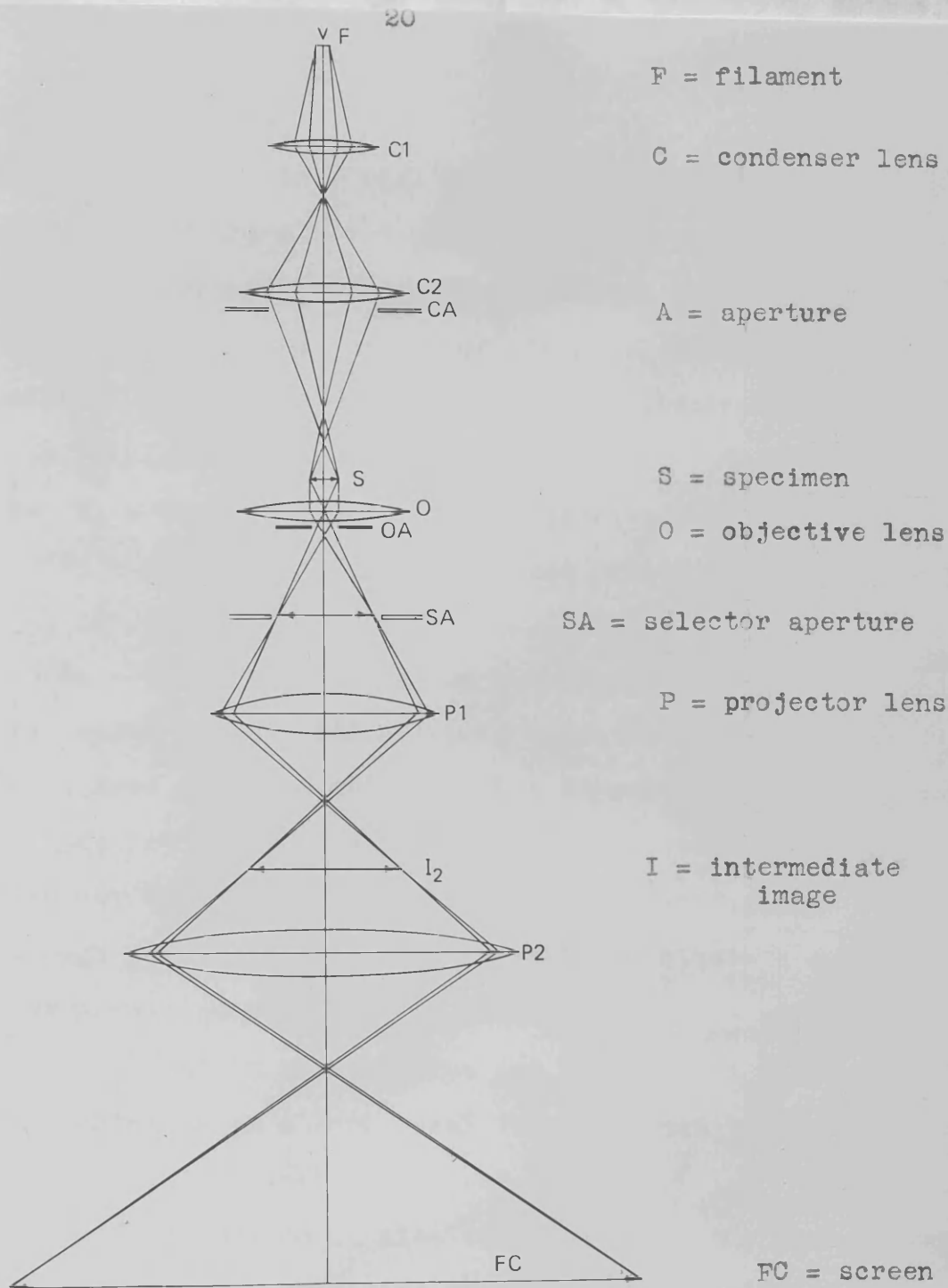


Figure 6 Ray diagram for transmission operation.

(from Glauert 1974)

and the quality of this lens largely determines the ultimate performance of the microscope. The objective lens also has a physical aperture, the diameter of which is an important parameter. The magnification of the final image, M_t , is the product of the magnification of the individual lenses. Thus:

$$M_t = M_o \times M_1 \times M_2$$

Where M_o = magnification of the objective lens.

M_1 = magnification of the first projector (or intermediate) lens.

M_2 = magnification of the second projector lens.

It is useful in an initial search operation to be able to view a large area of the specimen. This is achieved by switching off the objective lens and using the first projector lens to image the object directly. There is only one magnification at which the image is focussed. It is possible to obtain a whole range of low magnification focussed images in a three projector system, as used in the Phillips and the JEM, by using the first projector as a long focal length objective and varying the magnification with the second projector lens. The three projector lens system is also very useful in the diffraction mode of operation, providing a variable camera length.

Resolution

The resolving power of a microscope has been defined by Cosslett (1951) as the closest distance of approach of two point objects at which they can still be distinguished as separate entities as measured in at least two successive micrographs. To obtain meaningful resolution the information content in the electron beams scattered from the specimen must be recovered and interpreted. The information is represented by perturbations

in the electron waves, so that meaningful resolution may result only if the perturbations arising from structural features in the specimen are significantly greater than those arising from aberrations.

Factors limiting retrieval of information

Spherical aberration This is the most severe defect of the objective lens and results from peripheral rays passing through the lens being brought to a focus before those closer to the axis. Thus a point in the object is imaged as a disc by the objective lens as shown in Figure 7. Referred back to the object plane, the corresponding disc of confusion is of radius

r_s where

$$r_s = C_s \alpha^3$$

C_s is the spherical aberration constant of the lens,

α is the semi-angular aperture of the lens.

This relation can also be written :-

$$r_s = C f \alpha^3$$

where f is the focal length of the objective lens (Heidenreich 1964). Insertion of a limiting aperture in the back focal plane of the objective lens removes the most widely scattered electrons but also results in a loss of information due to removal of these scattered electrons. We also have to consider the aperture diffraction aberration limit to resolution, r_d given by

$$r_d = 0.61 \lambda / \alpha, \quad \lambda = \text{wavelength of the electrons.}$$

The optimum size of the objective aperture, α_{opt} , is a compromise between these effects given by

$$\alpha_{\text{opt}} = A \alpha^{\frac{1}{4}} C_s^{\frac{1}{4}} \quad A \text{ is a constant } \approx 1$$

The minimum aberration limit r_{\min} , is given by

$$r_{\min} = B \lambda^{\frac{3}{4}} C_s^{\frac{1}{4}} \quad B \text{ is a constant } 0.56 > B > 0.43$$

In practice α_{opt} , the angle subtended at the specimen by the objective aperture is $\approx 6 \times 10^{-3}$ radians, corresponding to an aperture diameter of $\approx 40 \mu \text{m}$. The spherical aberration constant can be reduced by shortening the focal length of the objective lens. Short focal length objective lenses are now an important feature of high resolution electron microscopes.

Chromatic aberration

Chromatic aberration arises from the energy spread in the electrons passing through the objective lens. Electrons of lower energy are brought to a focus before those of higher energy forming a disc of confusion at the image plane.

The focal length, f , of an electron lens is given by

$$f = K \cdot \frac{V_r}{(NI)^2} \quad \begin{array}{l} \text{where } K \text{ is a constant, } V_r \text{ is the} \\ \text{accelerating voltage,} \\ \text{relativistically corrected and} \\ NI \text{ is the ampere turns on the} \\ \text{excitation coils.} \end{array}$$

$$\text{Therefore } \frac{\Delta f}{f} = \frac{\Delta V_r}{V_r} - \frac{2\Delta I}{I}$$

showing that a variation in either accelerating voltage or lens current will cause a change in the effective focal length of the lens. The chromatic aberration constant C_c expresses the sensitivity of the objective lens to the above variations. The limit on resolution due to chromatic effects expressed as a disc of confusion of diameter dc , given by,

$$dc = C_c \alpha \left(\frac{\Delta V_r}{V_r} - \frac{2\Delta I}{I} \right)$$

The chromatic aberration coefficient is similar in magnitude to the focal length. For a resolution of 0.5nm a stability in the objective lens supply and high voltage supply of a few parts per million is required.

Astigmatism

This is caused by asymmetry in the objective lens field produced either by inaccuracies in manufacture or inhomogeneities in the soft iron pole piece. Astigmatism causes a point object to be imaged as two mutually perpendicular lines at different levels in image space, causing a directional structure in the image. This can be corrected using a compensating elliptical lens field.

Coherence

A coherent source produces rays which have the same plane of polarisation, the same wavelength and are exactly in phase. Coherent illumination is essential for resolving lattice images, fresnel fringes and observing other phase contrast effects. Coherence is improved by using a small condenser aperture and a pointed filament. Pointed filaments are formed by welding a small oriented single crystal of tungsten onto an ordinary filament tip and then etching down to a very fine point (Hibi 1964), (Fernandez-Moran 1966).

Depth of field

A diagrammatic representation of this is shown in Figure 8. Depth of field, D_o , of an electron lens is the axial distance over which the lens may be focussed without a perceptible change in image sharpness. O_1 and O_2 are object points

Figure 7 Spherical aberration

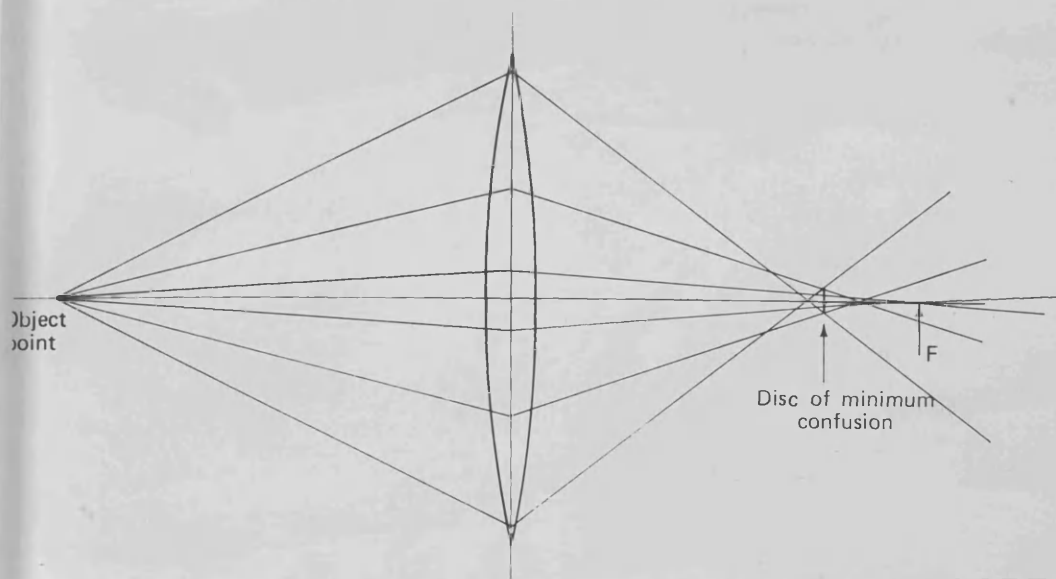
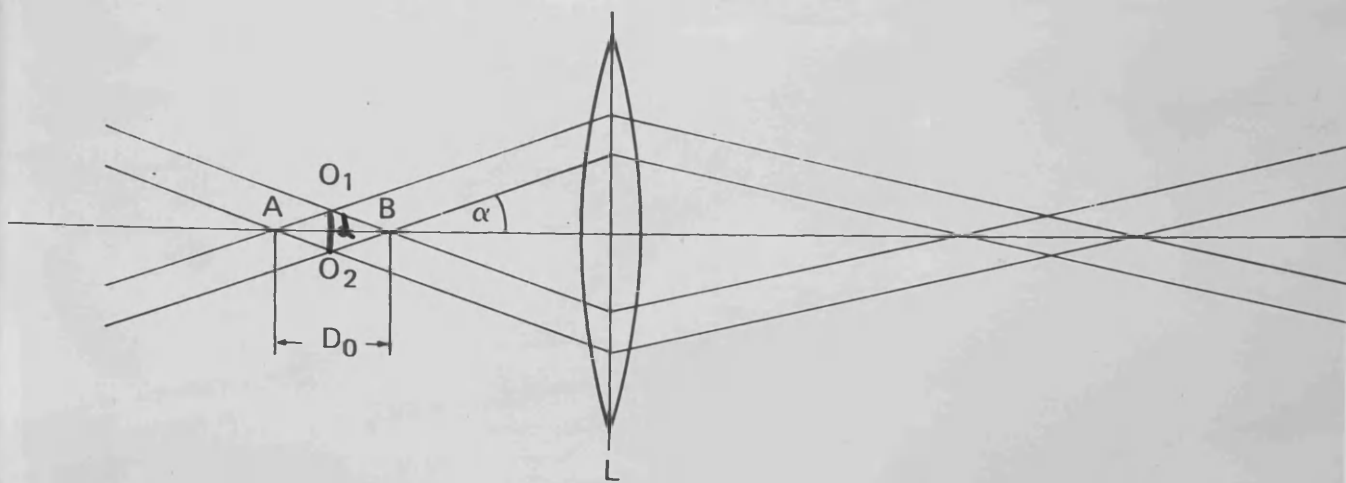


Figure 8 Depth of field.



separated by the limiting resolution distance, d , for the lens. Parallel rays through O_1 and O_2 cut the axis of the lens at A and B and any points within the distance AB will appear to be equally sharp. The distance AB is defined as the depth of field D_0 where

$$\frac{d}{2} = \frac{D_0 \tan \alpha}{2}$$

for small α ,

$$D_0 = d/\alpha$$

For a resolution of 1nm, where $\alpha = 5 \times 10^{-3}$ radians, $D_0 = 200\text{nm}$. This is greater than the thickness of any specimen normally examined in a 100kV electron microscope and therefore the specimen appears equally sharp throughout its thickness. If a resolution of 0.5nm is required, with $\alpha = 10^{-2}$ radians the depth of field is reduced to 5nm and becomes a limiting factor for some specimens.

Specimen.

Specimen damage may occur in the electron microscope by heating, bombardment by gaseous ions formed and by the electron beam. Electron diffraction is a sensitive monitor of specimen damage. If damage occurs in a crystalline specimen the diffraction pattern becomes streaked or disappears. An initially amorphous material may crystallise in the beam shown by the appearance of a spot or ring diffraction pattern. Ionic salts are known to break down to form oxides under intense beam irradiation, while delicate organic specimens deteriorate as a result of polymerisation and cross linking. An image intensifier allows use of a lower electron beam intensity thus reducing beam damage.

Contamination of the specimen by deposition of amorphous material was first noted by Watson (1947). The deposit was thought to be a hydrocarbon polymer (Konig 1951). Most modern electron microscopes are equipped with anticontamination devices, consisting of liquid nitrogen cooled jackets which surround the specimen and on which the organic vapours which lead to most contamination will preferentially condense. Contamination rates as low as 0.1\AA per minute are now possible.

Image Contrast

Contrast in electron microscopes images arises from interactions between the electron beam and the specimen.

Elastic scattering

When electrons interact with the nuclei of the specimen they do so elastically without any loss of energy. The resulting scattered beams of electrons are coherent with respect to the transmitted beam. In a crystalline specimen the angles through which electrons are elastically scattered are determined by the Bragg Law, relating crystal lattice geometry and the wavelength of the electrons.

$$\lambda = 2d_{hkl} \sin \theta$$

λ = electron beam wavelength,

θ = angle of scatter,

d_{hkl} = interplanar spacings for hkl planes.

Inelastic scattering

When an electron in the beam encounters one of the orbital electrons in an atom of a thin specimen, it loses energy and

is inelastically scattered. These electrons are scattered through a very small angle $\approx 10^{-4}$ radians. In general inelastically scattered waves are incoherent and do not contribute towards meaningful image contrast.

Three types of contrast may occur.

Thickness contrast

A thick specimen produces much scattering of the electron beam, and if the scattered electrons are prevented from contributing to the final image by inserting a limiting aperture in the back focal plane of the objective lens, the thick parts of the specimen will be imaged as dark areas. A similar situation arises with specimens containing heavy atoms. Transmission of electrons through material depends on the atomic number of the atoms of the material.

Elastic scattering cross section

The overall elastic scattering cross section, Q_{el} , was given by Hirsch et al (1965) as

$$Q_{el} = \int_{\alpha=0}^{2\pi} \int_{\beta=0}^{2\pi} |\psi_g|^2 \sin \beta \, d\beta \, d\alpha$$

α = angle variable about the optic axis

β = scattering angle

ψ_g = amplitude of the scattered wave.

The use of an aperture in the back focal plane of the objective lens makes it possible to separate the contrast due to elastic scattering into contributions from phase contrast and diffraction contrast.

In the equation:

$$Q_{el} = \int_{\alpha=0}^{2\pi} \int_{\beta=0}^{\beta_{obj}} |\psi g(\alpha\beta)|^2 \sin\beta d\beta d\alpha + \int_{\alpha=0}^{2\pi} \int_{\beta=\beta_{obj}}^{\pi} |\psi g(\alpha\beta)|^2 \sin\beta d\beta d\alpha$$

The first term is due to that fraction of the scattered waves which pass through the objective aperture giving phase contrast and the second term is due to diffracted electrons which are cut off by the aperture and do not contribute to the final image giving diffraction contrast.

Diffraction contrast

In a crystal specimen removal of Bragg diffracted beams from the image-forming electrons by insertion of a limiting objective aperture produces contrast in the image, those areas of the specimen in a strongly diffracting position being imaged as dark areas. For thin specimens where the electrons interact only once with the specimen, the kinematical theory has been developed to calculate the intensity of the diffracted beams. Although only a qualitative theory it accounts, with reasonable success, for contrast variations arising, in crystalline specimens, from dislocations, variations in thickness and other features (Whelan 1959, Hirsch et al 1965). Knowing the size of the limiting objective aperture, the total intensity of the remaining image-forming rays can be found by calculating the total scattered intensity. The information content of the scattered electron waves is not recovered. The information loss from the primary beam can be found from the operation of the kinematic theory. Although the primary beam itself carries no structural information, the knowledge of the total information loss, along with the contrast features observed, allows for

reasonably accurate interpretation of these contrast features. This type of contrast will highlight details down to 1nm in size. For thick crystals the kinematic theory is not accurate and the dynamical theory has been developed. The dynamical theory covers the case of 'double diffraction' in a crystal where the electrons diffracted from one set of planes may act as a primary beam for diffraction from a second set of planes and 'extra spots', unexpected from consideration of the crystal structure, may occur.

Phase contrast

If the object is thin enough to be regarded as a phase grating, usually less than 100\AA , phase contrast theory can be applied to explain contrast of features less than 10\AA in size.

If the electron source is coherent, electrons, transmitted through an object without interaction, interfere with those scattered by it. After a single elastic collision the wave vector associated with the scattered electrons undergoes a phase shift X with respect to the unscattered background wave due to the instrumental factors of defocus and spherical aberration. This phase shift is given by

$$X = \frac{-2\pi}{\lambda} \left(\frac{1}{4} C_s \alpha^4 - \frac{1}{2} \Delta f \alpha^2 \right)$$

where Δf is the defocus. (Johnson and Crawford 1972)

For an elastic collision the phase angle between scattered and unscattered waves is $\pi/2$, therefore the total phase shift at the image plane is

$$X = \frac{\pi}{2} - \frac{\pi}{2\lambda} C_s \alpha^4 + \frac{\pi}{\lambda} \Delta f \alpha^2$$

Since in the image plane the intensity change relative to the

background varies as $\cos X$ (Heidenreich 1964) contrast maxima occur at $X = n\pi$

Therefore

$$(2n-1) \frac{\lambda}{2} = -\frac{1}{2} C_s \alpha^4 + \Delta f \alpha^2$$

For a structure of spacing d , the Bragg scattering angle will be α where

$$\alpha = \frac{\lambda}{d}$$

Substituting this value of α in the above equation gives

$$\Delta f = \frac{(2n-1)d^2}{2\lambda} + \frac{1}{2} C_s \frac{\lambda^2}{d^2}$$

Since the wavelength of a 100kV electron beam is 0.037\AA and d is greater than 1\AA , α will be very small and the rays will be passing very near the optical axis of the lens thus the contribution from spherical aberration will be small and can be neglected giving

$$\Delta f = \frac{(2n-1)d^2}{2\lambda}$$

$$\text{for } n=0 \quad \Delta f = -\frac{d^2}{2\lambda}$$

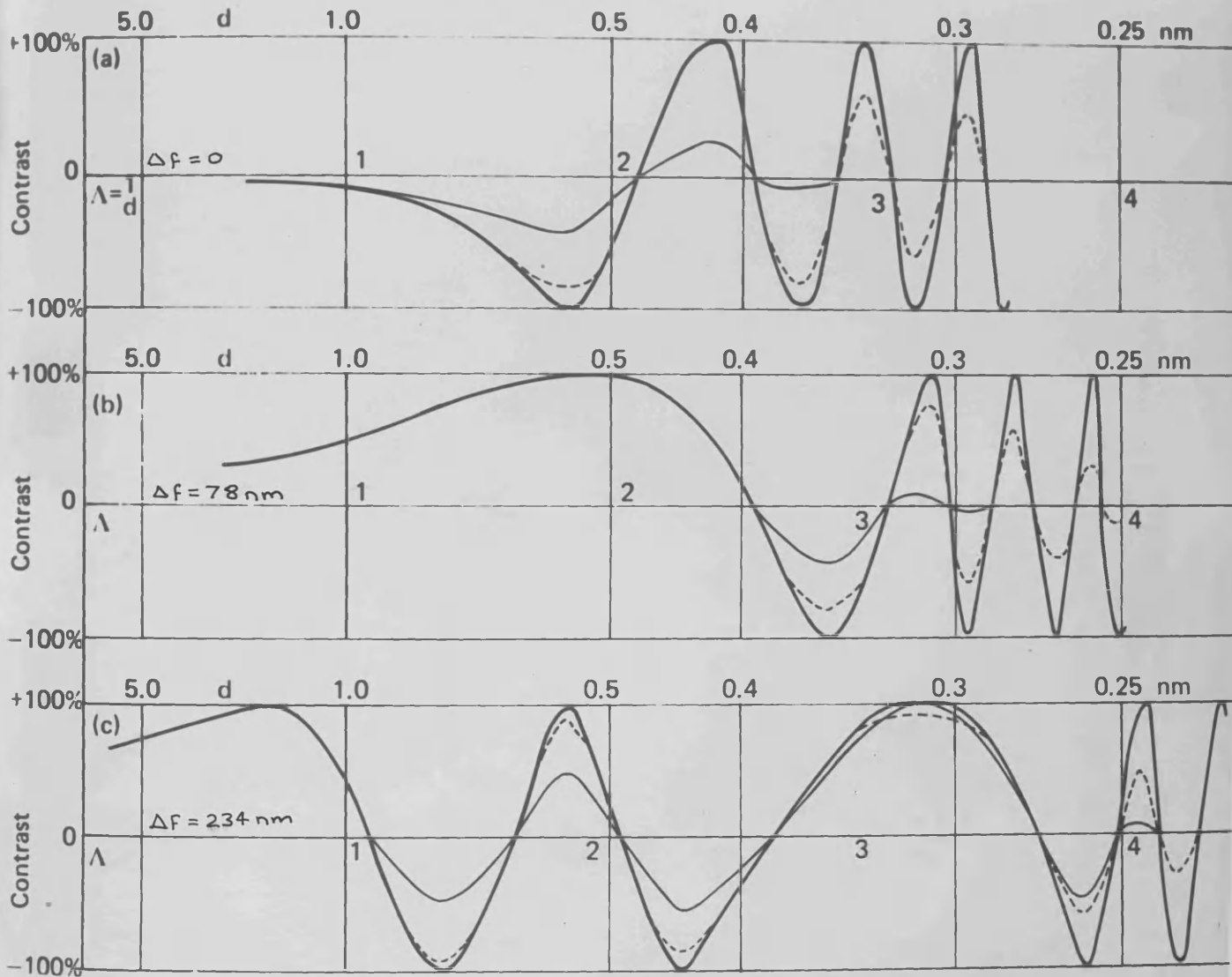
$$\text{for } n=1 \quad \Delta f = \frac{d^2}{2\lambda}$$

Positive defocus requires an underfocused objective lens i.e. reduced lens current and increased focal length. The relationship $\Delta f = d^2/\lambda$ can be useful in enhancing various periodicities by defocus phase contrast.

Alternatively the imaging properties of an electron optical system can be explained in terms of optical transfer theory, a detailed account of which is given by

Figure 9 Plots of image phase contrast against spatial frequency.

$$C_s = 1.6 \text{ mm}$$



Hanszen (1971). Optical transfer theory is expressed in terms of spatial frequencies. An infinite spectrum of spatial frequencies is related to an object point. Spatial frequencies which are measured in lines / nm are related to structure size in a way analagous to the relationship between electrical frequencies in cycles /second and wavelength. For any particular value of defocus Δf , there is a series of values of spatial frequencies which exhibit maximum contrast. Figure 9 shows plots of image phase contrast against spatial frequency λ , structure size d has been added for convenience. (Glauert 1974).

Figure 9a. The in-focus picture yields very little phase contrast until a structure size of 0.55nm is reached when maximum negative phase contrast appears. The heavy line represents contrast in the absence of any chromatic effects and with fully coherent illumination. The dotted curve shows the effect of a chromatic aberration coefficient of 1.3nm and a supply fluctuation of 5×10^{-6} . For an illumination aperture of 10^{-3} radians, the thin continuous line shows the resultant loss of contrast.

Figure 9b. With an objective lens defocus of 78nm there is a wide range of structure sizes for which there is a positive phase contrast, and neither supply fluctuation nor aperture angle causes any appreciable loss of contrast. However there is zero contrast for structure sizes 0.4nm, 0.33nm and 0.3nm, and for all structure sizes smaller than 0.35nm the contrast is almost negligible.

Figure 9c With an objective lens defocus of 234nm the phase contrast alternates between maxima at 1.3nm, 0.72nm, 0.54nm and 0.43 nm and then enters a broad maximum at about 0.31nm where the effect of the illumination aperture is minimised. Curves of this type were first shown by Komoda (1964). These curves can be helpful in choosing operating conditions to enhance phase contrast of particular structure size for example particular lattice spacings.

Diffraction mode of operation

The ray diagram for diffraction mode of operation is shown in Figure 10. The diffraction pattern is formed in the back focal plane of the objective lens. The intermediate lens is focussed on the back focal plane of the objective lens producing a magnified image of the diffraction pattern which is further magnified by the two projector lenses and displayed on the screen. Discrete diffraction spots or rings only occur with crystalline samples where the electron beam is diffracted according to the Bragg law.

Selected area diffraction

This technique was developed by Le Poole (1947) enabling diffraction patterns to be obtained from small areas of the specimen. The selector aperture is inserted in the image plane of the objective lens where the specimen is magnified approximately fifty times, allowing the selecting aperture to be fifty times larger than the area it selects. The minimum selected area in the JEM 100c is 0.23 μm . The accuracy of

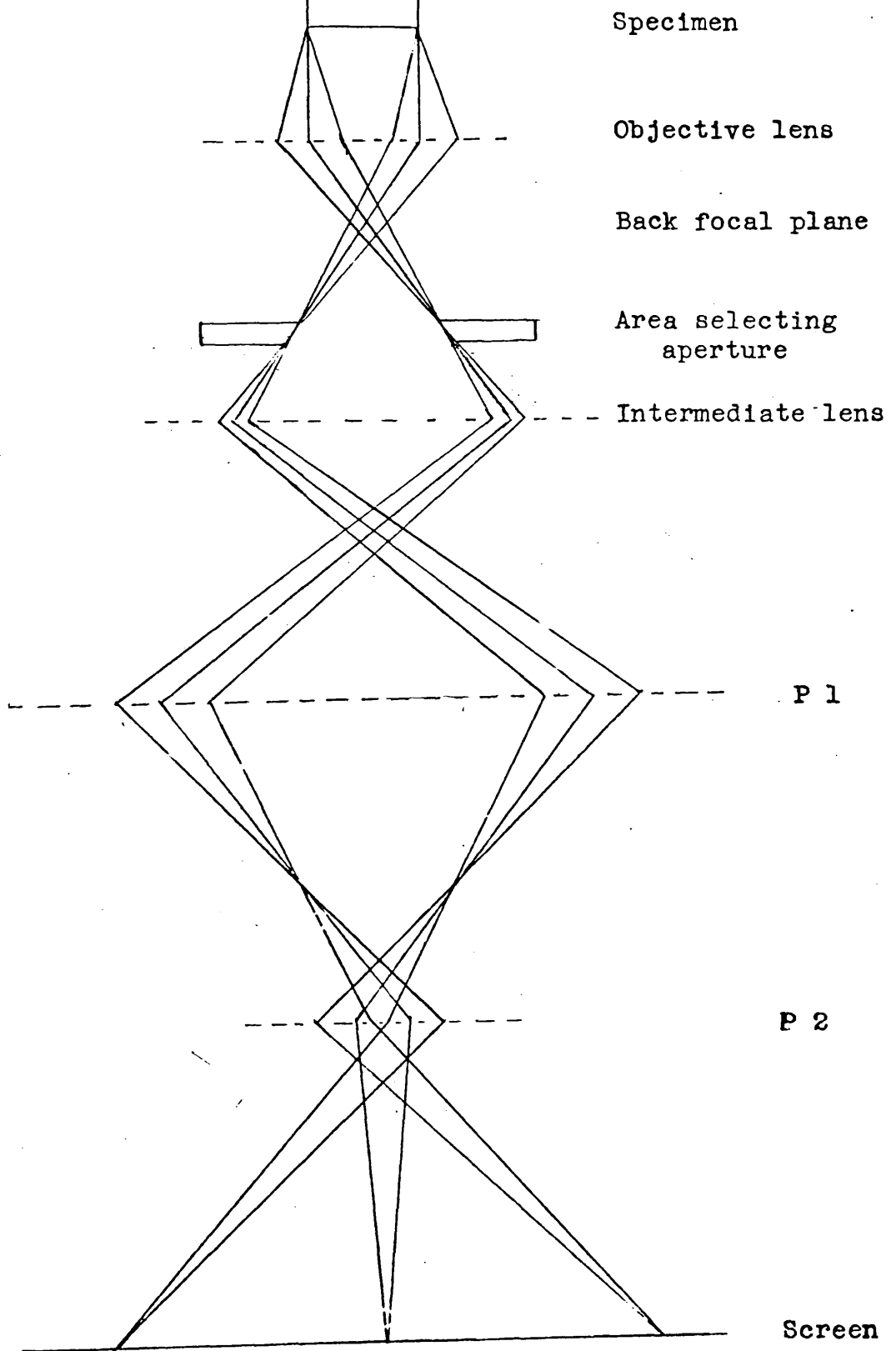


Figure 10 Ray diagram for diffraction.

(P = projector lens)

selected area diffraction has been discussed by Agar (1960), Phillips (1960) and Rieke (1961) and spherical aberration was shown to be one of the major sources of error in the selected area.

The interplanar spacings, d , are calculated from the diffraction pattern as follows :-

$$\frac{D/2}{L} = \tan 2\theta$$

where L is the effective camera length and D is the diameter of a pair of diffraction spots or a 'polycrystalline ring'.

The Bragg law states that :-

$$\lambda = 2d \sin\theta$$

Since the angles through which the electrons are diffracted are very small the approximation

$$\tan 2\theta = 2 \sin\theta$$

can be made. Then $\frac{D/2}{L} = \frac{\lambda}{d}$ or $\frac{D \cdot d}{2} = \lambda L$

Therefore $\frac{D \cdot d}{2} = K$ where K is the 'camera constant'.

The 'camera constant' may be found by calibration with a sample of known lattice parameters, which gives a sharp ring pattern. An evaporated film of thallous chloride is often used. The camera constant varies with the diffraction ring diameter due to the decreasing validity of the expression,

$$\tan 2\theta \simeq 2\sin\theta \simeq 2\theta,$$

as θ increases. The relationship is approximately linear (Andrews, Dyson and Keown 1967). The correction to the interplanar spacing is about 0.15 %.

Having calculated the interplanar spacings from the diffraction pattern, it may be possible to identify the selected area of the specimen using the A.S.T.M. index of crystallographic data. Electron diffraction is also used to monitor the specimen's stability in the electron beam.

Specimen support techniques

Conventional electron microscope specimen mounts consist of copper grids or perforated platinum-iridium discs. They are usually coated with a thin film of carbon prepared by evaporation (Bradley 1954). At high magnification the structure of the carbon film may affect the quality of the image. It has been suggested (Boiko et al 1968) that carbon films consist of particles about 12\AA in diameter, although the dependence of image granularity on the defocus of the objective lens makes accurate measurement difficult (Von Dorsten, Prensela 1966).

Various methods of avoiding background structure in high resolution images have been developed, the most widely employed being the use of perforated support films of nitro-cellulose or formvar reinforced with carbon. This technique was used by Bassett, Menter and Pashley (1956) to resolve the 6.93\AA (C20) lattice image in a MoO_3 crystal which was suspended over a hole in the support film. The use of perforated films has another advantage in that astigmatism checks may be carried out with the same specimen.

Fernandez-Moran (1966) used thin cleavage flakes of graphite less than 10\AA thick and thin mica flakes with regular 100\AA holes as supports. Silicon monoxide was used as an Hydrophilic support film by Taylor and Glasser (1973) and beryllium monoxide films have been used by Mihama (1974). Fibers of *crysotile* asbestos, used as a specimen support, provide background free micrographs of material suspended between the fibers while the 7.4\AA (001) lattice planes provide an internal calibration. A detailed study of *crysotile* asbestos as a support medium was carried out by Hutchison (1970), who showed that the disadvantages of mechanical instability and irradiation damage could be overcome by the use of a low beam current and by avoiding prolonged exposure of the specimen.

In this work fibres of *crysotile* asbestos, perforated films and evaporated carbon films were used as specimen supports. In the case of the precipitate obtained from the hydrolysis of vanadyl sulphate, no supporting film or fibre was used.

Specimen preparation techniques

Three methods of specimen preparation were used.

- (a) A drop of the sample, previously dispersed by ultrasonics, was allowed to evaporate onto the coated grid. (droplet method)
- (b) The sample was floated on to the copper grid with no supporting film.
- (c) The sample was sprayed from a glass atomiser onto the coated grid. (spray technique).

pH measurements

A Pye model 78 pH meter with a combination glass-calomel electrode was used. The calibration was checked frequently with standard buffer solutions. The hydrolyses at 40°C were carried out with the electrode in the solution, the pH meter being calibrated at 40°C.

Solid samples were prepared for Xray diffraction, differential thermal analysis and infra red spectroscopy by centrifuging the precipitates, washing with distilled water and vacuum drying.

Xray powder diffractions were obtained using a Phillips camera with cobalt K α radiation and an iron filter, or copper K α radiation and a nickel filter. The specimens were prepared for Xray work by rolling a finely ground sample into a thin fibre with 'durofix' glue.

Differential thermal analysis was carried out on a Du Pont 900 differential thermal analyser with temperature range from room temperature to 500°C and at a heating rate of 20°C per minute with ΔT sensitivity of 1°C per inch.

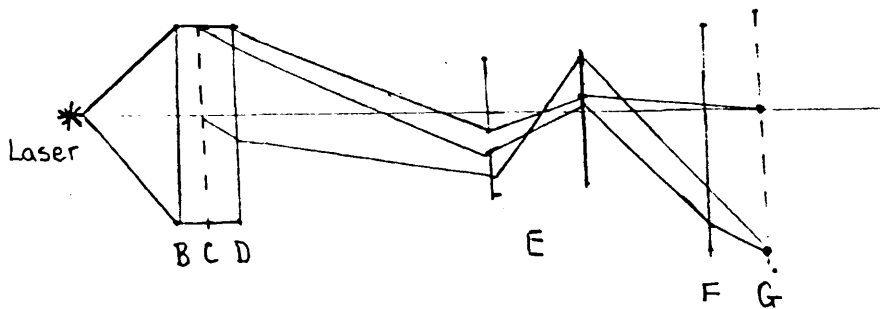
Infra red spectroscopy was carried out with a Perkin-Elmer 457 grating infra red spectrophotometer with KBr optics, capable of recording from 4000 cm^{-1} to 300 cm^{-1} . The samples were in the form of KBr discs.

A general survey of several metal salt hydrolyses and a more detailed study of the hydrolysis of iron (III) salts were carried out.

Laser diffraction

A 1 mW Helium -Neon laser was used. The optical bench was set up for diffraction as shown in figure 11.

Figure 11



The laser gives coherent light with a wavelength of 6328 \AA . The laser beam is 2mm in cross sectional diameter. The laser ray is expanded through a spatial filter into a plano convex lens. The plano convex lens B converts the divergent rays to a collimated beam of light approximately 1 cm in diameter incident on the specimen C. The specimen is mounted on an adjustable optical gate. The optical transform (diffraction pattern) of the specimen is imaged by the plano convex lens D. This image is magnified using a two lens telephoto system of lenses E and F. The transform can be viewed by placing the screen in a holder at position G. The diffraction pattern can be measured directly from the screen or can be recorded using the polaroid camera. The distance between E and F is proportional to the camera length and can be adjusted to increase or decrease the magnification of

the diffraction pattern. The theory of diffraction is the same as in the microscope and the same equation holds, viz.

$$\frac{D \cdot d}{2} = \lambda L$$

where D is the diametrical distance between a pair of spots in the diffraction pattern; d is the periodic spacing in the specimen; λ is the wavelength of the laser beam and L is the effective camera length.

The camera constant K, where $K = L$, for a particular lens setting can be calculated using a standard 0.16mm grating.

$$\text{Thus } K = 0.16 \times \frac{D}{2}$$

Ultracentrifugation

A Beckman model E analytical ultracentrifuge with a double beam ultraviolet absorption system was used. The ultracentrifuge measures the velocity of movement of macromolecules in a solution under the influence of a centrifugal field. This is known as the sedimentation velocity method. The output is a direct plot of solute concentration, c, against radial distance, x. During sedimentation the concentration of a solute increases towards the bottom of the cell. Between the supernatant and the solution of uniform concentration, the plateau region, there is a transition zone in which concentrations of species vary with the distance from the axis of rotation. This transition zone is called the boundary and the sedimentation velocity method is based on observation of the movement of boundaries i.e. movement of the solute molecules in the plateau region. The most commonly calculated solute parameter is the S_{20w} value i.e. the sedimentation

coefficient corresponding to the value it would have in a solvent having the same viscosity and density as water at 20°C. In this work the S_{20w} values were calculated from the output curves using a computer programme developed by Dr. Easson.

Materials used.

Johnson-Matthey 'Specpure' $UO_2(NO_3)_2 \cdot 6H_2O$

Analar $FeCl_3 \cdot 6H_2O$, $SnCl_2 \cdot 2H_2O$, $SnCl_4$

Koch-Light $Pr(NO_3)_3$, $Sm(NO_3)_3$, $GdCl_3$, $NdCl_3$, $Nd(NO_3)_3$, $CeCl_3$

$Ce(NO_3)_3$, $TiCl_4$, $Fe(ClO_4)_3 \cdot 9H_2O$

G.P.R. $Fe(NO_3)_3 \cdot 9H_2O$, $Fe_2(SO_4)_3 \cdot 9H_2O$, $VOSO_4$, $TiCl_3$, $AlCl_3 \cdot 6H_2O$

$Al(NO_3)_3 \cdot 9H_2O$, $Al_2(SO_4)_3 \cdot 16H_2O$

A general survey of several metal salt hydrolyses and a more detailed study of the hydrolysis of iron (III) salts were carried out.

Unless otherwise stated all solutions were made up to 0.01 molar with distilled water. The general survey hydrolyses were studied at room temperature and by boiling under reflux. Where there were no signs of precipitation after 2 months, excess NH_4OH was added to samples of the solution at room temperature. The pH of the solutions was noted on various occasions during the hydrolyses. The hydrolysis of $VOSO_4$ was also studied at 40°C and 60°C and pH measurements were taken over 109 hours. The final precipitates formed were examined in the electron microscope, specimens being prepared mainly by the droplet method except in the case of the precipitate from $VOSO_4$ which was floated onto copper grids.

The end product of the hydrolyses of iron(III) chloride and iron(III) nitrate at room temperature and under reflux, were examined by electron microscopy, electron diffraction, I.R. spectroscopy, D.T.A. and X ray diffraction. The hydrolysis products from refluxing iron(III) sulphate and iron(III) perchlorate solutions were examined in the microscope. The products from the hydrolysis of iron(III) chloride at temperatures below 70°C were examined in the electron microscope. The precipitates from hydrolysis of solutions of iron(III) nitrate containing various amounts of iron(III) chloride at room temperature, were examined in the microscope and by X ray diffraction. Solutions of iron(III) nitrate and iron(III) chloride were made up with absolute ethanol. Room temperature and reflux hydrolyses were examined by the above techniques. A solution of iron(III) chloride was allowed to hydrolyse at room temperature. A sample was withdrawn daily, over a period of 16 days, examined in the ultracentrifuge and sprayed onto asbestos fibres and examined in the electron microscope. Iron(III) chloride and iron(III) nitrate solutions were hydrolysed at 40°C and the pH of the solutions recorded over a period of 109 hours. Samples were withdrawn at several stages and examined in the microscope. The following iron(III) chloride solutions were made up from a stock 0.1 molar solution by dilution; 0.0005molar, 0.001 molar, 0.005 molar, 0.01 molar, 0.025 molar and 0.05 molar. They were thermostated at 40°C, and pH readings were taken over a period of time. The products were examined by electron microscopy and electron diffraction and where 'pods' of β FeOOH were produced size distributions

were obtained.

Table 1 shows the run codes and conditions of hydrolysis for the iron(III) system.

Table 1 Hydrolysis of iron(III) solutions

run code	Solution	Conditions of hydrolysis
Fe1	$\text{Fe}(\text{NO}_3)_3 \cdot 9\text{H}_2\text{O}$ (I)	room temperature
Fe2a	do	reflux
Fe2b	$\text{FeCl}_3 \cdot 6\text{H}_2\text{O}$ (II)	reflux
Fe4	do	room temperature
Fe3	$\text{Fe}(\text{NO}_3)_3 \cdot 9\text{H}_2\text{O}$ (alcohol)	room temperature
Fe6	do do	reflux
Fe7	$\text{FeCl}_3 \cdot 6\text{H}_2\text{O}$ (alcohol)	reflux
Fe5	do do	room temperature
Fe8	$\text{Fe}_2(\text{SO}_4)_3 \cdot 9\text{H}_2\text{O}$	reflux
Fe9	$\text{Fe}(\text{ClO}_4)_3 \cdot 9\text{H}_2\text{O}$	reflux
T1	$\text{FeCl}_3 \cdot 6\text{H}_2\text{O}$	25°C
T2	do	38°C
T3	do	46°C
T4	do	67°C
N1	200ml (I) + 50ml (II)	room temperature
N2	240ml (I) + 10ml (II)	do.
N3	249ml (I) + 1ml (II)	do.
N4	99ml (I) + 1ml (II)	do.
N5	50ml (I) + 50ml (II)	do.
N6	50ml (I) + 25ml (II)	do.
A	0.1M $\text{FeCl}_3 \cdot 6\text{H}_2\text{O}$	40°C
B	0.05M $\text{FeCl}_3 \cdot 6\text{H}_2\text{O}$	40°C
C	0.025M $\text{FeCl}_3 \cdot 6\text{H}_2\text{O}$	40°C
D	0.01M $\text{FeCl}_3 \cdot 6\text{H}_2\text{O}$	40°C
E	0.005M $\text{FeCl}_3 \cdot 6\text{H}_2\text{O}$	40°C
G	0.001M $\text{FeCl}_3 \cdot 6\text{H}_2\text{O}$	40°C
H	0.0005M $\text{FeCl}_3 \cdot 6\text{H}_2\text{O}$	40°C

RESULTS

General survey

Tin. SnCl_4 hydrolysed immediately on addition of water, while the SnCl_2 solution hydrolysed more slowly. Both solutions produced a creamy white precipitate. Reflux of SnCl_4 was carried out to investigate ageing effects. Reflux of both solutions was stopped after 2 months, by which time a white precipitate had been produced in the SnCl_2 solution, and the solutions were kept at room temperature for a further 2 years.

pH results. The pH of the SnCl_4 solution remained constant at 1.6 throughout the experiment, refluxing having no effect, whereas the pH of the SnCl_2 solution changed with time. The initial pH of the Sn(II) solution was 2.2, which had dropped to 1.6 while standing at room temperature for $2\frac{1}{2}$ years. The pH of the refluxed solution after $2\frac{1}{2}$ years was 1.8.

Electron microscopy. Samples of all four precipitates, prepared by the 'droplet method' were examined in the electron microscope. Electron diffraction patterns were recorded for all samples and all were identified as SnO_2 (cassiterite). Table 2 shows the measured 'd' spacings for the four samples of SnO_2 compared with the values for cassiterite given in the A.S.T.M. powder diffraction file, card no. 5-0467. Cassiterite has tetragonal symmetry with $a = 4.738\text{\AA}$ and $c = 3.188\text{\AA}$ and has a rutile structure as shown in figure 12.

Plate 1 shows the electron diffraction pattern of the precipitate from the refluxed SnCl_2 solution, and the transmission image of this material is shown in Plate 2. Plate 3 shows the SnO_2 produced from the room temperature hydrolysis of SnCl_2 . Crystals of SnO_2 , precipitated from the tetrachloride

Table 2 Electron diffraction 'd' spacings of SnO_2

source of SnO_2				Standard	
room temperature		reflux		SnO_2 (cassiterite)	
hydrolysis of		hydrolysis of		A. S. T. M. 5-0467	
SnCl_2	SnCl_4	SnCl_4	SnCl_2	d. Å	hkl
3.38	3.34	3.32	3.35	3.351	110
2.66	2.67	2.64	2.62	2.644	101
2.35	2.35	2.34	2.39	2.369	200
			2.29	2.309	111
			2.08	2.120	210
1.77	1.78	1.77	1.74	1.765	211
1.69			1.67	1.675	220
			1.58	1.593	002
			1.48	1.498	310
1.43	1.45	1.43	1.44	1.439	112
			1.41	1.415	301
			1.33	1.322	202
	1.21		1.22	1.215	321
			1.19	1.184	400
		1.16	1.16	1.155	222
	1.10		1.09	1.092	312
		1.08	1.08	1.081	411
		0.97	0.95	0.9505	402
			0.93	0.9291	510
			0.92	0.9143	332

Figure 12 The structure of Cassiterite.

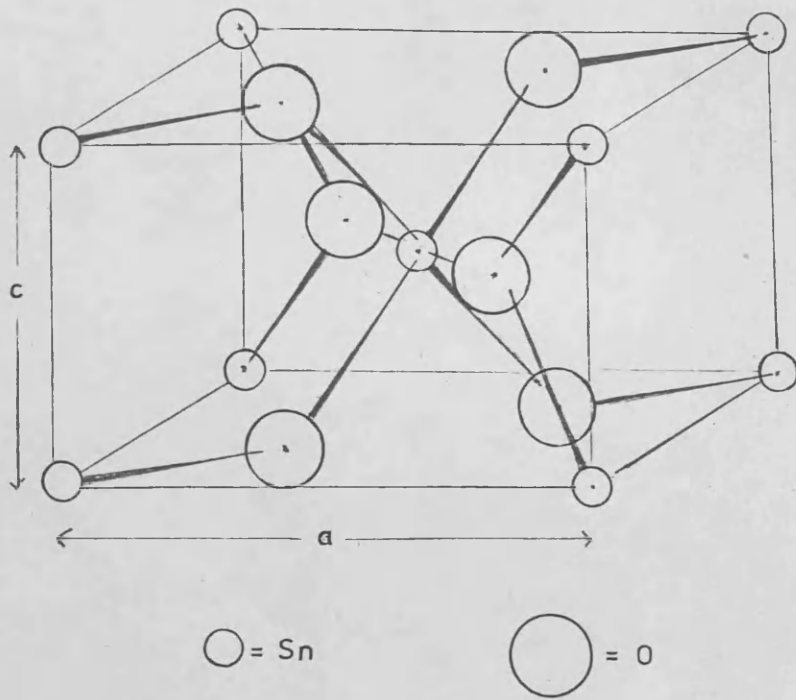
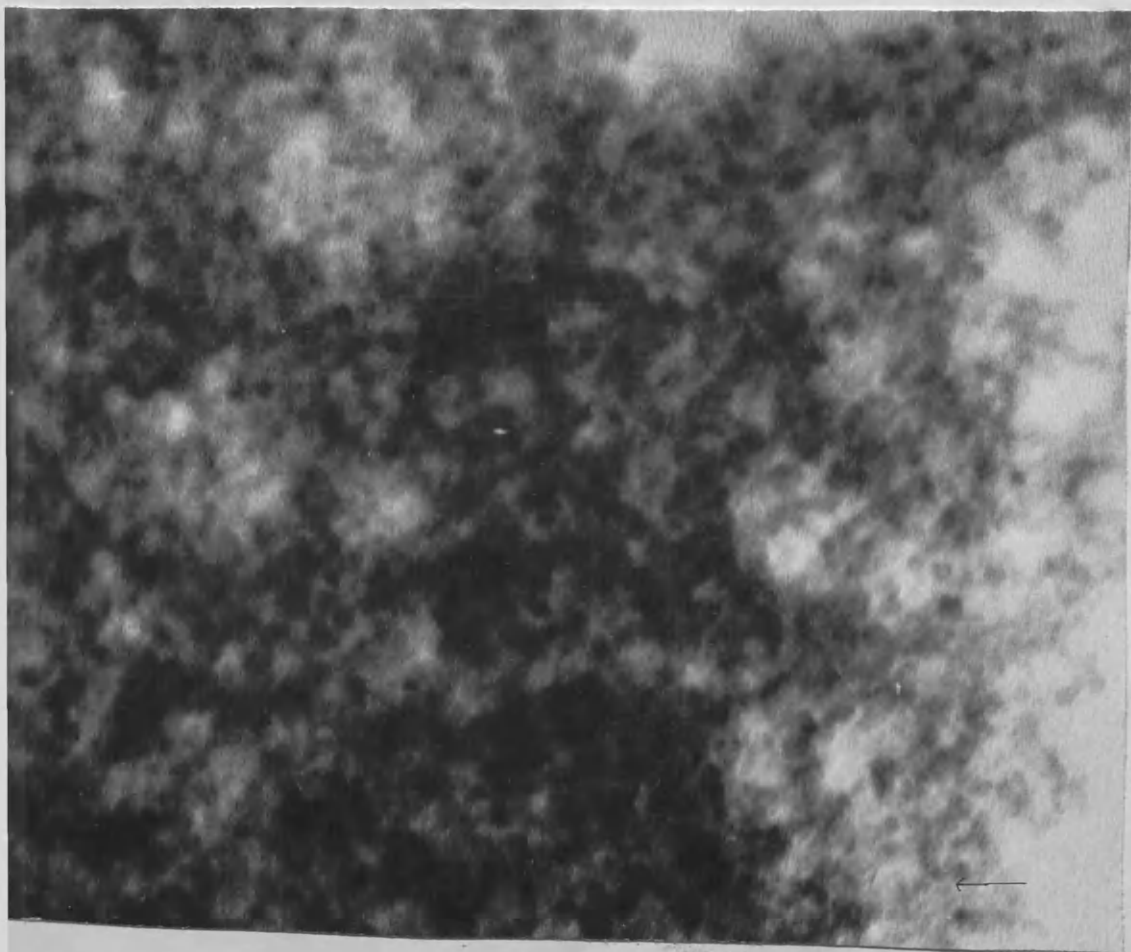


Plate 3 x 1260 K

335 =

solution by refluxing and at room temperature are shown in Plates 4 and 5 respectively. The (110) lattice spacing of 3.35 Å is clearly visible in Plates 3, 4 and 5 and is indicated by arrows. The crystals in these plates appear to be about 30-50 Å in diameter and seem to be arranged in chains. The material in plate 2 shows a 'sheet like' morphology.

Plate 5 x 940 K



Titanium. On making up the solutions the TiCl_4 hydrolysed immediately, becoming opalescent, while the TiCl_3 formed a clear solution which hydrolysed more slowly giving a pale opalescence. Samples of both solutions were refluxed, the TiCl_3 for 23 days and the TiCl_4 for 35 days, and both produced white precipitates. The solutions were kept at room temperature for a further $2\frac{1}{2}$ years. After $2\frac{1}{2}$ years the solutions which had not been refluxed remained opalescent but had not precipitated.

pH results The pH of the TiCl_4 solution remained constant at 1.6 throughout the experiment, refluxing having no effect, whereas the pH of the TiCl_3 solution decreased with time. The pH of the initial clear solution of TiCl_3 was 2.3, after $2\frac{1}{2}$ years at room temperature this had dropped to 2.0. The sample of TiCl_3 solution which had been refluxed had a pH of 1.9 after $2\frac{1}{2}$ years.

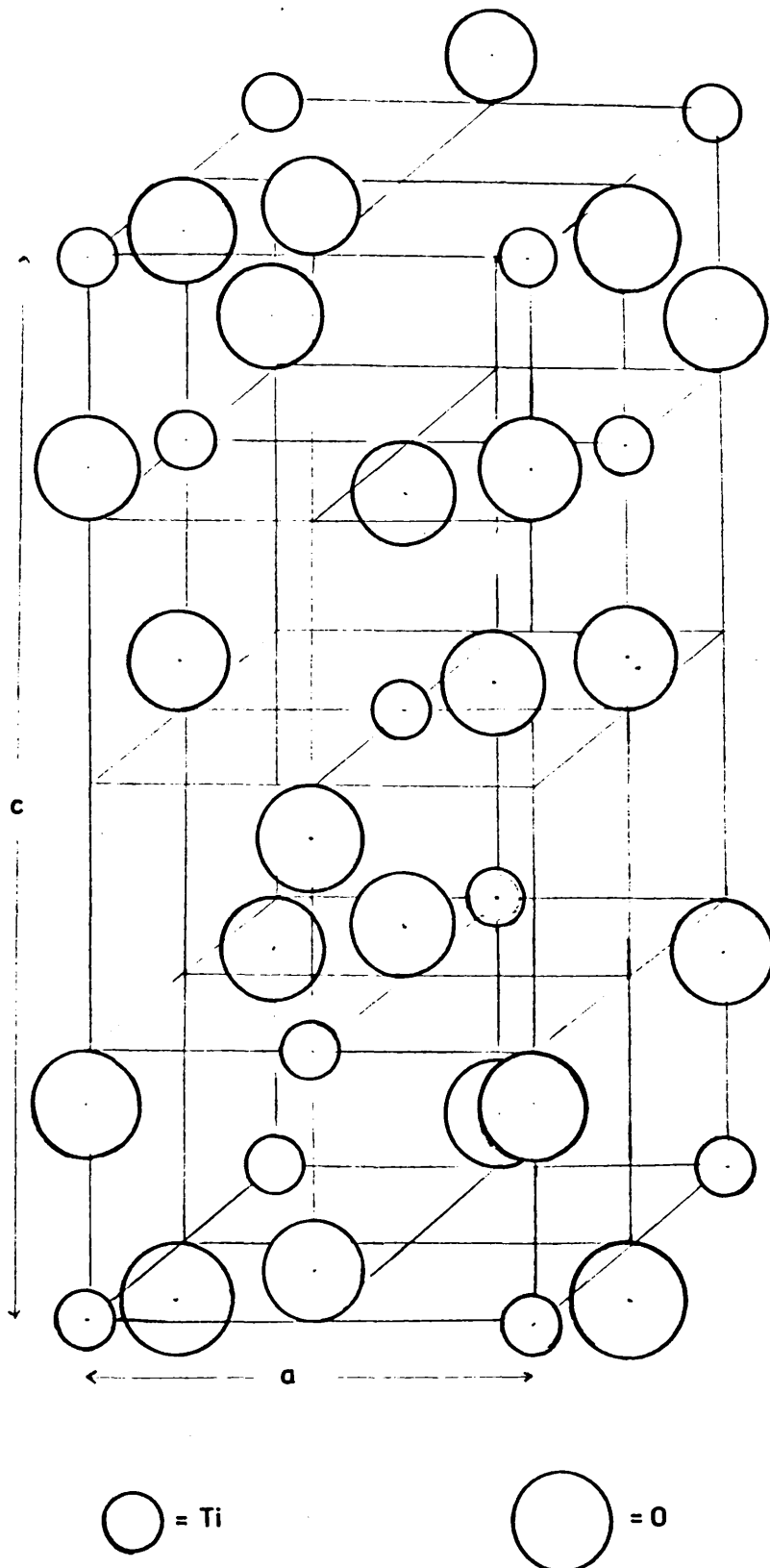
Electron microscopy. Samples from all four hydrolyses, prepared by the 'droplet method' were examined in the electron microscope. Electron diffraction patterns were recorded from all samples. The measured diffraction spacings are shown in Table 3 and are compared with TiO_2 (anatase). The spacings correspond well with anatase (A.S.T.M. card no. 21-1272). Anatase has tetragonal symmetry with $a = 3.785\text{\AA}$ and $c = 9.514\text{\AA}$ and its structure is shown in Figure 13. The TiO_2 crystals from the 4 different methods of preparation appear to have the same 'chain like' morphology as the SnO_2 crystals. Plate 6 shows crystals of TiO_2 prepared from refluxing TiCl_4 solution, and the diffraction pattern of the these crystals is shown in Plate 7. Plates 8 and 9 show TiO_2 produced by refluxing TiCl_3 and from the room temperature hydrolysis of TiCl_4 , respectively. Plate 10 shows TiO_2 produced

Table 3 Electron diffraction 'd' spacings for TiO_2 (anatase)

source of TiO_2				Standard	
room temperature		reflux		A. S. T. M. 21-1272	
hydrolysis of		hydrolysis of		TiO_2 (anatase)	
TiCl_3	TiCl_4	TiCl_3	TiCl_4	d, Å	hkl
3.52	3.54	3.53	3.49	3.52	101
	3.19		3.15	3.171*	003
2.94	2.93	2.92	2.92	2.96*	102
	2.47		2.44	2.431	103
2.36	2.36	2.38	2.37	2.378	004
1.92	1.88	1.91	1.90	1.892	200
1.69	1.68	1.68	1.69	1.6999	105
1.46	1.48	1.47	1.50	1.4808	204
1.37	1.36	1.36	1.35	1.3641	116
1.25	1.25	1.26	1.27	1.2649	215

* 'd' value calculated from the cell parameters.

Figure 13 The structure of Anatase.



after $2\frac{1}{2}$ years, by the room temperature hydrolysis of TiCl_3 solution. The 3.51 \AA (101) lattice spacing is resolved and is marked by an arrow. The lattice marked A has a spacing of 4.7\AA which corresponds to the (002) spacing of anatase.

PLATE 1

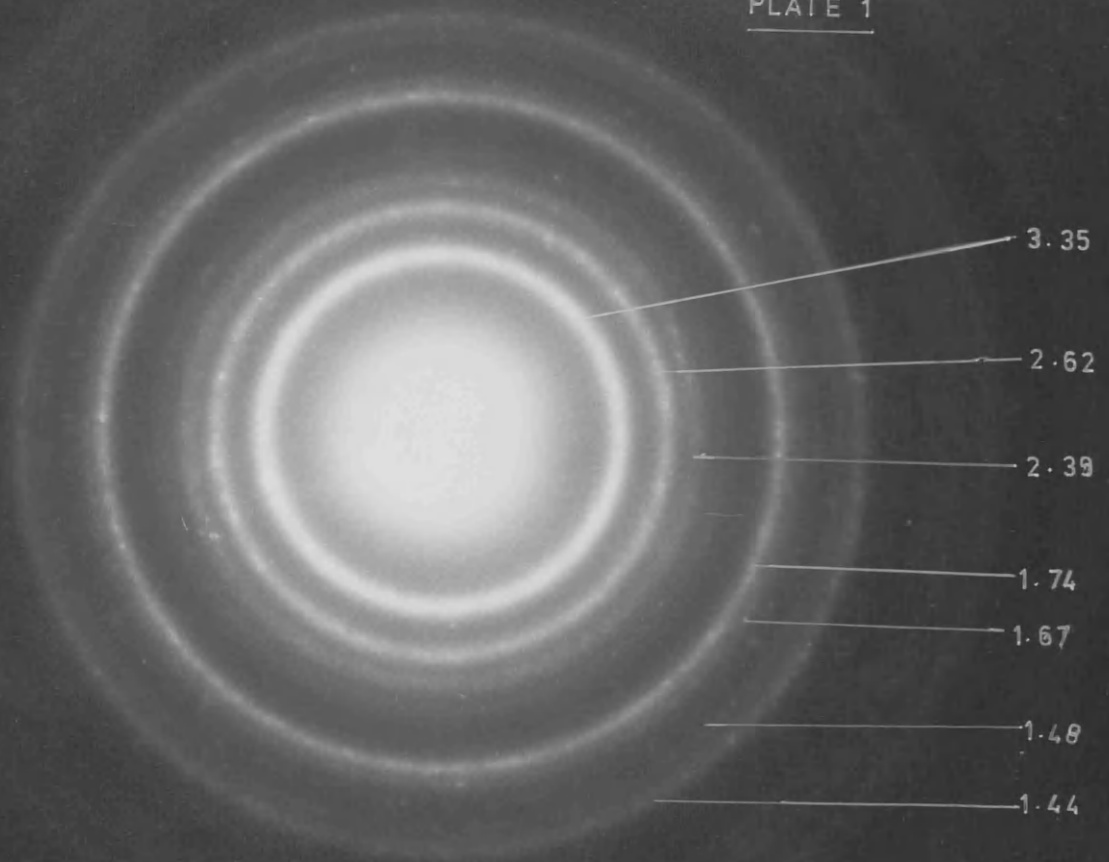
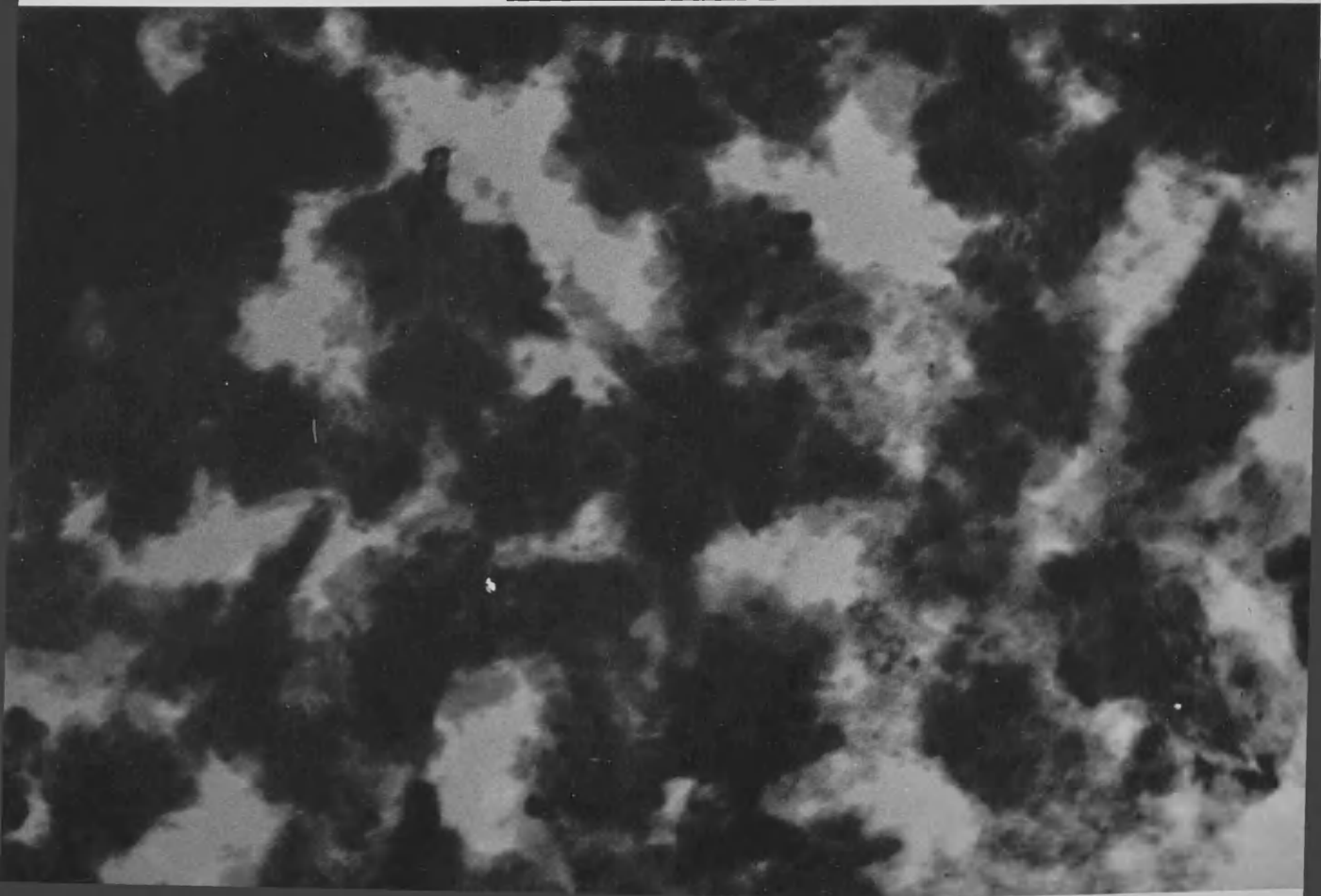


PLATE 2 X 466,000



→

335

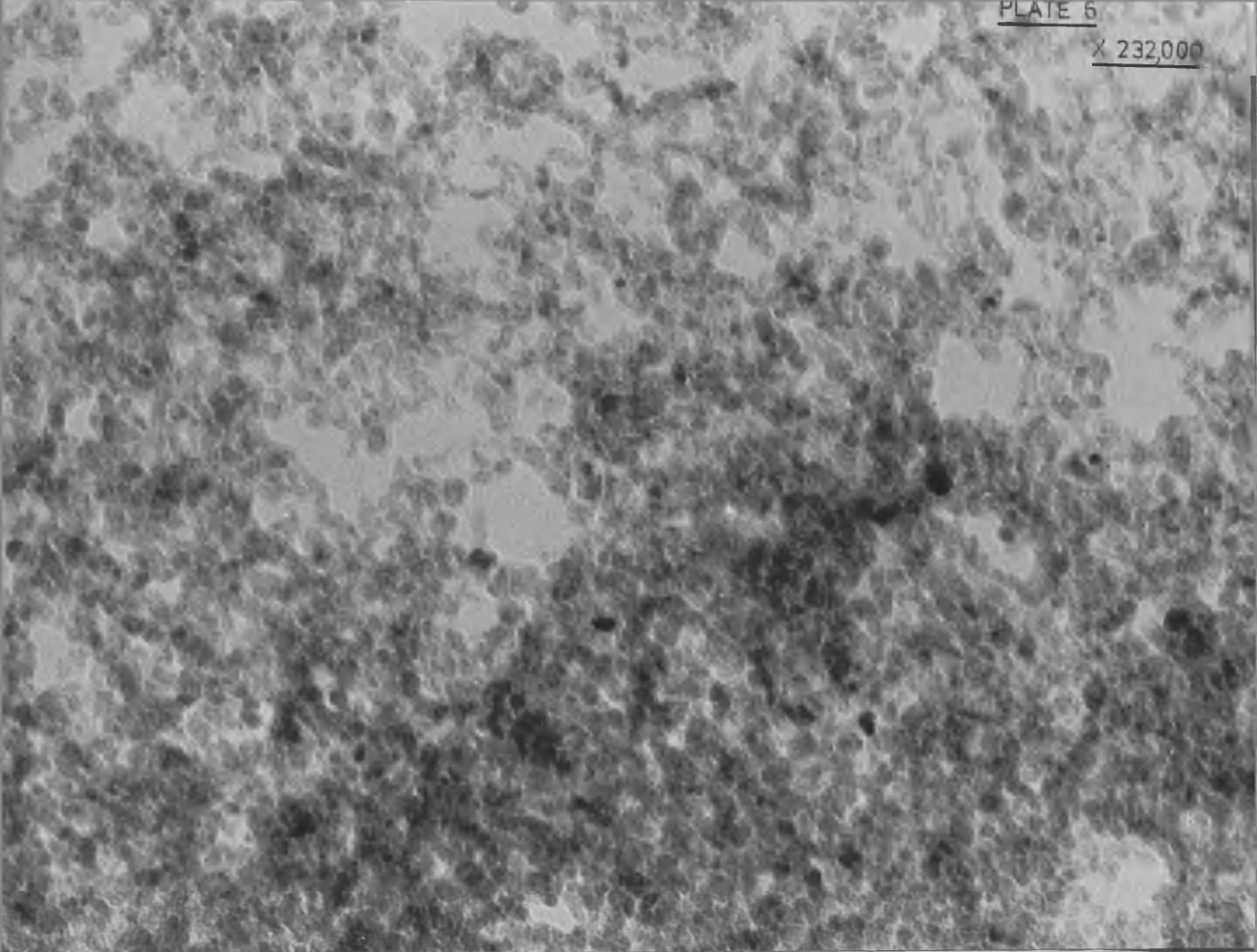
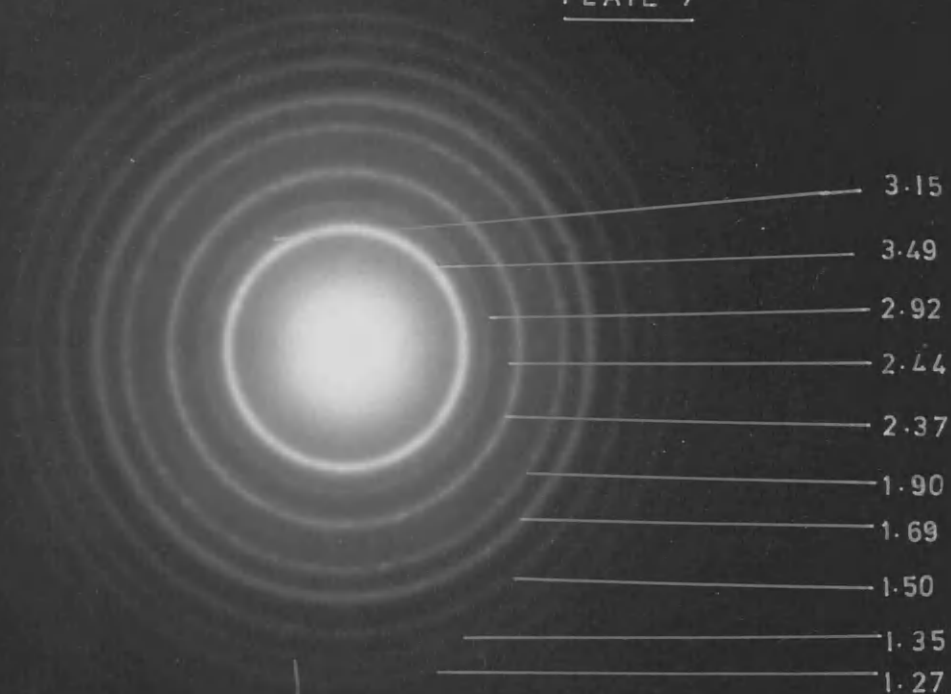


PLATE 7



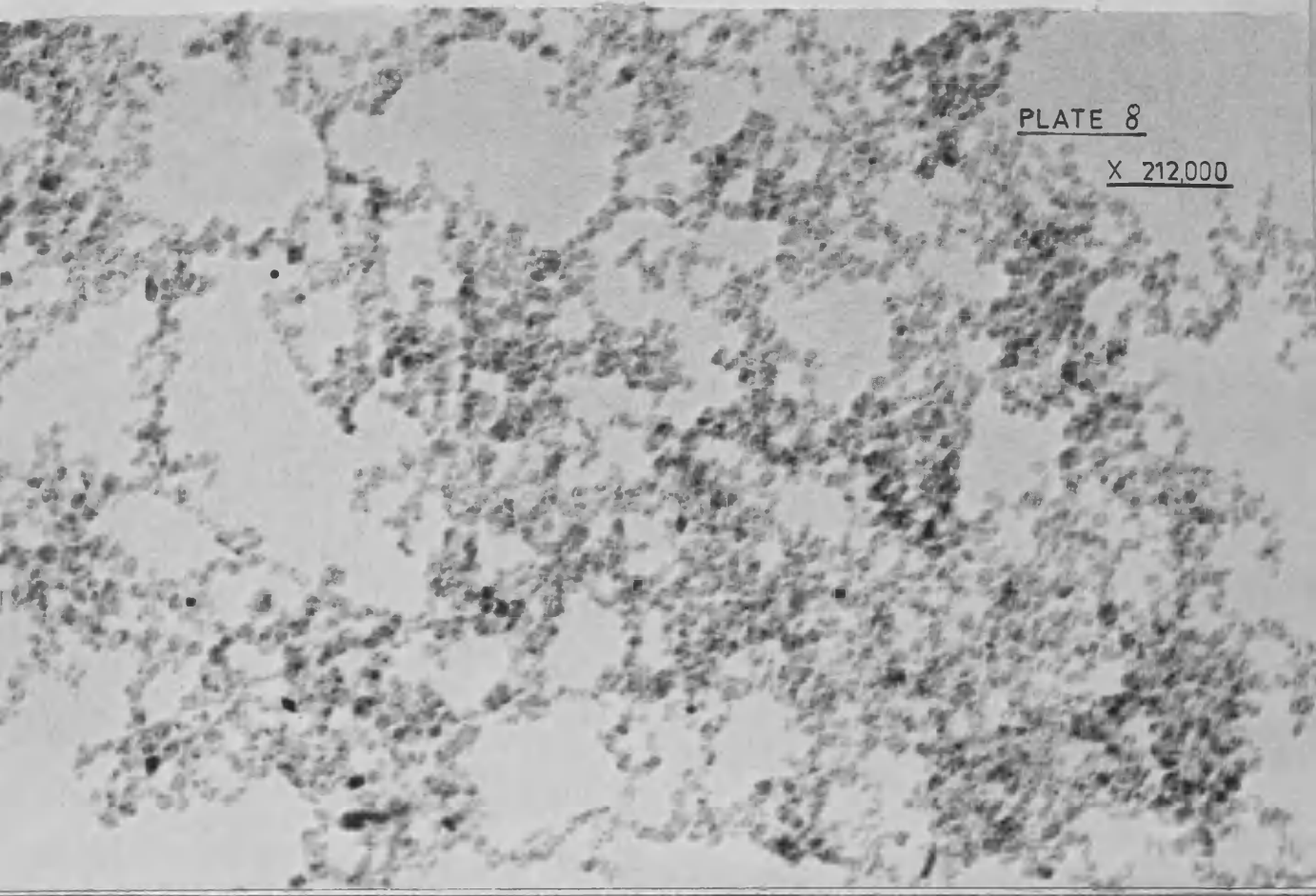


PLATE 8

X 212,000

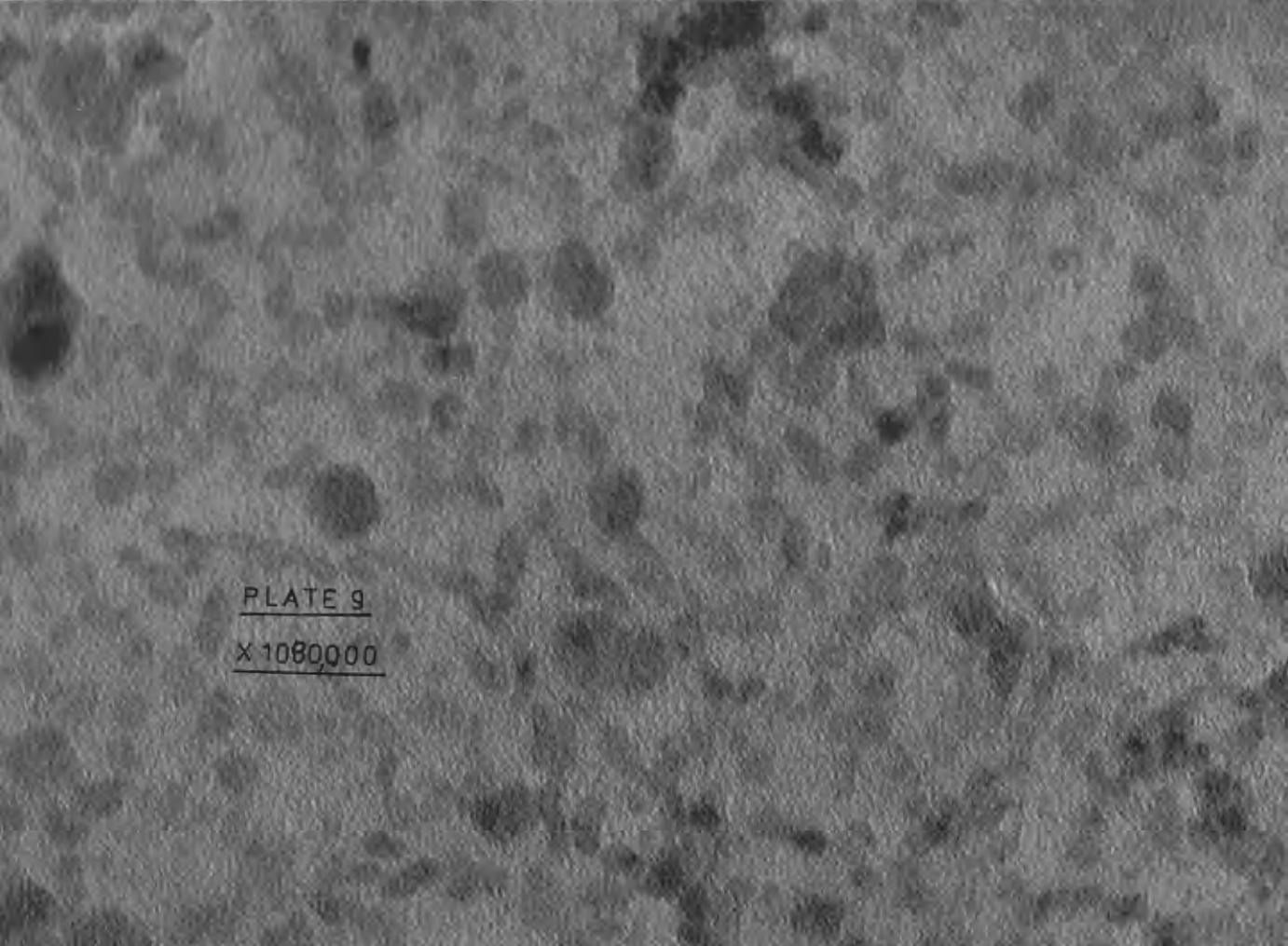


PLATE 9

X 1080000



4.7 μ

3.5 μ

Uranium. A 0.01M. solution of uranyl nitrate was refluxed for 2 months but showed no signs of precipitation. The solution remained unchanged after a further 2 years at room temperature.

Addition of excess ammonia solution to uranyl nitrate solution caused formation of a yellow precipitate. A specimen of this was prepared for electron microscopy by the 'droplet method' and transmission micrographs and electron diffraction patterns were obtained. The material was in the form of large thin sheets (plate 11). Overlapping sheets are visible in this micrograph. The electron diffraction pattern of this area is shown in plate 12. An Xray powder diffraction pattern was recorded and is given in Table 4. The pattern corresponds with that of ' $\text{UO}_3 \cdot 1\frac{3}{4}\text{H}_2\text{O} \cdot \frac{1}{4}\text{NH}_3$ ', A.S.T.M. card no. 14-340, reported by Garner (1961). The crystal is orthorhombic with $a = 7.16\text{\AA}$, $b = 12.21\text{\AA}$ and $c = 15.06\text{\AA}$ and is very similar to $\text{UO}_3 \cdot 2\text{H}_2\text{O}$. The electron diffraction 'd' spacings from plate 12 and the Xray powder diffraction spacings are compared with those of ' $\text{UO}_3 \cdot 1\frac{3}{4}\text{H}_2\text{O} \cdot \frac{1}{4}\text{NH}_3$ ' in Table 4.

Table 4. Diffraction results for the hydrolysis of Uranyl

<u>nitrate with ammonia.</u>		
<u>S. A. D.</u>	<u>Xray</u>	<u>A. S. T. M. 14-340</u>
		'UO ₃ . 1 $\frac{3}{4}$ H ₂ O. $\frac{1}{4}$ NH ₃ '
d, Å	d, Å	d, Å hkl
	7.56	7.55 002
	6.10	6.13 020
5.72	5.69	5.72 111
5.15		5.18* 102
	4.79	4.77 112
	3.76	3.77 004
3.52	3.56	3.54 130
3.24	3.21	3.233 202
2.84	2.86	2.854 222
	2.59	2.576 134
	2.51	2.509 006
	2.32	2.322 026 240
	2.22	2.215 242
2.14	2.16	2.122 017
	2.06	2.055 330
	1.99	1.985 332
1.89	1.89	1.885 008 063
	1.80	1.806 334
	1.67	1.693 170

* calculated from the cell parameters.

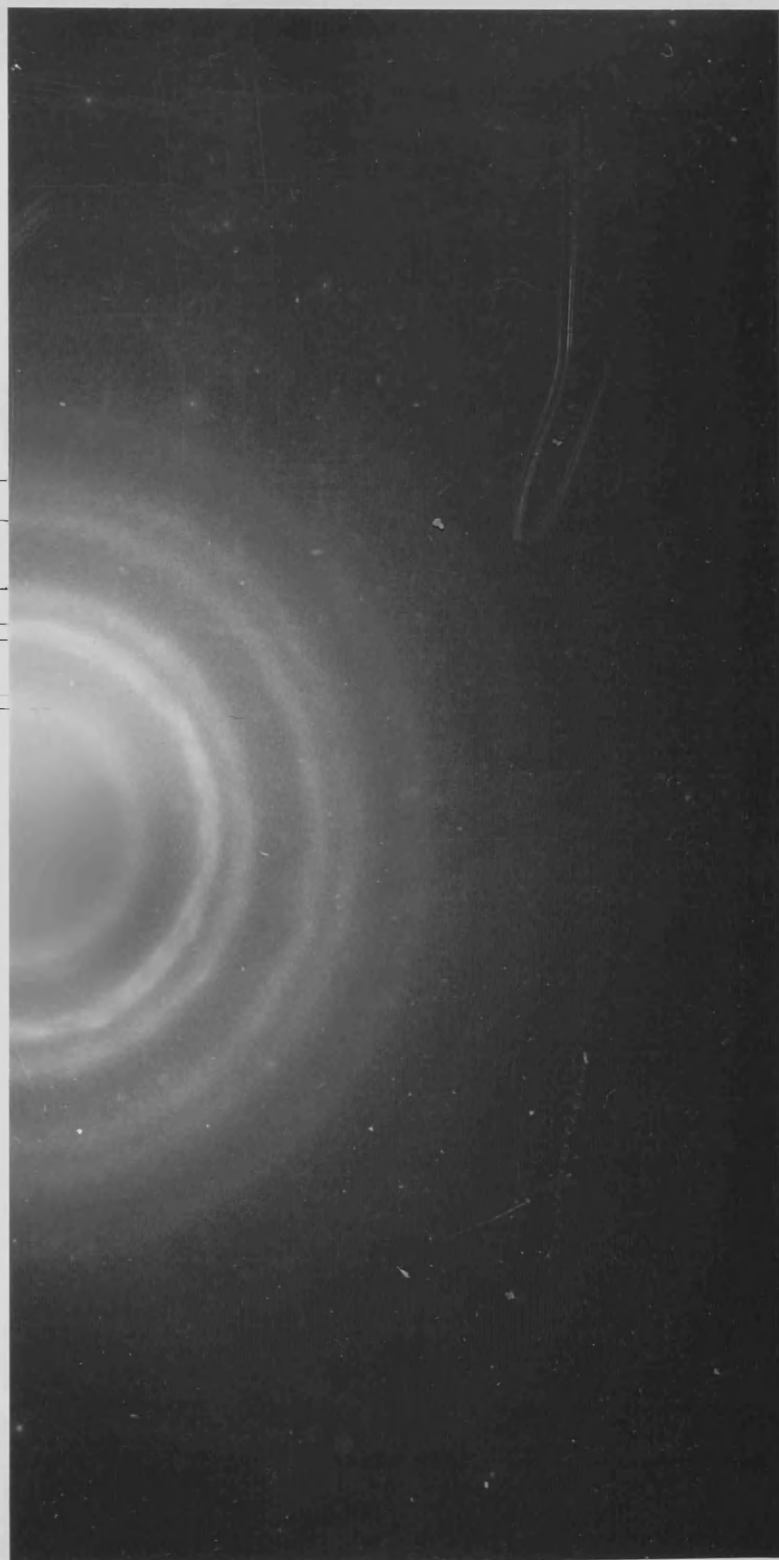


PLATE 11

X 318,000

Plate 12 The diffraction pattern of ' $\text{UO}_3 \cdot 1\frac{3}{4}\text{H}_2\text{O} \cdot \frac{1}{4}\text{NH}_3$ '

d Å
1.89 —
2.14 —
2.84 —
3.24 —
3.52 —
5.15 —
5.72 —



Rare earths. 0.01 molar solutions of CeCl_3 , $\text{Ce}(\text{NO}_3)_3$, $\text{Sm}(\text{NO}_3)_3$, $\text{Pr}(\text{NO}_3)_3$, NdCl_3 , $\text{Nd}(\text{NO}_3)_3$ and GdCl_3 were refluxed for two months but showed no signs of precipitation. On addition of excess ammonia solution Sm, Nd and Pr formed white pearly precipitates, Gd formed a white precipitate while Ce formed a pale brown precipitate, which changed colour to pale yellow in a few days. Specimens of each precipitate were prepared for electron microscopy by the 'droplet method'. Large cigar shaped crystals were observed from the Sm, Nd and Pr precipitates as shown in plates 13, 14 and 15. In plate 15 a lattice spacing of 5.6 \AA is resolved. Electron diffraction patterns were recorded for these precipitates (plates 16, 17 and 18) and are compared with the corresponding trihydroxides in table 5. The Ce specimen (plate 19) has a possible cigar morphology which gives a diffraction pattern (plate 20) which can be correlated with CeO_2 (table 5) while the Gd sample seems to be amorphous (plate 21).

Table 5 Rare earth precipitates with ammonia.

			<u>A. S. T. M. 6-117</u>			<u>A. S. T. M. 6-601</u>		
<u>Pr</u>	<u>Pr(OH)₃[*]</u>		<u>Sm</u>	<u>Sm(OH)₃</u>		<u>Nd</u>	<u>Nd(OH)₃</u>	
<u>dÅ</u>	<u>dÅ</u>	<u>hkl</u>	<u>dÅ</u>	<u>dÅ</u>	<u>hkl</u>	<u>dÅ</u>	<u>dÅ</u>	<u>hkl</u>
5.55	5.559	100	5.55	5.54	100	5.54	5.57	100
3.21	3.193	110	3.16	3.16	110			
3.10	3.077	101	3.00	3.03	101	3.09	3.08	101
2.76	2.765	200	2.72	2.734	200	2.73	2.768	200
2.46	2.447	111				2.42		
2.23	2.216	201	2.19	2.183	201	2.23	2.217	201
1.87	1.844	300	1.82	1.821	300	1.84	1.848	300
1.75	1.767	102	1.77	1.795	211			
1.62	1.601	220				1.62		
						1.31	1.310	401

A. S. T. M. 4-593

<u>Ce</u>	<u>CeO₂</u>	
<u>dÅ</u>	<u>dÅ</u>	<u>hkl</u>
3.10	3.121	111
2.68	2.706	200
1.91	1.913	220
1.62	1.632	311
1.24	1.241	331

* values given by Hardy, Buxton and Lloyd 1967.

PLATE 13
X 240,000

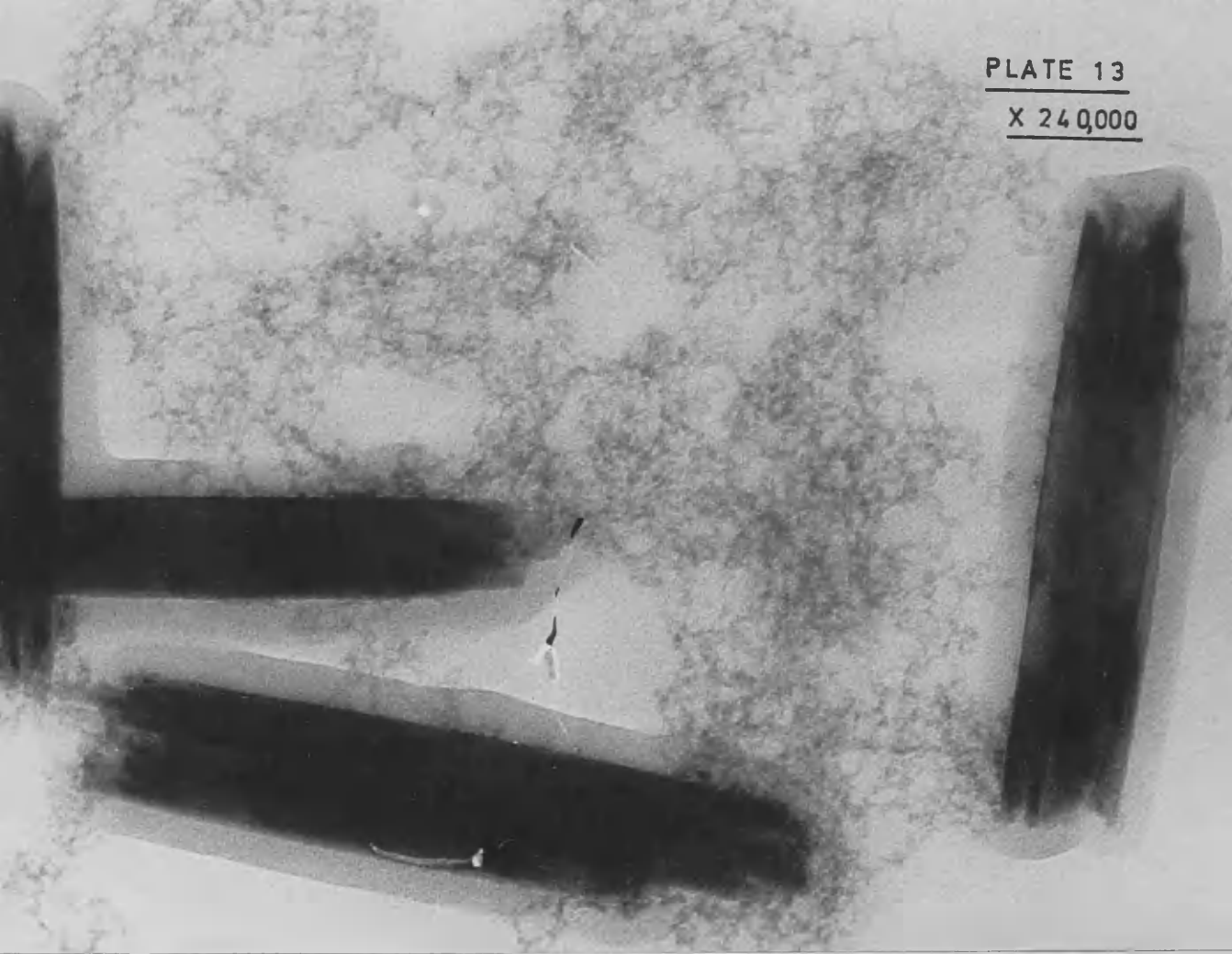


PLATE 14
X 240,000

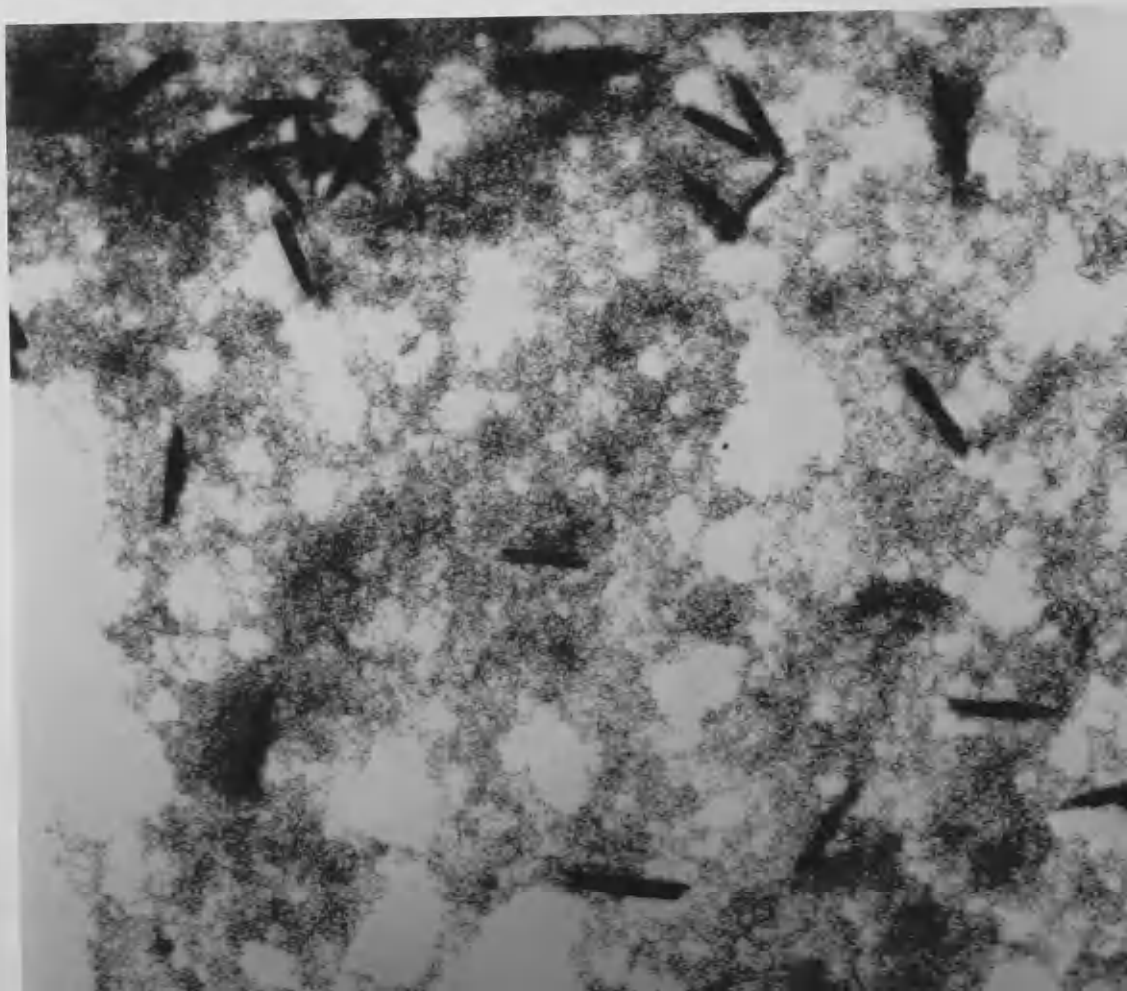


PLATE 15

X 5,170,000

Pr(OH)₃

Sm(OH)₃
PLATE 16

$d \text{ \AA}$
5.55

3.16

3.00

2.72

2.19

1.82

1.77

Nd(OH)₃

PLATE 17

$d \text{ \AA}$
5.54

3.09

2.73

2.42

2.23

1.84

1.62

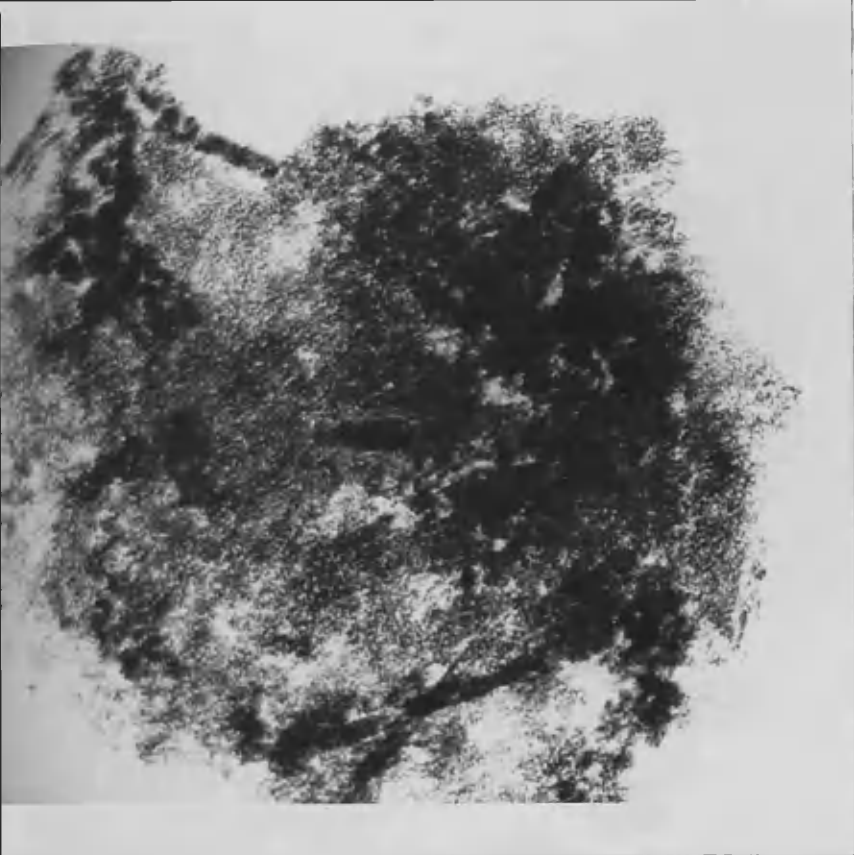


Plate 19 x 120,000

Plate 20 CeO_2

PLATE 20



Plate 18 Diffraction of $\text{Pr}(\text{OH})_3$

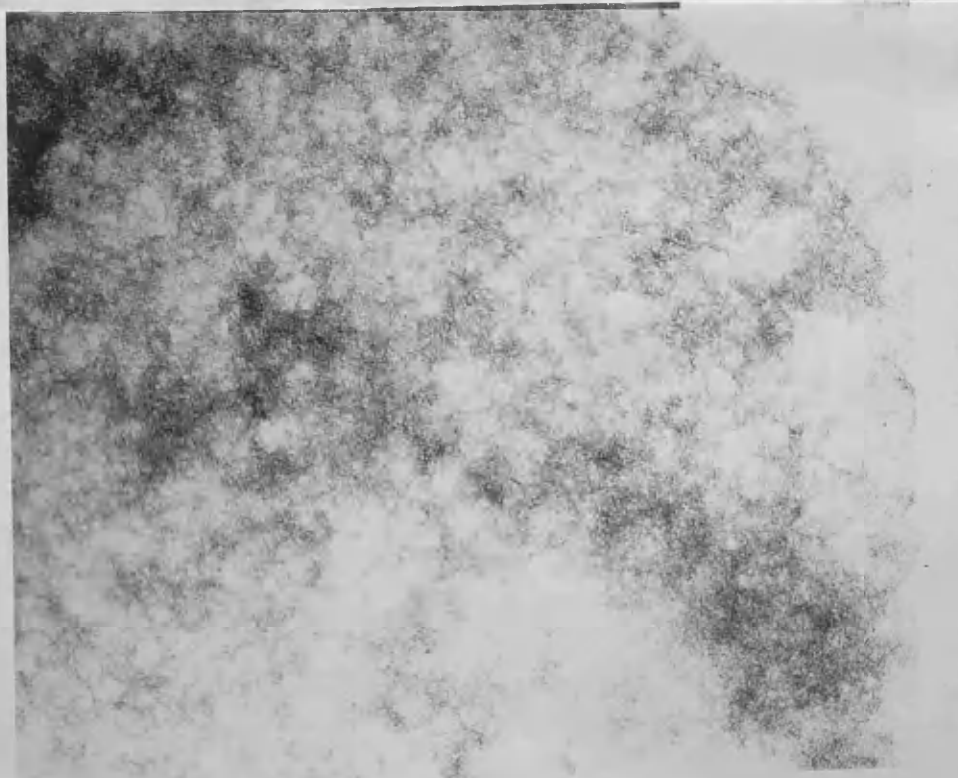
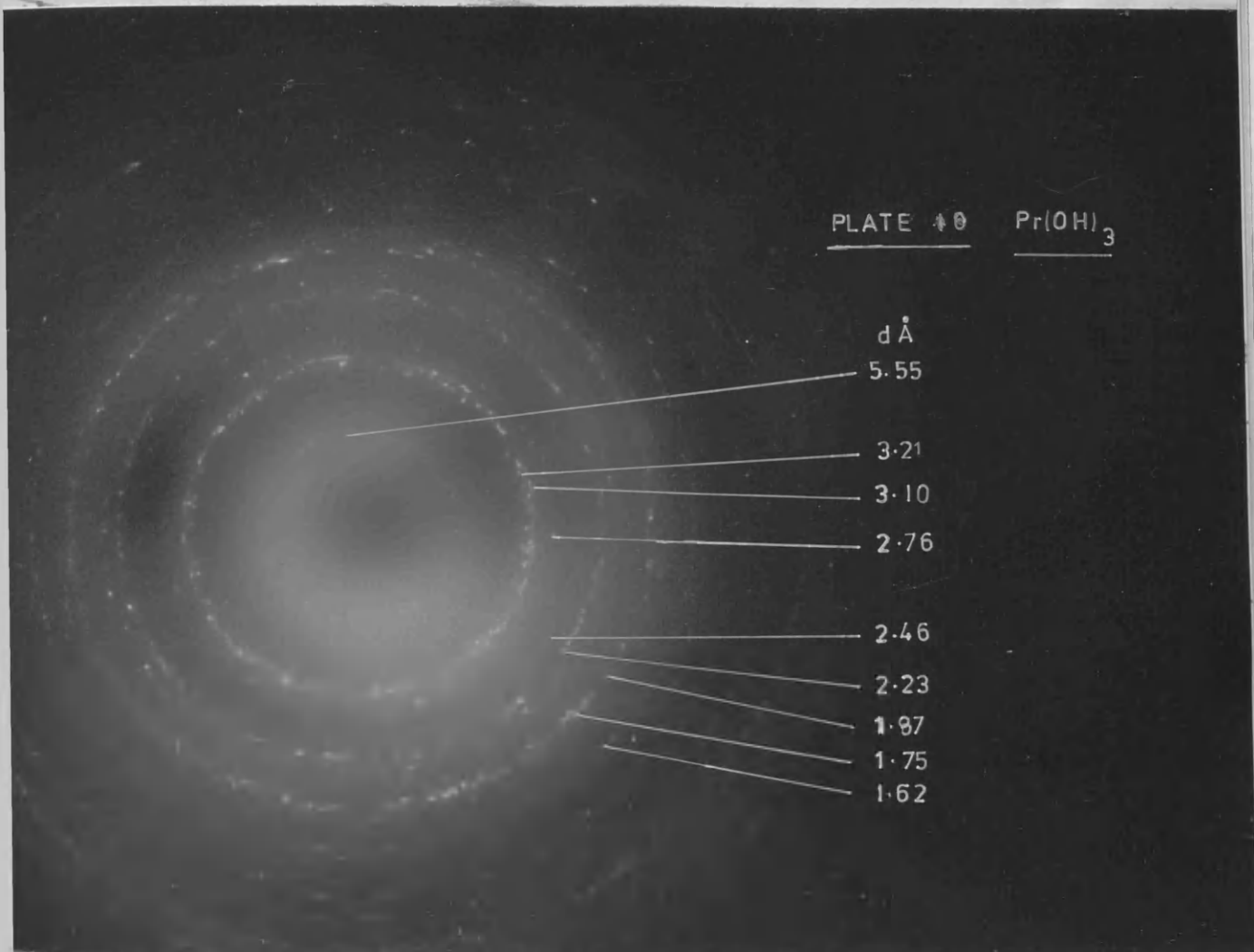


Plate 21
x 120,000
Gadolinium
precipitate

Aluminium. Plate 22 shows the initial material for the hydrolysis, $\text{AlCl}_3 \cdot 6\text{H}_2\text{O}$, identified by electron diffraction. The measured electron diffraction d spacings are given in table 6 and compared with the standard values for $\text{AlCl}_3 \cdot 6\text{H}_2\text{O}$ given in the A.S.T.M. powder diffraction file card no. 8-455. This material appeared to be unstable in the electron beam. A 0.01 molar AlCl_3 solution was refluxed for two months but showed no signs of precipitation. The reflux was then stopped and the solution was allowed to stand at room temperature. After one month at room temperature a greyish-white precipitate formed. The initial pH of the solution was 3.8 and this had dropped to 1.9 after precipitation. Electron microscopy showed the material to be in the form of large 'sheets' (plate 23), which in some cases appeared to have folded up (plate 24). A more irregular although less common morphology was also evident (plate 25). Electron diffraction patterns were recorded from the areas shown in plates 24 and 25. The measured d spacings are given in table 6. Identification from the electron diffraction patterns was very difficult so an X ray powder diffraction pattern was obtained. The d spacings calculated from this are shown in table 7 and are compared with those given for Boehmite in the A.S.T.M. card no. 21-1307. All the lines in the X ray pattern could be attributed to Boehmite and there were no unidentified lines.

The sheets appear to be made up from a network of fibrils (plate 23), which may aggregate to give an irregular morphology (plate 25). Plate 26 is the electron diffraction pattern from the area shown in plate 23. The measured d spacings from the electron diffraction patterns were correlated

with those of Boehmite. By calculating, from the cell dimensions, spacings not recorded in the ASTM card, all the electron diffraction values could be accounted for.

0.002 molar solutions of $\text{Al}_2(\text{SO}_4)_3$ and $\text{Al}(\text{NO}_3)_3$ were refluxed. Signs of precipitation were observed in the nitrate after 4 days and in the sulphate after 7 days. Refluxing was stopped after 24 days and the solutions were aged at room temperature for a further 11 days. The products of the hydrolyses were examined in the electron microscope (samples prepared by the spray method) and electron diffraction patterns were recorded. The measured d spacings are shown in table 6. Both precipitates can be identified as Boehmite. Plate 27 shows a thin sheet morphology from $\text{Al}(\text{NO}_3)_3$ hydrolysis and plate 28 is the corresponding diffraction pattern. The material from aluminium sulphate hydrolysis was similar to that shown in plate 27. Plate 29 shows the rolling up of the sheets. The diffraction pattern of this area is shown in plate 30. The initial pH of the solutions was 3.6 for the nitrate and 3.7 for the sulphate. The pH of the solutions after precipitation was 2.25.

Table 6 Electron diffraction d spacings from the hydrolysis
of Al^{3+} solutions.

Fresh AlCl_3 solution.

A. S. T. M. 8-453 $\text{AlCl}_3 \cdot 6\text{H}_2\text{O}$

dÅ
3.30
2.92
2.04
1.74
1.66
1.44

dÅ	hkl
3.297	113
2.949	220
2.056	134
1.758	152
1.673	035
1.456	434

AlCl_3 reflux

$\text{Al}(\text{NO}_3)_3$ reflux

$\text{Al}_2(\text{SO}_4)_3$

A. S. T. M. 21-1307

Plate 28

Plate 30

reflux

γAlOOH

calculated

dÅ	dÅ	dÅ	dÅ	dÅ	hkl	dÅ	hkl
			6.10	6.11	020		
4.04	3.66					4.07	030
	3.66					3.70	100
	3.54		3.56			3.54	110
3.16		3.19		3.16	120		
	3.05		3.08			3.06	040
			2.89			2.87	001
						2.74	130
2.71							
2.35	2.33	2.34		2.346	140		
	2.20		2.20	2.230	111		
2.05				2.045	150		
1.97				1.980	131		
1.86	1.83	1.86	1.89	1.860	051		
				1.850	200		
1.76	1.75		1.78	1.770	220		
1.67				1.662	151		
1.59						1.58	240
	1.52			1.527	080		
1.46		1.47		1.453	231		
1.37				1.389	171		
1.32		1.32		1.312	251		

Table 7 X ray d spacings for the product of AlCl_3 hydrolysis.

product	$\gamma\text{AlOOH(Boehmite)}$ ASTM 21-1307
dA	dA
6.09	6.11
3.16	3.164
2.34	2.346
1.86	1.860
1.66	1.662
1.53	1.527
1.45	1.453
1.43	1.434
1.33	1.312

Plate 26

PLATE 26

d Å

3.16

2.71

2.35

2.05

1.86

1.76

1.67

1.59

1.97

1.46

1.37

1.32




Plate 22 x 160,000

This micrograph shows a large, irregularly shaped, light-colored crystal of $\text{AlCl}_3 \cdot 6\text{H}_2\text{O}$ in the upper half, with a darker, more textured material below it.

$\text{AlCl}_3 \cdot 6\text{H}_2\text{O}$

Plate 23 x 96,000 Boehmite



This micrograph shows a complex arrangement of dark, irregularly shaped crystals of Boehmite on a lighter, granular background. The crystals vary in size and shape, some appearing as large, dark masses and others as smaller, more defined grains.

Plate 24 x 96,000



Plate 25 x 200,000



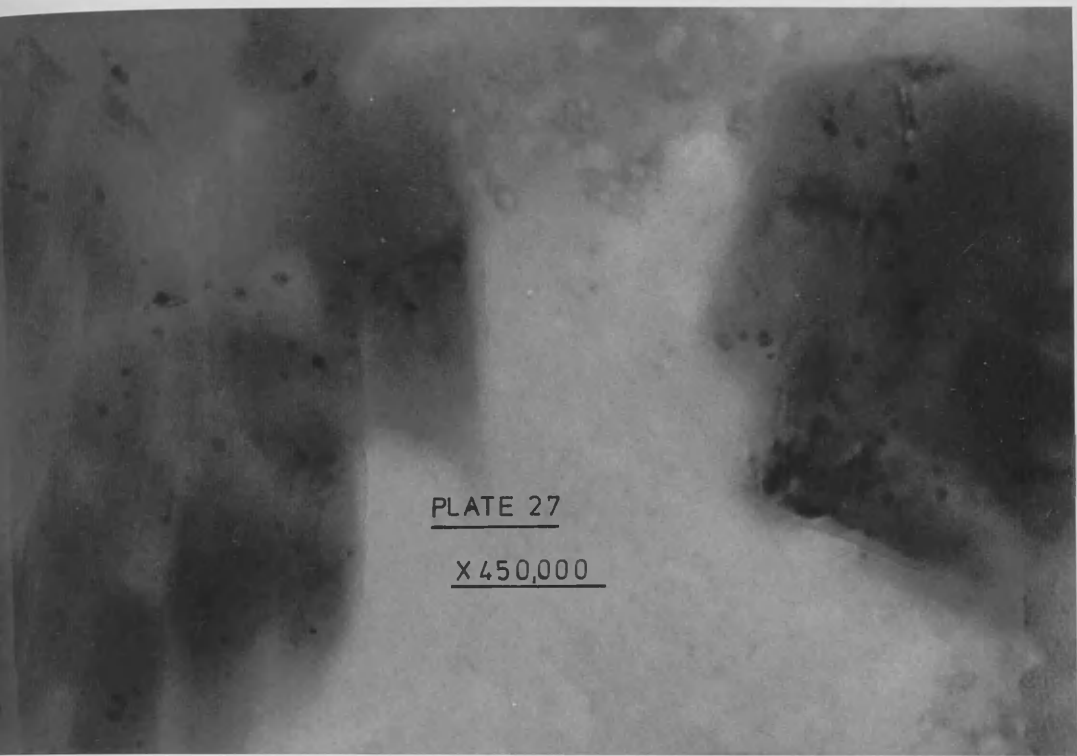


PLATE 27

X 450,000

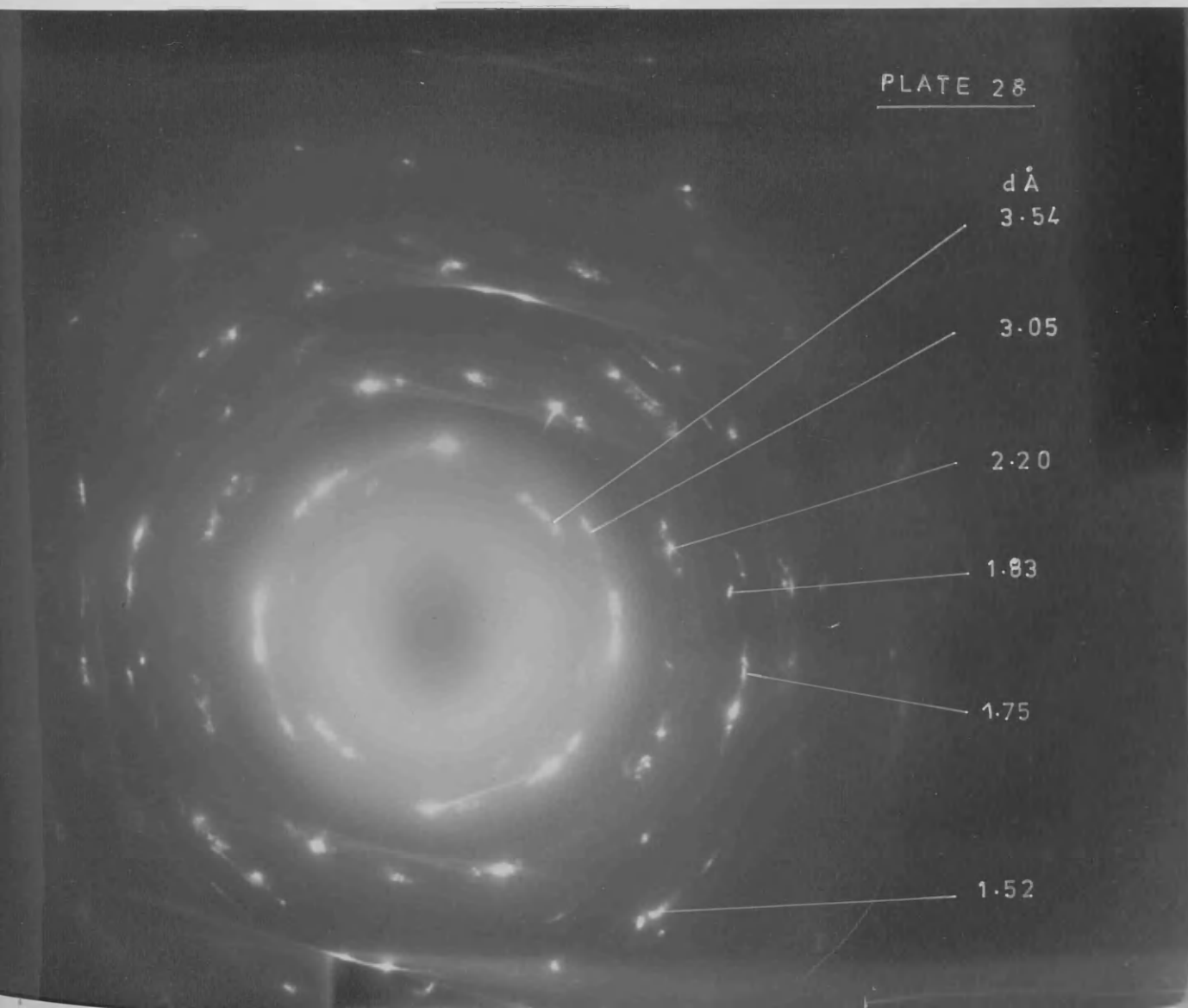


PLATE 28

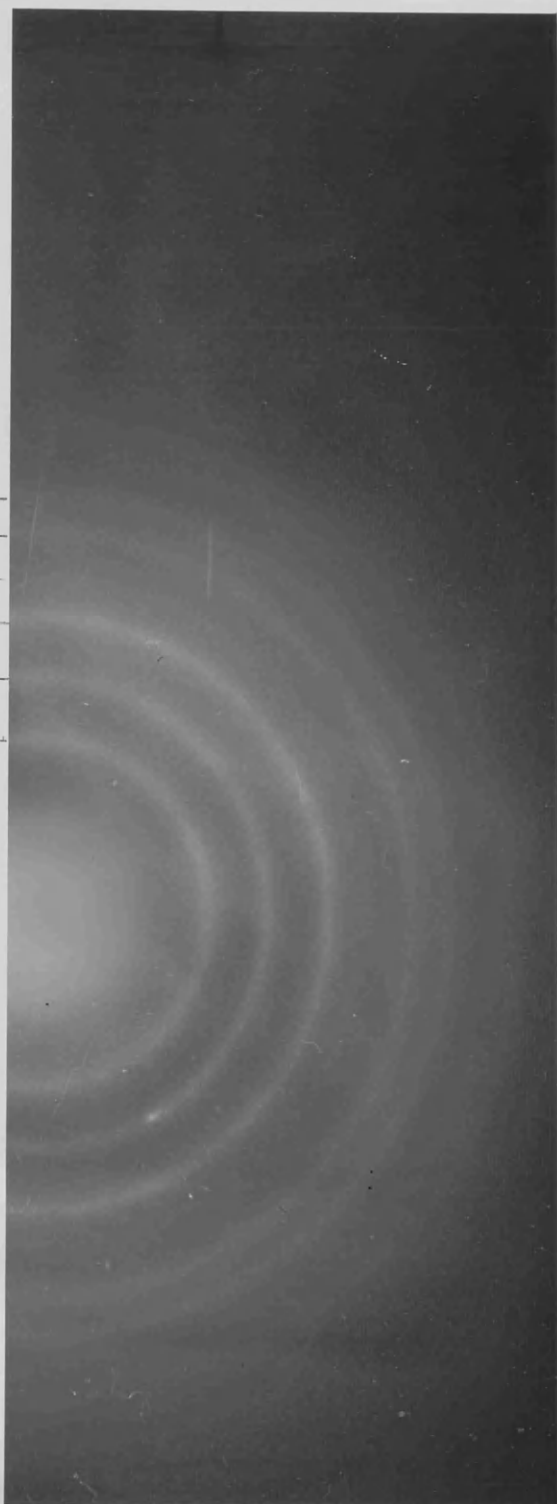


PLATE 29

X 50000

PLATE 30

$d \text{ \AA}$
1.32 —
1.47 —
1.67 —
1.86 —
2.34 —
3.19 —



Vanadium. A 0.01 molar vanadyl sulphate solution, originally blue in colour, formed a dark green precipitate after refluxing for one day. The supernatant remained blue. A sample was prepared for microscopy by the 'spray method' and transmission micrographs and electron diffraction patterns were obtained. The material was in the form of thin 'sheets' which formed thicker 'fibrils' (plate 31). Plate 32 is the electron diffraction pattern of this material. The lattice spacings of this pattern are shown in table 8 and compared with the only possible correlation found in the A.S.T.M. (1971) index, card no. 11-673, $V_2O_5 \cdot H_2O$. The crystal structure of this compound is not given in the quoted reference (La Salle and Cobble(1955)).

Refluxing was continued for 22 days to investigate ageing effects. The colour of the supernatant changed from blue to green and finally became colourless. A sample was then prepared for electron microscopy by the 'spray method' and transmission micrographs were obtained. The crystals were in the form of 'needles' (plate 33). A single crystal electron diffraction pattern was obtained (plate 34). This could not be indexed as $V_2O_5 \cdot H_2O$ as no crystal structure information was available and its identification is discussed later.

A fresh vanadyl sulphate solution was made up and, after standing at room temperature for four months, the solution which had now turned green, produced large sheets of green precipitate which could be seen to roll off the sides of the flask. It was possible to prepare specimens for the electron

microscope by floating the 'sheets' onto copper grids. No supporting carbon film was required. Very thin films, which seemed to be rolled or folded up were seen in the microscope (plate 35). Lattice fringe spacings of 7.9\AA and 5.4\AA were resolved. An electron diffraction pattern of a thicker sample of this material was recorded (plate 36), the d spacings from which are compared with those of $\text{V}_2\text{O}_5 \cdot \text{H}_2\text{O}$ in table 8. A.S.T.M. card no. 11-673, $\text{V}_2\text{O}_5 \cdot \text{H}_2\text{O}$ shows no recorded spacings higher than 5.75\AA , therefore the lattice spacings of 7.9\AA observed in plate 35 could not be accounted for. The micrograph of plate 35 was examined in the laser diffractometer and periodicities of 10.0\AA , 8.0\AA , 6.7\AA and 5.4\AA were obtained. X ray powder diffractions of a reflux and a room temperature precipitate were obtained. The patterns were identical and showed a strong reflection at 14\AA . None of the vanadium compounds quoted in the A.S.T.M. index (1971) have a reflection at 14\AA . The precipitate was finally identified as Bariandite, a mineral which was discovered in 1971 by Cesbron and Vachey. Further information on this mineral is given in the discussion. Table 9 shows a comparison of the X ray d spacings of the VOSO_4 room temperature precipitate with the d spacings given for bariandite by Cesbron and Vachey (1971) and with spacings calculated from the cell constants. The strength of the reflections, judged visually, are different from those given by Cesbron and Vachey. The single crystal diffraction pattern (plate 34) from the reflux of VOSO_4 was indexed as bariandite with the crystals lying on the (001) plane (table 10). The lattice spacings recorded

for the VOSO_4 room temperature precipitate from the electron micrograph (plate 35) could be assigned as the 8.12\AA (102) and 5.39\AA (201) spacings of bariandite. The periodicities obtained from the diffractometer are compared with bariandite spacings in table 11. This suggests that the thin films are lying on the (010) plane. The d spacings calculated from plates 32 and 36 are compared to **bariandite in table 10.**

A fresh 0.01 molar solution of VOSO_4 was made up and the hydrolysis studied at 60°C , 40°C and again at room temperature. After 20 days at room temperature the solution was still blue and electron microscopy showed large crystals (plate 37) which gave an electron diffraction pattern similar to that of VOSO_4 . The comparison is given in table 12. After 30 days the solution had turned green and a sample was sprayed onto asbestos grids. Electron microscopy showed a thin film of material stretched between the asbestos fibres (plate 38). After four months the large green 'sheets' were precipitated as before.

When the hydrolysis was carried out at 60°C , the solution became green after 2 hours and a precipitate formed after one day. The precipitate was in the form of 'sheets'. A sample of the solution after 2 hours at 60°C was prepared for microscopy by spraying. The specimen consisted of thin sheets with denser rounded particles about 200\AA in diameter (plate 39). A sample of the precipitate was floated onto a copper grid and examined in the electron microscope (plate 40). The sheets seem to be very thin, (an overlap is indicated by the arrow) and many lattice

Table 8 Electron diffraction lattice spacings fromVOSO₄ hydrolysis.

<u>VOSO₄</u>	<u>VOSO₄ at room temperature</u>	<u>A. S. T. M 11-673</u>
<u>refluxed 1 day</u>	<u>for four months</u>	<u>V₂O₅·H₂O</u>
dÅ	dÅ	dÅ
5.75	5.75	5.78
5.00	4.98	5.02
3.48	3.48	3.56
2.88	2.84	2.892
2.63	2.61	2.580
	2.49	2.488
	2.19	
	2.04	2.021
1.95	1.92	1.907
1.83	1.86	1.851
	1.63	1.640
1.54	1.53	1.578
1.34		

Table 9 X ray diffraction data

<u>room temperature</u>		<u>Bariandite</u>			<u>calculated</u>	
<u>precipitate from VOSO₄</u>		<u>(Cesbron and Vachey 1971)</u>				
dÅ	intensity	dÅ	intensity	hkl	dÅ	hkl
14.15	S	14.20	VVS	002		
11.40	w				11.46	100
7.14	mw	7.08	mw	004		
5.72	w	5.72	mw	200		
3.47	S	3.48	S	110	3.52	302
3.22	w	3.206	mw	113	3.23	108
2.84	w	2.852	MS	400		
2.69	w	2.632	mw	310	2.70	402
2.56	M	2.593	mw	311	2.57	209
2.39	M	2.360	vvw	0012		
2.06	S	2.018	vvw	1111	2.03	0014
1.94	w	1.939	MS	510	1.91	600
1.82	w	1.827	MS	4010		
1.74	w					
1.60	S	1.621	vw	225	1.62	5010
1.52	mw	1.511	mw	3114		

Table 10 Electron diffraction lattice spacings from VOSO₄ hydrolysis. Comparison with Bariandite.

<u>VOSO₄ 1 day</u>	<u>VOSO₄ four months</u>	<u>Bariandite</u>			
<u>reflux.</u>	<u>at room temperature</u>	<u>Cesbron + Vachey 1971</u>		<u>calculated</u>	
$d\text{\AA}$	$d\text{\AA}$	$d\text{\AA}$	hkl	$d\text{\AA}$	hkl
5.75	5.75	5.72	200		
			20 $\bar{2}$		
5.00	4.98	4.98	202		
			20 $\bar{4}$		
3.48	3.48	3.48	110		
			11 $\bar{1}$		
2.88	2.84	2.852	400		
			40 $\bar{4}$		
			0010		
2.63	2.61	2.632	310	2.57	209
			31 $\bar{3}$		
	2.49			2.49	404
					40 $\bar{8}$
	2.19			2.19	502
	2.04	2.018	1111	2.03	001
					408
1.95	1.92	1.939	510	1.91	600
			51 $\bar{5}$		
1.83	1.86	1.827	4010		
			4014		
	1.63			1.66	606
1.54	1.53	1.542	42 $\bar{2}$	1.56	608
1.34				1.35	804

VOSO₄ refluxed for 22 days

Bariandite

single crystal pattern

calculated from Cesbron and Vachey.

$d\text{\AA}$	$d\text{\AA}$	hkl
5.72	5.733	200
3.47	3.46	110
2.87	2.866	400
2.63	2.632	310
1.81	1.815	020
1.72	1.73	220
1.54	1.532	420
1.18	1.185	130
1.15	1.153	330

Table 11 Laser diffractometer results

A	B	Bariandite	
dÅ	dÅ	dÅ	hkl
10.0	9.95	9.96	101
8.0	8.07	8.12	102
6.74	6.74	6.70	103
5.37	5.36	5.39	201
	5.06	4.98	202
	4.78	4.74	105

A= values from plate 35, room temperature hydrolysis of VOSO_4 .

B= values from plate 40, hydrolysis at 60°C .

Table 12 Electron diffraction of the blue solution

C	D	
dÅ	dÅ	hkl
3.94	3.96	111
3.58	3.54	002
3.20	3.185	102
2.90	2.90	211
2.53	2.555	202
2.37	2.385	220
2.23	2.24	122
2.01	2.006	031
1.90	1.896	213
1.77	1.770	{004 410}

C= values from the material shown in plate 37

D= standard values for VOSO_4 (Kierkegaard and Longo 1965)

Table 13 Electron diffraction spacings from the reactions
at 60°C and 40°C.

<u>A</u>	<u>B</u>	<u>Bariandite</u>		<u>C</u>	
<u>dÅ</u>	<u>dÅ</u>	<u>dÅ</u>	<u>hkl</u>	<u>dÅ</u>	<u>hkl</u>
8.15				8.12	102
	5.75	5.72	200		
5.58				5.58	104
4.76		4.73	006		
3.69				3.69	205
3.31	3.36			3.35	206
3.05				3.04	109
	2.89	2.852	400		
2.69	2.70	2.697	402		
2.33		2.360	0012		
			2010		
2.06	2.04			2.065	2012
1.88				1.91	600
	1.81	1.827	4010		
1.74				1.76	604
1.60				1.61	2016
1.47				1.51	609

A= values from plate 42, VOSO_4 at 60°C for 1 day.

B= values from plate 44, VOSO_4 at 40°C for 2 days.

C= values calculated from the cell constants given by Cesbron
and Vachey, 1971.

spacings are visible. An area of this plate at a higher magnification is shown in plate 41. The lattice spacings of 9.6\AA and 5.3\AA corresponding to the 101 spacing of 9.9\AA and the 201 spacing of 5.39\AA in bariandite are shown. The micrograph of plate 40 was studied in the laser diffractometer using various camera lengths to obtain accurate values for the smaller periodicities. Many measurements were taken and the averages are shown in table 11 where they are compared with the lattice spacings for bariandite. An electron diffraction pattern of plate 40 was also recorded (plate 42). The d spacings calculated from this pattern are compared with those of bariandite in table 13.

The hydrolysis at 40°C was followed by pH measurements. A graph of pH against time of reaction is shown in figure 14. After 22 hours the solution had become green and the pH had dropped from 3.1 to 2.6. After 48 hours the pH had dropped to 2.35. A sample sprayed onto asbestos fibres at this stage showed a film suspended between the fibres with denser rounded areas about 40\AA in diameter (plate 43). A S.A.D pattern was obtained (plate 44). The lattice spacings from this are compared with those of bariandite in table 13. After 5 days the green 'sheets' of precipitate appeared. The pH had dropped to 2.1.

An infrared spectrum of the room temperature precipitate was recorded and is shown in figure 15. The spectrum was compared with those of V_2O_5 and $\text{V}_2\text{O}_4 \cdot \text{H}_2\text{O}$ (or wet) given by Nyquist (1971). The strong bond at 1000 cm^{-1} indicates a vanadium-oxygen double bond (Nakamoto 1971). This mode

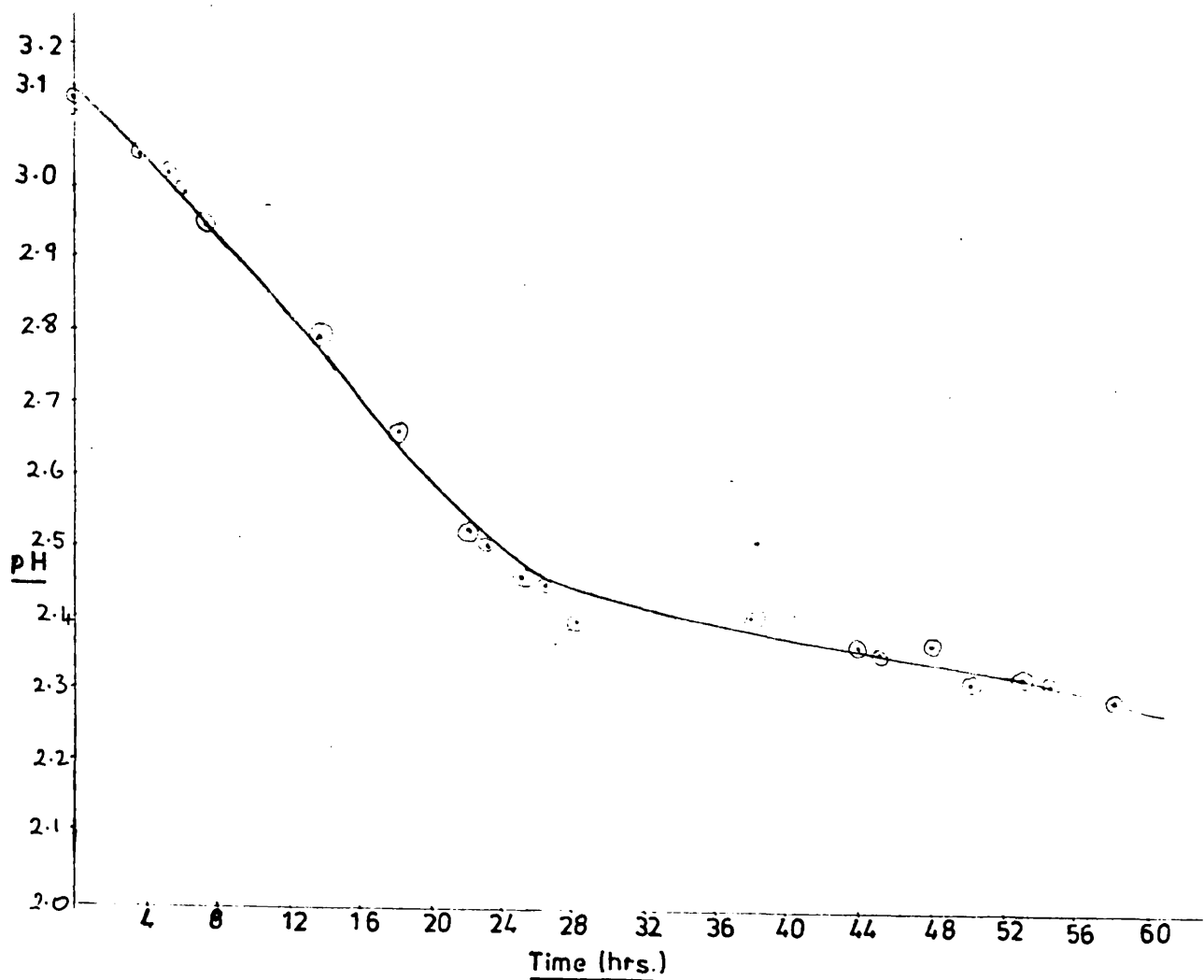
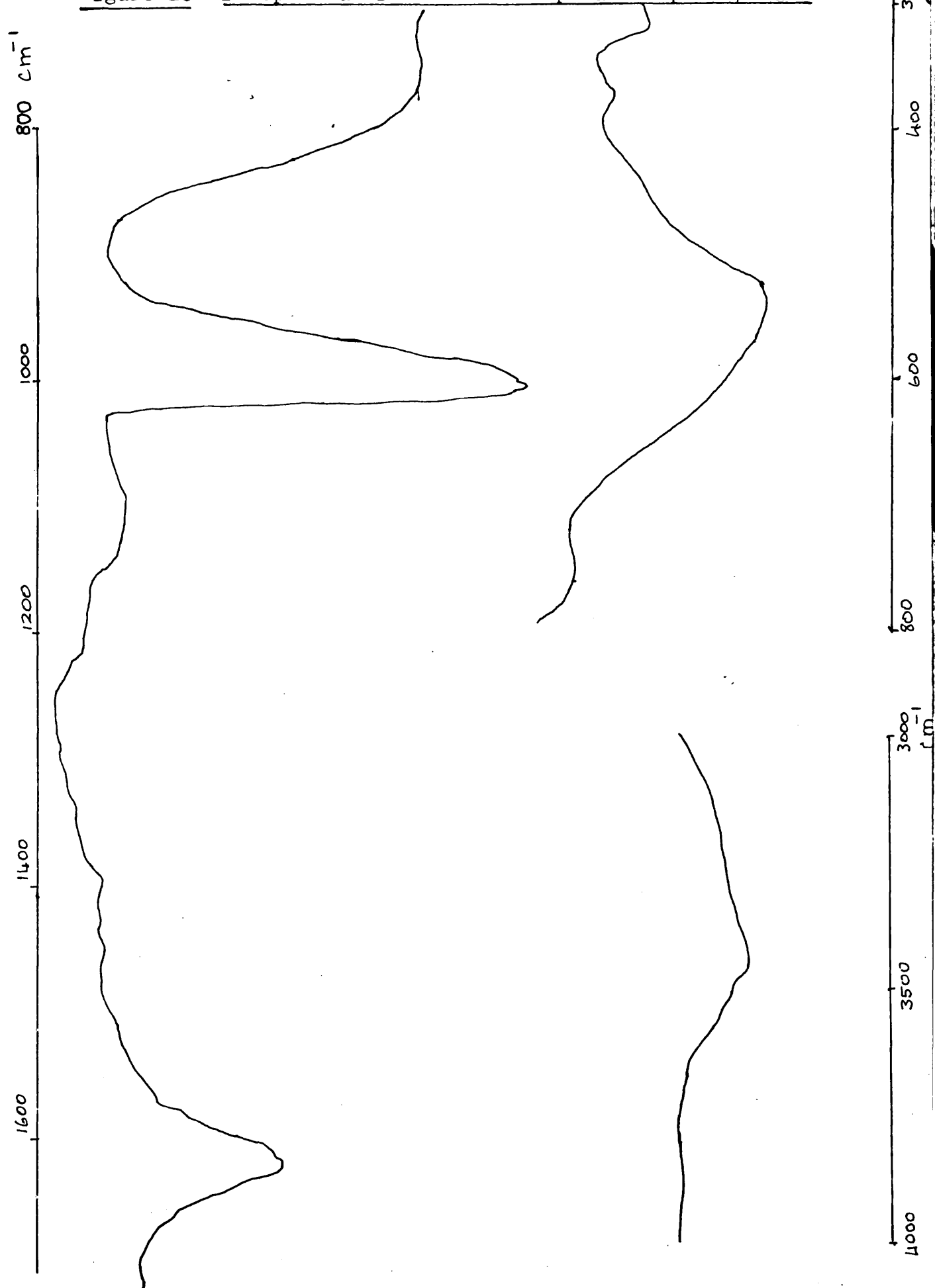
Figure 14 VOSO_4 Hydrolysis at 40°C Graph of pH v time

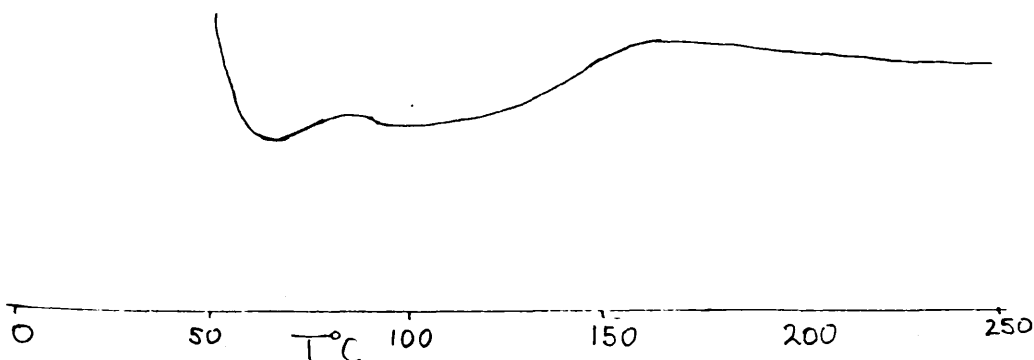
Figure 15 ir spectra of the room temperature precipitate



occurs at 1020cm^{-1} in the V_2O_5 spectrum and at 1015cm^{-1} in the $\text{V}_2\text{O}_4 \cdot \text{H}_2\text{O}$ spectrum. In the region below 900cm^{-1} , $\text{V}_2\text{O}_4 \cdot \text{H}_2\text{O}$ shows strong bands at 760cm^{-1} , 630cm^{-1} and 550cm^{-1} and weaker bands at 350cm^{-1} and 300cm^{-1} , while V_2O_5 has strong bands at 830cm^{-1} , $600\text{--}500\text{cm}^{-1}$ (broad), 380cm^{-1} and 300cm^{-1} (Nyquist 1971). The spectrum in figure 15 has a strong band at 760cm^{-1} , a broad assymmetric band at 550cm^{-1} and weak bands at 380cm^{-1} and 320cm^{-1} . Above 1200cm^{-1} the spectrum has bands at 1605cm^{-1} , 1615cm^{-1} and 3400cm^{-1} (broad) which are due to water (in $\text{V}_2\text{O}_4 \cdot \text{H}_2\text{O}$ they occur at 1615cm^{-1} , 1675cm^{-1} and 3500cm^{-1}).

A D.T.A. curve was recorded for the room temperature precipitate (figure 16). Two endotherms occur at 65°C and 100°C . The colour of the sample changed from green to black. These results are in agreement with the dehydration of bariandite as described later.

Figure 16 D.T.A. curve for the room temperature precipitate



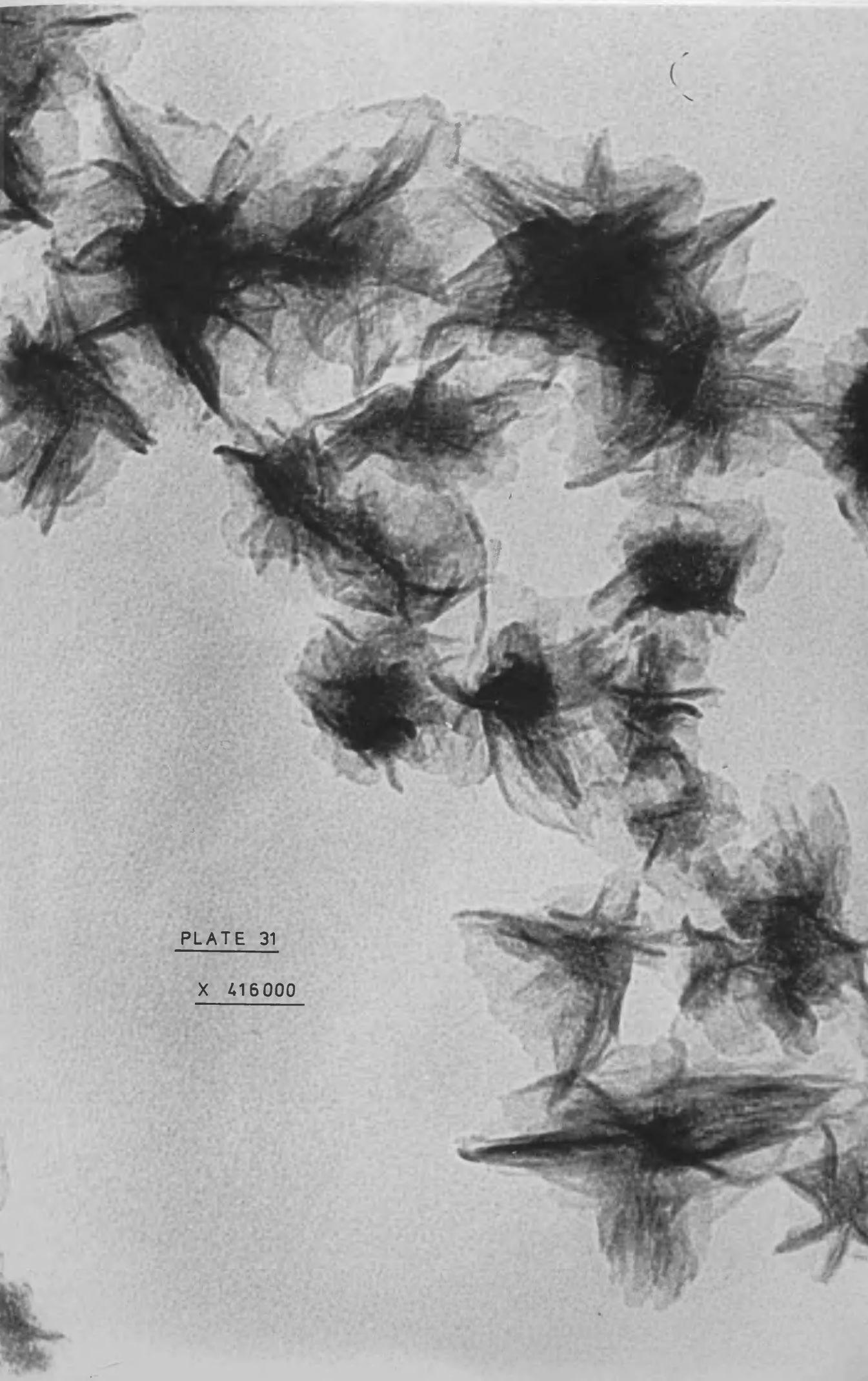


PLATE 31

X 416000

Plate 32 Electron diffraction of VOSO_4 refluxed for one day.

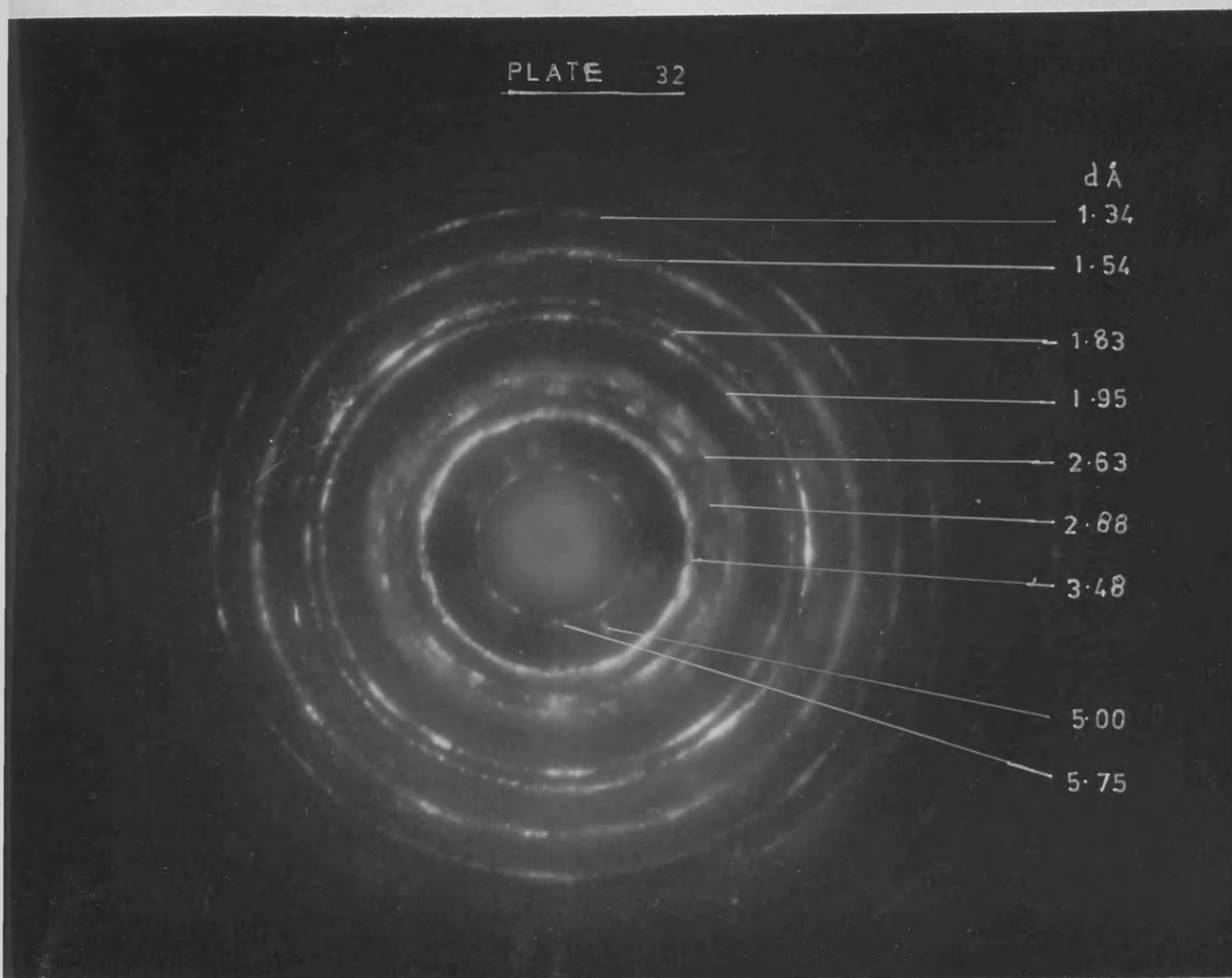


PLATE 33

X 110000



PLATE 34

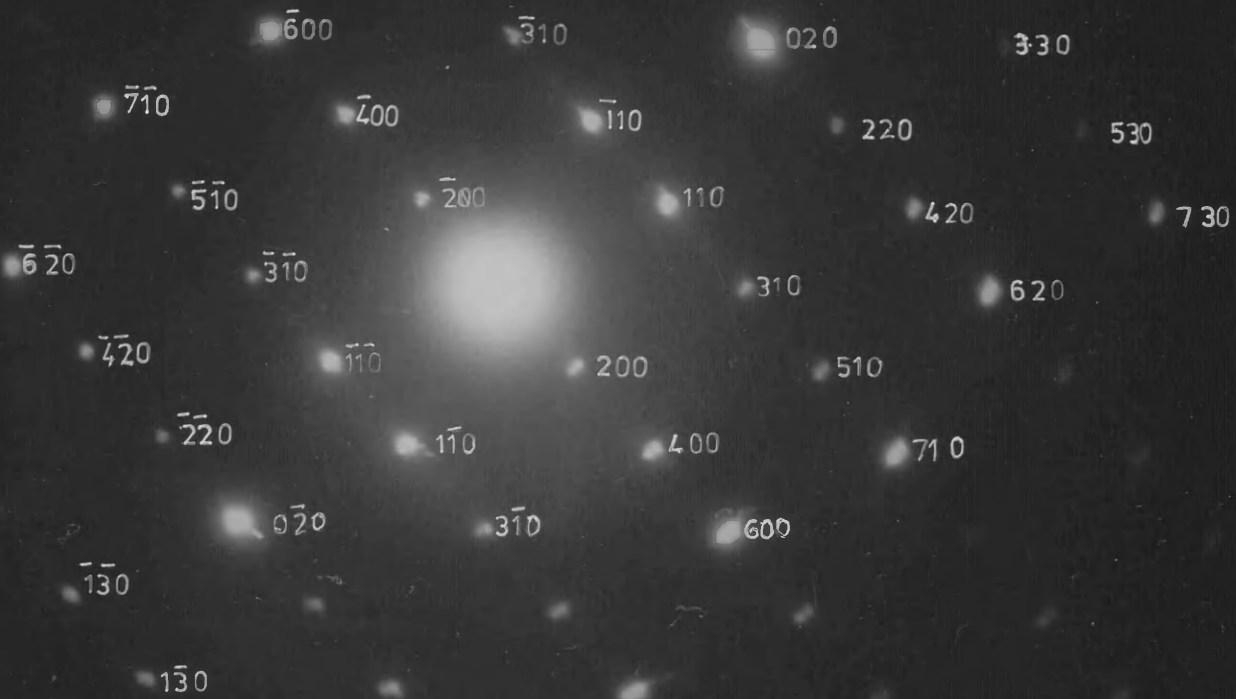




Plate 36 Electron diffraction of the product formed after
four months at room temperature.

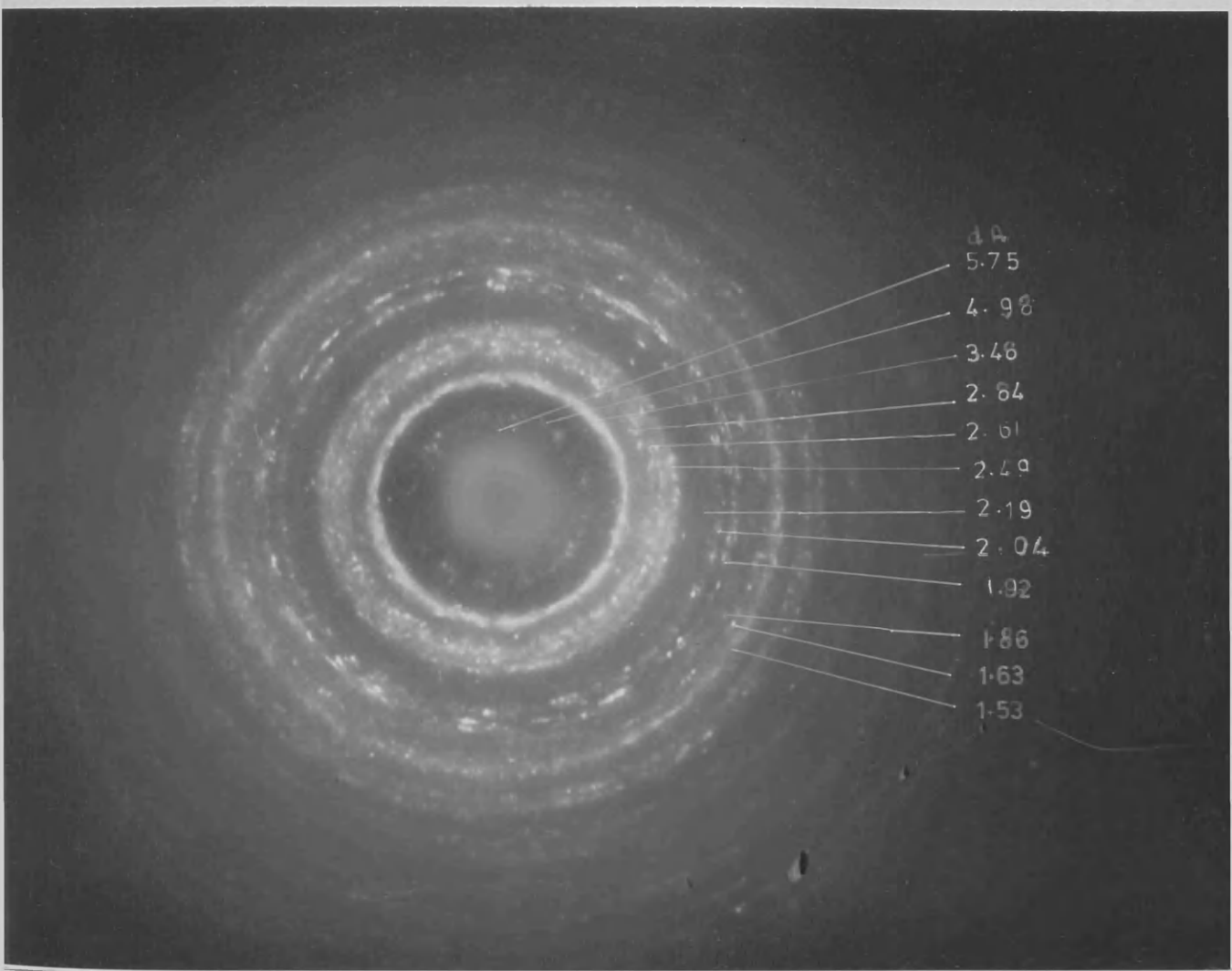


PLATE 37

X161,000





PLATE 38

X 552,000

Plate 39

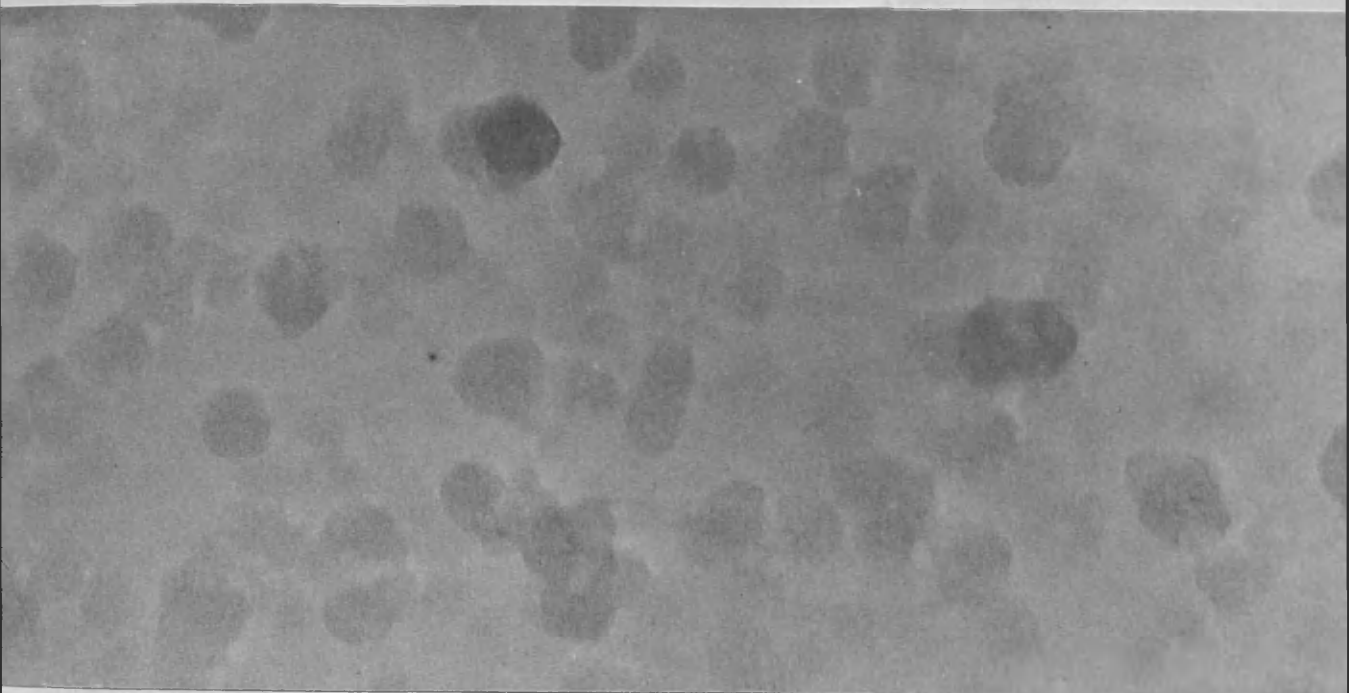


Plate 42

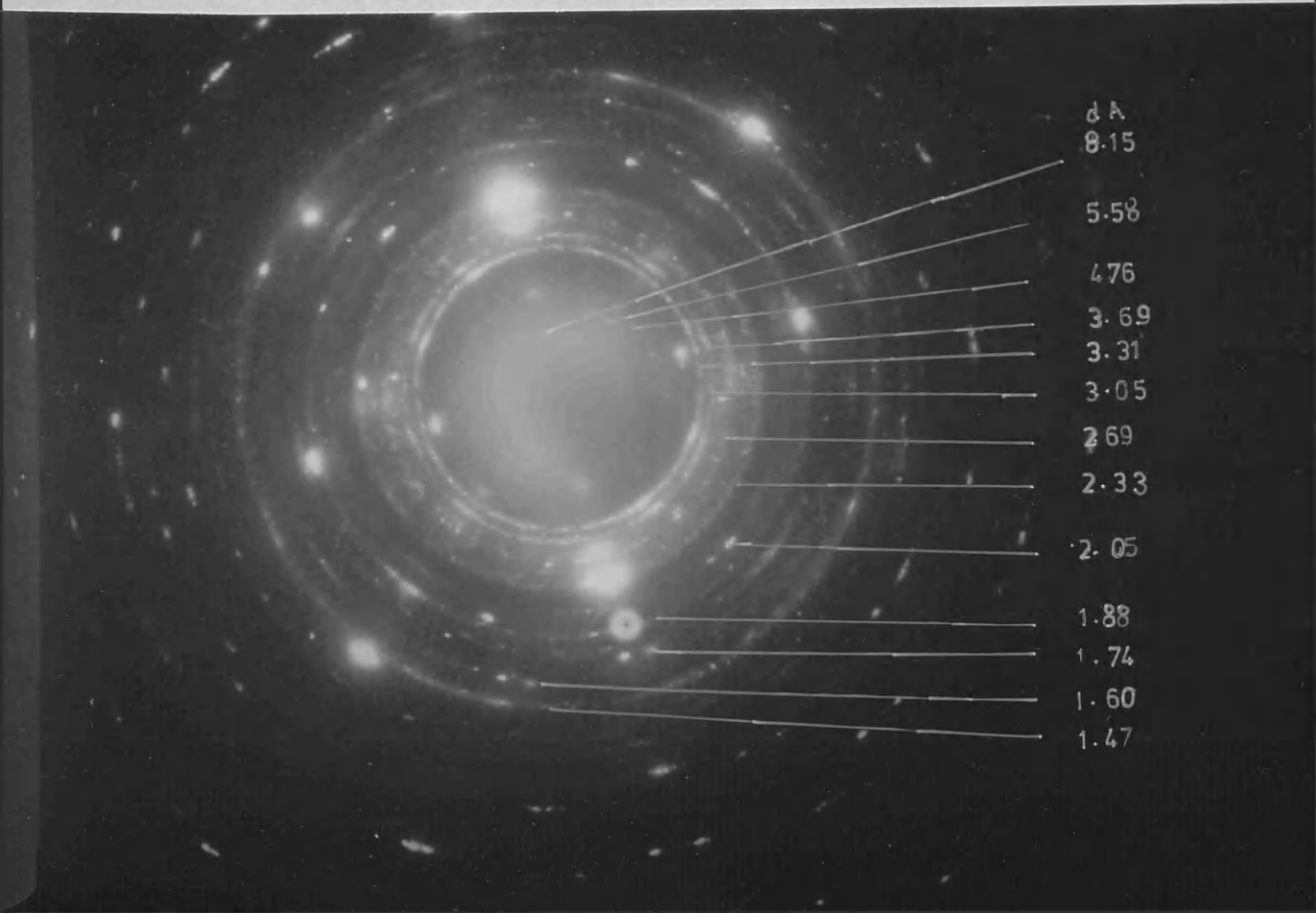


PLATE 40

X 564,000

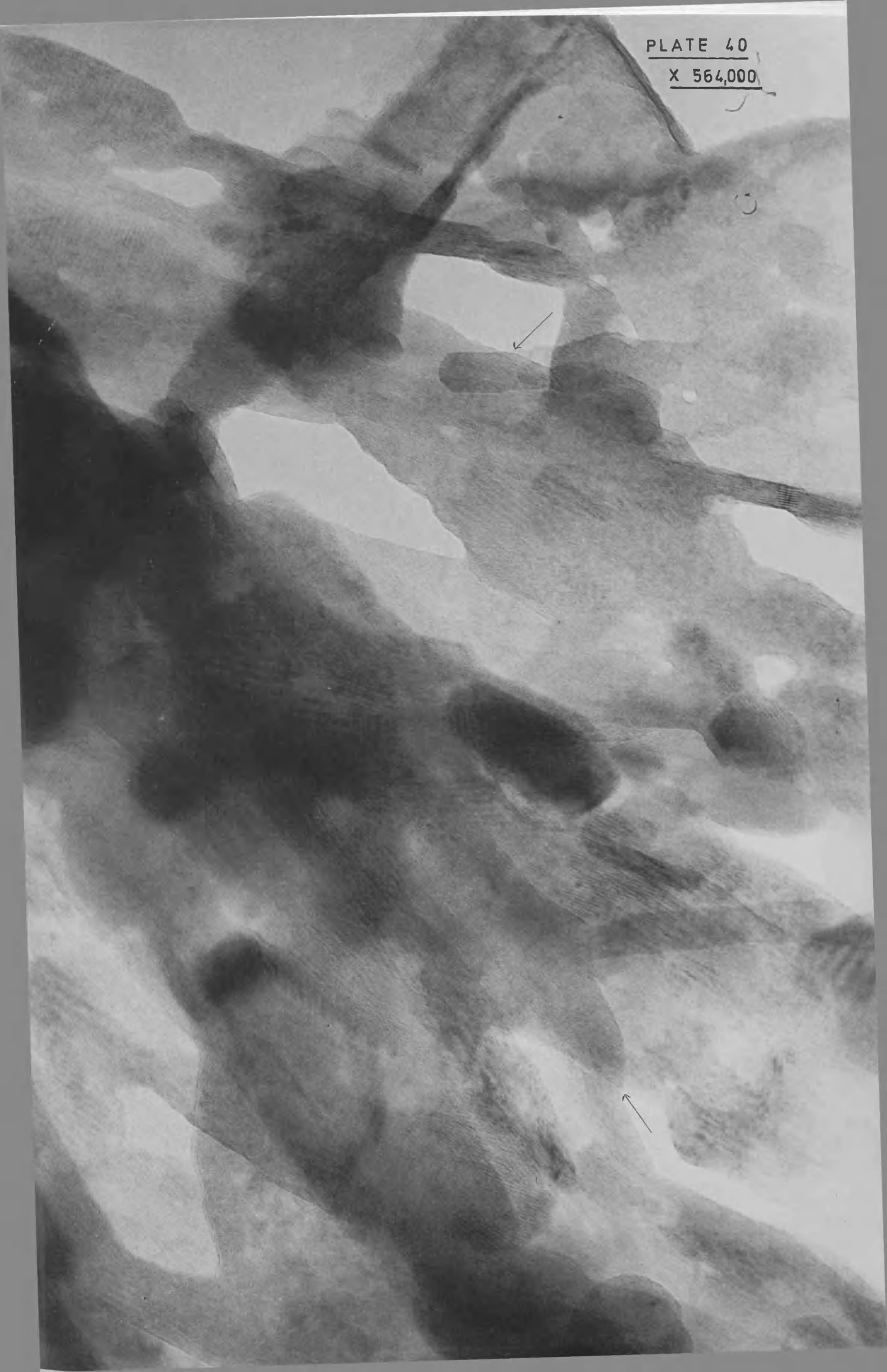




PLATE 43

X 552,000

Plate 44 Electron diffraction of the product after
two days at 40°C

PLATE 44

d Å
5.75
3.36
2.89
2.70
2.04
1.81

Iron. Ferric chloride solution hydrolysed on refluxing, the colour of the solution changing from pale yellow to deep red and finally precipitating a red-brown material, designated Fe2b (table 14). Electron microscopy revealed that the precipitate contained crystals with a 'cube' morphology as shown in plate 45. The electron diffraction pattern, shown in plate 46, can be correlated with that of $\alpha\text{-Fe}_2\text{O}_3$ (hematite) and the measured d spacings of the electron diffraction pattern are compared with those of hematite in table 15. The ferric chloride solution also hydrolysed at room temperature. The solution deepened in colour, becoming colloidal and then precipitating a yellow-orange material, designated Fe4, after 14 days. The precipitate was examined in the electron microscope, samples being prepared by the spray method, and cigar shaped crystals with an approximate length of 1500\AA were observed as shown in plate 47. The electron diffraction pattern of these crystals is shown in plate 48. The crystals were identified as $\beta\text{-FeOOH}$ by comparing their electron diffraction pattern with the standard values for $\beta\text{-FeOOH}$ (table 15).

The ferric nitrate solution hydrolysed on reflux. Again the solution changed colour from pale yellow to deep red then became colloidal and finally produced a red-brown precipitate designated Fe2a. Electron microscopy showed that this had a similar 'cube' morphology to Fe2b but that in this case the cubes were smaller as shown in plate 49. The electron diffraction pattern of Fe2a is shown in plate 50 and the measured d spacings are compared with those of hematite in table 15. Room

temperature hydrolysis of ferric nitrate also occurred giving a yellow brown precipitate designated Fe1. This hydrolysis was slower than that producing Fe4. Electron microscopy of Fe1 showed 'lath' like crystals which gave a diffraction pattern that could be identified as α -FeOOH (goethite) as shown in table 15. The precipitate was examined after standing for two years in the mother liquor and the same morphology was observed (plate 51). The electron diffraction pattern of this material is shown in plate 52, and compared with goethite in table 15.

The hydrolysis, by refluxing, of ferric perchlorate solution gave a red-brown precipitate designated Fe9 which was identified by electron diffraction as α -Fe₂O₃. The measured d spacings are given in table 15. Samples were prepared for microscopy by the droplet method and showed a 'cube' morphology similar to Fe2a and Fe2b. Plate 53 shows the material produced in this way and its diffraction pattern is shown in plate 54. The lattice spacings of 3.66Å(102) and 4.35Å(100) are resolved. There was no sign of precipitation in a ferric perchlorate solution which had been standing at room temperature for more than a year..

Ferric sulphate solution hydrolysed on reflux giving an orange-brown precipitate designated Fe8, which was identified by electron diffraction as α -FeOOH (goethite) as shown in table 15. Electron microscopy of samples prepared by the spray method showed 'cigar' crystals similar to Fe4 (plate 55). The diffraction pattern produced by these crystals is shown in plate 56. Ferric sulphate solution showed no signs of precipitation even after one year at room temperature.

To aid identification X ray powder diffraction patterns were recorded for Fe1, Fe2a, Fe2b and Fe4. The calculated d spacings are shown in table 16. Infrared spectra and differential thermal analysis curves were recorded for these precipitates.

Figures 17 and 18 show the IR spectra of Fe1 and Fe2a respectively. In the 3500cm^{-1} to 3000cm^{-1} region Fe2a has only one band at 3400cm^{-1} due to surface water whereas Fe1 has two bands, one at 3400cm^{-1} due to surface water and one at 3170cm^{-1} indicating a hydrogen bonded hydroxyl group. The two bands at 800cm^{-1} and 890cm^{-1} in figure 17 also indicate hydroxyl groups. Below 700cm^{-1} the spectra of Fe1 agrees with that given for αFeOOH by M^{re}. Carbannes-Ott (1957) and the spectrum of figure 18 shows the typical $\alpha\text{Fe}_2\text{O}_3$ pattern (Nyquist 1971). Figure 19 shows the IR spectrum of Fe4. In the region 3600cm^{-1} to 3000cm^{-1} there is a broad absorption centered on 3350cm^{-1} with a shoulder at 3450cm^{-1} . The lack of absorption in the range 3300cm^{-1} to 3000cm^{-1} indicates that there are no hydrogen bonded hydroxyls, but the small shoulder at 3450cm^{-1} and the band at 840cm^{-1} could indicate a 'free' hydroxyl group. The spectrum below 700cm^{-1} agrees with that given for βFeOOH by Nyquist(1971).

The DTA curve for Fe1 (figure 20) shows two small endotherms at 120°C and at 140°C due to loss of surface water and a stronger endotherm at 290°C . This corresponds with the DTA curve given for αFeOOH by M^cKenzie (1970). The endotherm at 290°C is due to the formation of $\alpha\text{Fe}_2\text{O}_3$. There is also a change in the colour of the specimen from yellow to red-brown. The DTA curve for Fe2a does not show any peaks in

the region studied. $\alpha\text{Fe}_2\text{O}_3$ is stable up to 1430°C . The DTA curve of Fe4 (figure 21) has endotherms at 85°C and 120°C due to loss of surface water, and a sharp endotherm at 250°C . The specimen changed colour from orange-yellow to red-brown. The DTA curve of Fe4 agrees with Gallacher's results for βFeOOH (1972). The IR spectra of Fe1 and Fe4 after DTA were recorded and both showed the typical $\alpha\text{Fe}_2\text{O}_3$ pattern (figure 22).

The results of this general study of the hydrolysis of iron (III) salts are summarised in table 17 below.

Table 17' Products of iron(III) hydrolyses.

Code	Product	Methods of identification			
		<u>E. Diff.</u>	<u>DTA</u>	<u>IR</u>	<u>X ray diffraction</u>
Fe1	αFeOOH	+	+	+	+
Fe2a	$\alpha\text{Fe}_2\text{O}_3$	+		+	+
Fe2b	$\alpha\text{Fe}_2\text{O}_3$	+			+
Fe4	βFeOOH	+	+	+	+
Fe8	αFeOOH	+			
Fe9	$\alpha\text{Fe}_2\text{O}_3$	+			

Table 14 Precipitate codes for Iron results.

Code	Original solution	Method of precipitation
Fe1	$\text{Fe}(\text{NO}_3)_3$	Room temperature
Fe2a	$\text{Fe}(\text{NO}_3)_3$	Reflux
Fe2b	FeCl_3	Reflux
Fe4	FeCl_3	Room temperature
Fe8	$\text{Fe}_2(\text{SO}_4)_3$	Reflux
Fe9	$\text{Fe}(\text{ClO}_4)_3$	Reflux

Plate 48 Electron diffraction of Fe4

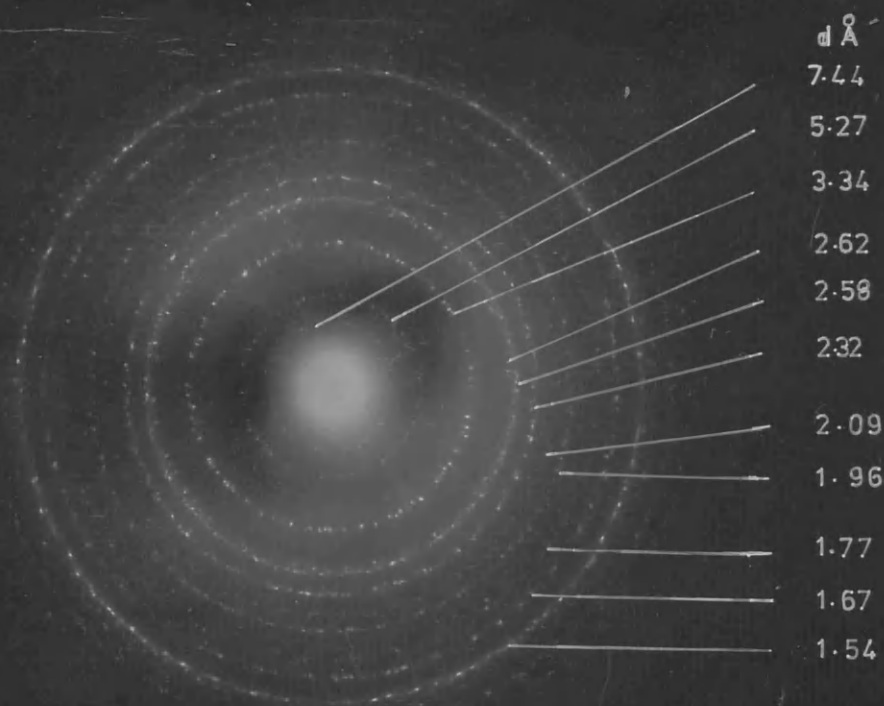


Table 15 Electron diffraction results.

<u>Lattice spacings.</u>			<u>A. S. T. M. 13-534</u>		<u>calculated</u>	
<u>Fe2b</u>	<u>Fe2a</u>	<u>Fe9</u>	<u>$\alpha\text{Fe}_2\text{O}_3$</u>			
<u>dÅ</u>	<u>dÅ</u>	<u>dÅ</u>	<u>dÅ</u>	<u>hkl</u>	<u>dÅ</u>	<u>hkl</u>
	4.14				4.14	101
3.66	3.64	3.66	3.66	012		
2.74					2.75	005
2.68	2.71	2.70	2.69	104		
2.51	2.50	2.51	2.51	110		
2.19	2.21	2.20	2.201	113		
1.85	1.83	1.84	1.838	024		
1.71	1.70	1.69	1.690	116		
1.60	1.60	1.60	1.596	018		
1.50	1.50	1.48	1.484	214		
	1.44	1.45	1.452	300		
	1.32		1.310	119		
				1010		

<u>A. S. T. M. 13-157</u>			<u>A. S. T. M. 17-536</u>			
<u>Fe4</u>	<u>βFeOOH</u>		<u>Fe1</u>	<u>Fe8</u>	<u>αFeOOH</u>	
<u>dÅ</u>	<u>dÅ</u>	<u>hkl</u>	<u>dÅ</u>	<u>dÅ</u>	<u>dÅ</u>	<u>hkl</u>
7.44	7.40	110		5.02	4.98	020
5.27	5.25	200	4.20	4.21	4.18	110
3.34	3.311	310	3.39	3.38	3.38	120
2.62	2.616	400	2.69	2.72	2.69	130
2.58	2.543	211		2.59	2.58	021
2.32	2.343	420	2.49	2.47	2.490	040
2.09	2.097	321	2.43		2.452	111
1.96	1.944	411	2.26	2.27	2.252	121
1.77	1.746	600	2.19	2.21	2.192	140
1.67	1.635	521	2.01		2.009	131
1.54	1.515	002	1.94	1.96	1.920	041
1.46	1.480	112	1.82	1.83	1.799	211
		710	1.72	1.72	1.721	221
1.39	1.374	730		1.64	1.661	060
		312	1.57	1.57	1.564	151,160
1.32	1.303	800		1.52	1.509	250,002
				1.46	1.467	320
				1.40	1.418	112
				1.33	1.317	321

Table 16 X ray powder diffraction results.

ASTM 13-534		
<u>Fe2a</u>	<u>Fe2b</u>	<u>α Fe₂O₃</u>
3.66	3.69	3.66
2.70	2.70	2.69
2.51	2.51	2.51
2.21	2.22	2.201
1.83	1.83	1.838
1.70	1.70	1.69
1.60	1.61	1.596
1.49	1.49	1.484
1.45	1.46	1.452

ASTM 17-536		ASTM 13-157		
<u>Fe1</u>	<u>α FeOOH</u>	<u>Fe4</u>	<u>β FeOOH</u>	<u>A</u>
<u>dÅ</u>	<u>dÅ</u>	<u>dÅ</u>	<u>dÅ</u>	<u>dÅ</u>
5.03	4.97	7.47	7.40	
4.17	4.18	5.28	5.25	
3.37	3.38	3.32	3.31	
2.68	2.69	3.04		3.08
2.56	2.58	2.75		2.75
2.44	2.452	2.63	2.616	
2.25	2.252	2.54	2.543	
2.18	2.192	2.45		2.43
1.82	1.799	2.36	2.343	
1.72	1.721	2.29	2.285	
1.57	1.564	2.02	2.064	
1.51	1.509	1.95	1.944	
1.46	1.453	1.86	1.854	
		1.76	1.746	
		1.65	1.635	

A= extra values reported by Watson, Heller and Schuster 1960.

The ir spectra of Fe1 and Fe2a

Figure 17

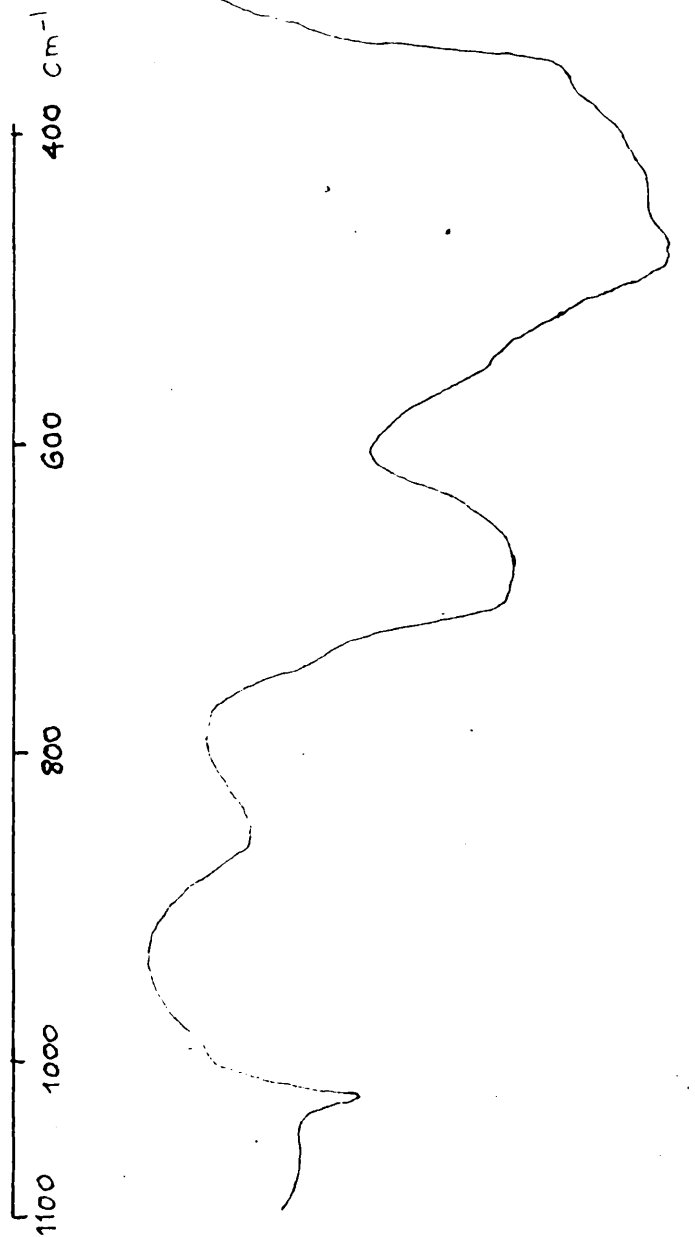
Fe1

Figure 18

Fe 2 a

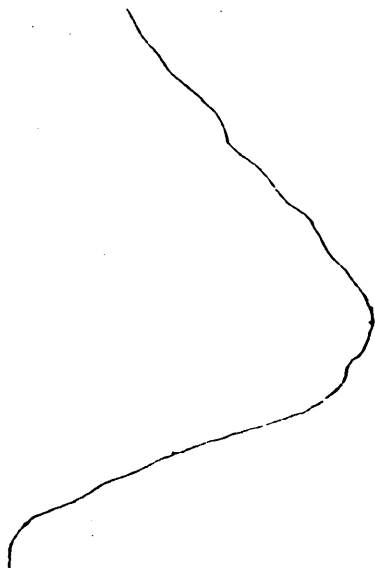


Figure 19 IR spectra of Fe₄



80

3500 3300 3000 cm⁻¹



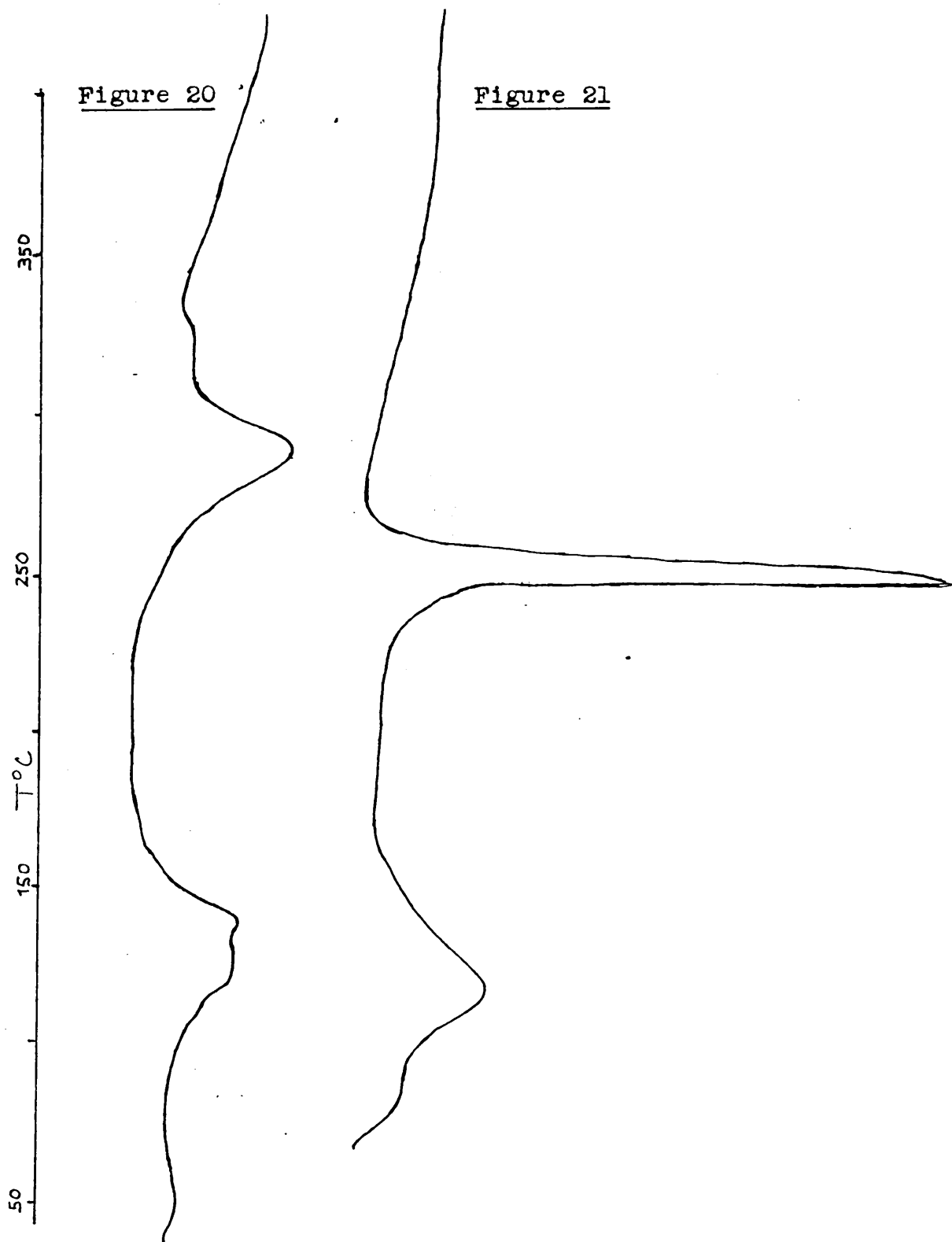
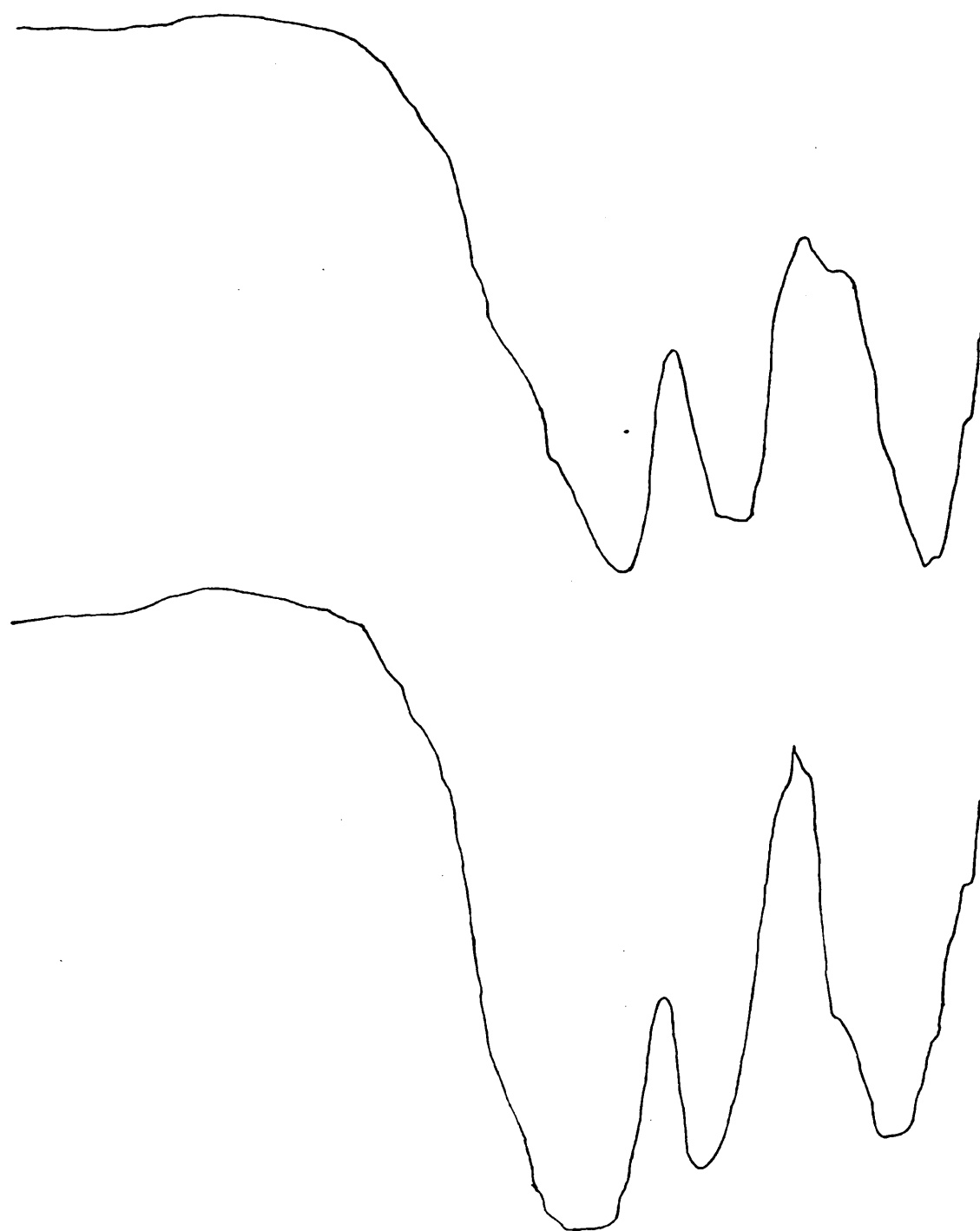
The DTA curves for Fe1 and Fe4

Figure 22 IR spectra of Fe1 and Fe4 after DTA.



1000

800

600

400

 cm^{-1}

PLATE 45

x 604,000

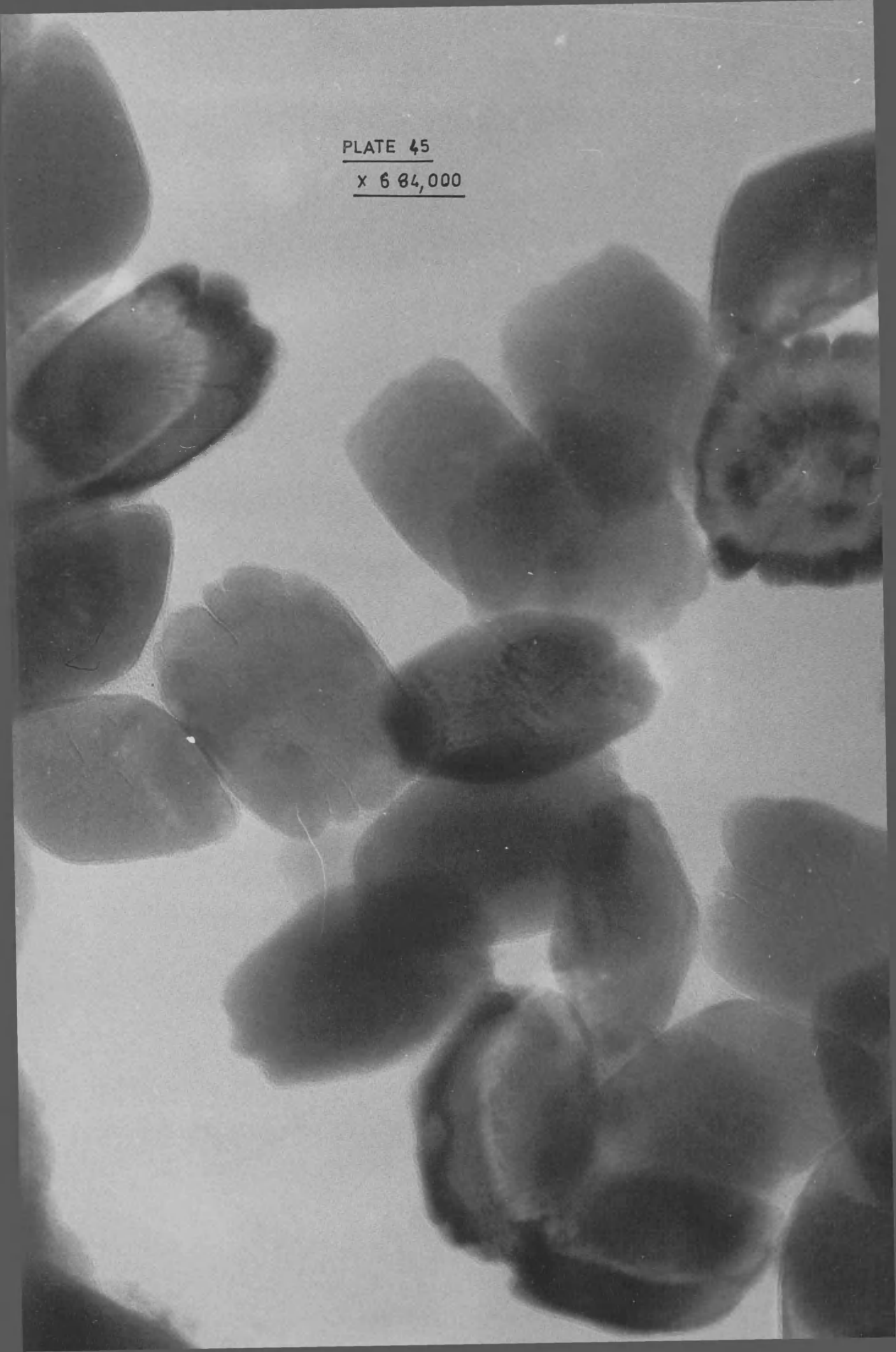
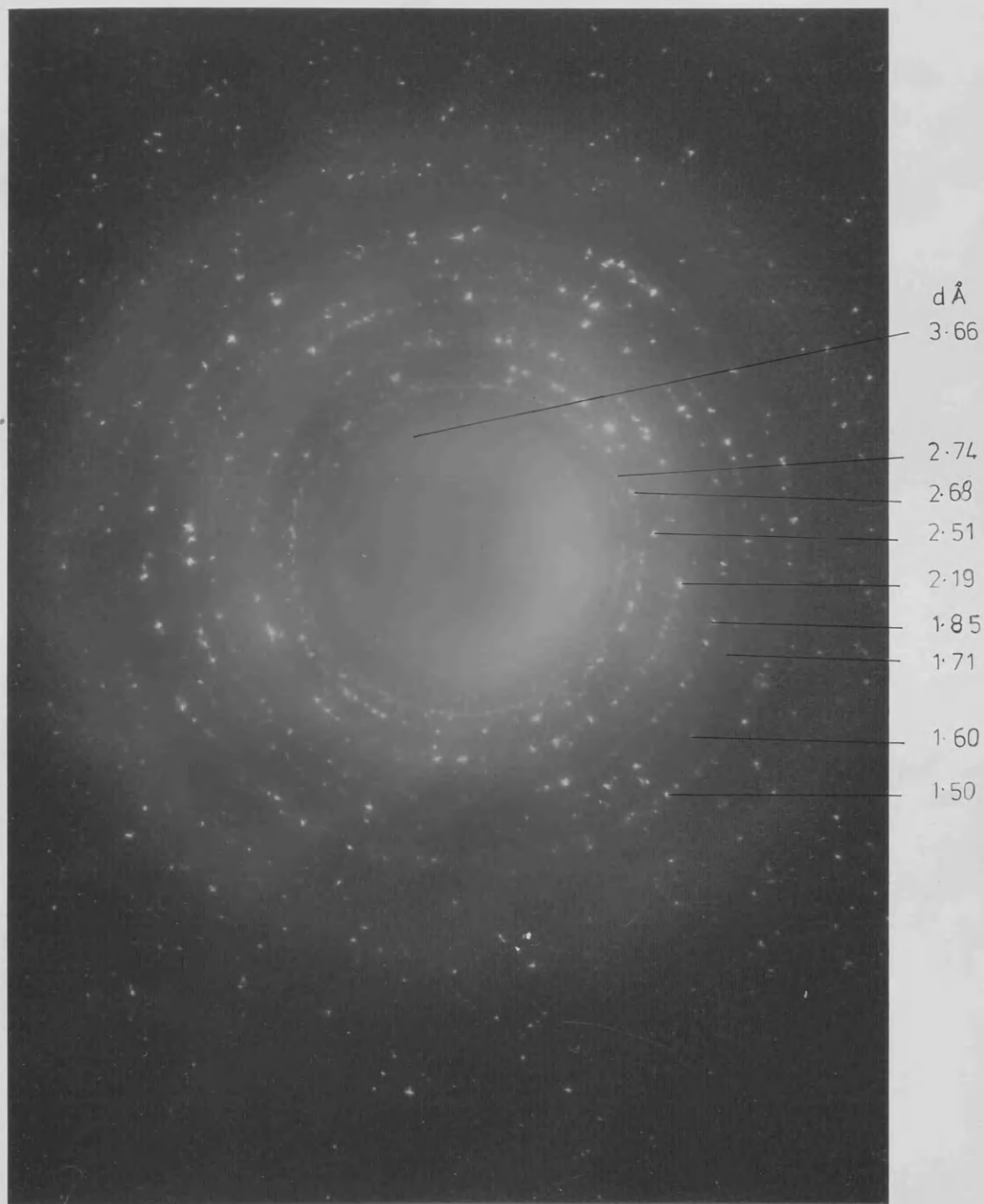


Plate 46 Electron diffraction of Fe₂b



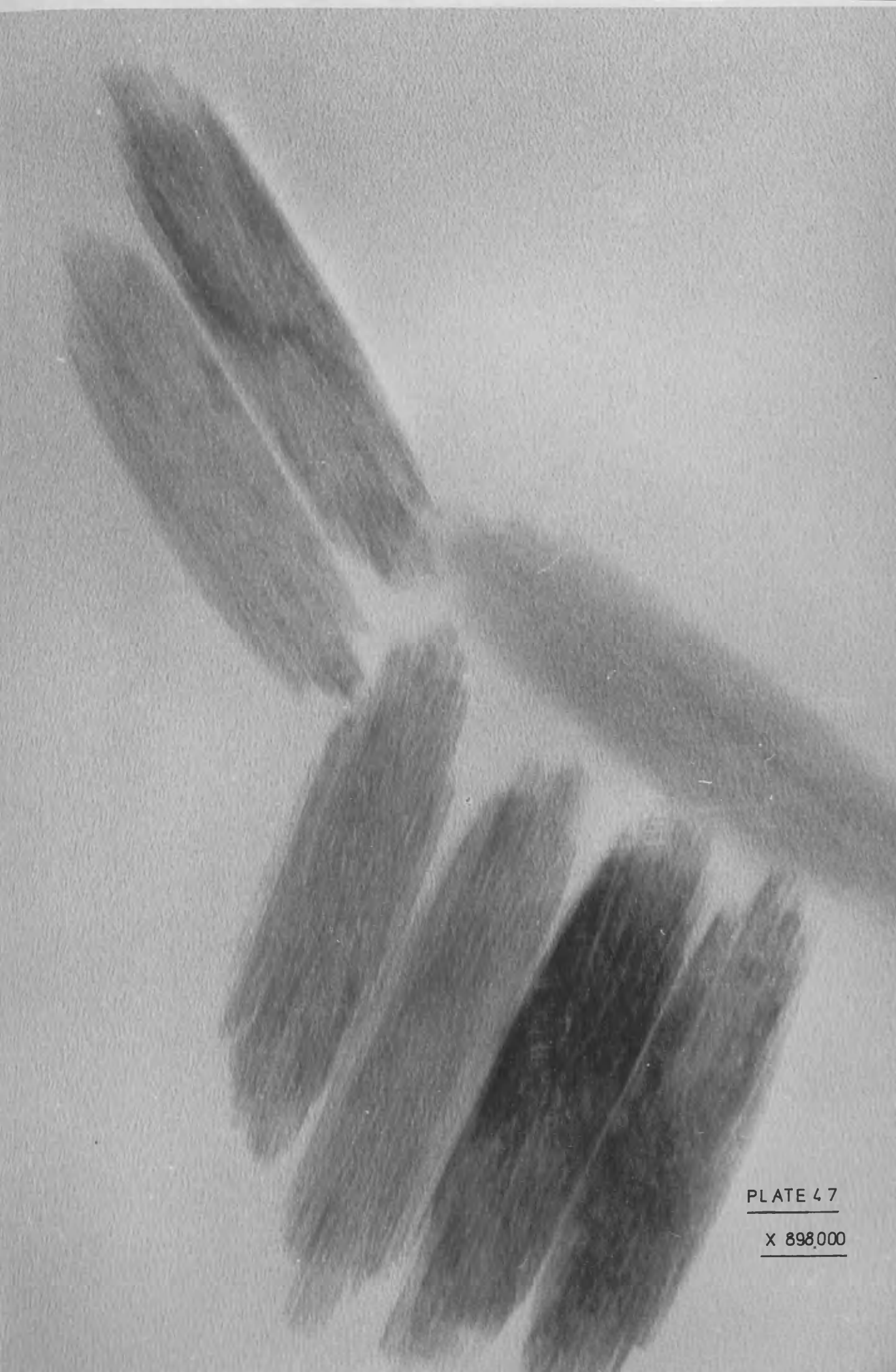


PLATE 47

X 898,000

PLATE 49

X 456,000

PLATE 50

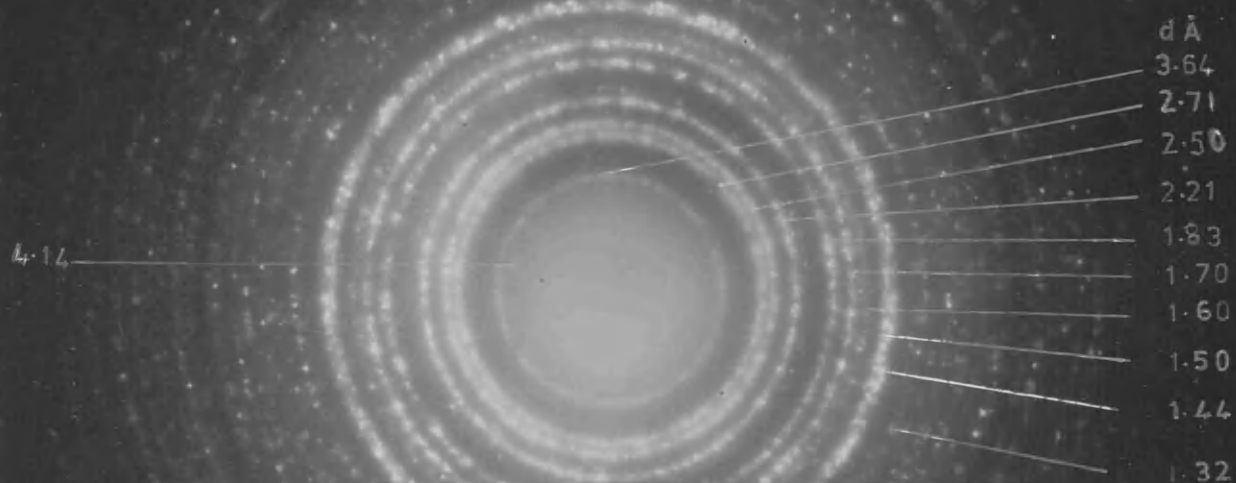
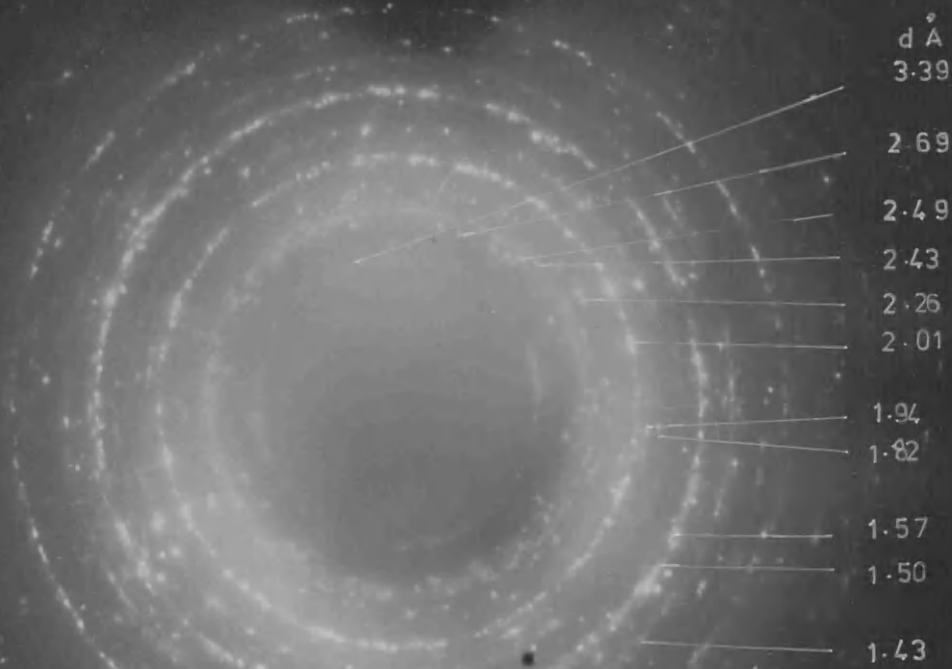


PLATE 52



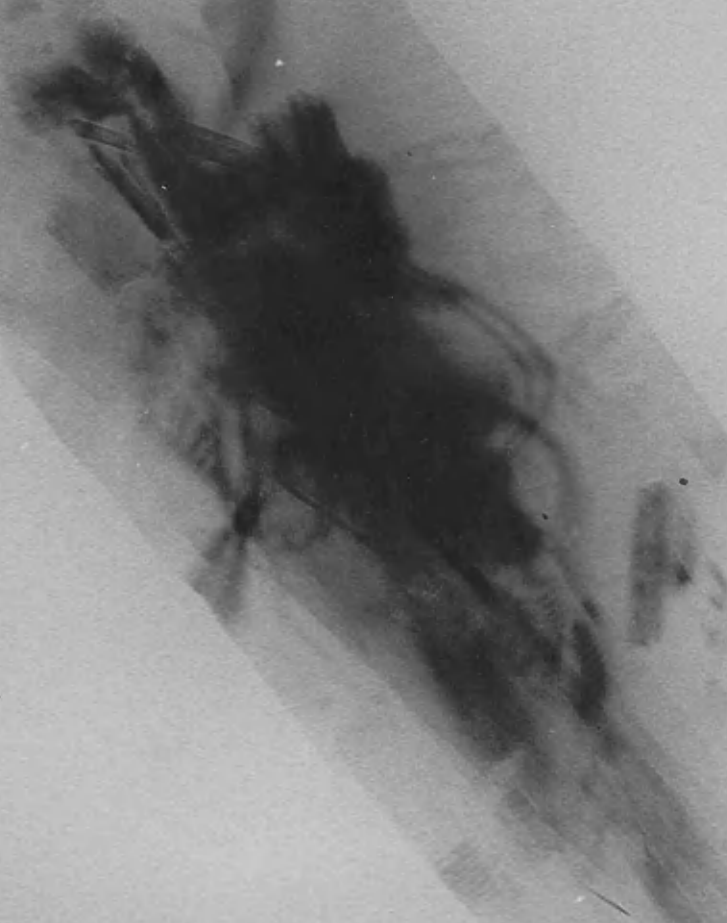


PLATE 51
X 228,000



4.35 Å

3.66 Å

PLATE 53

X 3,000,000



PLATE 55

x 865,000

Further work on the hydrolysis of iron (III) solutions.

Ferric nitrate hydrolysis was studied at 40°C and the reaction was followed by pH measurements. A graph of the pH changes against time of reaction is shown in Figure 23a. After 4 hours the pH had dropped from 2.3 to 2.05 and a sample was withdrawn, sprayed onto asbestos and examined in the microscope. The specimen consisted of thin films suspended between the asbestos fibres with thicker areas shown as rounded darker portions (plate 57). The material appears to be amorphous. After 2 days the pH had dropped to 1.9 and microscopy showed the presence of 'lath-like' α -FeOOH (plate 58). A SAD of this is shown in plate 59 and the lattice spacings are recorded and compared with those of α -FeOOH in table 18. Refluxing at this stage produces α -Fe₂O₃.

While refluxing a 0.01M ferric nitrate solution a sample was extracted at the stage where the solution was deep red in colour but still clear. An electron micrograph of this material is shown in plate 60 and its diffraction pattern in plate 61. The lattice spacings from the electron diffraction pattern are compared with those of α -Fe₂O₃ in table 19.

Ferric sulphate hydrolysis was studied at 65°C. Samples were withdrawn after 1 hour, 3 hours and one day. The 1 hour and 3 hour samples were sprayed onto asbestos fibres while the one day sample was prepared for microscopy by the droplet method. The 1 hour specimen showed a film suspended between the fibres (plate 62) while the 3 hour

specimen showed development of the final fibril like crystals of αFeOOH (plate 63). The one day specimen shows the crystals of αFeOOH (plate 64).

The hydrolysis of ferric chloride was also studied at 40°C and the reaction was followed by pH measurements and electron microscopy. The graph of pH against reaction time is shown in Figure 23b. The initial pH was 2.25. After four hours the colour of the solution had deepened to orange and the pH had dropped to 2.05. A sample was sprayed onto asbestos and showed thin films similar to those in plate 67 in the microscope. After 30 hours the pH had dropped to 1.9 and a sample sprayed onto asbestos showed pods of βFeOOH similar to those in plate 70.

The hydrolysis of ferric chloride was carried out at 25°C , 38°C , 46°C and 67°C and in all cases pods of βFeOOH were formed within 10 days. Plate 65 shows the product of T2 and the electron diffraction lattice spacings of T1, T2, T3 and T4 are recorded in table 20. Table 21 explains the codes used in this section. Ferric chloride solution was set to reflux on the sand bath and a sample was withdrawn after one day when the solution was clear but had a deep red colour. The specimen was prepared for microscopy by the spray method and showed pods of βFeOOH with the 7.4\AA (110) lattice and the 5.25\AA (200) lattice resolved (plate 66). An electron diffraction pattern was recorded and the lattice spacings values are shown in table 20.

After further refluxing $\alpha\text{Fe}_2\text{O}_3$ was produced as before.

The formation of pods of βFeOOH from the room temperature hydrolysis of ferric chloride was studied in more detail by examining ferric chloride solutions of different ages. Table 22 gives details of the codes used. The hydrolysis was followed by electron microscopy and ultracentrifugation. Samples were prepared for microscopy by spraying onto asbestos fibres except for No5 which was sprayed onto a carbon coated grid. The fresh sample No1 showed no detectable deposit on the asbestos fibres and the ultracentrifuge curve (figure 24a) shows only a plateau region indicating that there are no sedimenting species present. No2 showed a thin film suspended between asbestos fibres (plate 67) and the ultracentrifuge curve (figure 24b) indicates a slowly sedimenting species. The thin film appeared to have thickened in No3 (plate 68) where a pod is forming in the film and the ultracentrifuge curve (figure 24c) shows an increase in sedimenting rate. The lattice resolved in plate 68 was calculated as the 7.4\AA (110) lattice of βFeOOH using the 7.4\AA lattice of asbestos as an internal calibration. No4 sample shows further growth of the pods in the film (plate 69) and the corresponding ultracentrifuge curve (figure 24d) is similar to that of No3. The final sample No5 shows discrete pods of βFeOOH (plate 70) and the ultracentrifuge curve (figure 24e) shows the fastest sedimenting rate of the series. The ultracentrifuge curve of No1 remained unchanged at higher rotation speeds. Figure 24f shows a further ultracentrifuge

curve of No4 at higher rotation speed. There appears to be a secondary species present which is sedimenting out only slowly. This type of curve could not be observed for No2, No3 or No5. Using a computer programme devised by Dr Easson, percentage populations and S_{20}^w values were calculated for each of the first curves for No2, No3, No4 and No5. These were plotted and the results are shown in Figures 25, 26, 27 and 28

The room temperature hydrolyses of 'mixed' solutions containing both ferric chloride and ferric nitrate were investigated. The composition of these solutions is shown in table 21 and the ration of Fe^{3+} ion to Cl^- ion is shown below.

Code	Ratio Fe^{3+}/Cl^-	
N1	250/150 ie 5/3	
N2	250/30	25/3
N3	250/3	250/3
N4	100/3	100/3
N5	100/150	2/3
N6	75/75	3/3

The precipitate from each solution was examined by electron microscopy, electron diffraction and X ray powder diffraction. Plates 71, 73, 75 and 77 show transmission electron micrographs of N1, N2, N3 and N6 respectively. In all of these, the morphology of the crystals is closer to that of β FeOOH 'pods' (plate 70) than to the lathe-like crystals of α FeOOH

(plate 51) produced from the room temperature hydrolysis of ferric nitrate, but their electron diffraction patterns (plates 72, 74, 76 and 78 and table 23) indicate that the material is α FeOOH. In plates 71, 73 and 75 of N1, N2 and N3 the 4.18 (110) lattice of α FeOOH is resolved and is indicated. In the case of plate 77 (N3) the 7.4 \AA lattice of asbestos is also resolved and was used as an internal calibration. Plate 79, the transmission micrograph of N4, shows α FeOOH with a morphology similar to the α FeOOH formed in the ferric sulphate hydrolysis (plate 65). The electron diffraction pattern of N4 is shown in plate 80 and the calculated lattice spacings are recorded in table 23. Plate 81, a transmission micrograph of N5, shows crystals with a 'pod' morphology but in this case the diffraction pattern (plate 82) can be compared with β FeOOH (table 23) and the 7.4 \AA (110) lattice of β FeOOH is resolved. To confirm the identity of the precipitates N1 to N6, X ray powder diffraction patterns were recorded and the lattice spacings calculated from these are given in table 24. An IR spectra of N6 was recorded and is shown in figure 29 and compared with that of Fe1 (figure 17) (α FeOOH).

A sample of an 0.01 M $\text{FeCl}_3 \cdot 6\text{H}_2\text{O}$ solution made up with alcohol and a sample of an 0.01 M $\text{Fe}(\text{NO}_3)_3 \cdot 9\text{H}_2\text{O}$ solution made up with alcohol were refluxed for 9 days. In both cases precipitates were formed. These precipitates were designated Fe5 and Fe6 respectively. The solution of ferric nitrate in alcohol also formed a precipitate at room temperature after 10 days and this was designated Fe3. The solution of

ferric chloride in alcohol at room temperature remained a clear pale green-yellow even after two years. The precipitates were examined in the electron microscope, samples were prepared by the droplet method, and transmission micrographs and electron diffraction patterns were recorded. IR spectra were recorded for all three precipitates. X ray powder diffraction patterns and DTA curves were recorded for Fe3 and Fe6.

The transmission micrograph of Fe5 is shown in plate 83. No clear 'pods' or 'cubes' were detected. The sample gave a diffraction pattern, the lattice spacings of which are shown in table 25. The IR spectrum of Fe5, shown in figure 30a was compared with that of Fe4 (figure 19). From the IR and electron diffraction data Fe5 was identified as β -FeOOH.

Fe6 was red. Electron microscopy showed small clusters of cube-like material as shown in plate 84, with the diffraction pattern of α -Fe₂O₃ (table 26). X ray powder diffraction patterns confirmed this identification (table 26). The DTA curve showed no peaks over the range studied which is consistent with α -Fe₂O₃ and the IR spectrum (figure 30b) showed absorption typical of hematite. There was no change in the IR spectrum after the sample had been heated to 450°C in DTA.

Fe3 was red-brown. An electron micrograph of this material is shown in plate 85. Lattices of 3.3Å and 2.6Å have been resolved. The electron diffraction pattern of Fe3 is shown in plate 86 and the lattice spacings are recorded in table 27. The spacings calculated from the X ray powder diffraction pattern are also given in table 27. No fit for either pattern was found in the ASTM index. The IR spectrum

was recorded (figure 31) and compared with that of Fe2a (figure 18) ($\alpha\text{Fe}_2\text{O}_3$), and that of Fe1 (figure 17) (αFeOOH). The IR of Fe3 resembles that of Fe1 more closely than that of Fe2a. The DTA curve of Fe3 was also recorded (figure 32). This curve has an endotherm at 120°C , a small endotherm at 290°C followed by an exotherm at 330°C . After DTA the IR spectrum is that of hematite.

Different concentrations of ferric chloride were hydrolysed at room temperature and at 40°C . Changes in pH were recorded for the 40°C hydrolyses. The lengths of the pods obtained from the hydrolysis were recorded. Table 28 shows the concentrations of the ferric chloride solutions which were studied and their codes. Solutions which were hydrolysed at 40°C have the postscript 40.

Concentration and pod size.

A sample of each solution was heated at 40°C for 2 days and the remainder of each solution was kept at room temperature. Solution B40 was examined in the microscope after 24 hours. After 2 days the solutions at 40°C were removed from the thermostat and kept at room temperature for a further 70 days to ensure that the pods had reached their final length. Specimens of each solution, prepared by the droplet method, were examined in the electron microscope. Distinct pods were obtained from A, A40, B, B40, C, C40 and D. Plate 87 is a micrograph of B40 and plate 88 is its diffraction pattern. The lengths of the pods were measured directly from the negative micrographs for several plates of A, B, C, C40 and D and from 1 plate of A40 and of B40 and the results were recorded in the form of histograms

(figures 33, 34, 35, 36 and 37). Means and standard deviations were calculated for all samples although the sample sizes for A40 and B40 were really too small for statistical analysis to be valid. The means were calculated assuming that each pod had the length of the mid point of the class interval. Standard deviations, SD, were calculated using the formula.

$$SD = \frac{((m-a)^2 \times F)}{n} \quad \text{where } n = \text{sample size}$$

m = mean
F = frequency
a = mid point value of
class interval

The results are shown in table 29.

pH changes.

pH readings were taken during the hydrolyses of all the ferric chloride solutions except D40 at 40 C over 50 hours. The results are shown in the form of graphs (figures 38 and 39). In all cases there is a sharp initial drop in pH followed by a slower pH drop. Electron microscopy of samples indicated that the sharp pH drop accompanies film formation in solutions A40 to E40 and that the pods form later. The pH changes during the hydrolysis of 0.01M ferric chloride (D40) were reported earlier in this section (figure 23b).

For solutions E, G, H, E40, G40 and H40 no distinct pods formed although E (plate 89) contained β FeOOH, identified by electron diffraction (table 30).

Table 18 Electron diffraction result for ferric nitrate
after three days at 40°C

from plate 59	α FeOOH	
	ASTM 17-536	
dÅ	dÅ	hkl
3.39	3.38	120
2.58	2.58	021
2.45	2.452	111
2.28	2.252	121
1.99	2.009	131
1.92	1.920	041
1.77	1.770	141
1.58	1.564	151
1.51	1.509	250
1.42	1.418	112
1.37	1.317	321
1.23	1.226	222

Table 19 Electron diffraction result for ferric nitrate
after one day's reflux.

from plate 61	α Fe ₂ O ₃	
	ASTM 13-543	
dÅ	dÅ	hkl
3.67	3.66	012
2.70	2.69	104
2.49	2.51	110
1.845	1.834	024
1.70	1.690	116
1.455	1.452	300
2.21	2.201	113

Table 20 Electron diffraction results from ferric chloride
hydrolyses at different temperatures.

T1	T2	T3	T4	reflux 1 day	<u>β FeOOH ASTM 13-157</u>	
dÅ	dÅ	dÅ	dÅ	dÅ	dÅ	hkl
7.40		7.38	7.37	7.39	7.40	110
5.28	5.26	5.22	5.21	5.23	5.25	200
				3.67	3.70	220
3.34	3.34	3.31	3.34	3.34	3.311	310
2.62					2.616	400
	2.52	2.52	2.56	2.52	2.543	211
2.36			2.33		2.343	420
	2.28	2.28		2.25	2.285	301
			2.12		2.097	321
2.04	2.06	2.08		2.08	2.064	510
	1.92	1.97	1.97	1.98	1.944	411
	1.75		1.77	1.73	1.746	600
1.60	1.64	1.67	1.66	1.64	1.635	521
	1.53	1.52	1.54	1.52	1.515	002

Table 22 Codes for ultracentrifuge work on 0.1M ferric chloride

<u>Code</u>	<u>age of solution</u>
No1	fresh
No2	2 days
No3	4 days
No4	6 days
No5	16 days

Table 21 Hydrolysis of iron(III) solutions

<u>Run code</u>	<u>Solution</u>	<u>Conditions of hydrolysis</u>
Fe1	$\text{Fe}(\text{NO}_3)_3 \cdot 9\text{H}_2\text{O}$ (I)	room temperature
Fe2a	"	reflux
Fe2b	$\text{FeCl}_3 \cdot 6\text{H}_2\text{O}$ (II)	reflux
Fe4	"	room temperature
Fe3	$\text{Fe}(\text{NO}_3)_3 \cdot 9\text{H}_2\text{O}$ (alcohol)	room temperature
Fe6	"	reflux
Fe5	$\text{FeCl}_3 \cdot 6\text{H}_2\text{O}$ (alcohol)	room temperature
Fe7	"	reflux
Fe8	$\text{Fe}_2(\text{SO}_4)_3 \cdot 9\text{H}_2\text{O}$	reflux
Fe9	$\text{Fe}(\text{ClO}_4)_3 \cdot 9\text{H}_2\text{O}$	reflux
T1	$\text{FeCl}_3 \cdot 6\text{H}_2\text{O}$	25°C
T2	"	38°C
T3	"	46°C
T4	"	67°C
N1	200ml (I) + 50ml (II)	room temperature
N2	240ml (I) + 10ml (II)	" "
N3	249ml (I) + 1ml (II)	" "
N4	99ml (I) + 1ml (II)	" "
N5	50ml (I) + 50ml (II)	" "
N6	50ml (I) + 25ml (II)	" "
A	0.1M $\text{FeCl}_3 \cdot 6\text{H}_2\text{O}$	40°C
B	0.05M $\text{FeCl}_3 \cdot 6\text{H}_2\text{O}$	"
C	0.025M $\text{FeCl}_3 \cdot 6\text{H}_2\text{O}$	"
D	0.01M $\text{FeCl}_3 \cdot 6\text{H}_2\text{O}$	"
E	0.005M $\text{FeCl}_3 \cdot 6\text{H}_2\text{O}$	"
G	0.001M $\text{FeCl}_3 \cdot 6\text{H}_2\text{O}$	"
H	0.0005M $\text{FeCl}_3 \cdot 6\text{H}_2\text{O}$	"

Table 23 Electron diffraction results for the N series.

<u>N1</u>	<u>N2</u>	<u>N3</u>	<u>N4</u>	<u>N6</u>	<u>α FeOOH</u>	
<u>dÅ</u>	<u>dÅ</u>	<u>dÅ</u>	<u>dÅ</u>	<u>dÅ</u>	<u>ASTM 17-536</u>	<u>hkl</u>
	4.22	4.16	4.17		4.18	110
				3.40	3.38	120
3.03					3.02*	001
	2.57	2.60	2.60	2.56	2.58	021
		2.50	2.49		2.52	101
2.40	2.44			2.42	2.452	111
	2.26				2.252	121
2.14		2.19	2.19		2.192	140
				1.99	2.009	131
1.80					1.799	211
	1.71	1.68	1.69		1.721	221
			1.55	1.58	1.564	160
	1.505	1.48	1.48		1.509	250
1.40					1.418	112
				1.24	1.226	222

<u>N5</u>	<u>β FeOOH ASTM 13-157</u>	
<u>dÅ</u>	<u>dÅ</u>	<u>hkl</u>
7.44	7.40	110
5.26	5.25	200
3.31	3.311	310
2.61	2.616	400
2.33	2.343	420
1.96	1.944	411
1.65	1.635	521
1.52	1.515	002

* calculated from the cell constants.

Table 24 X-ray diffraction values for the N series.

<u>N1</u>	<u>N2</u>	<u>N3</u>	<u>N4</u>	<u>N6</u>	<u>α FeOOH ASTM 17-536</u>
$\text{d}\overset{\circ}{\text{A}}$	$\text{d}\overset{\circ}{\text{A}}$	$\text{d}\overset{\circ}{\text{A}}$	$\text{d}\overset{\circ}{\text{A}}$	$\text{d}\overset{\circ}{\text{A}}$	$\text{d}\overset{\circ}{\text{A}}$
4.17	4.21	4.16	5.01		4.98
3.36			4.20	4.18	4.18
	3.06			3.38	3.38
2.71	2.72	2.68	2.71		2.69
2.56	2.60	2.56	2.59	2.59	2.58
				2.50	2.49
2.44	2.46	2.44	2.45	2.44	2.452
2.27	2.27	2.24	2.24		2.252
2.18	2.21	2.18	2.16	2.20	2.192
1.91				1.92	1.920
1.72	1.74	1.72	1.70	1.74	1.721
1.65				1.67	1.661
1.57	1.59	1.56	1.57	1.58	1.564
	1.54			1.53	1.509

<u>N5</u>	<u>β FeOOH ASTM 13-157</u>
$\text{d}\overset{\circ}{\text{A}}$	$\text{d}\overset{\circ}{\text{A}}$
7.40	7.40
5.24	5.25
3.33	3.311
2.50	2.543
2.25	2.285
2.08	2.064
1.94	1.944
1.63	1.635

Table 25 Electron diffraction of Fe5

<u>Fe5</u>	<u>β FeOOH ASTM 13-157</u>
$\frac{C}{d\text{\AA}}$	$\frac{D}{d\text{\AA}}$
3.32	3.311
3.09	3.08*
2.28	2.285
1.87	1.854
1.75	1.746
1.61	1.635
1.53	1.515

* = value reported by Watson Heller and Schuster 1960

Table 26 Electron diffraction and X-ray diffraction for Fe6.

<u>A</u>	<u>B</u>	<u>α Fe₂O₃ ASTM 13-534</u>
$\frac{C}{d\text{\AA}}$	$\frac{D}{d\text{\AA}}$	$\frac{D}{d\text{\AA}}$
	3.64	3.66
2.69	2.71	2.69
2.54	2.52	2.51
2.21	2.21	2.201
1.87	1.84	1.834
1.69	1.71	1.690
1.48		1.484

A = electron diffraction results.

B = X-ray diffraction results.

Table 27 Electron diffraction and X-ray diffraction results
for Fe3

$\frac{C}{d\text{\AA}}$	$\frac{D}{d\text{\AA}}$
3.04	3.06
2.75	
	2.49
	2.29
	2.09
	1.93
1.87	1.86
1.60	1.60
1.32	

D = X-ray diffraction results.

C = electron diffraction result

Table 28 Concentrations of FeCl₃ solutions.

<u>Code</u>	<u>Concentration (molar)</u>
A	0.1
B	0.05
C	0.025
D	0.01
E	0.005
G	0.001
H	0.0005

Table 29 Pod sizes.

<u>Solution</u>	<u>Sample size</u>	<u>Mean(\AA)</u>	<u>Standard deviation (\AA)</u>
A	204	1237	177.5
B	209	1302	179.6
C	336	1265	191.3
D	193	1206	188.2
A40	33	1247	158.6
B40	33	1179	187.9
C40	204	1300	185.4

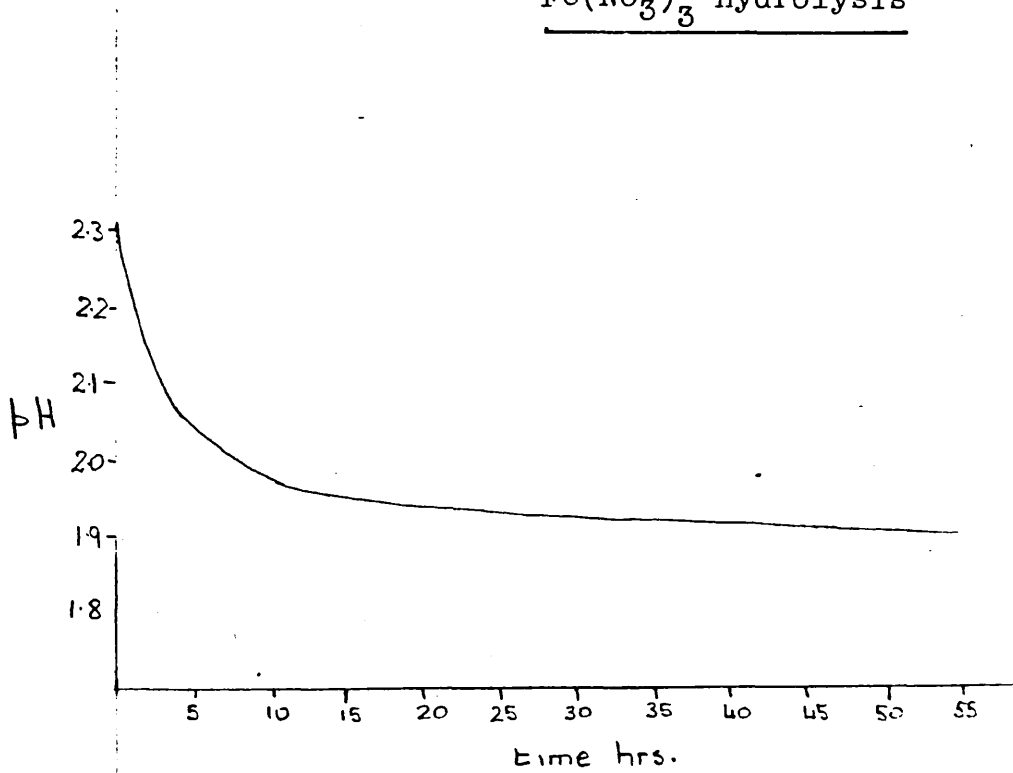
Table 30 Electron diffraction result for the hydrolysis of
solution E after 70 days.

from E	β -FeOOH: ASTM 13-157	β -FeOOH: from Watson, Heller and Schuster
$\text{d}\overset{\circ}{\text{\AA}}$	$\text{d}\overset{\circ}{\text{\AA}}$	$\text{d}\overset{\circ}{\text{\AA}}$
5.22	5.25	
3.81		3.81
3.30	3.311	
2.62	2.616	
2.35		2.35
2.27	2.285	
1.92	1.944	
1.79		1.76
1.62	1.635	
1.51	1.515	
1.31		1.31

Figure 23 pH v time graphs for hydrolysis at 40°C

(a)

$\text{Fe}(\text{NO}_3)_3$ hydrolysis



(b)

FeCl_3 hydrolysis

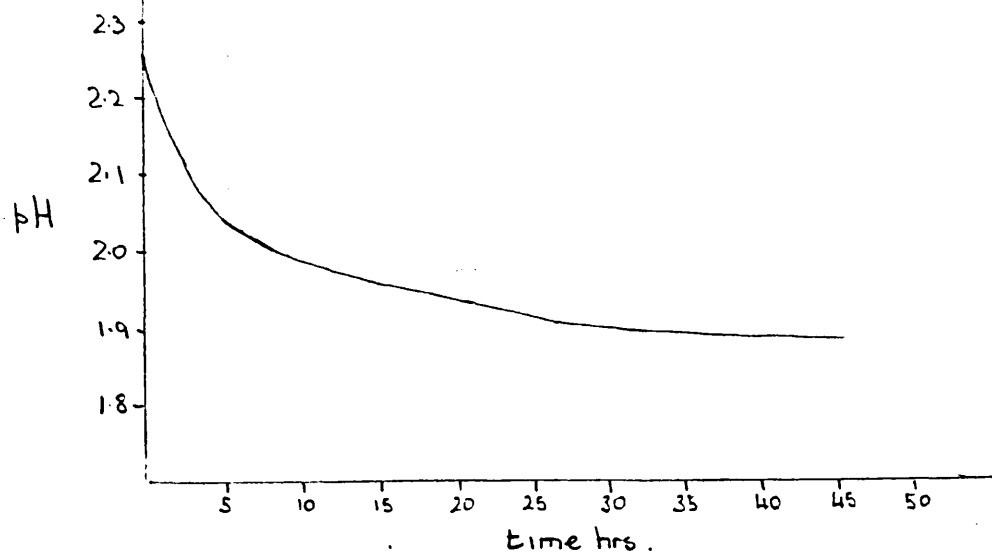


Figure 24 a to f Ultracentrifuge curves.

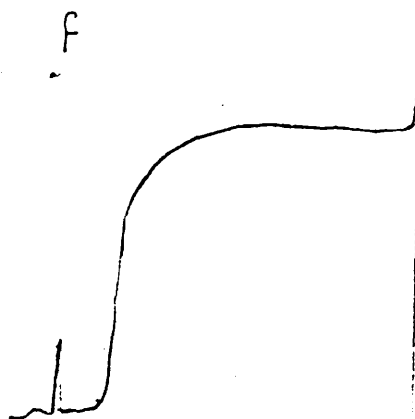
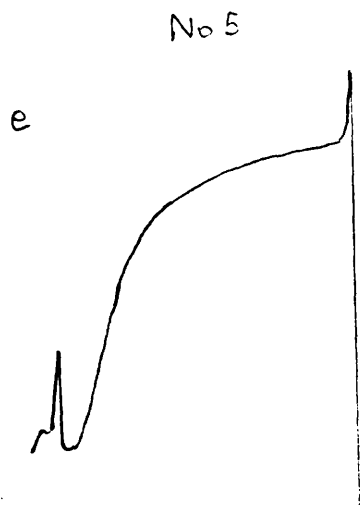
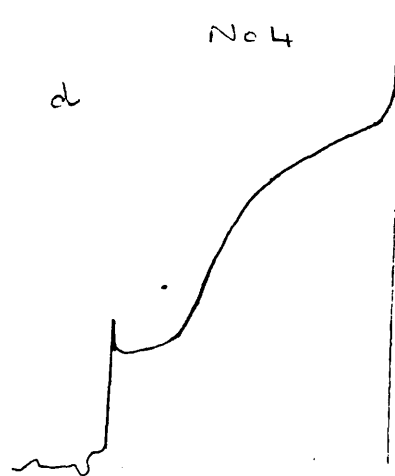
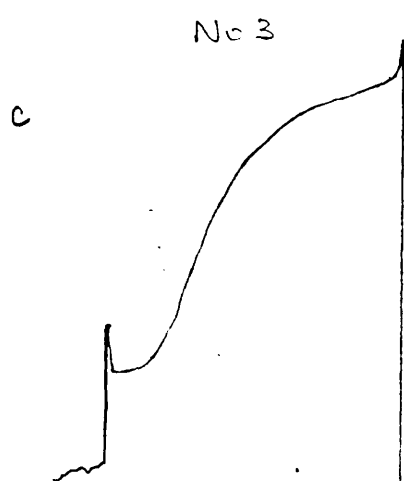
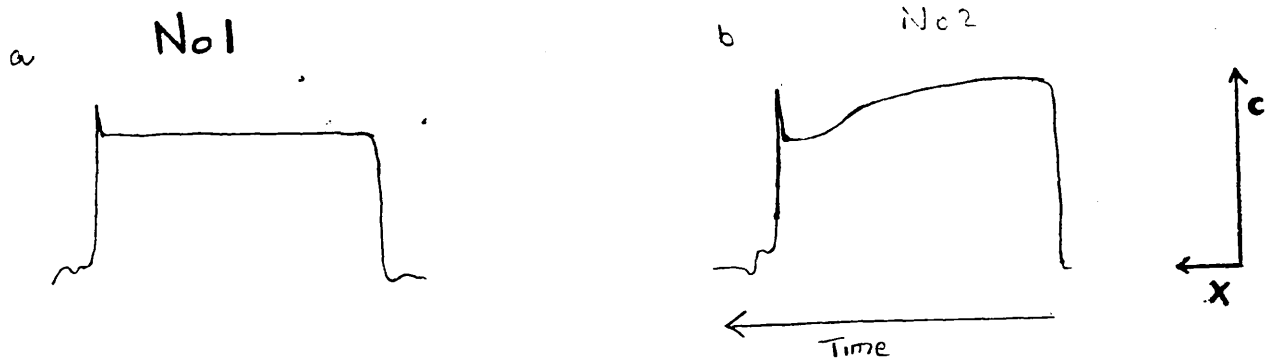


Figure 25 S_{20W} V population for No2

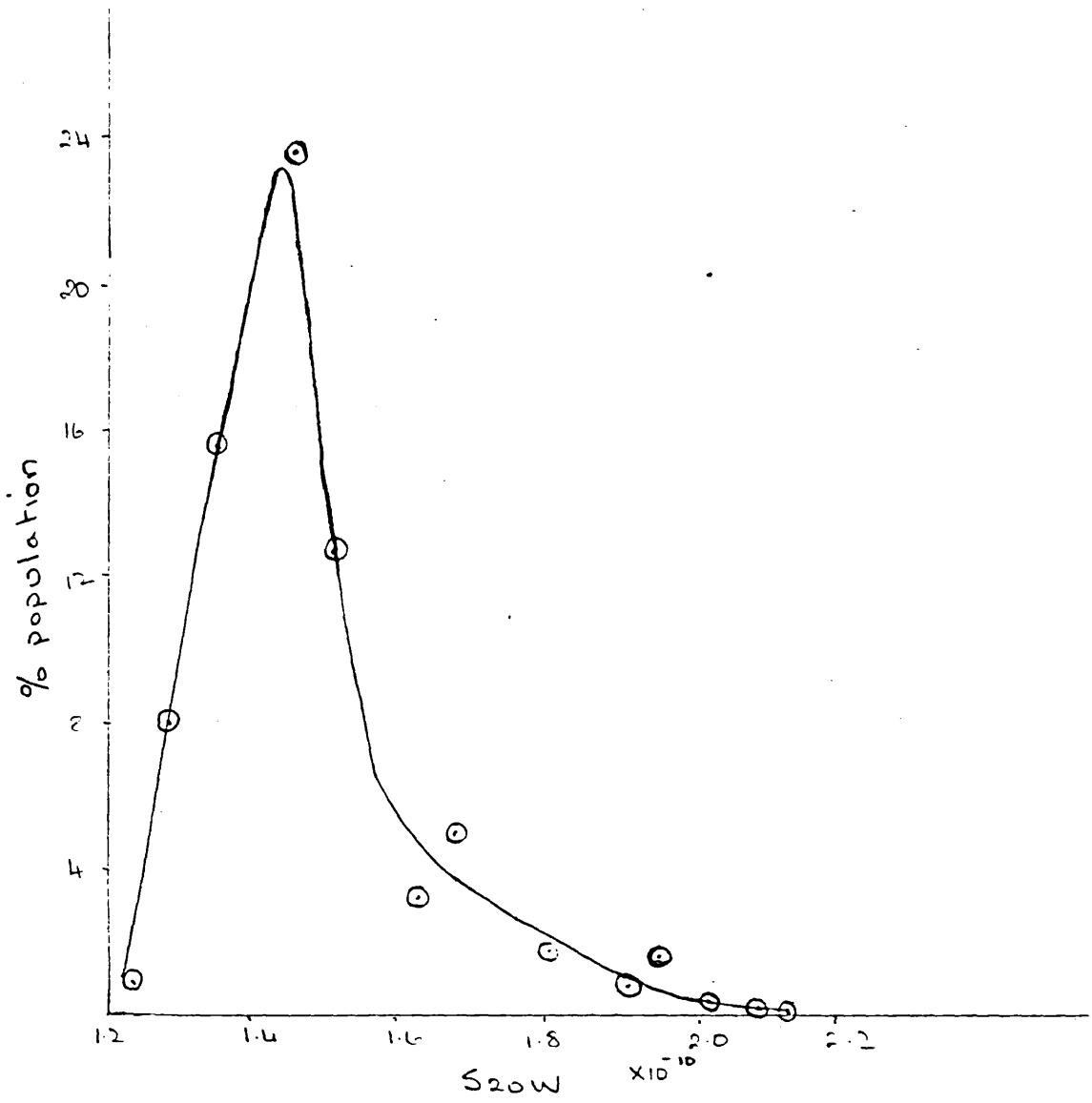


Figure 26 % population v S_{20W} for No3

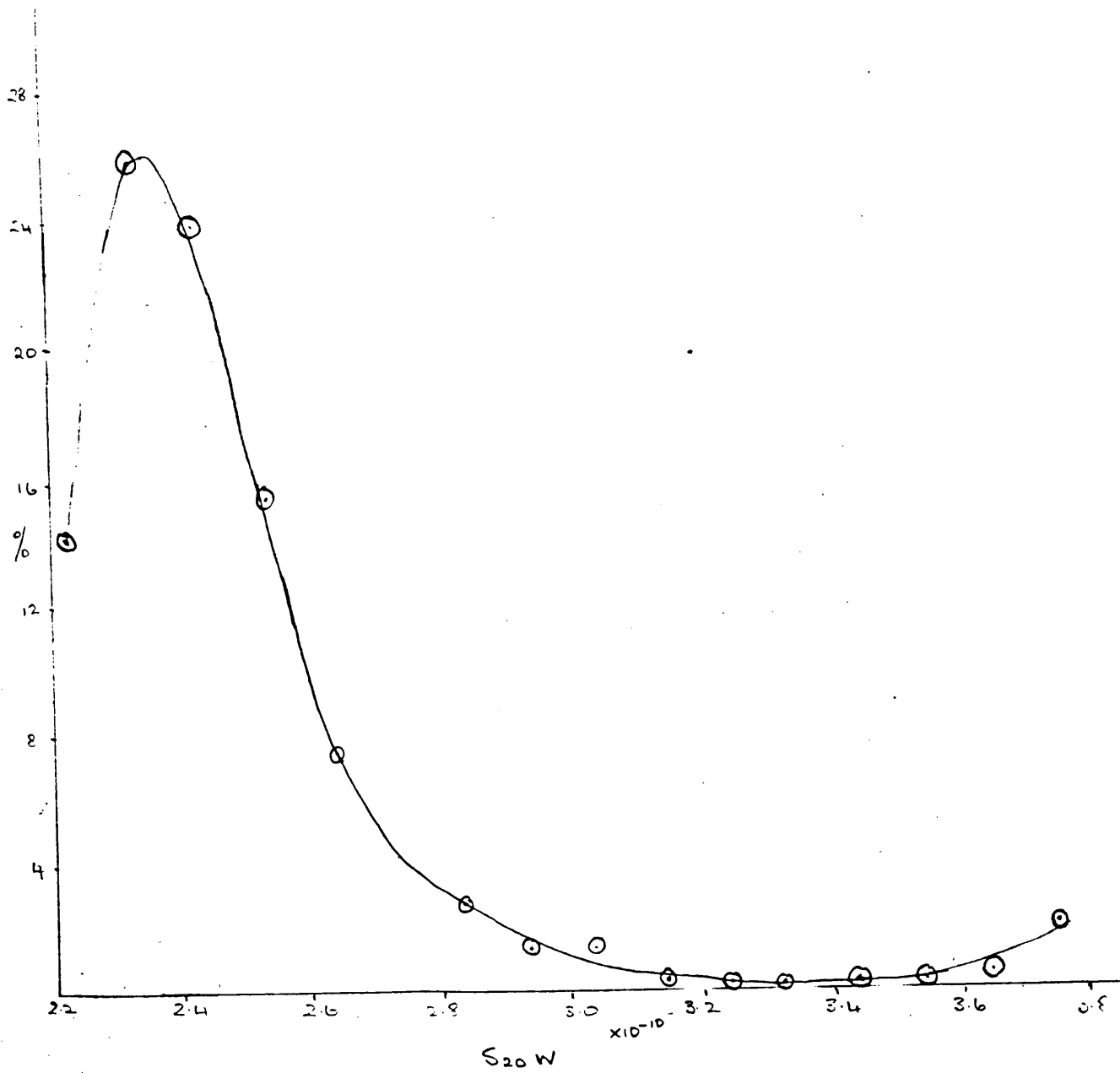


Figure 27 % population v S_{20W} for No4

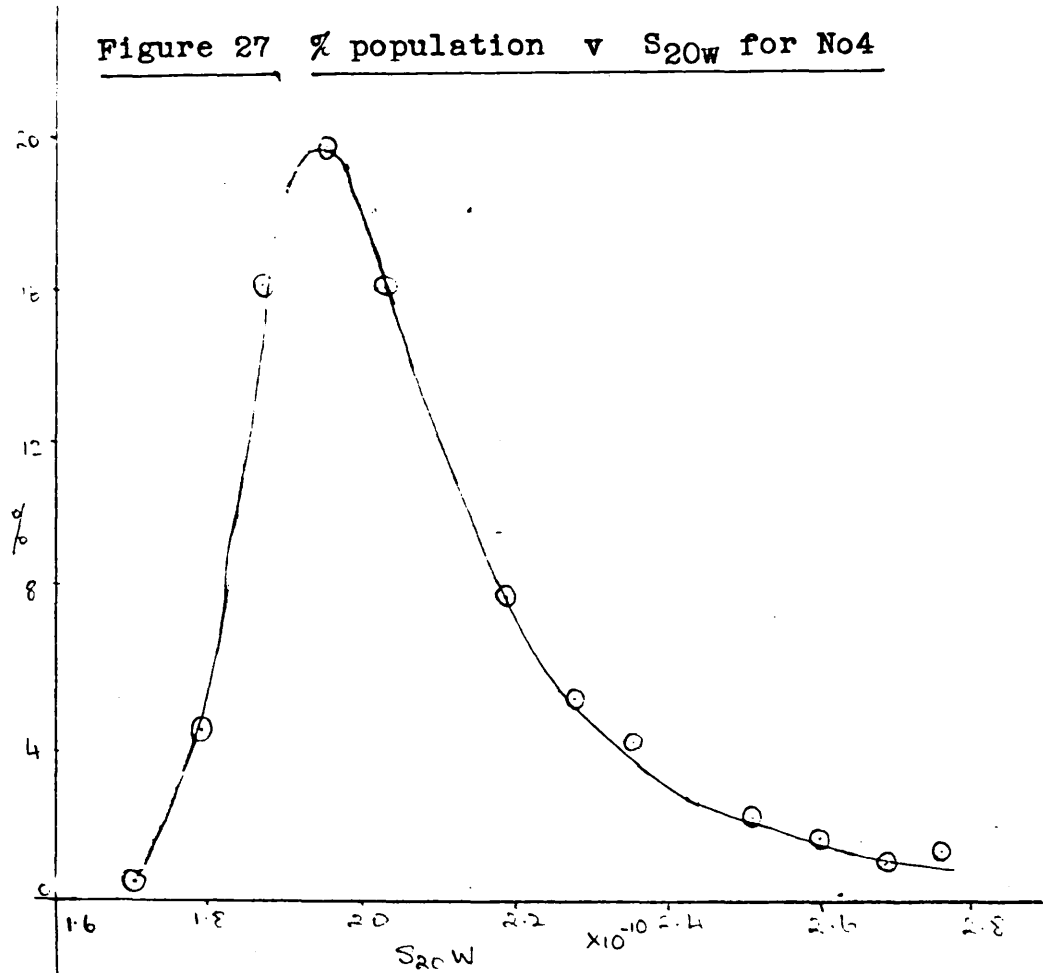
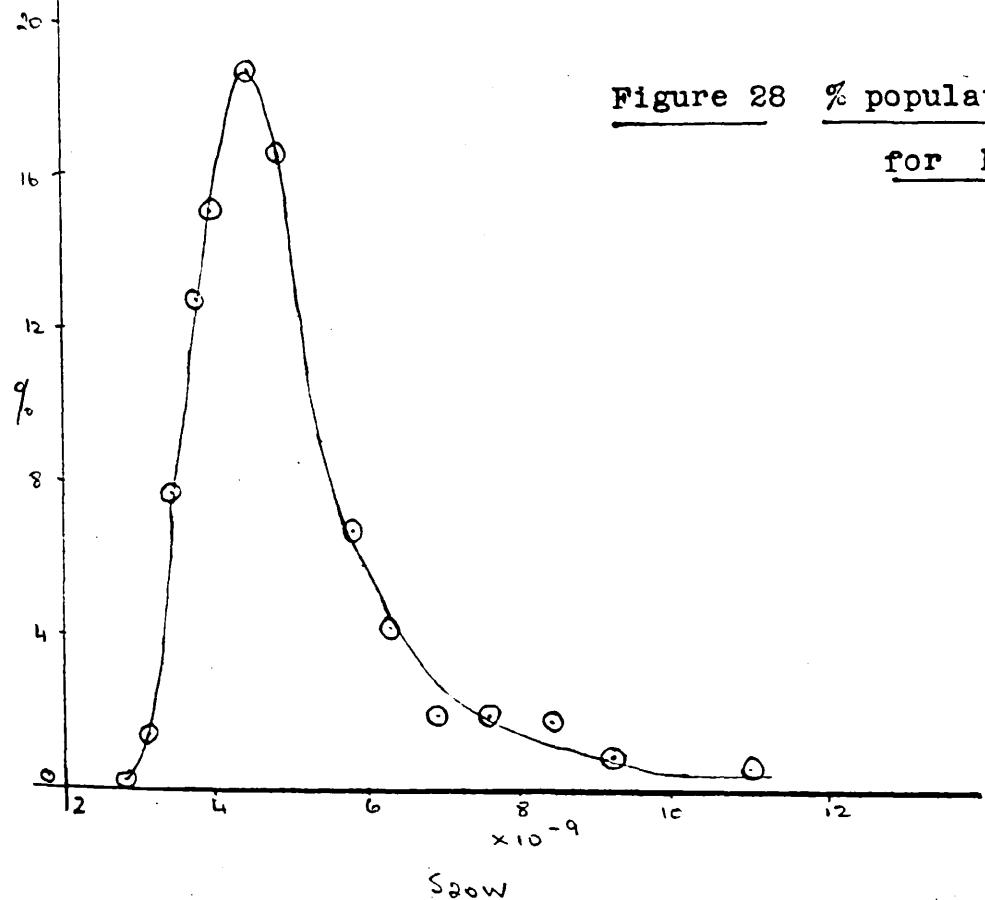


Figure 28 % population v S_{20W}
for No5



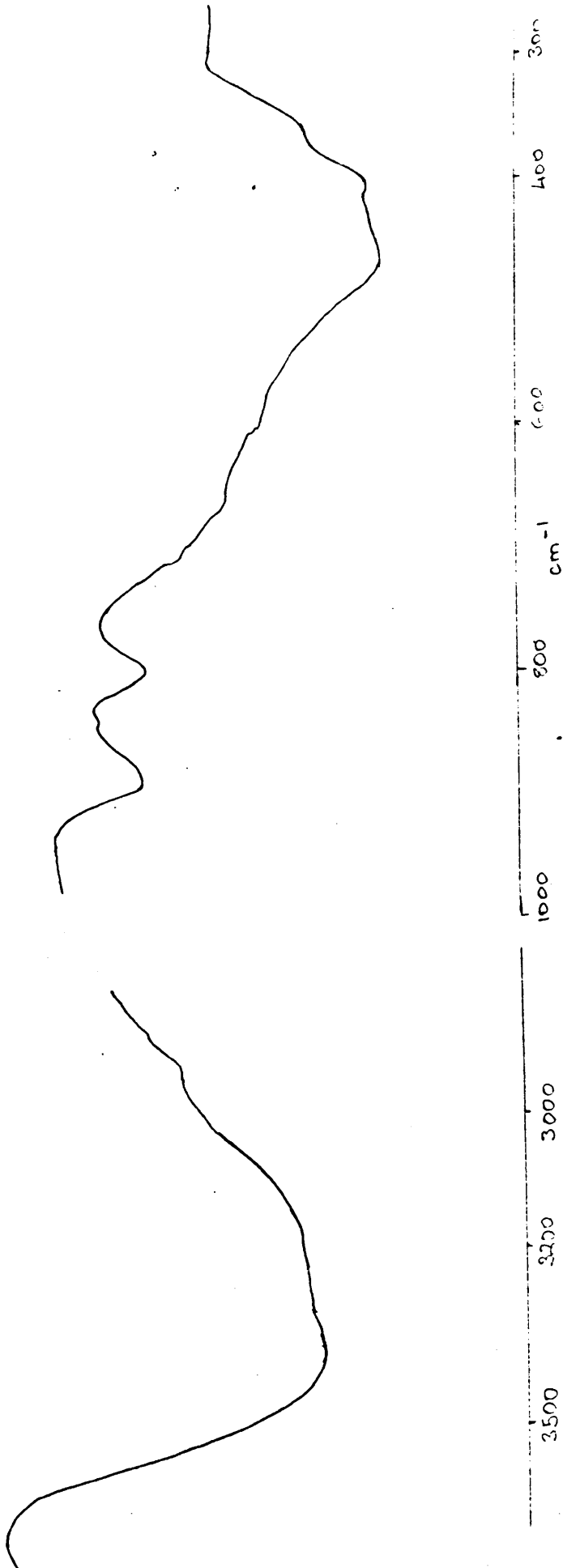


Figure 29

ir spectrum of N6

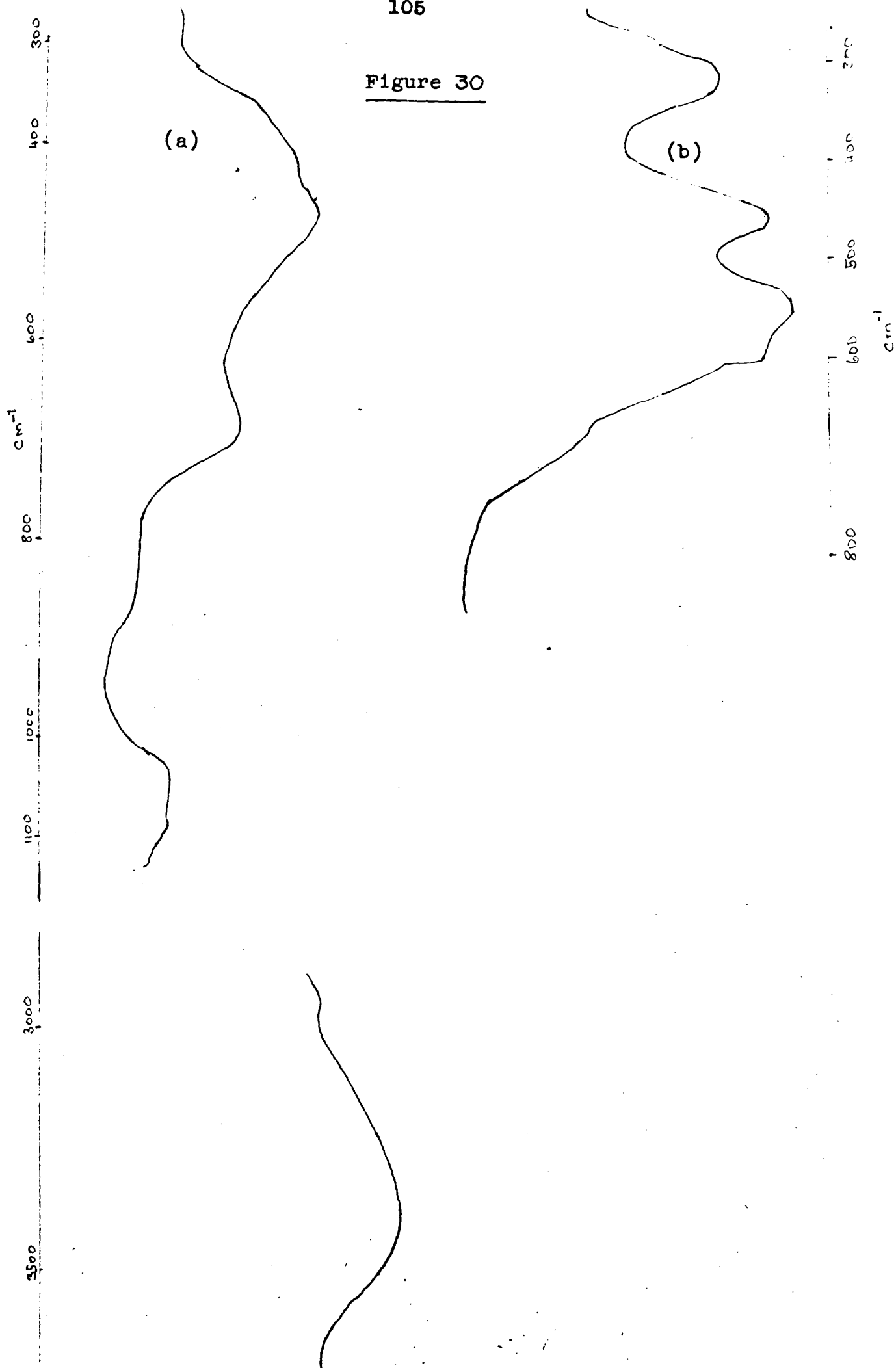
Figure 30

Figure 31 ir spectrum of Fe3

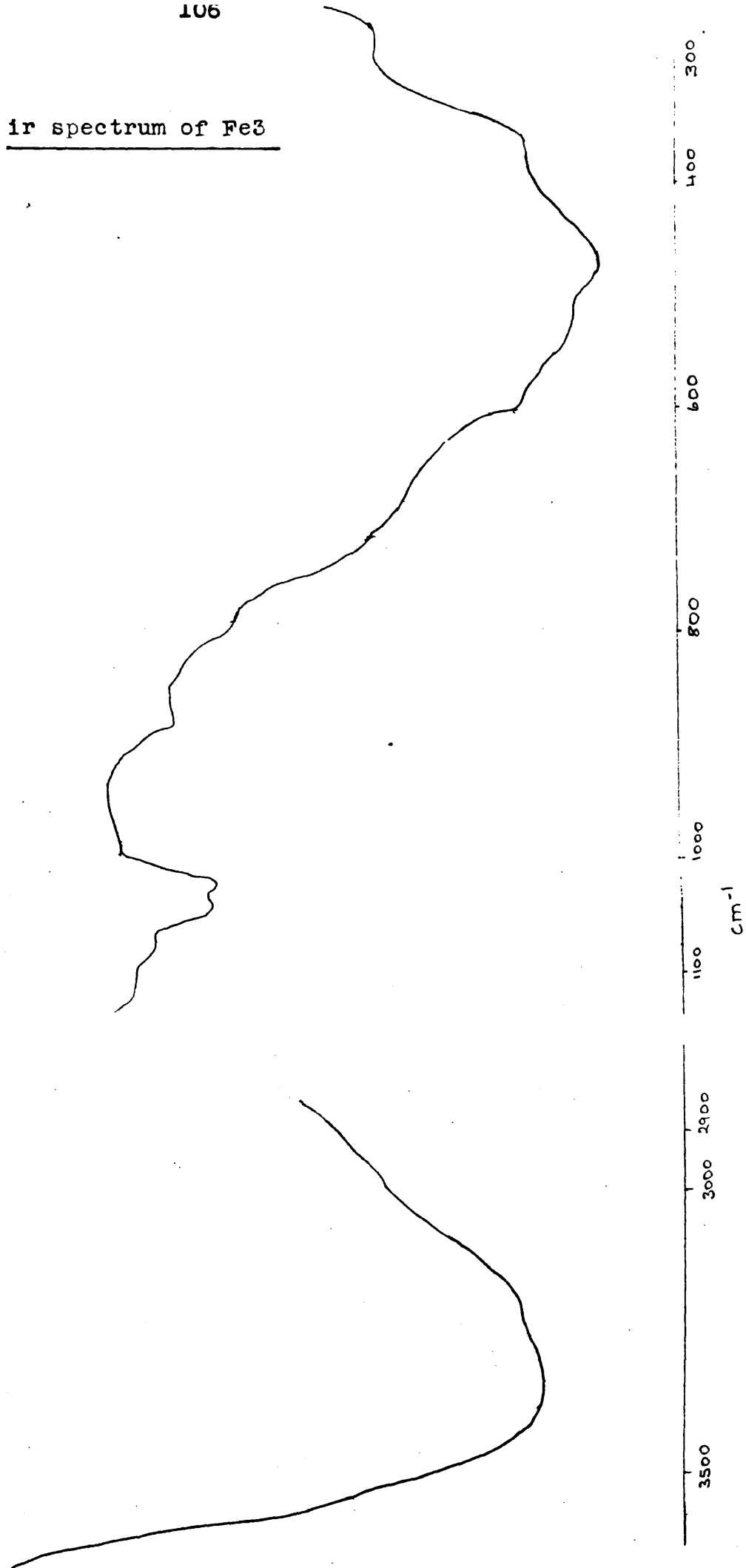


Figure 32 DTA of Fe₃

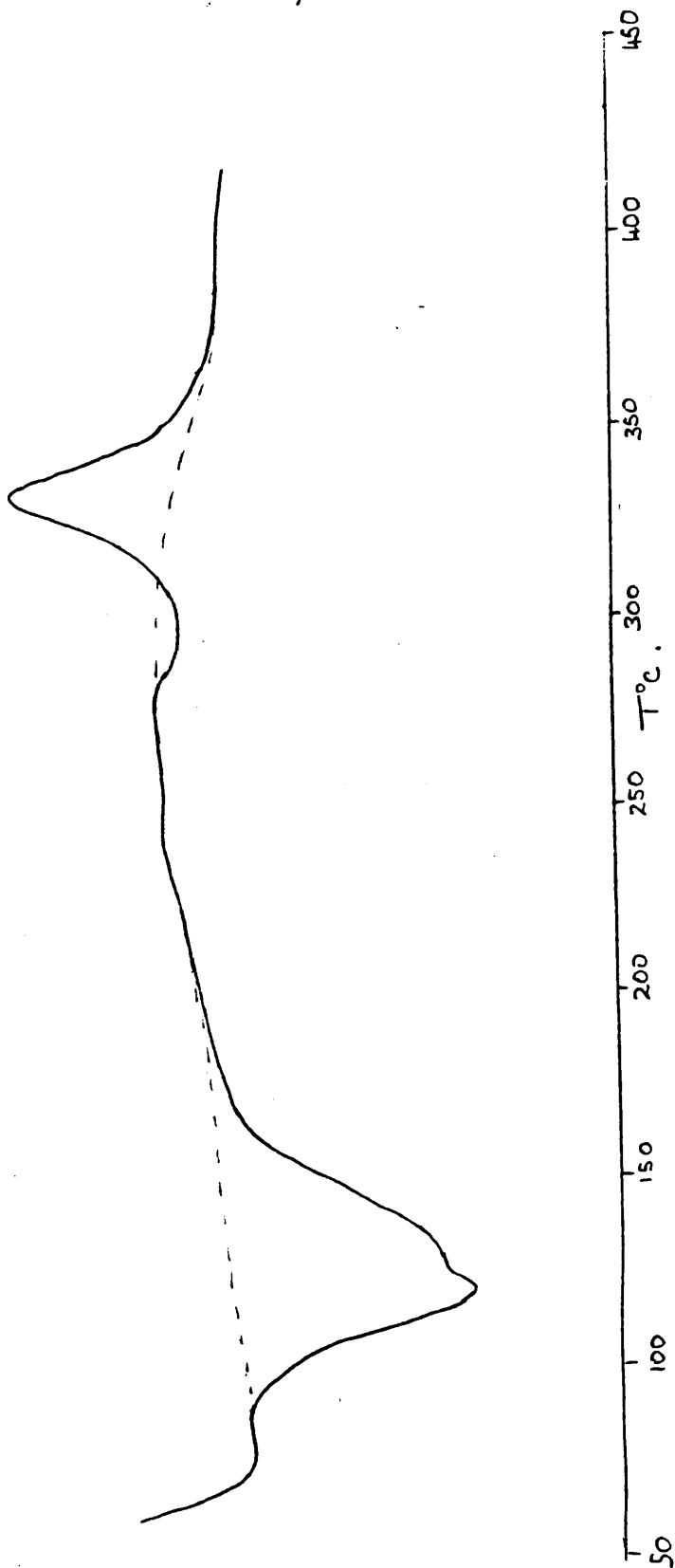
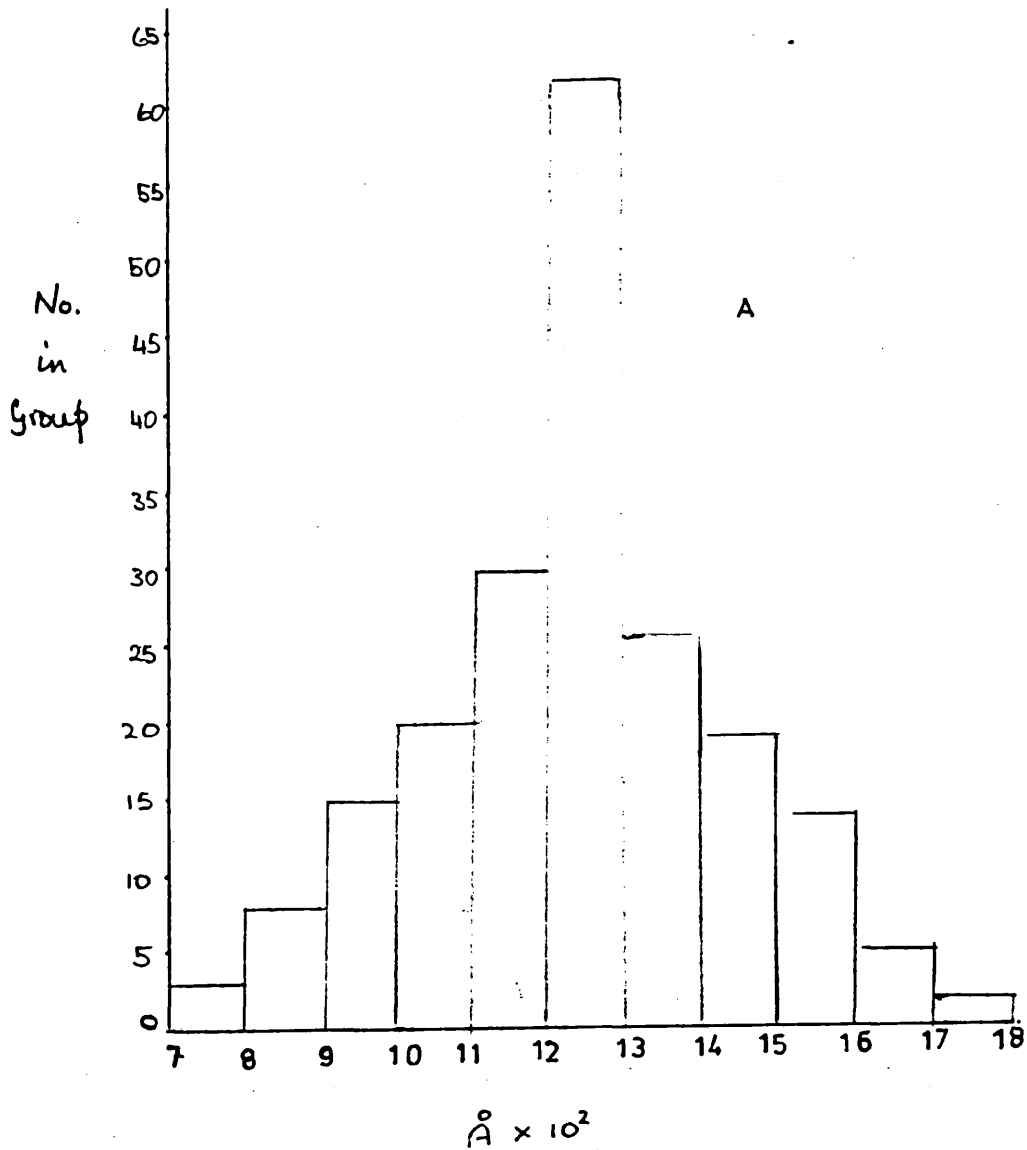
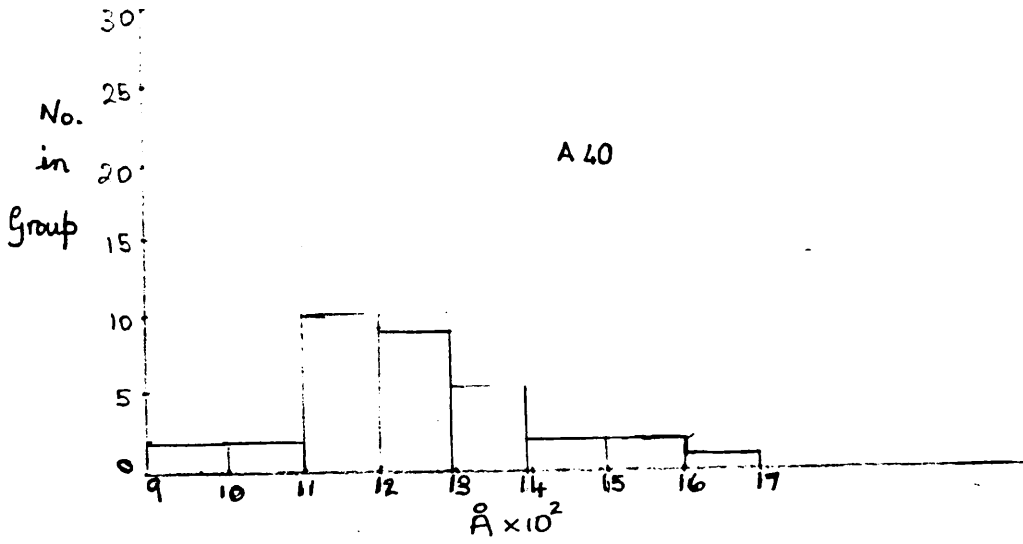
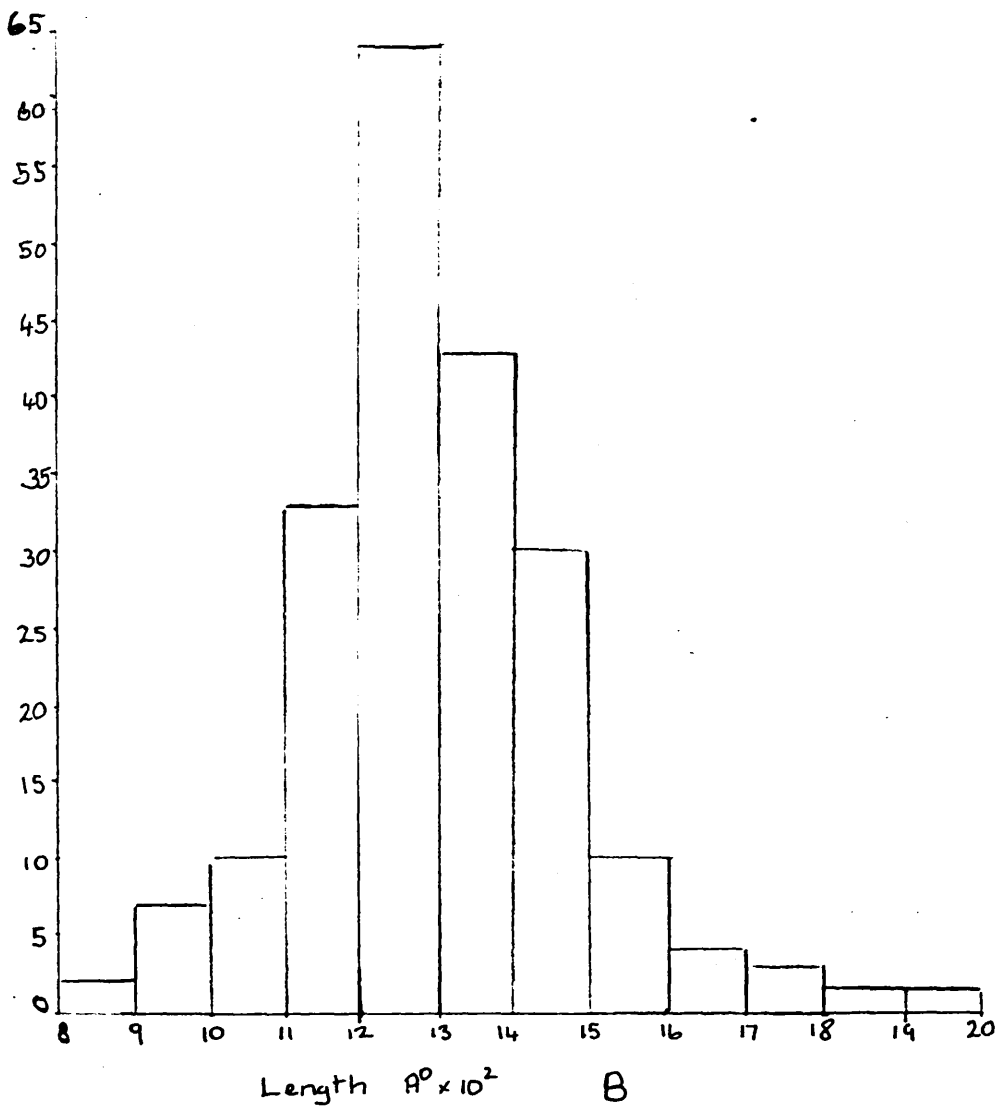
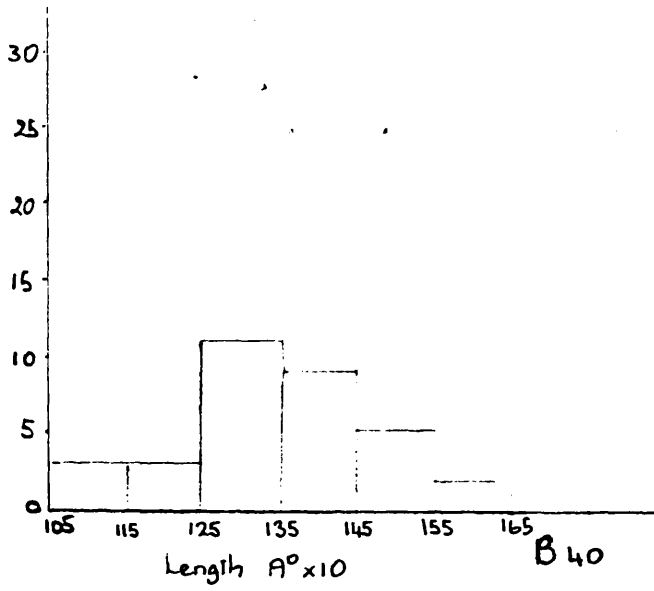


Figure 33

Length of pads

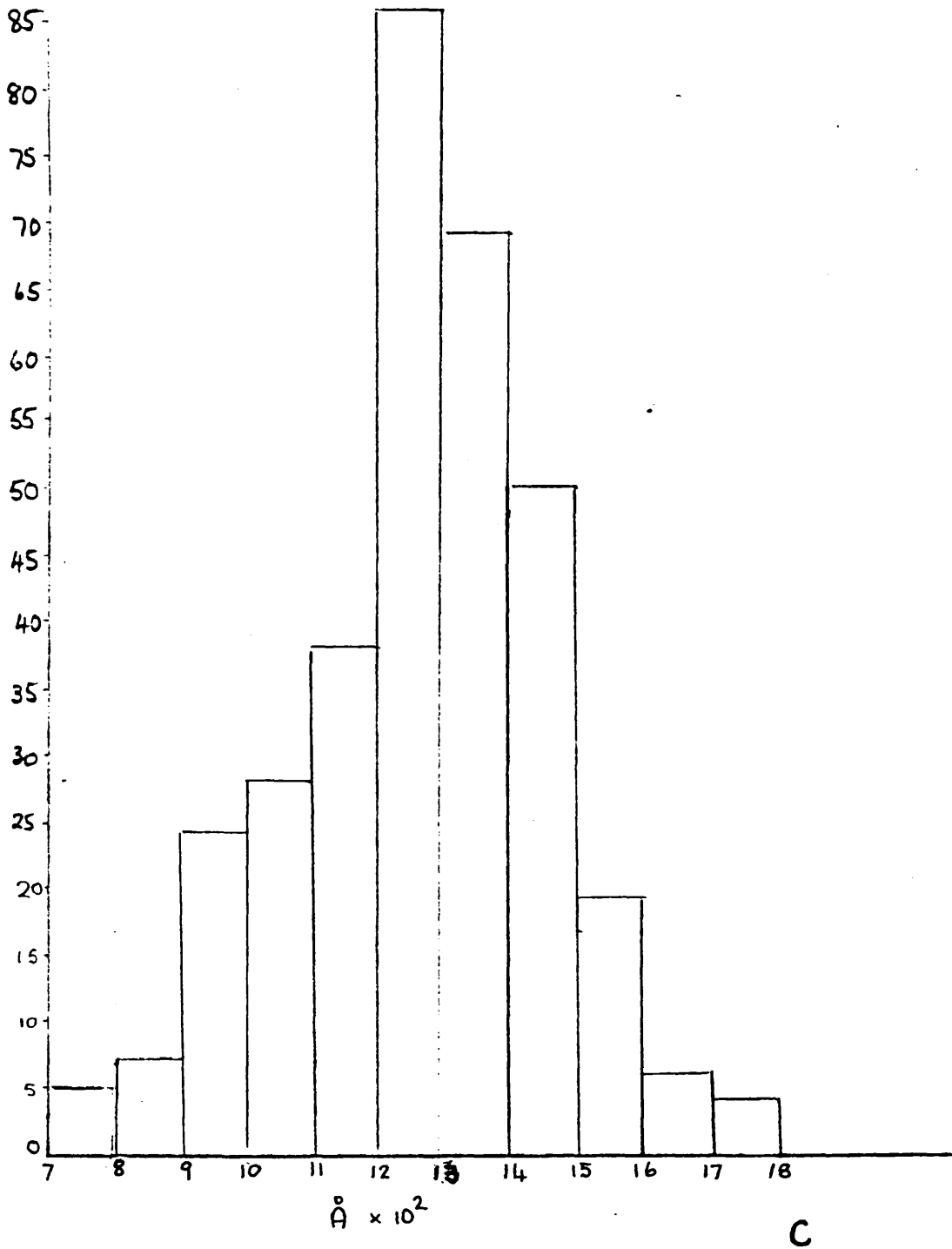
Length of pods

Figure 34



Length of pods

Figure 35



Length of pods

Figure 36

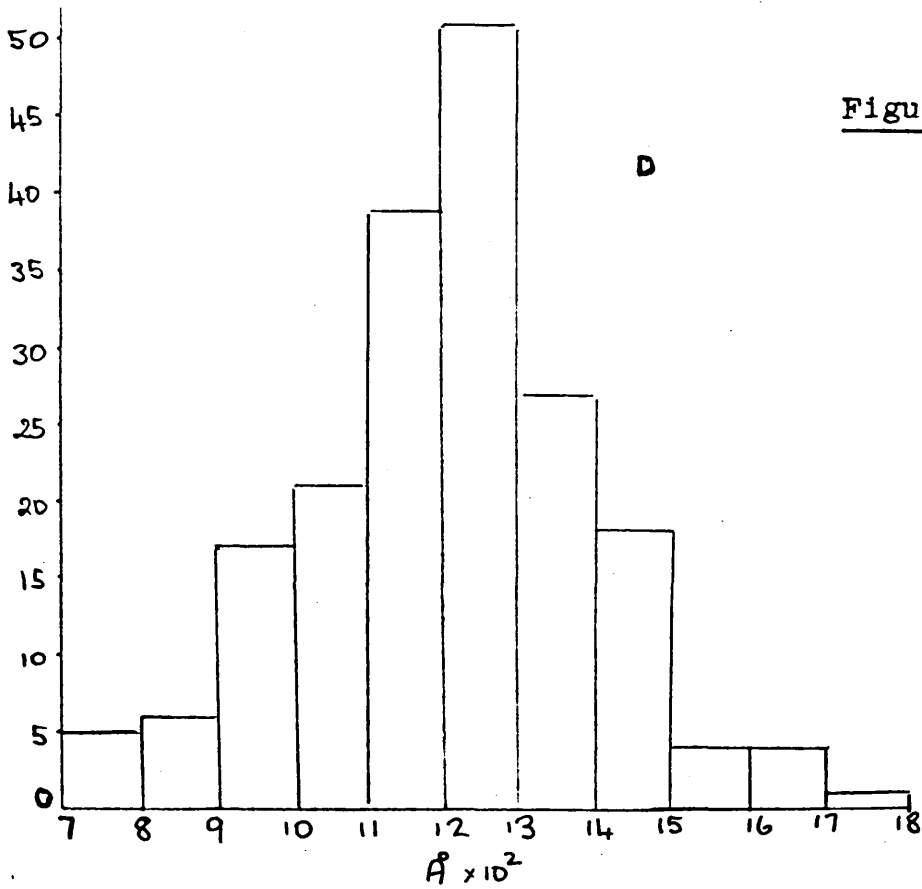
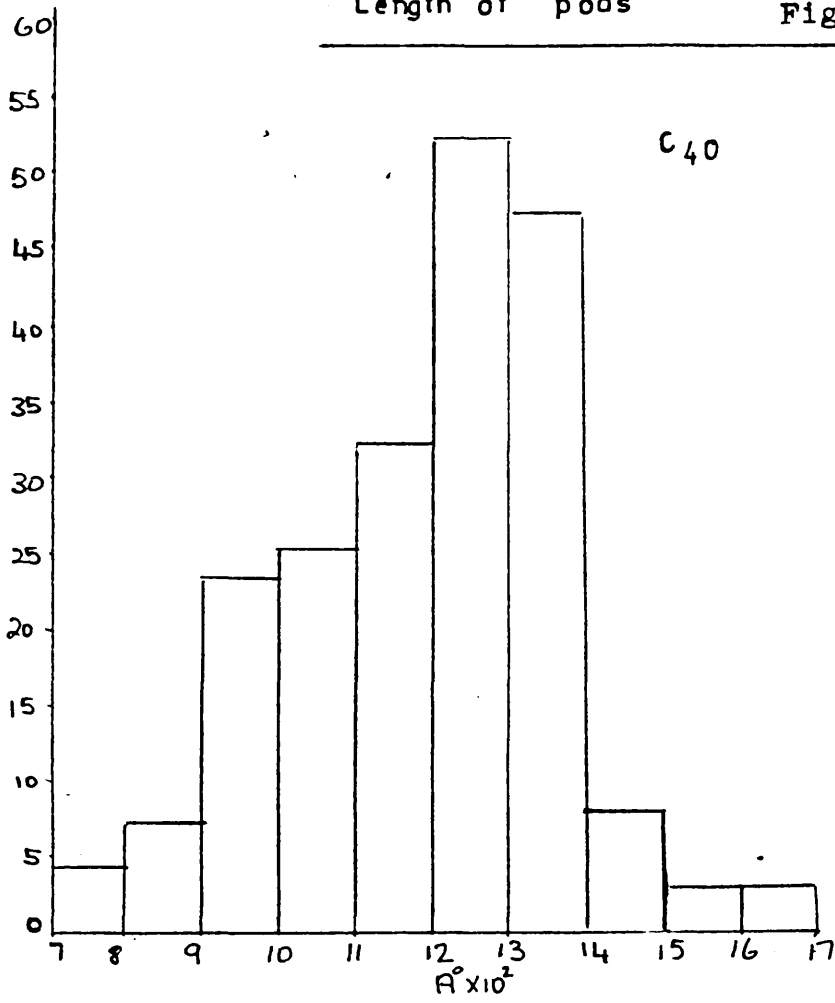


Figure 37

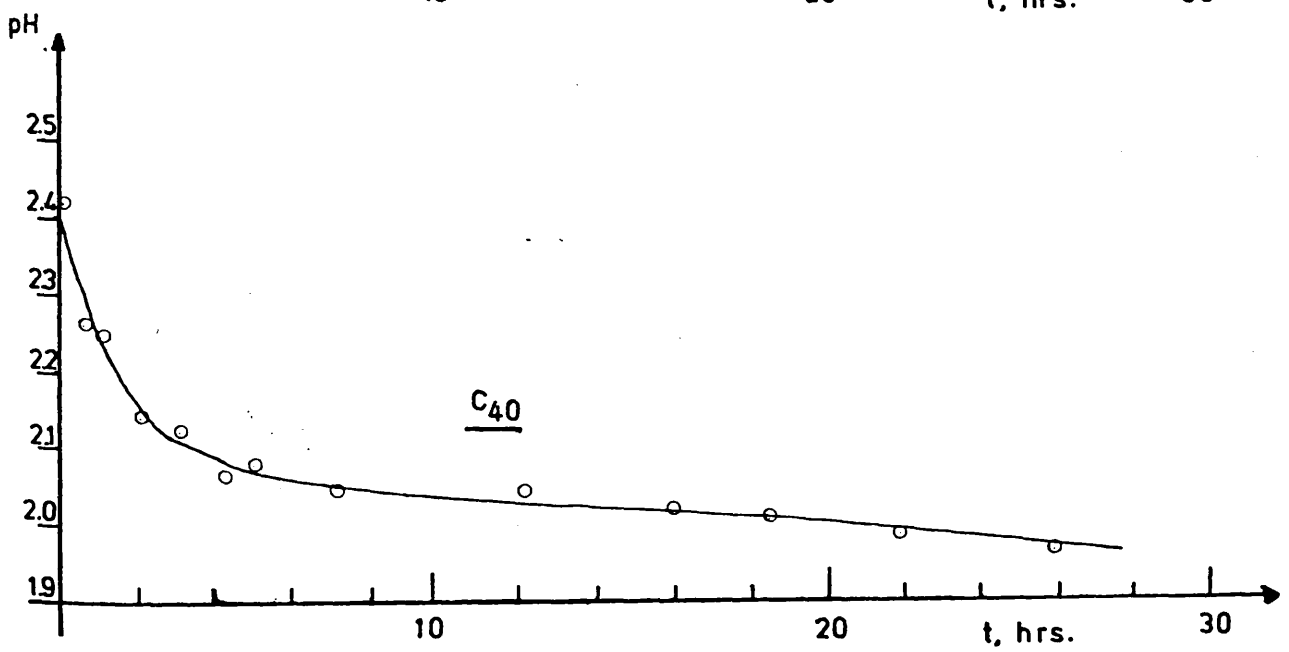
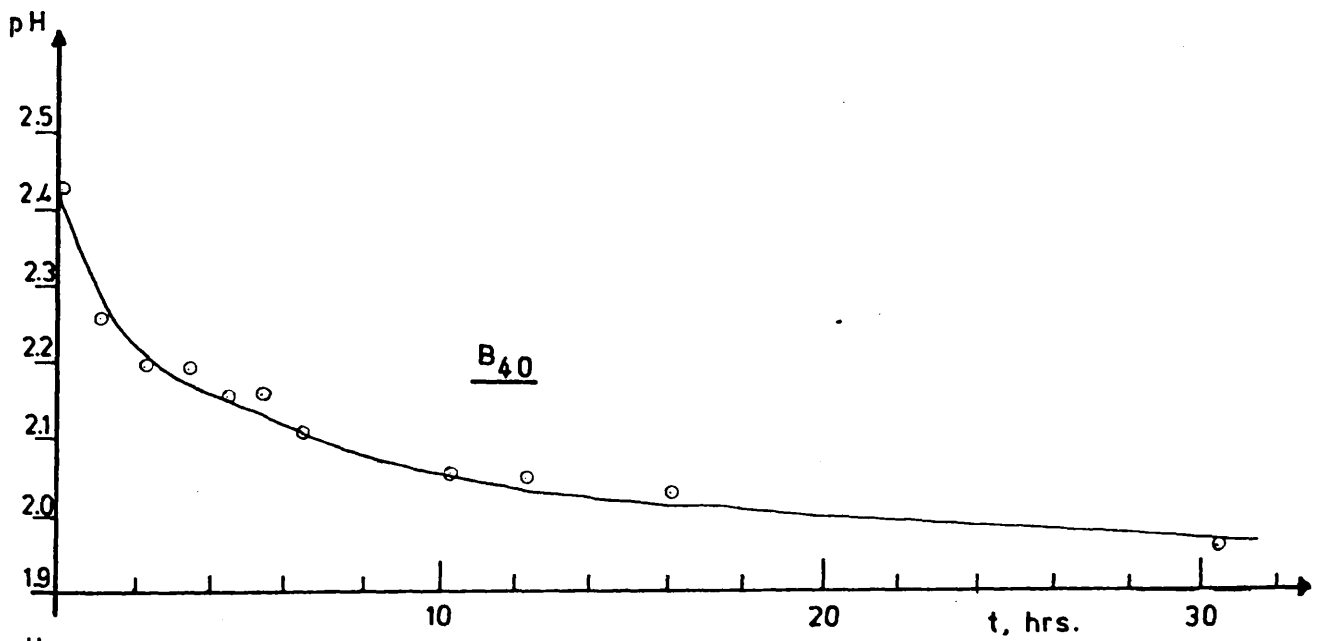
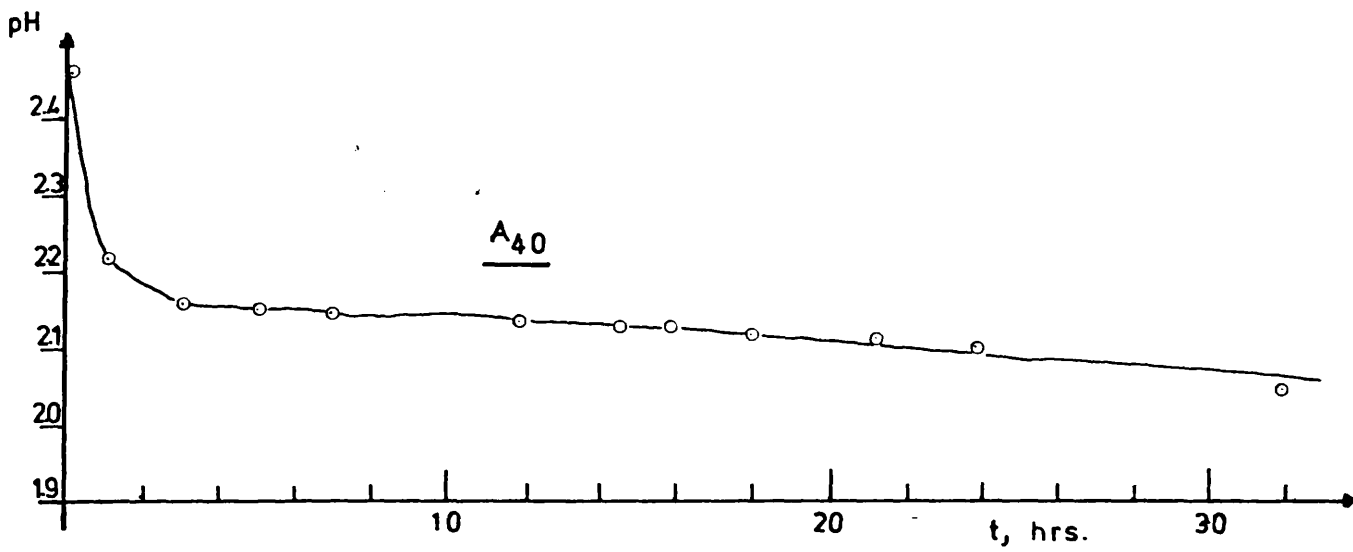
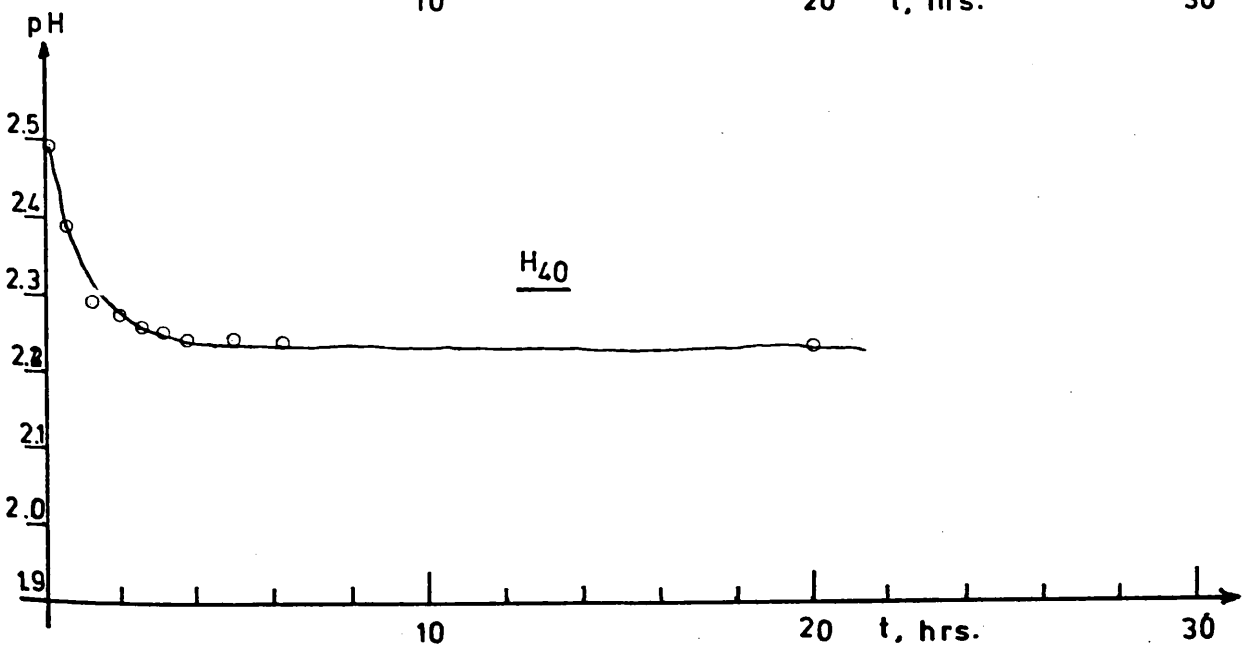
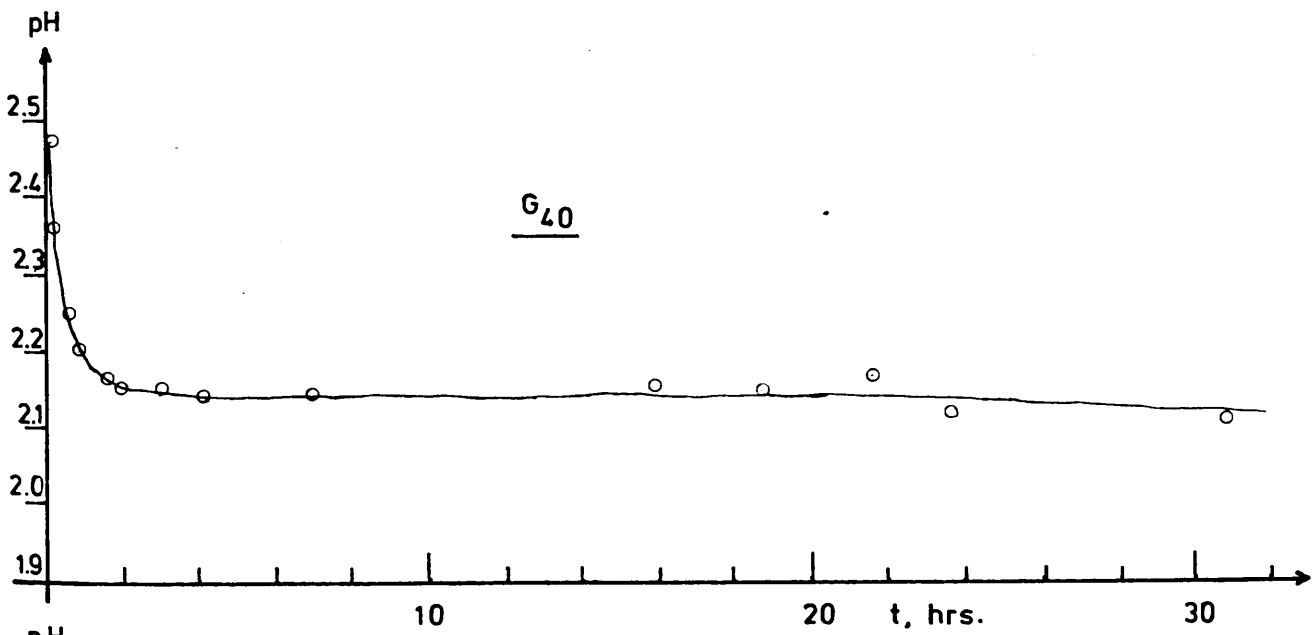
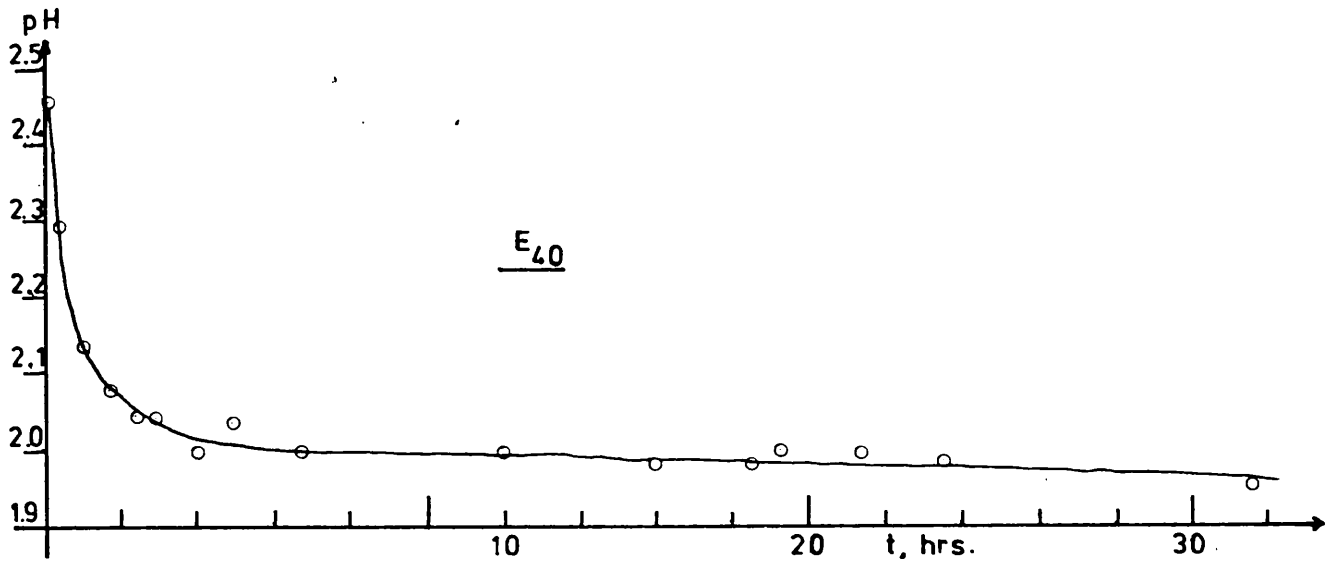
FIGURE 38

FIGURE 39

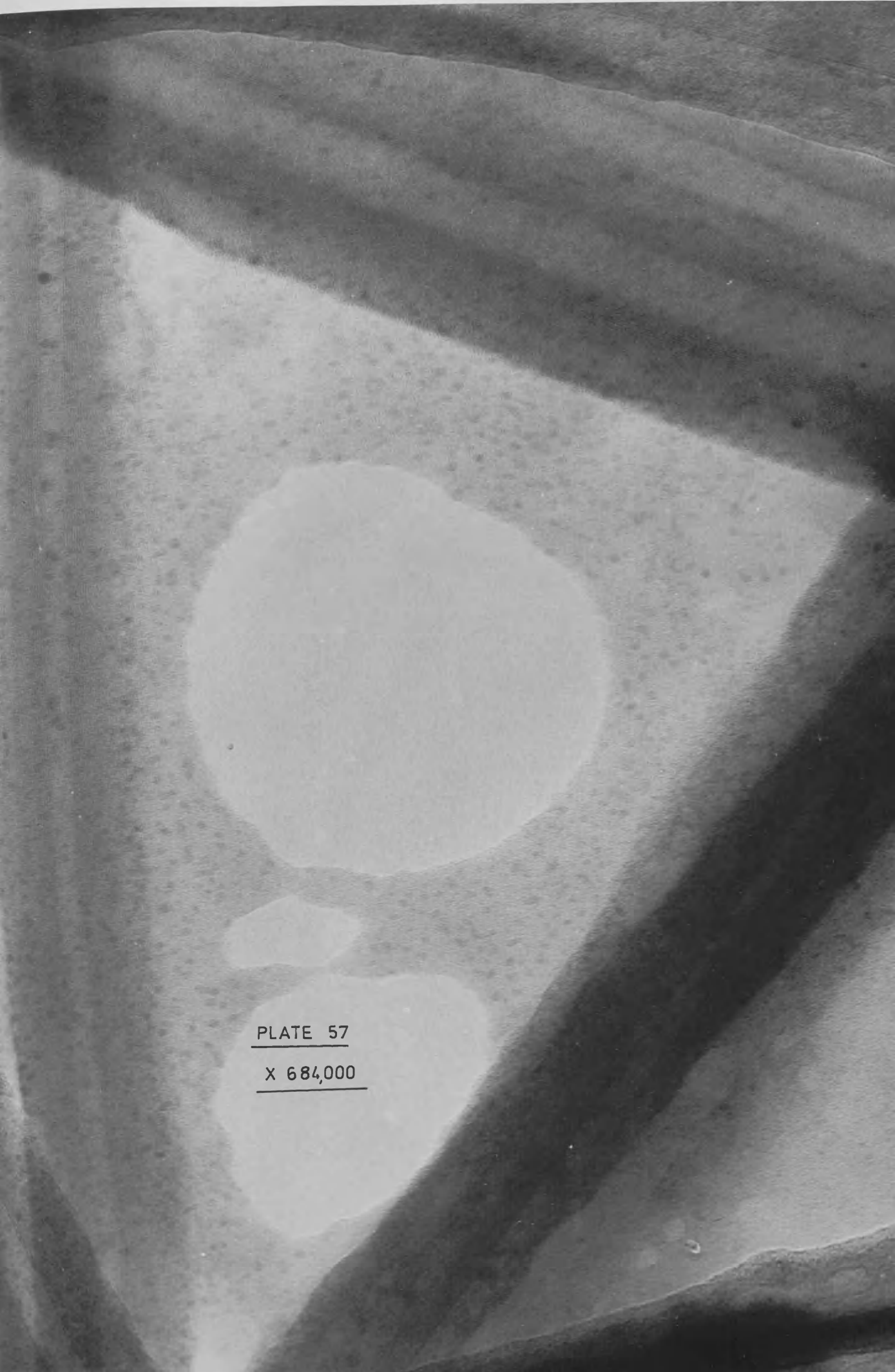
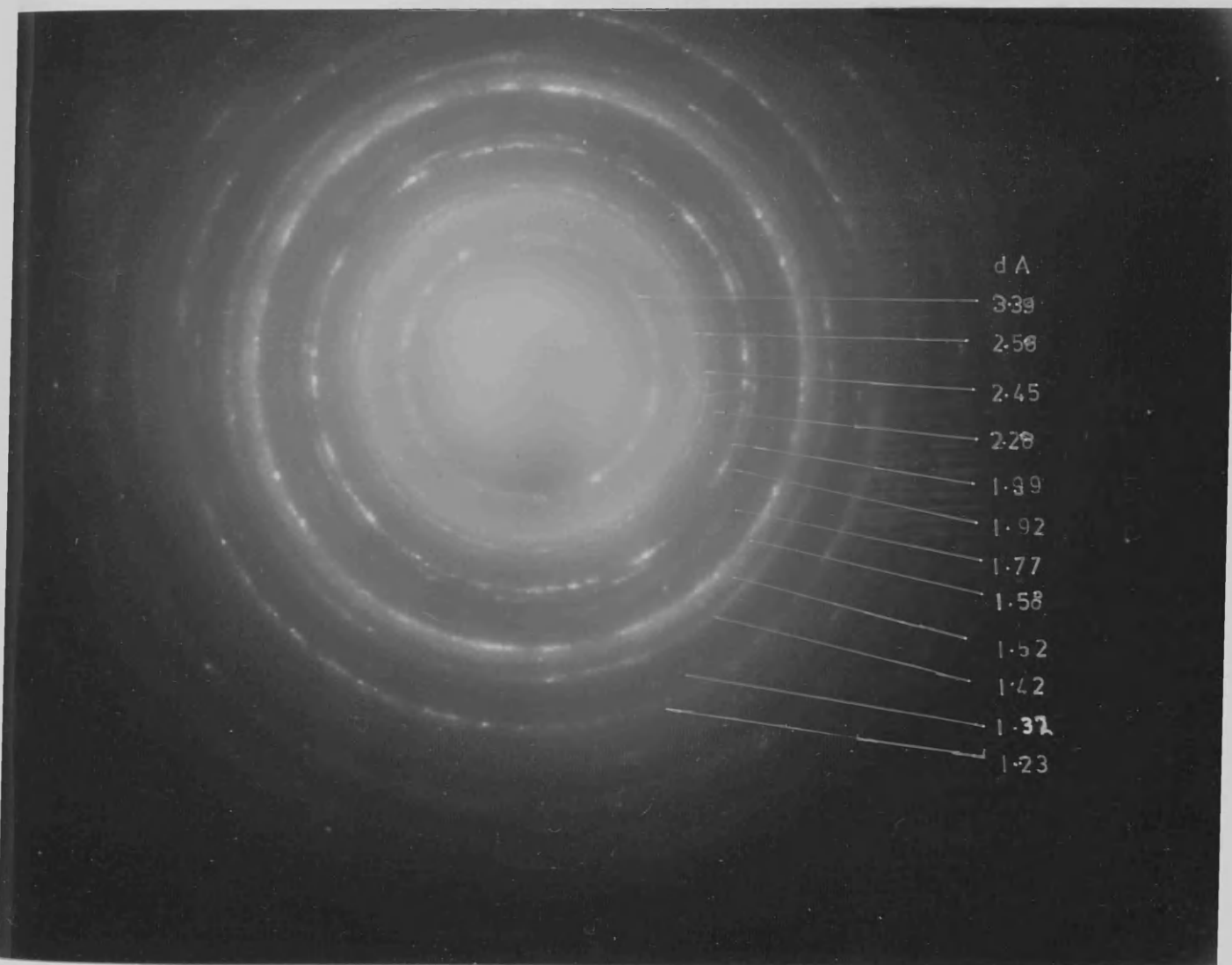


PLATE 57

X 684,000

PLATE 58
X 684000

Plate 59 Electron diffraction of $\text{Fe}(\text{NO}_3)_3$ at 40°C for 2 days



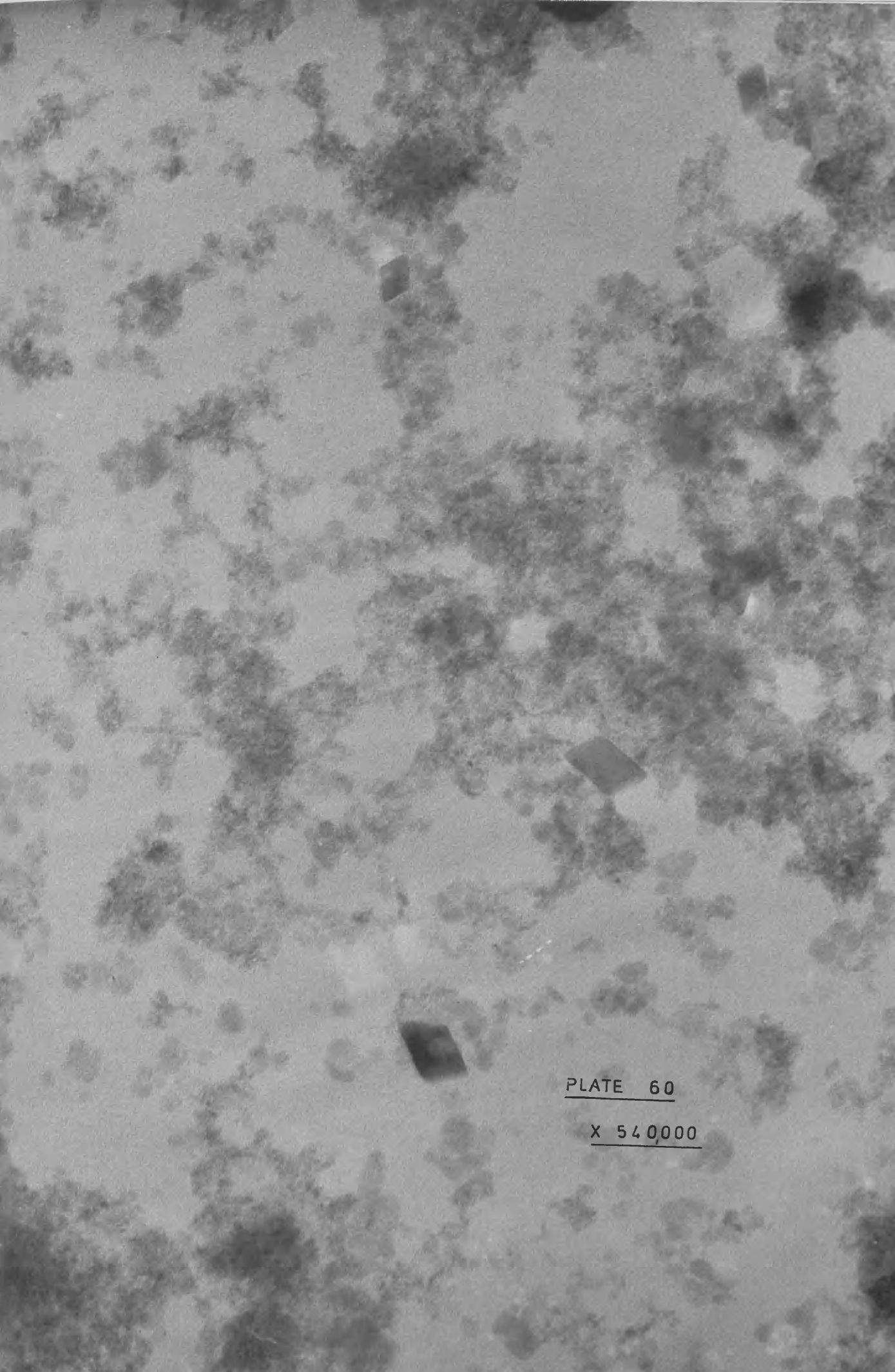
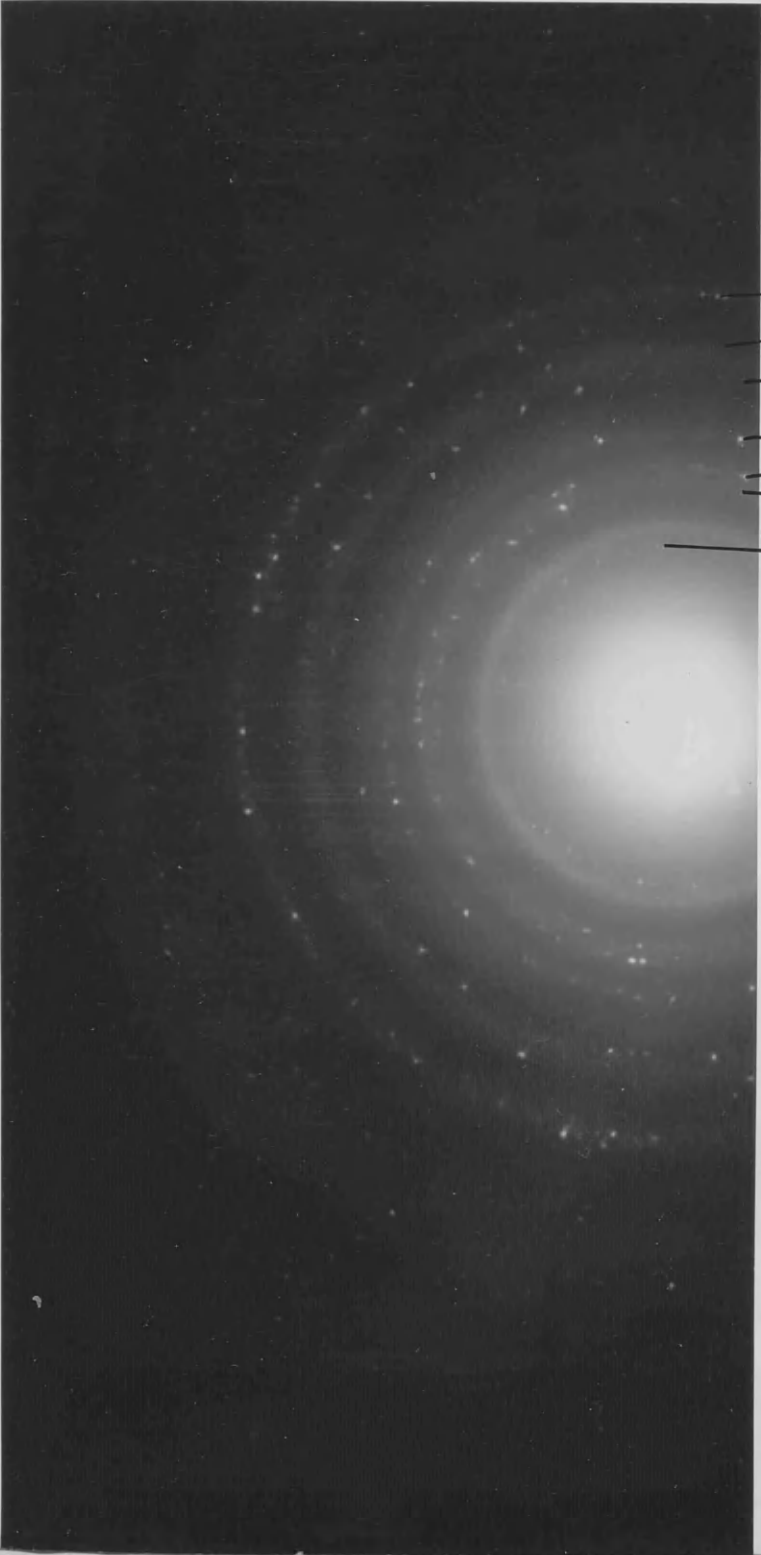


PLATE 60

X 54,000

Plate 61



d A

1.45

1.70

1.845

2.21

2.49

2.70

3.67




PLATE 62
X 424,000

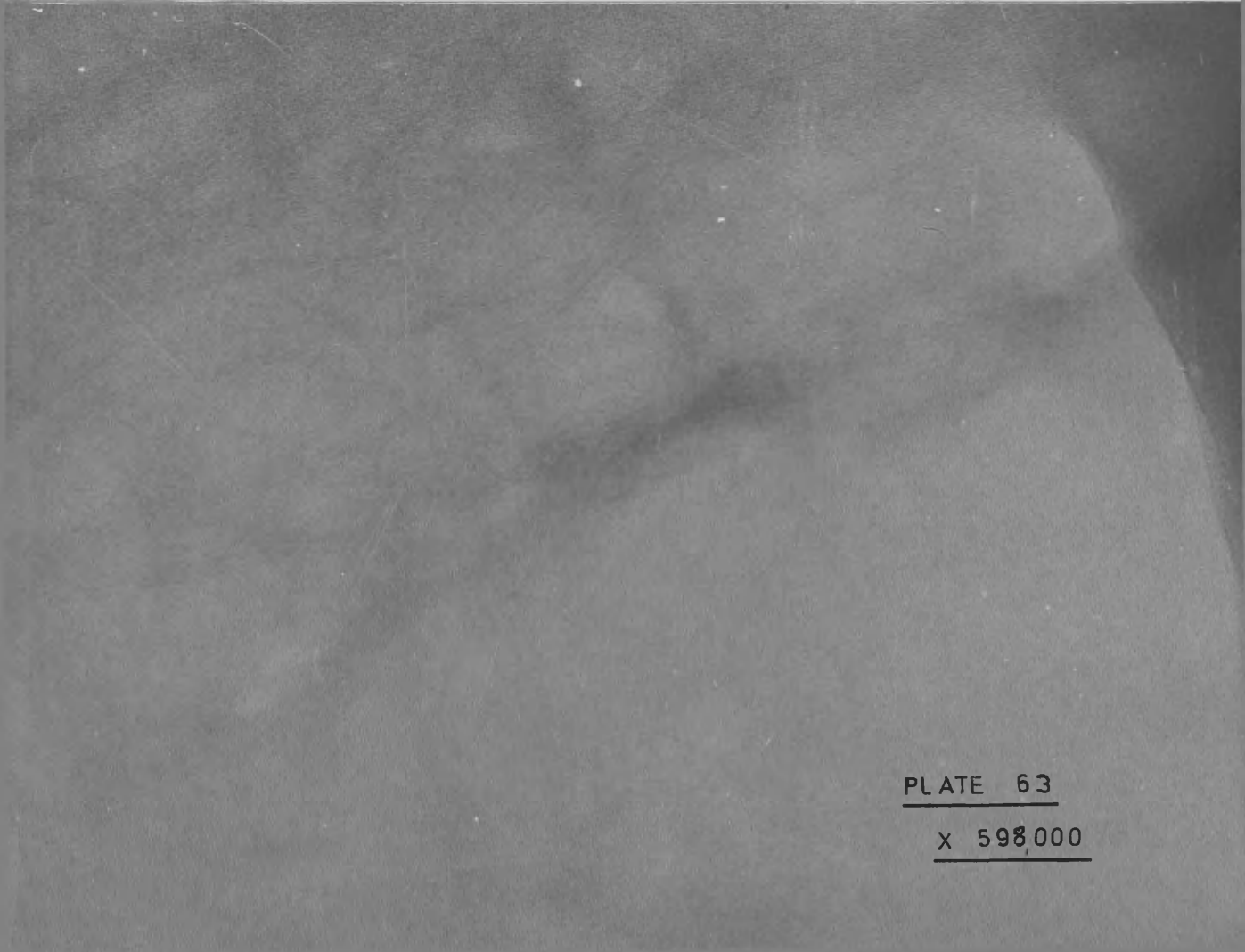
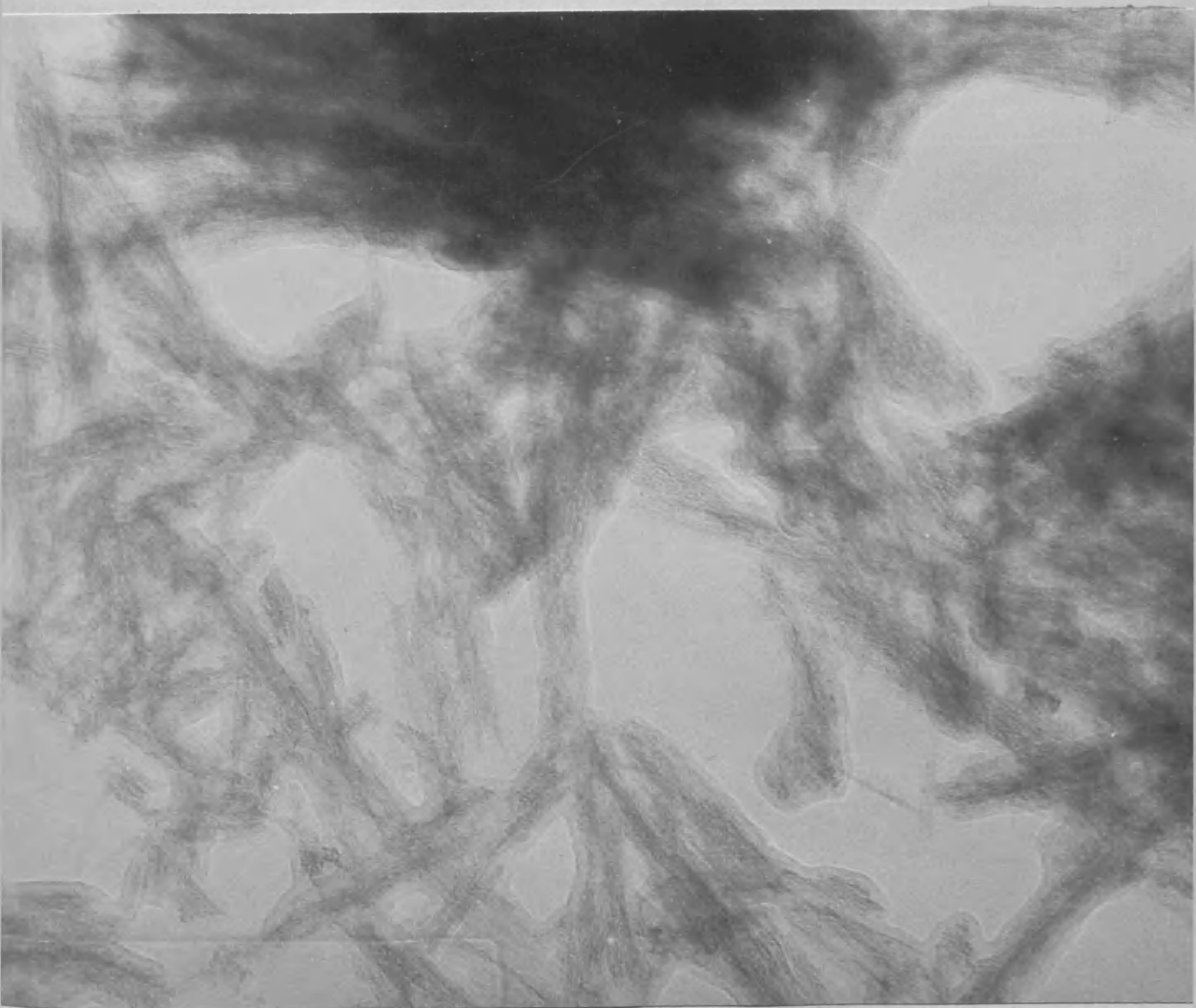


PLATE 63
X 598,000

Plate 64 Product of the $\text{Fe}_2(\text{SO}_4)_3$ hydrolysis after one
day at 65°C. x 478800



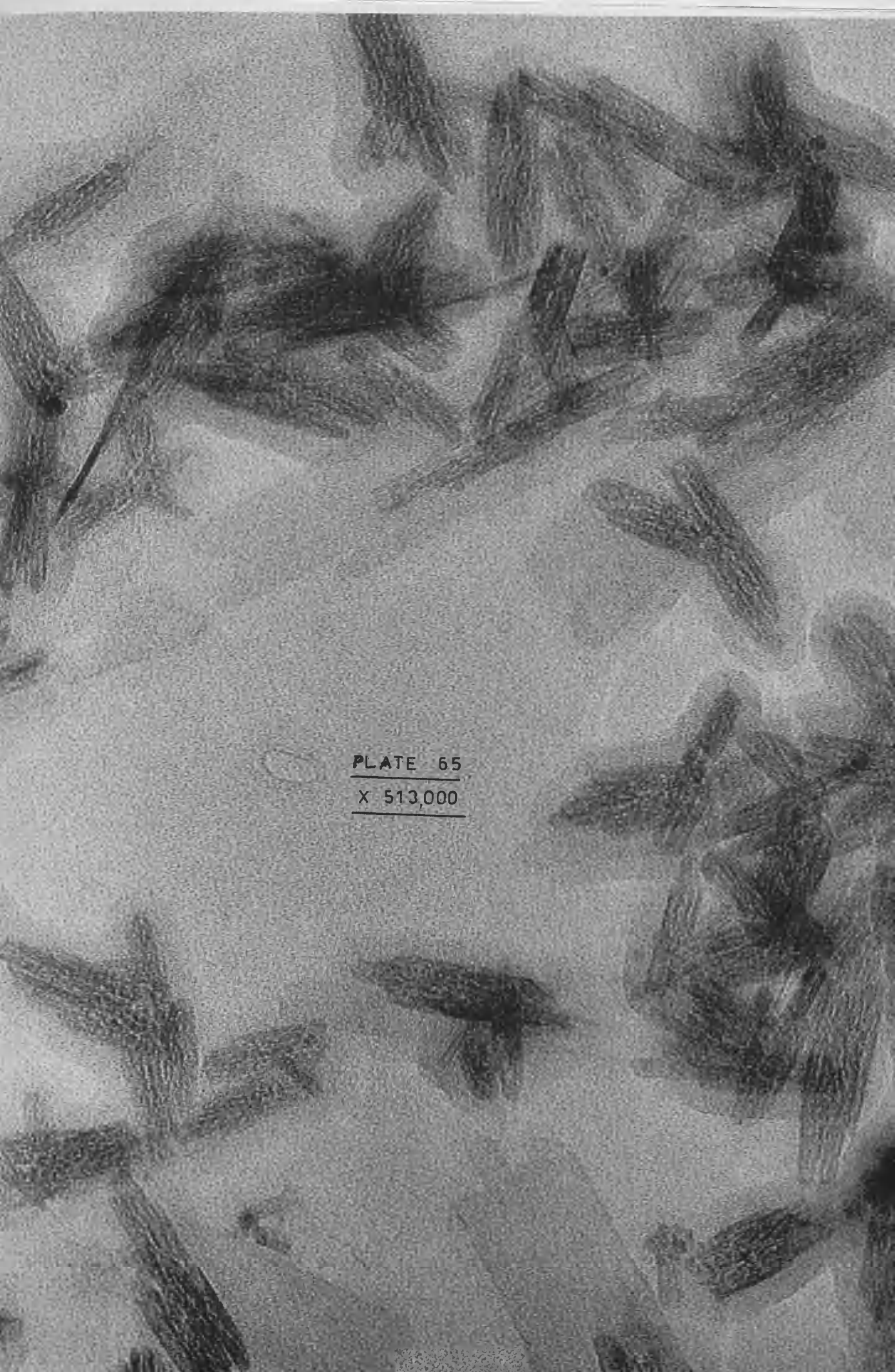
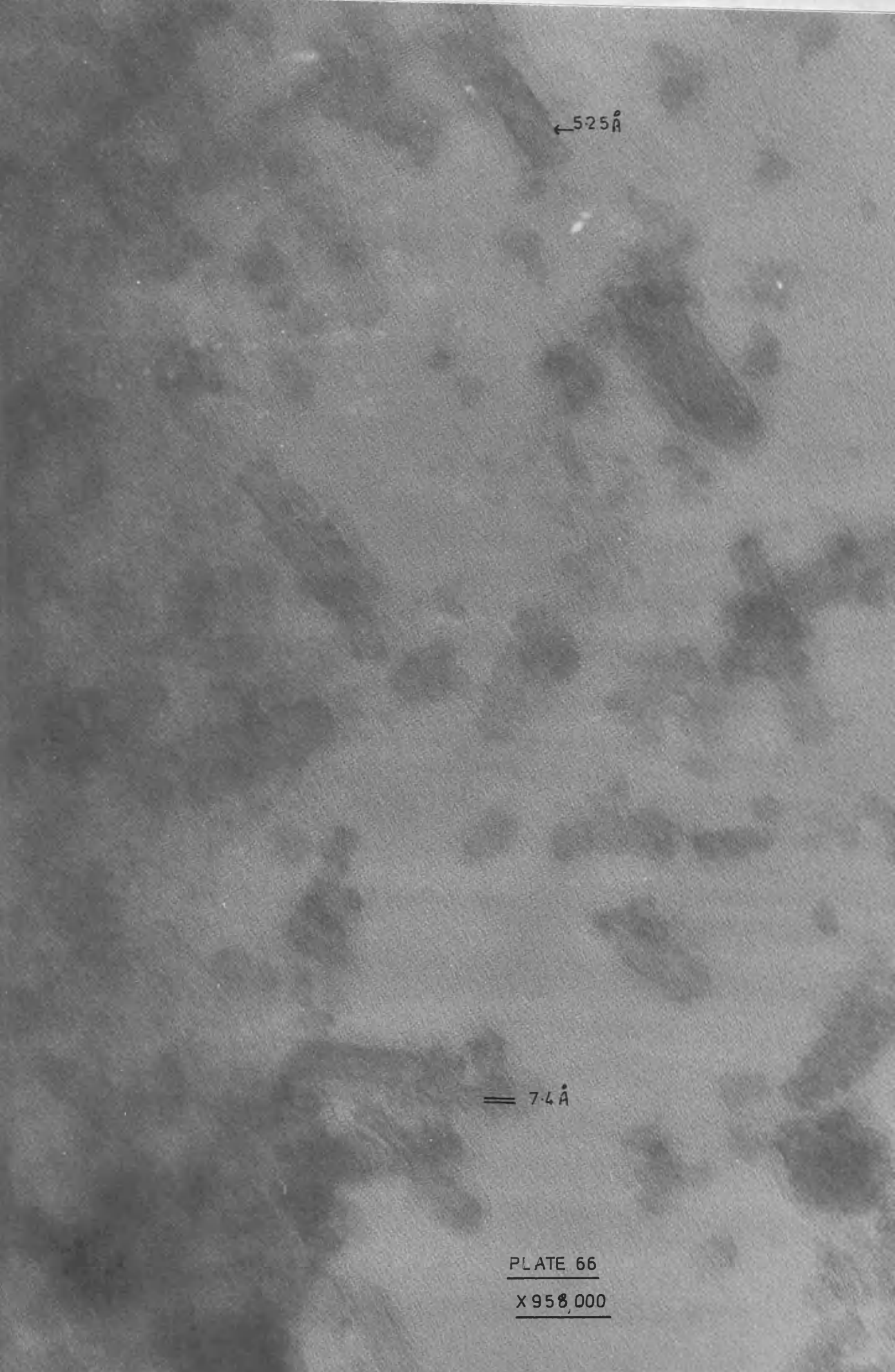
The image is a black and white micrograph showing numerous elongated, needle-shaped clefts scattered across a light-colored, granular background. These clefts are characteristic of cholesterol crystals. In the center of the image, there is a small rectangular label with the text 'PLATE 65' and 'X 513,000' printed on it.

PLATE 65
X 513,000

This is a high-magnification electron micrograph showing various dark, elongated, and somewhat irregular structures against a lighter, grainy background. These structures appear to be biological in nature, possibly representing viral particles or cellular components. The structures are distributed across the field of view, with some appearing more distinct than others. Two specific features are highlighted with labels: one in the upper right and another in the lower center.

← 525 Å

== 7.4 Å

PLATE 66

X 958,000

PLATE 67

X 684,000

No 2



← 74 Å

PLATE 68

X 684000

No3

PLATE 69

X 684,000

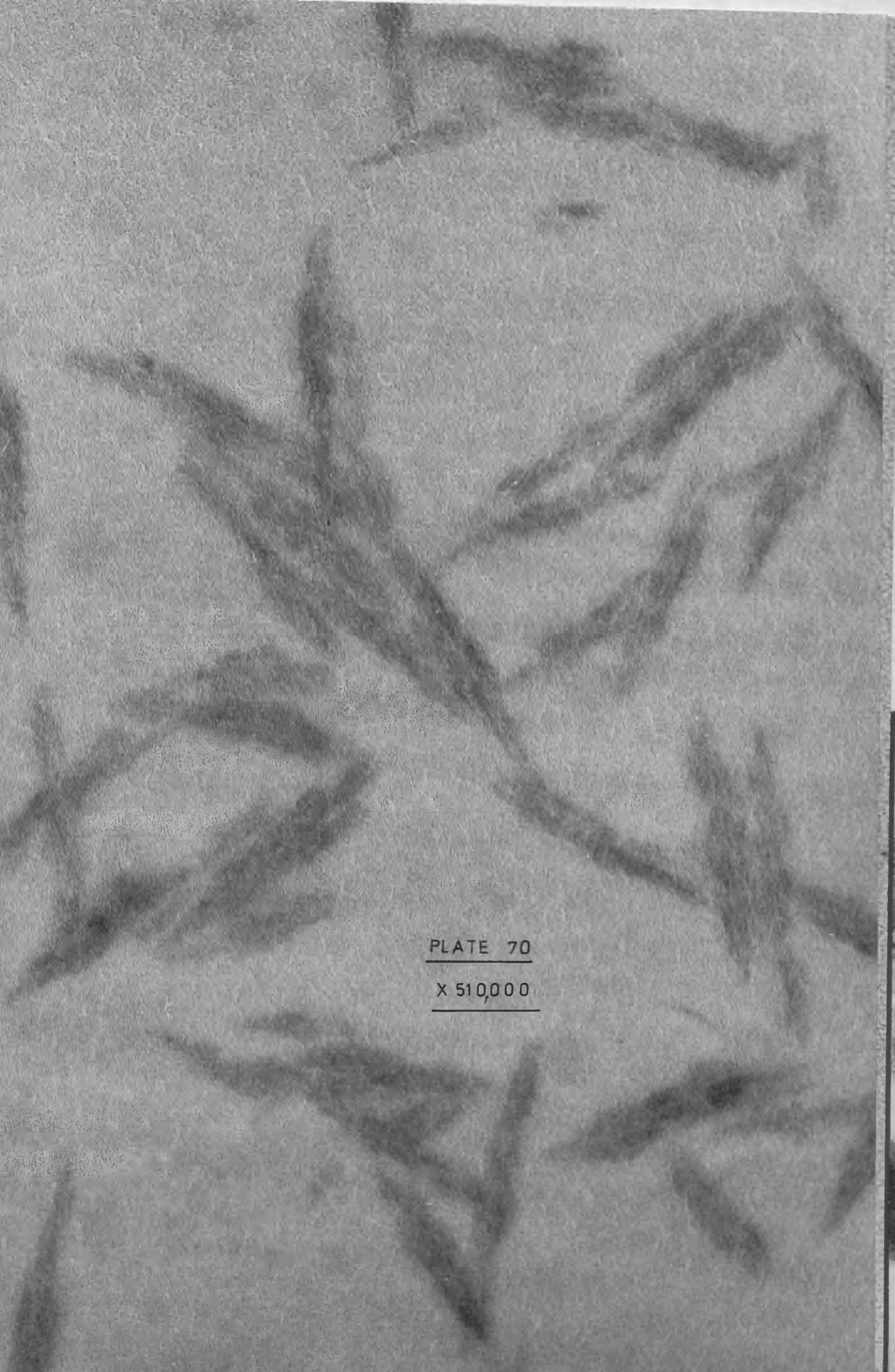


PLATE 70

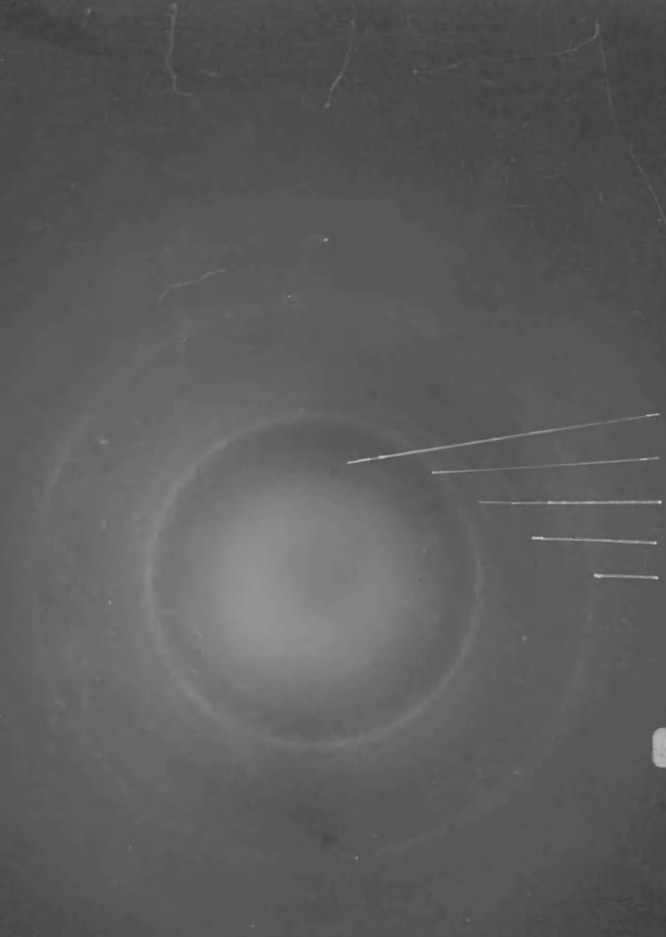
X 510,000

PLATE 71

X 1,026,000

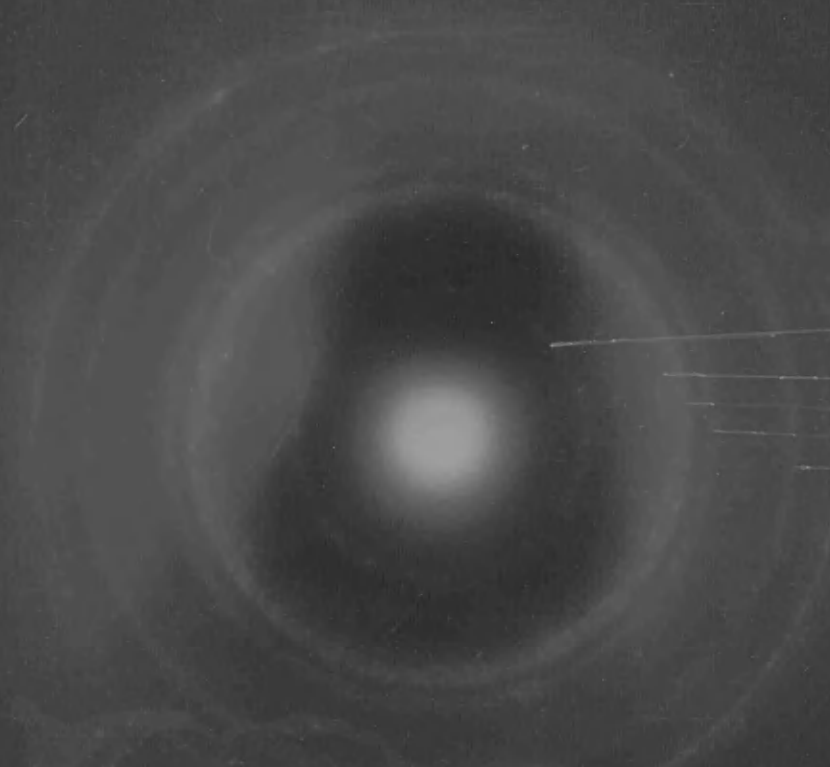
4.2 μ

4.2 μ



d Å
3.03
2.40
2.14
1.80
1.40

PLATE 72 N1



d Å
4.22
2.57
2.44
2.26
1.71
1.505

PLATE 74 N2

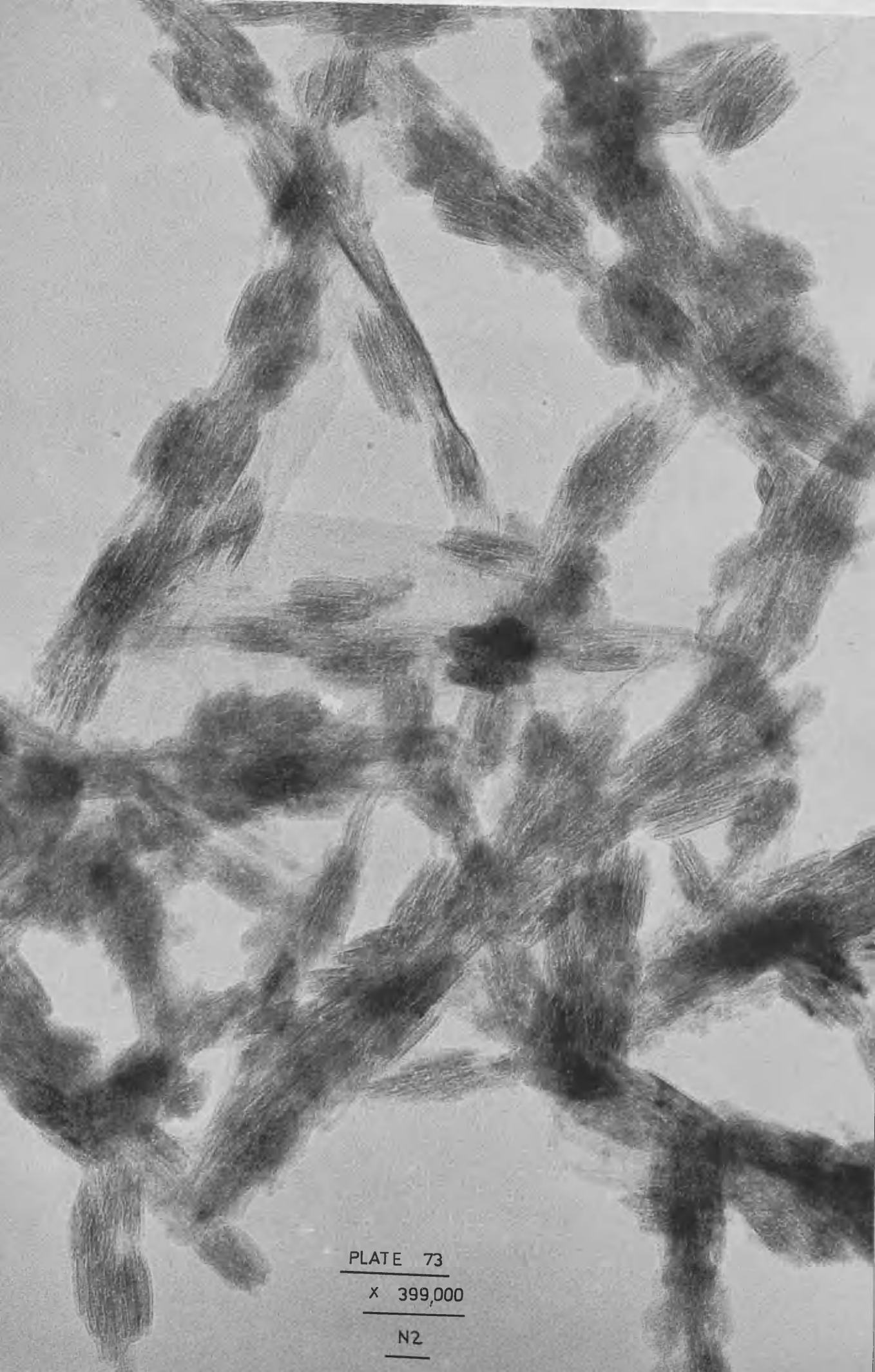


PLATE 73
x 399,000
N2

PLATE 75
X 1,026,000
N 3

← 42 Å

↑ 42 Å

↖
↗
42 Å

d A

1.48

1.58

2.19

2.50

2.60

4.16

PLATE 76

N3

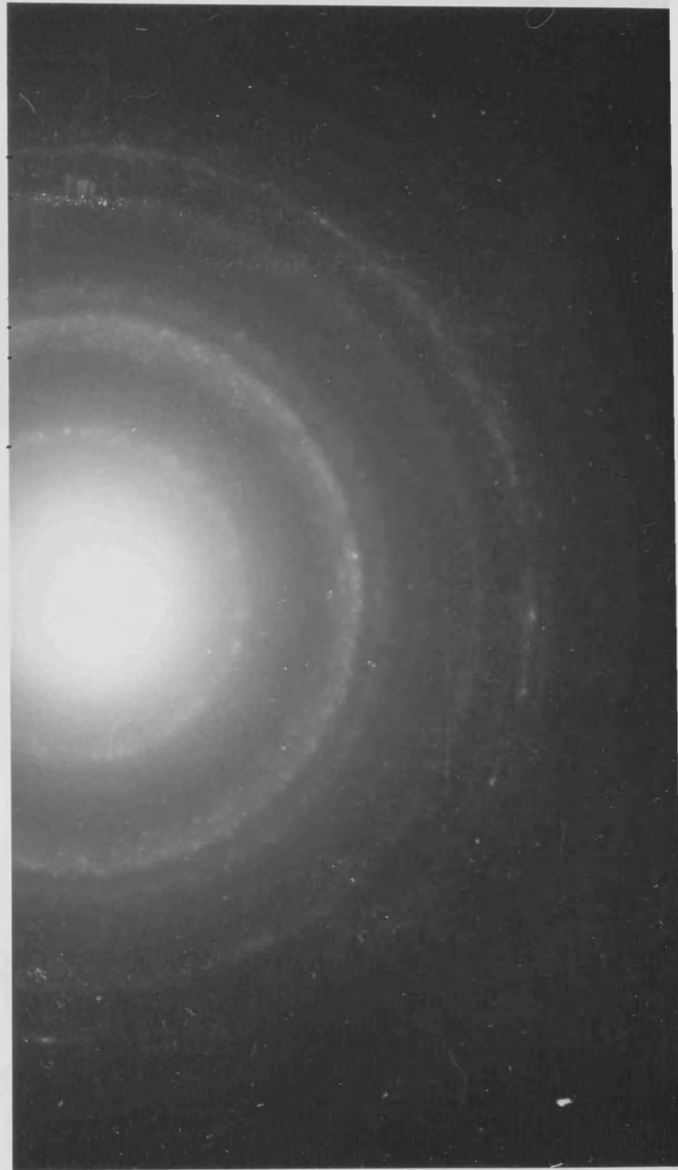
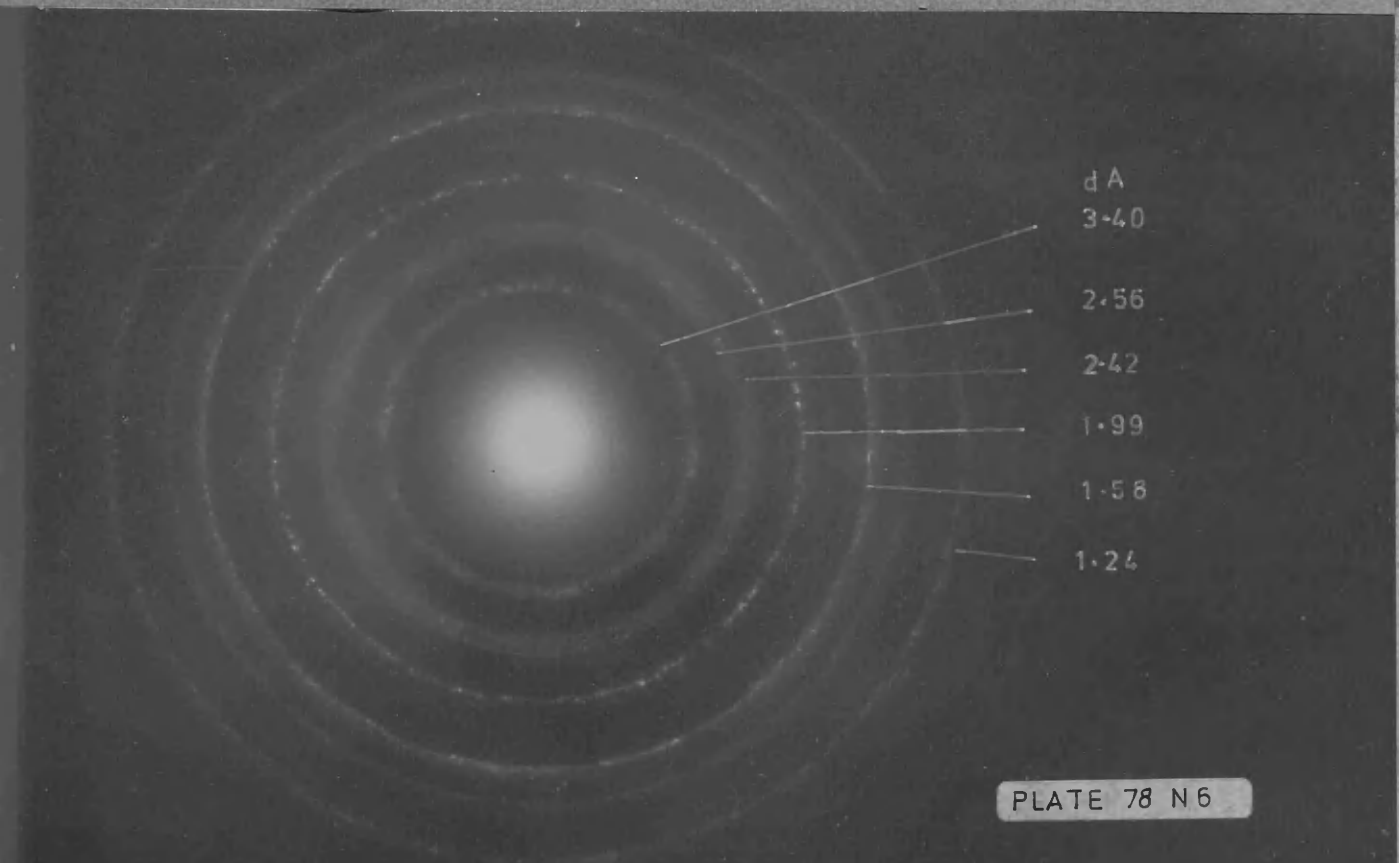




PLATE 77

X 17 000

N6



dA
3.40

2.56

2.42

1.99

1.58

1.24

PLATE 78 N6

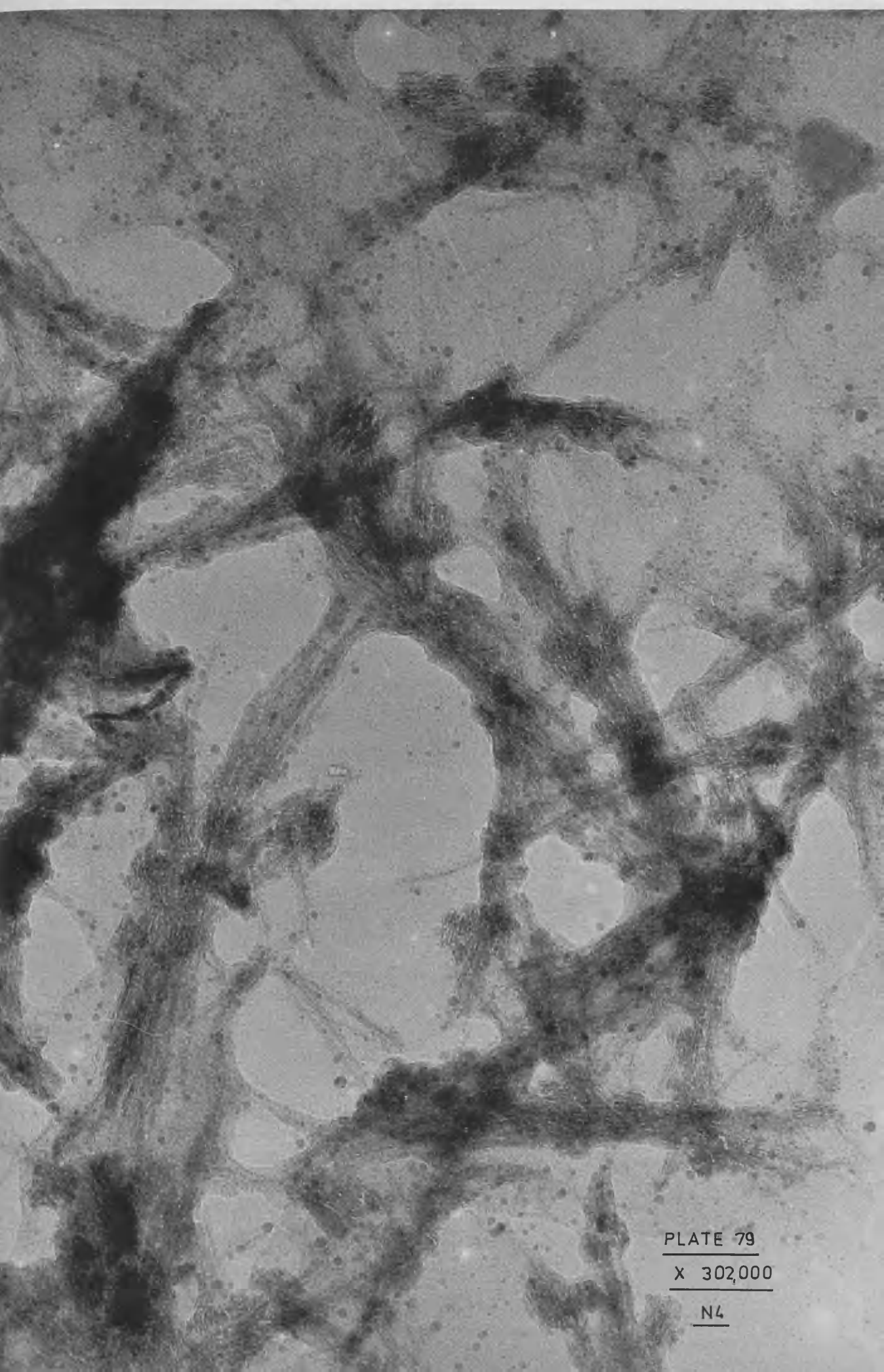


PLATE 79

X 302,000

N4

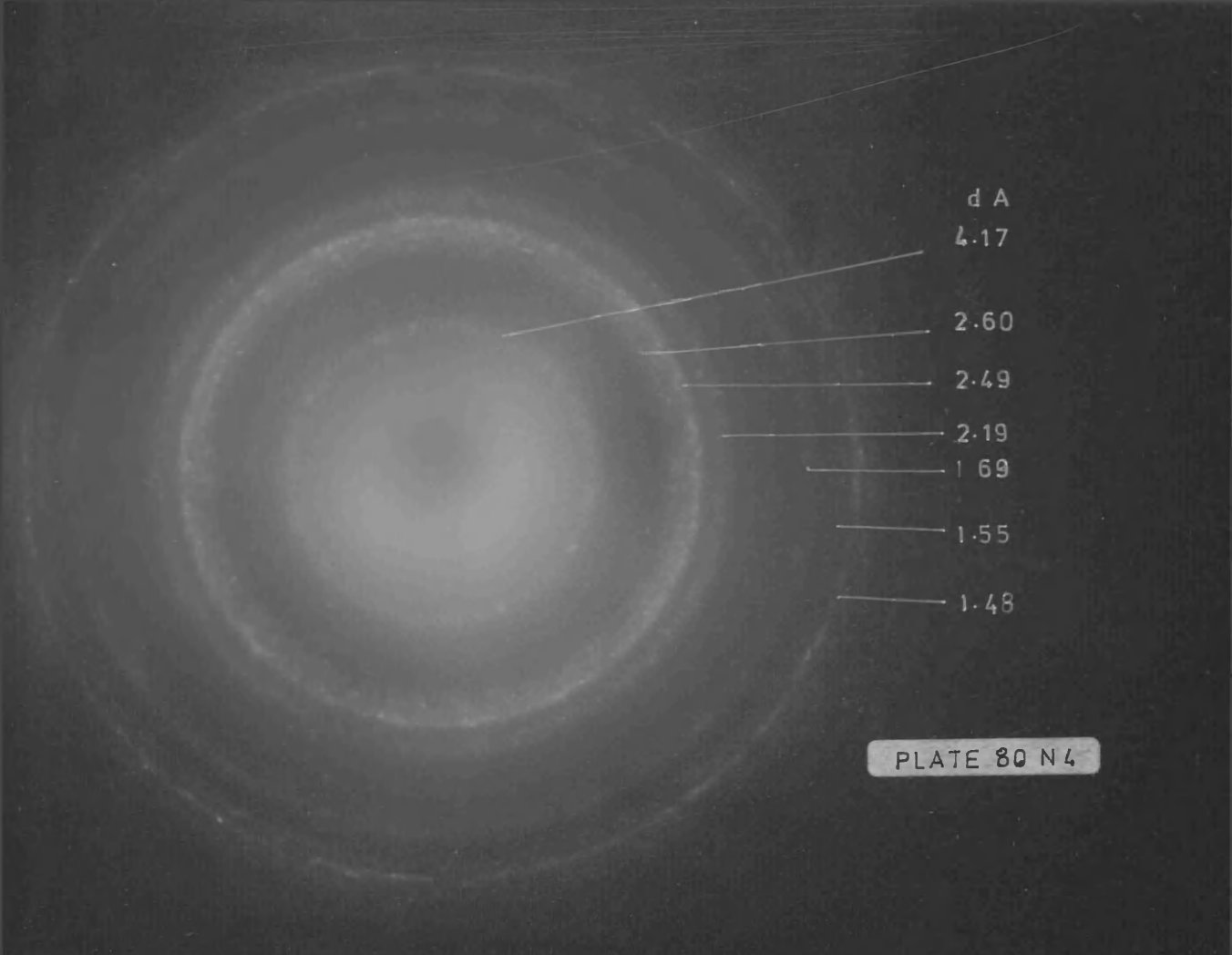


PLATE 80 N 4

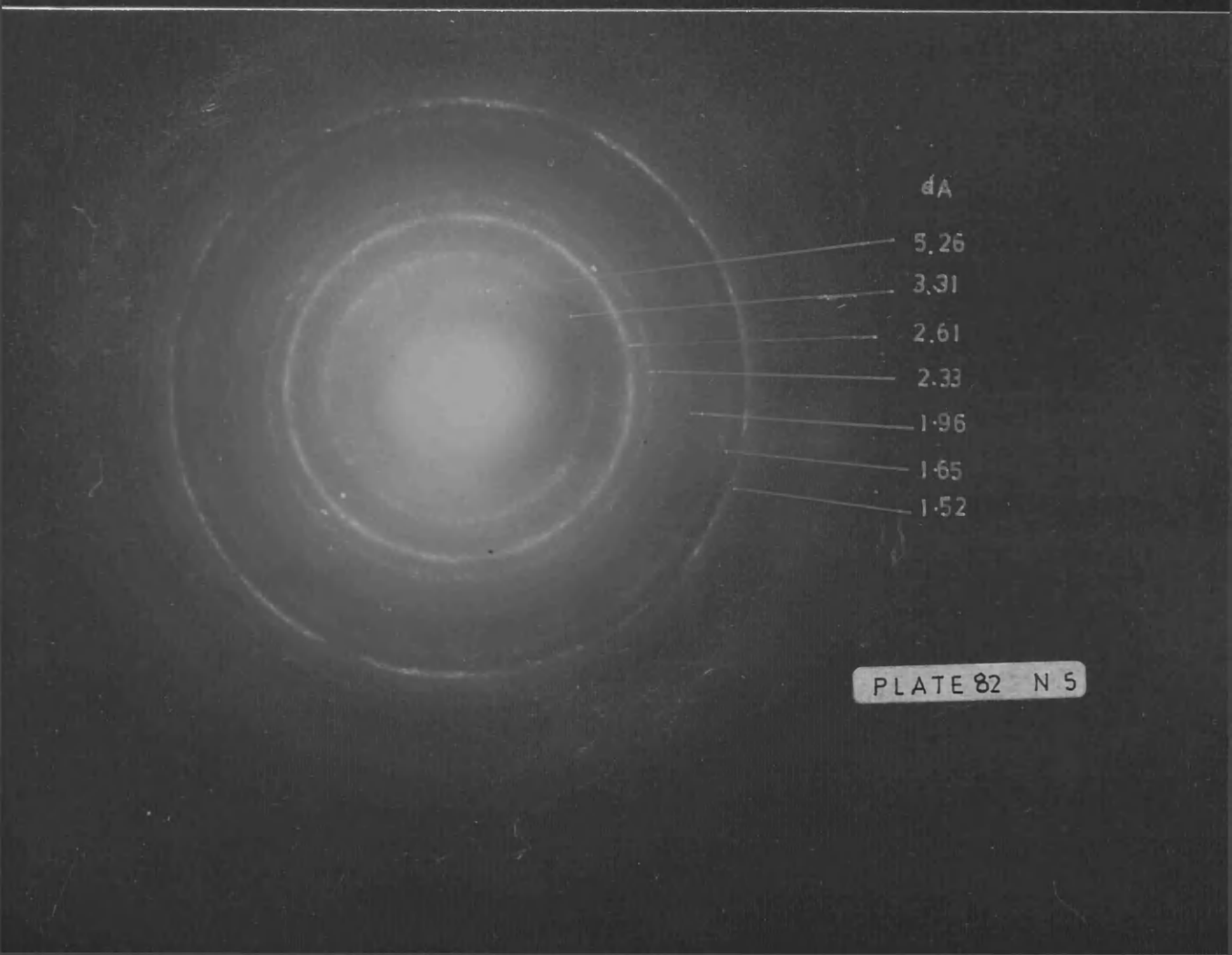


PLATE 82 N 5




PLATE 81

X 684,000

N5

↙ 7.4 Å



Plate 83

Fe5

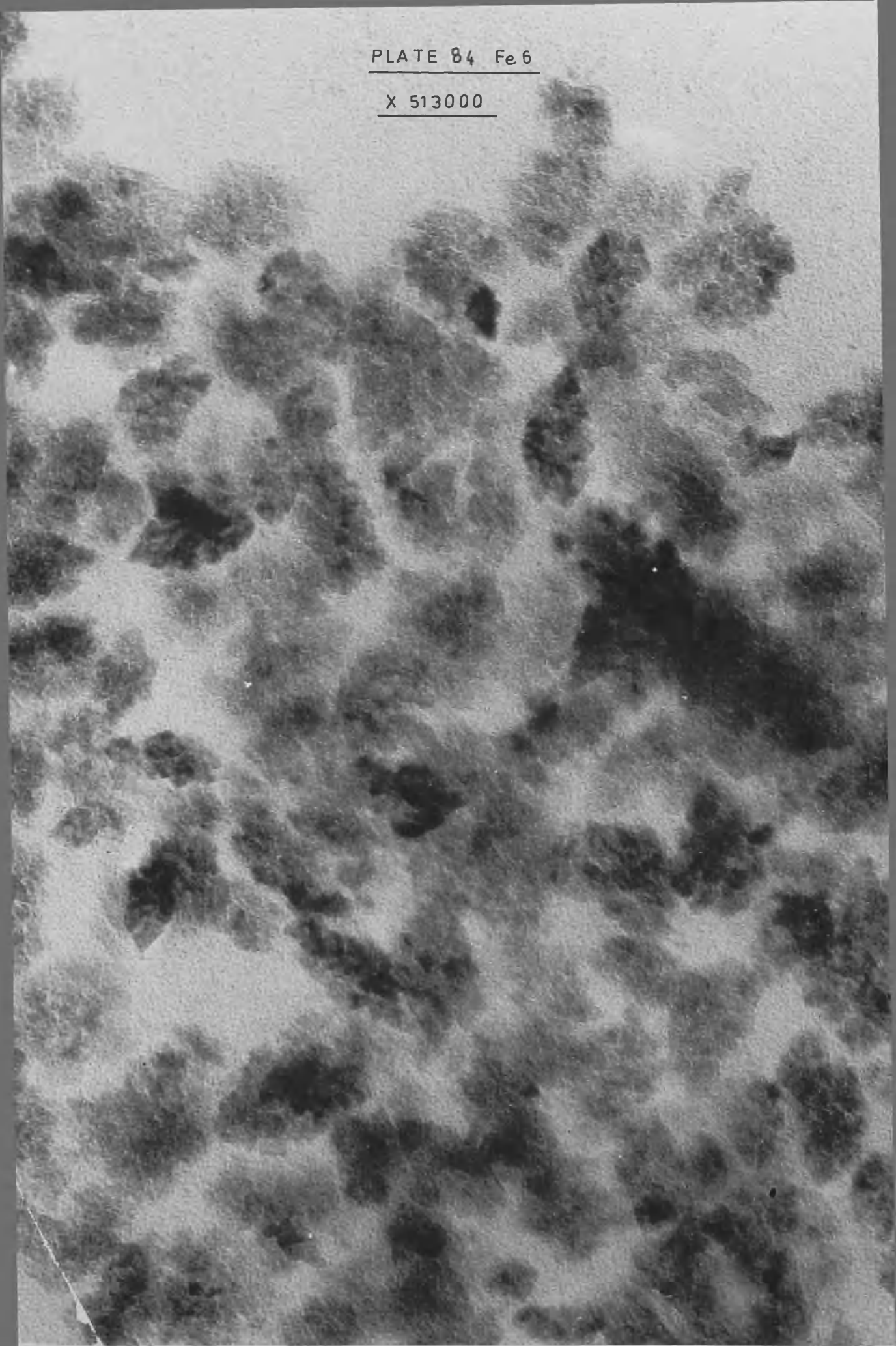
x 60,000

Plate 87 x 240,000



PLATE 84 Fe 6

X 513000



2.69

336

PLATE 85

X 2220,000

PLATE 86

Fe₃

d Å

3.04

2.75

1.87

1.60

1.32

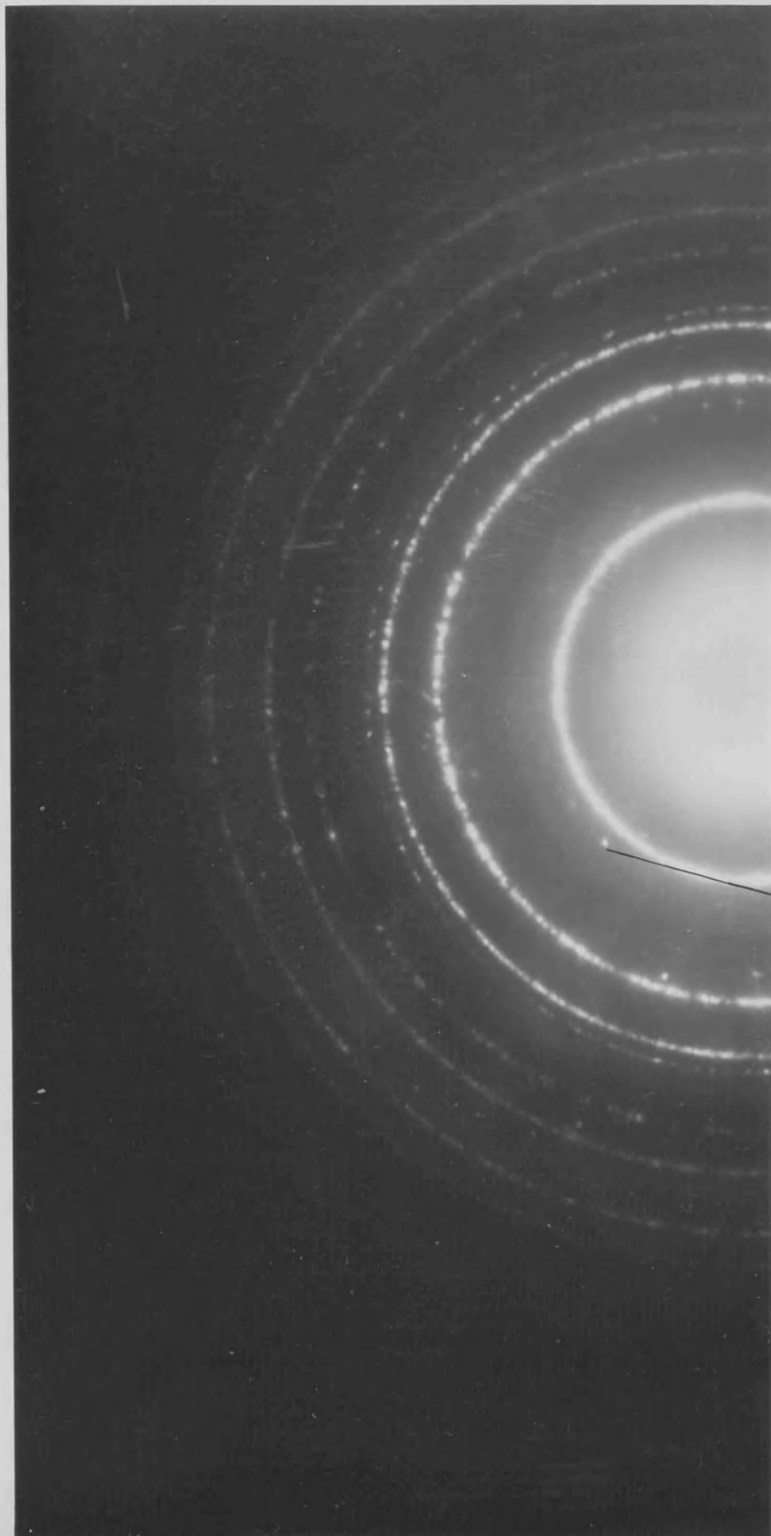


Plate 88 Electron diffraction of B4O

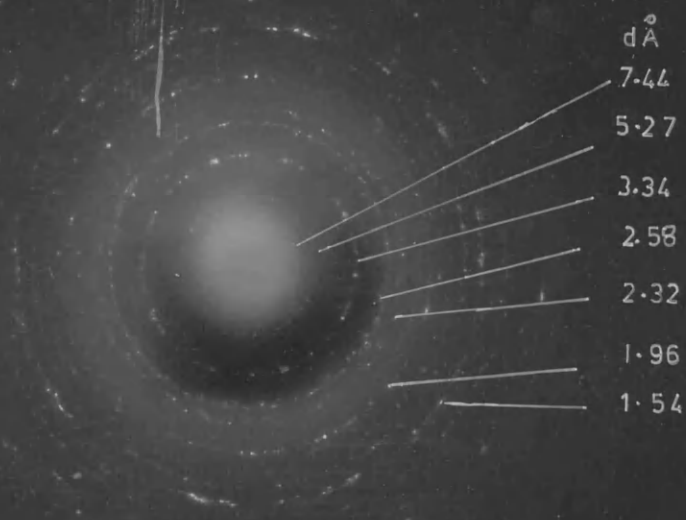


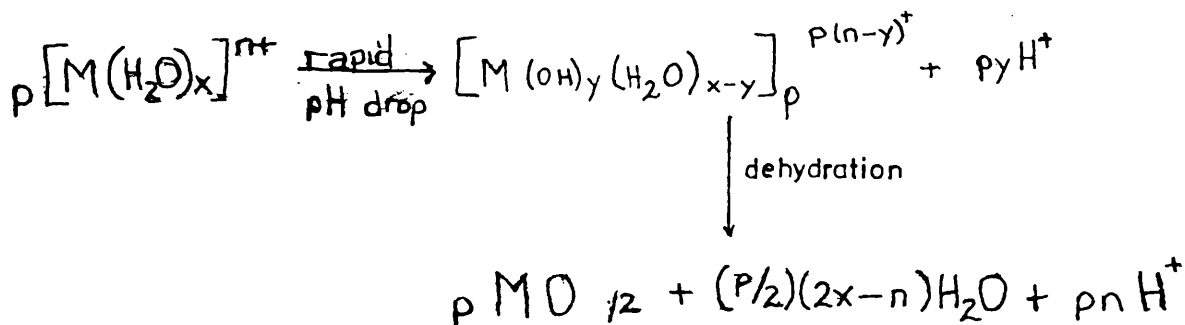
PLATE 89 E

X 520000

Discussion

General

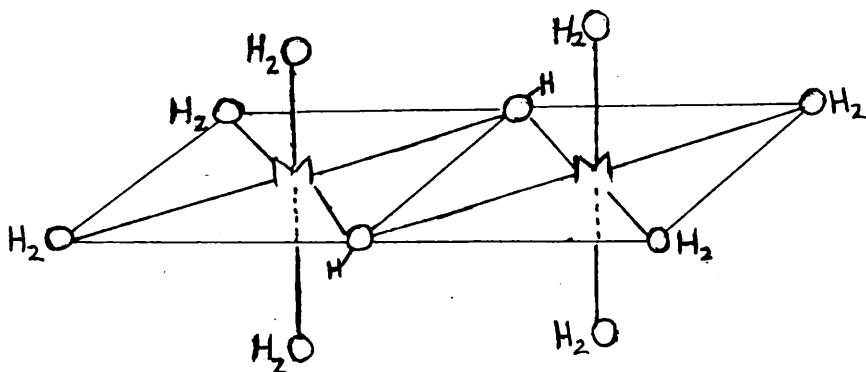
Precipitation mechanisms in metal oxide hydrolyses involve the condensation of polynuclear cations, and detailed reaction schemes for the hydrolysis of aqueous zirconyl chloride solutions, (Clearfield 1964) and the hydrolysis of iron (III) solutions (Knight, Sylva 1974) have been proposed. These can be generalised as,



where x is the co-ordination number of the metal ion M^{n+} , y has values from 0 to x and p is the number of molecules involved. (Fryer, Gildawie and Paterson 1974.) Partial oxide formation may occur giving rise to oxide hydroxide compounds. Fryer, Hutchison and Paterson (1970), working on the hydrolysis of aqueous zirconyl chloride, found that the final product was monoclinic zirconia, ZrO_2 , the crystals of which were of regular size with a 'pod' morphology. Using the electron microscope they also discovered a thin film precursor and identified the tetrameric metal cation.

This work was undertaken to investigate other metal salt hydrolyses and possible 'pod' morphologies, notably that of $\beta FeOOH$ (Gallagher 1970) and to examine their precursors.

Many workers have postulated the formation of polynuclear cations during the hydrolysis of metal salt solutions. Mulay and Selwood (1955) proposed the diol $(\text{Fe}(\text{OH}))_2^{4+}$ from iron(III) solutions; Sillen and co-workers (1959) proposed the species $(\text{VO})_2(\text{OH})_2^{2+}$, $\text{Bi}_6(\text{OH})_{12}^{6+}$, $\text{Sc}((\text{OH})_2\text{Sc})_n^{(n+3)+}$, $\text{In}((\text{OH})_2\text{In})_n^{(n+3)+}$, $\text{UO}_2((\text{OH})_2\text{UO}_2)_n^{2+}$, $\text{Th}((\text{OH})_3\text{Th})_n^{(n+4)+}$, $\text{Sn}((\text{OH})_2\text{Sn})_2^{2+}$ and $\text{Be}_3(\text{OH})_3^{3+}$; Muha and Vaughan (1960) proposed $(\text{Zr}(\text{OH})_2 \cdot 4\text{H}_2\text{O})_4^{8+}$ and Brossett (1952) postulated $\text{Al}_2(\text{OH})_5^+$. A dimer $(\text{M}(\text{OH})_2 \cdot 4\text{H}_2\text{O})_2^{n+}$ could be represented by,



As the hydrolysis develops the dimers polymerise by a process of olation. Oxolation also occurs within the dimers. The polymerisation may give rise to either a 2 dimensional network formed by chain growth or a 3 dimensional framework. The chain mechanism would predominate if the axial positions in the dimer were blocked by anions. This would require anions such as chloride, fluoride or sulphate with a high co-ordinating ability. Work by Kiyama (1974) shows that chloro and sulphato complexes are formed in acidic solutions of iron(III) chloride and iron(III) sulphate whereas iron (III) nitrate forms aquo complexes. Mossbauer studies on iron(III) salt solutions (Vertes 1971) also indicate that in the sulphate and chloride

solutions the anion is incorporated into the dihydroxy dimer but in the perchlorate and nitrate cases the dimers are free of anions. There is evidence from n.m.r. studies (Martin and Stockton 1973) that in AlCl_3 solutions the anion is involved in solvated structures.

It is intended to examine the results from this work in the light of the structural theory proposed for Zirconia polymerisation (Hutchison 1970). The major facets being that:

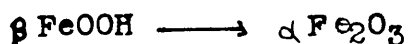
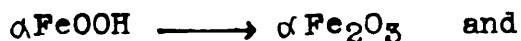
- (1) the pod morphology occurs in systems other than zirconia
- (2) there is a thin film precursor to the pods
- (3) the final pods occur by a rolling up of the thin films.

Polymerisation which proceeds via a chain growth, 2 dimensional mechanism would be more likely to lead to a thin film stage and then by rolling up to the final pod morphology.

Iron

The transformations among the oxides and hydroxides of iron have been investigated by Bernal, Dasgupta and Mackay (1959).

The transformations



occur on heating.

βFeOOH can only be produced by the hydrolysis of dilute solutions of FeCl_3 or FeF_3 (Gallagher 1970) whereas αFeOOH can be precipitated from many iron(III) salt solutions. It is formed at room temperature from the oxalate, nitrate, acetate and bromide (Weiser and Milligan 1935) and the sulphate (Posnak 1922). It can also be formed by aging, at room temperature, the gel produced by adding base to $\text{Fe}(\text{NO}_3)_3$ and $\text{Fe}(\text{ClO}_4)_3$ solutions, (Atkinson, Posner and Quirk 1968) although aging at higher temperatures gives $\alpha\text{Fe}_2\text{O}_3$. When base is used the αFeOOH is in the form of acicular crystals.

In this work the room temperature hydrolysis of 0.01M FeCl_3 solution gave βFeOOH ; the room temperature hydrolysis of $\text{Fe}(\text{NO}_3)_3$ solution produced αFeOOH with a 'lath' morphology; but 0.01M $\text{Fe}_2(\text{SO}_4)_3$ solution and 0.01M $\text{Fe}(\text{ClO}_4)_3$ solution gave no precipitate at room temperature. Reflux hydrolyses of FeCl_3 , $\text{Fe}(\text{NO}_3)_3$ and $\text{Fe}(\text{ClO}_4)_3$ produced $\alpha\text{Fe}_2\text{O}_3$ which was also formed on refluxing the room temperature hydrolysis products of $\text{Fe}(\text{NO}_3)_3$ and FeCl_3 . During the refluxing of FeCl_3 and $\text{Fe}(\text{NO}_3)_3$ solutions a stage was reached at which the solutions were a clear wine red. At this stage the hydrolysis products were identified as βFeOOH and $\alpha\text{Fe}_2\text{O}_3$.

respectively. The compound reported by Towe and Bradley (1967) which is formed by heating 0.06M $\text{Fe}(\text{NO}_3)_3$ solution to 85°C until the solution is clear wine red was not identified in this study probably because at reflux temperatures the reaction had already proceeded to $\alpha\text{Fe}_2\text{O}_3$. βFeOOH was detected at this stage in the reflux hydrolysis of FeCl_3 solution; the final $\alpha\text{Fe}_2\text{O}_3$ must therefore be formed from it. Hydrolysis of FeCl_3 at temperatures up to and including 67°C produces βFeOOH but at these higher temperatures the pods of βFeOOH are less well separated. The reflux hydrolysis of $\text{Fe}_2(\text{SO}_4)_3$ produced αFeOOH with a pod morphology.

The techniques used to identify the products were, electron diffraction, X ray powder diffraction, i.r. spectroscopy and D.T.A. To confirm identification or as an aid to identification where the electron diffraction results were inconclusive, X ray powder diffraction patterns were recorded. The standard ASTM X ray powder diffraction patterns of $\alpha\text{Fe}_2\text{O}_3$, βFeOOH and αFeOOH have very similar lattice spacings below 3.3\AA so that, unless the higher spacings of 7.4\AA (βFeOOH) or 4.18\AA (αFeOOH) can be resolved from the electron diffraction pattern, differentiation among αFeOOH , βFeOOH and $\alpha\text{Fe}_2\text{O}_3$ is very difficult. These high spacings can often be obscured by the central transmitted beam especially if the camera constant is low. Where ir spectra and DTA curves were recorded they were mainly used for comparison with literature curves or with each other and in some cases to give a little information on the environment of the hydroxyl groups.

In the ir spectra of Fe1 (produced from $\text{Fe}(\text{NO}_3)_3$ figure 17) the bands at 800cm^{-1} , 890cm^{-1} and 3170cm^{-1} indicate a hydrogen bonded hydroxyl group whereas in the spectrum of Fe4 (from FeCl_3 figure 19) the lack of absorption in the range 3300cm^{-1} to 3000cm^{-1} indicates that there are no hydrogen bonded hydroxyl groups, but the small shoulder at 3450cm^{-1} and the band at 840cm^{-1} could indicate a 'free' hydroxyl group. The lack of hydrogen bonded hydroxyls is an unusual feature of βFeOOH (Gallagher 1970). The spectrum of Fe4 below 700cm^{-1} is similar to that shown for βFeOOH by Nyquist (1971).

The DTA curve of Fe4 (figure 21) has endotherms at 85°C and 120°C due to loss of surface water and a sharp endotherm at 250°C . Conflicting results have been reported for the DTA curve of βFeOOH . MacKenzie (1970) reports two curves for synthetic βFeOOH , one showing a sharp exotherm at 450°C and one showing an endotherm at 275°C . MacKay (1960b) suggests that the reaction $\beta\text{FeOOH} \longrightarrow \alpha\text{Fe}_2\text{O}_3$ is exothermic. Babcan and Kristin (1971) obtained a DTA curve for βFeOOH which showed an exotherm at 310°C . In this case the βFeOOH was made by adding alkali to boiling FeCl_3 solution. Gallagher and Braun (1972) suggest that the initial reaction on heating βFeOOH is a loss of water of decomposition which escapes from within the solid via the large channels without disruption of the lattice forming $\beta\text{Fe}_2\text{O}_3$. The transformation $\beta\text{Fe}_2\text{O}_3 \rightarrow \alpha\text{Fe}_2\text{O}_3$ then occurs at about 280°C and is endothermic. The DTA curve for Fe4 agrees with Gallagher and Braun's result.

It was thought that using ethanol in place of water would slow down the hydrolysis of FeCl_3 and $\text{Fe}(\text{NO}_3)_3$.

The solution of FeCl_3 in alcohol remained a clear pale green-yellow after 2 years showing that the hydrolysis had not proceeded very far since there were no signs of the deepening orange colour which indicates increasing hydrolysis. At the temperature of an alcohol reflux the FeCl_3 (alcohol) solution gives βFeOOH but the reaction is slow. The hydrolysis of $\text{Fe}(\text{NO}_3)_3$ seemed to proceed faster in alcohol. Room temperature hydrolysis produced the precipitate Fe_3 after 10 days whereas room temperature hydrolysis in water precipitated after one month. The reflux hydrolysis product in both alcohol and water solutions is $\alpha\text{Fe}_2\text{O}_3$. The room temperature water hydrolysis product has been identified as αFeOOH but the alcohol product Fe_3 is unidentified.

The ir spectrum of Fe_3 (figure 31) shows the presence of hydroxyl groups by the bands at 1625 cm^{-1} and 1050 cm^{-1} . These are broader than the corresponding bands for FeI (figure 17). The band at 3150 cm^{-1} shows that the hydroxyl groups are hydrogen bonded. The spectrum is similar to that of FeI .

The DTA curve (figure 32) has an endothermic peak at 120°C , a small endotherm at 290°C followed by an exotherm at 330°C . This indicates that Fe_3 is not αFeOOH since the transformation $\alpha\text{FeOOH} \rightarrow \alpha\text{Fe}_2\text{O}_3$ is endothermic and occurs in the range 190°C to 380°C depending on the size of the particles (MacKenzie 1970). Curves similar to that of Fe_3 occur with ferric oxide gels. The temperature and shape of the exothermic peak depend on the final pH of the suspension

and the temperature of precipitation (Mackenzie 1970). The physical significance of this exothermic peak is speculative. Early interpretations were that it represents the crystallisation of amorphous material to $\alpha\text{Fe}_2\text{O}_3$ (Böhm 1925, Mitchell 1953) or a rapid reduction of surface area (Wöhler 1926). Towe and Bradley (1967) suggest the peak is due to continuing diffusion of molecular water from the structure leaving a residue that readily nucleates to $\alpha\text{Fe}_2\text{O}_3$. The peak represents the final development of $\alpha\text{Fe}_2\text{O}_3$ from the protohematite present before the peak. An iron oxide hydrate reported by Van der Giessen (1968) has a similar appearance, in the electron microscope, to Fe_3 and gives a DTA curve with a broad endotherm from 20°C to 200°C due to evaporation of water, and an exotherm from 350°C to 450°C caused by the recrystallisation of the dehydrated iron oxide. The X ray powder diffraction of this material has no spacings higher than 2.7\AA . Fe_3 has an irregular morphology and is certainly crystalline giving electron diffraction patterns and X ray powder diffraction patterns. It could be a distorted form of αFeOOH where the layer structure has been distorted by the ethanol groups so that the inter layer (200) and (011) spacings do not occur in the diffraction.

Electron microscopy of the room temperature hydrolysis of aqueous FeCl_3 solutions shows the development of βFeOOH through the stages of thin film, pods developing in films and finally pods (plates 67, 68 and 70). The 60°C hydrolysis of aqueous $\text{Fe}_2(\text{SO}_4)_3$ shows a similar progression through film to pod but this time the product is αFeOOH .

That the film observed in the electron

microscope exists as a polynuclear species in solution is confirmed by the ultracentrifuge curves (figure 24 a to f). While the fresh ferric chloride solution, which must contain some low polynuclear species eg. dimers since hydrolysis begins quickly (Mulay and Selwood 1955) changing the colour from the purple of the hexaquo Fe^{3+} ion to the yellow orange of the polymerised species, shows no sedimenting species even after prolonged rotation at high rotor speeds, sample No2 (a 'thin film' sample) shows a slowly sedimenting species (at 8k rotation speed) and sample No3 (pods in films) shows a faster sedimenting rate. The progression from thin film to pod which is observed in the electron microscope is paralleled by an increase in sedimenting rates, indicating an increase in molecular weight of the species in the ultracentrifuge curves (figure 24 a to f). The computer results plotted in figures 25 to 28 show an increase in S20w values from No2 to No3, No3 and No4 are similar and No5 is an order of magnitude larger. The secondary sedimenting species for No4 indicated by figure 24f was not investigated further but could probably be due to unused pieces of film after the 'pod in film' species had been removed.

The process of film growth and thickening observed in the electron microscope for the chloride and sulphate hydrolyses is similar and is consistent with the chain growth mechanism in which the anion builds into the growing polynuclear species blocking the axial positions for further hydrolysis. The final pod morphology occurs by a rolling up of the film and in the case of the FeCl_3 hydrolysis some Cl^- ions may be incorporated into the final pods of βFeOOH (varying proportions

of Cl^- ions have been found in βFeOOH (Gallagher 1970). The sulphate anion is probably too large to be built into the final structure and αFeOOH results. It seems that Cl^- or F^- ions are necessary to hold the hollandite structure of βFeOOH together. The presence of the sulphate anion may stabilise αFeOOH and make the transformation $\alpha\text{FeOOH} \longrightarrow \alpha\text{Fe}_2\text{O}_3$ more difficult.

A film precursor was also observed in the hydrolysis of $\text{Fe}(\text{NO}_3)_3$ solution but the process of crystal growth is different. The tendency for multilayer formation is much greater accounting for the more general thickening of the films. (plates 57 and 58). The nitrate anion has a much lower complexing ability than the sulphate or chloride anions and so will not build into the polynuclear species thus leaving the axial positions available for hydrolysis. The thin films observed in the hydrolysis systems appear to be amorphous since no diffraction patterns were observed.

The pH of the solutions drops to approximately 2 at the onset of film formation which would correspond to the production of one hydrogen ion per Fe^{3+} ion. Since four equatorial hydroxyl groups would be shared between four Fe^{3+} ions this agrees with a monomolecular film formation in solution.

Acicular crystals of αFeOOH are produced by adding base to $\text{Fe}(\text{NO}_3)_3$ solution (Atkinson et al 1968). Only a small proportion of the gel particles formed at precipitation are able to grow to crystals at the expense of dissolution of other particles. In the hydrolysis of the solutions containing Cl^- and NO_3^- anions the products obtained were αFeOOH except for N5 where the $\text{Fe}^{3+}/\text{Cl}^-$ ratio was 2/3 and βFeOOH was formed.

However in each case the morphology of the α -FeOOH was acicular or pod like rather than lath like. At a $\text{Cl}^-/\text{Fe}^{3+}$ ratio of 1/1 or lower, eg. 3/5, the product of the hydrolysis is α -FeOOH not β -FeOOH although the product has a pod morphology. If the $\text{Cl}^-/\text{Fe}^{3+}$ ratio is 3/2 or more the product is β -FeOOH. Feitknecht et al (1973) have proposed a mechanism for the formation of β -FeOOH in which four $(\text{Fe}_2(\text{OH})_2(\text{H}_2\text{O})_8)^{4+}$ units cluster round a Cl^- ion and further deprotonation and replication lead to hollandite, β -FeOOH. We would therefore expect β -FeOOH to be formed with a $\text{Cl}^-/\text{Fe}^{3+}$ ratio of as low as 1/8 but this was not observed in this work indicating that the Cl^- ion has a more important role in the polymerisation process than Feitknecht suggests. Sulphate ion and chloride ion even in small quantities ($\text{Cl}^-/\text{Fe}^{3+}$ ratio of 3/250) promote a 'pod' morphology possibly by blocking some of the axial positions in the low polynuclear species and inducing the 2 dimensional chain growth network of the thin film. A $\text{Cl}^-/\text{Fe}^{3+}$ ratio of 2/3 ensures that 3 out of the 4 axial positions in the dimer are blocked by Cl^- ions preventing 3 dimensional growth and this seems to be necessary for β -FeOOH formation.

The pods of β -FeOOH occur over a narrow size range and show no significant variation of length with initial concentration of ferric chloride solution. Watson et al (1960) conclude that pod size varies with concentration of starting material but their results were not conclusive.

The 2 dimensional film could grow into pods by rolling up, expulsion of Cl^- and further hydrolysis. It is

possible that chloride bridges could form which would help the rolling up process. (figure 40 a to d) Further hydrolysis would lead to tubes having the hollandite structure where Cl^- ions can occupy the small tunnels (figure 40e). The tubes would then pack together as envisaged by Gallagher (1970).

Washing with water cannot remove all the chloride ions, (Ellis, Giovanoli and Stumm 1976), a residual amount of 2% remain. The Cl^- ion has a radius of 1.81\AA compared with the 1.35\AA radius of the Ba^{2+} ion which occupies the tunnels of the true hollandite structure $\text{BaMn}_8\text{O}_{16}$ and the large size of the chloride ion could lead to strain within the tube limiting its length and thus controlling the length of the final pod. In this case the length of the pods would be independent of the concentration of the original FeCl_3 solution above a lower limit necessary for extensive film formation. The formation of a pod rather than a cuboid supports this strain theory since the strain in the tunnels of the central tube (AB in figure 41) would be shared with adjacent tunnels but nearer the edge the amount of strain that could be shared is unequal and thus these tubes would be shorter (CD in figure 41).

Since βFeOOH has a tetragonal unit cell with two long axes and one short axis the crystals would be expected to lie on the specimen grid with their short axis parallel to the beam as can be seen in plate 90.

Figure 40

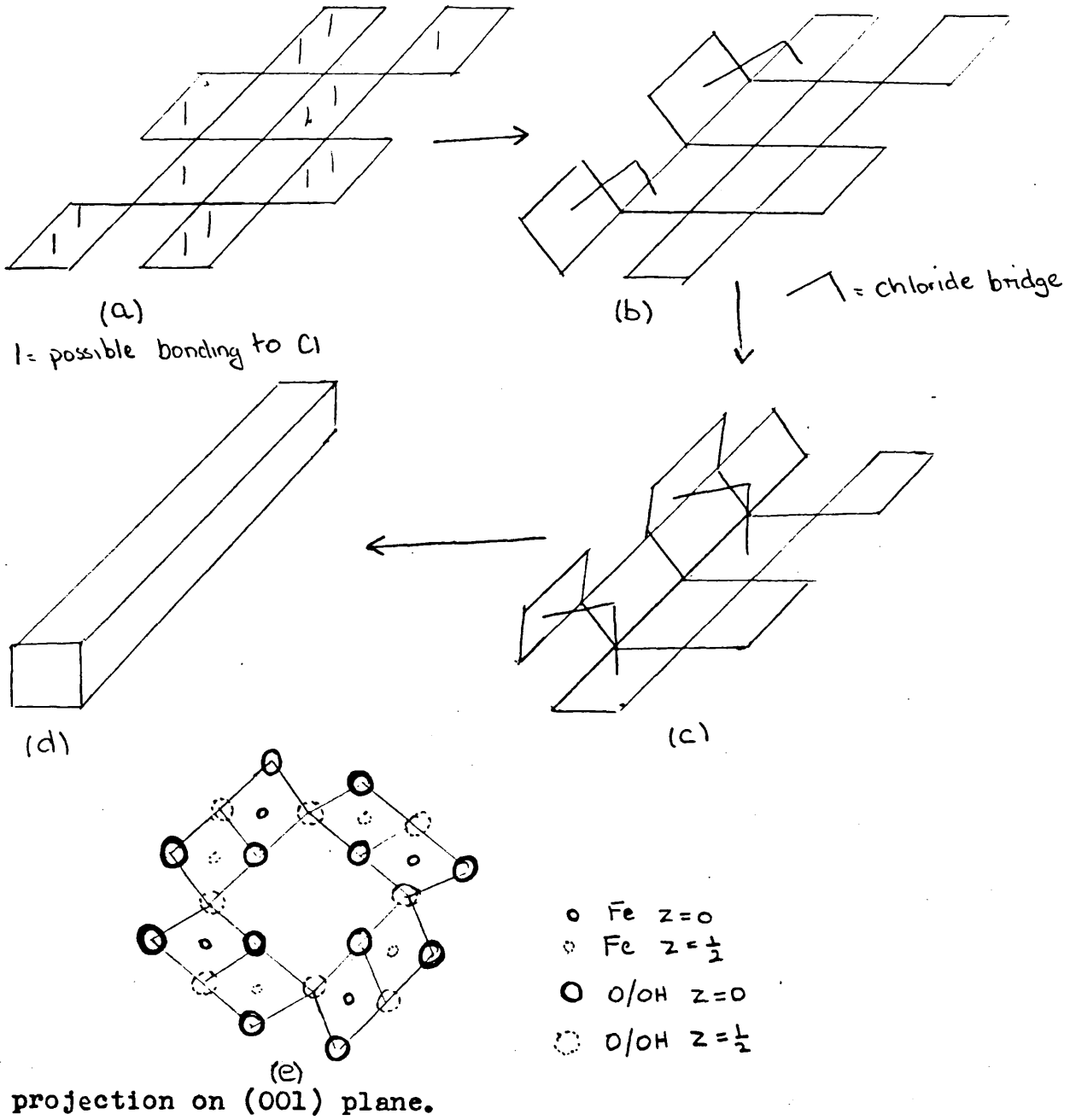
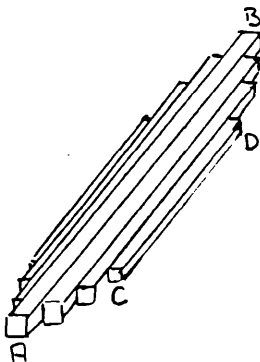


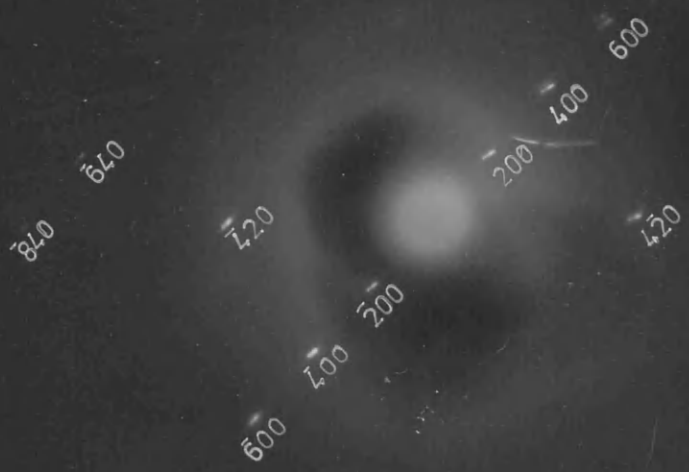
Figure 41



Vanadium

The prototype of the Vanadium hydride was prepared by the reaction of Vanadium with Hydrogen at 400°C. and 100 atm. pressure. The product was a dark, lustrous, metallic solid, which was found to be identical with the Vanadium hydride prepared by the reaction of Vanadium with Hydrogen at 400°C. and 100 atm. pressure.

PLATE 90



Vanadium

The products from the vanadium hydrolyses were difficult to identify. Electron diffraction showed that the products from the room temperature and reflux hydrolyses were the same, and they were at first thought to be ' $V_2O_5 \cdot H_2O$ ' by comparing the electron diffraction patterns with vanadium compound patterns quoted in the ASTM index. The agreement was fairly good (table 8). No crystal structure data on ' $V_2O_5 \cdot H_2O$ ' was given in the ASTM card so that the single crystal diffraction pattern (plate 34) could not be indexed. X ray powder diffraction showed a strong 14\AA spacing which was not reported for ' $V_2O_5 \cdot H_2O$ '. Further investigation of the vanadium literature revealed several other vanadium-oxygen compounds. Theobald et al (1970) have prepared several hydrates of vanadium oxides by an hydrothermal method. They report two new hydrates, ' $V_2O_4 \cdot 8.n_1H_2O$ ' and ' $V_2O_4 \cdot 8.n_2H_2O$ '. Their sample, which was green in colour but poorly crystalline, became black on drying. They recorded two different X ray patterns, one from the green sample and one from a black sample. The X ray pattern of the green sample had a strong 14\AA reflection whereas the one from the black sample had a strong 17\AA reflection. The two forms were interconvertible by varying the humidity. The authors compare the spectrum of the black form with 'Navajoite' (ASTM 7-332) and that of the green sample with 'Bariandite'. They gave no information on 'Bariandite' but referred to the then unpublished work of Cesbron and Vachey (1970). This paper when published, however, contained work on 'Lenoblite' (Bull. Soc. fr. Mineral. Cristallogr., 93 1970)

and not on bariandite. The bariandite paper was published in 1971 (Cesbron and Vachey). The mineral bariandite was found in uranium- vanadium deposits at Mouana . It is monoclinic with $a = 11.70$, $b = 3.63$, $c = 29.06$ Å and $\beta = 101^{\circ}30'$ and crystallises in the space group $c2/c$. The formula given for bariandite is $V_2O_4 \cdot 4V_2O_5 \cdot 12H_2O$ and it is distinguishable from corvusite $V_2O_4 \cdot 6V_2O_5 \cdot nH_2O$ by the sharp reflection at 14.2Å in its X ray spectrum. The crystals are elongated on 010 with a perfect (001) cleavage. The vanadium product in this present work was identified as bariandite by its X ray diffraction pattern. (table 9) The electron diffraction patterns from the hydrolysis products are compared with that of bariandite in Table 10. The single crystal pattern (plate 34) was indexed as bariandite oriented on the 001 plane. The room temperature hydrolysis of VO_2SO_4 produces large sheets. Resolved periodicities from the laser diffractometer, transmission electron micrographs and electron diffraction spacings indicate that the thin sheets are oriented on the 010 plane (table 11), that is with the b axis parallel to the electron beam.

The pH curve recorded from the hydrolysis at $40^{\circ}C$ is similar to that obtained by Hutchison 1970 for the hydrolysis of zirconyl chloride. An initial induction period was followed by a sharp pH drop, during which film formation occurred, and then a slower pH decrease as precipitation occurred.

The IR spectrum of the product was compared with those of V_2O_5 and $V_2O_4 \cdot H_2O$ given by Nyquist (1971). The strong band at 1000 cm^{-1} indicates a vanadium-oxygen double bond

(Nakamoto 1971). This mode occurs at 1015cm^{-1} in the $\text{V}_2\text{O}_4 \cdot \text{H}_2\text{O}$ spectrum and at 1020 cm^{-1} in the V_2O_5 spectrum. In the region below 900 cm^{-1} $\text{V}_2\text{O}_4 \cdot \text{H}_2\text{O}$ shows strong bonds at 760 cm^{-1} , 630 cm^{-1} and 550 cm^{-1} and weaker bands at 350 cm^{-1} and 300 cm^{-1} while V_2O_5 has strong bonds at 830 cm^{-1} , $600\text{--}500\text{ cm}^{-1}$ (broad), 380 cm^{-1} and 300 cm^{-1} (Nyquist 1971). The spectrum in figure 15 has a strong band at 760 cm^{-1} , a broad assymmetric band at 550cm^{-1} and weak bands at 380 cm^{-1} and 320 cm^{-1} . Above 1200 cm^{-1} the spectrum has bands at 1605 cm^{-1} , 1615 cm^{-1} and 3400 cm^{-1} (broad) which are due to water (in $\text{V}_2\text{O}_4 \cdot \text{H}_2\text{O}$ they occur at 1615 cm^{-1} , 1675 cm^{-1} and 3500 cm^{-1}). The spectrum in figure 15 contains bands typical of both reference spectra.

The DTA curve is shown in figure 16 . This is in agreement with the dehydration of bariandite (Cesbron and Vachey 1971) where loss of water occurs at 60°C giving $\text{V}_2\text{O}_4 \cdot 4\text{V}_2\text{O}_5 \cdot 7\text{H}_2\text{O}$ and at 90°C giving $\text{V}_2\text{O}_4 \cdot 4\text{V}_2\text{O}_5 \cdot 3\text{H}_2\text{O}$. The final formation of V_2O_5 occurs at 670°C and so could not be detected with our equipment.

Room temperature hydrolysis gives sheets oriented on the 010 plane while refluxing gives 'needle' crystals oriented on the 001 plane. Thin films oriented on the 010 plane were observed as precursors in the reaction at 40°C (plate 29) and at 60°C and it is likely that these films are precursors at reflux temperatures. There are two possible mechanisms of formation of the needle crystals from the thin films. Both are illustrated in figure 42. As bariandite is elongated in the

010 direction the thin films may stack together like cards, (figure 42a) and may then be cleaved in the 001 direction giving thin needle crystallites (figure 42b). When these crystallites are deposited on carbon films they will lie on the 001 plane (figure 42c). However the stacked cards may roll up giving a cylinder shaped crystal (figure 42d), which may then be cleaved in the 001 direction giving thin needle crystals (figure 42e) which will lie on the (001) plane on the carbon film (figure 42f). If the first mechanism (figure 42 a,b,c) occurred the final 'needle' crystals should be of very different diameters but the same length whereas the second mechanism (figure 42 a,d,e,f) should result in 'needle' crystals of the same diameter but different lengths. The crystals shown on plate 33 are of different lengths but their diameters appear similar therefore the second mechanism is more probable.

The hydrolysis of VOSO_4 is similar to that of the iron(III) system, involving formation of a thin film which in the vanadium system is crystalline and which then rolls up to give the final morphology, unlike the FeCl_3 hydrolysis where crystallinity is a function of the rolling up process.

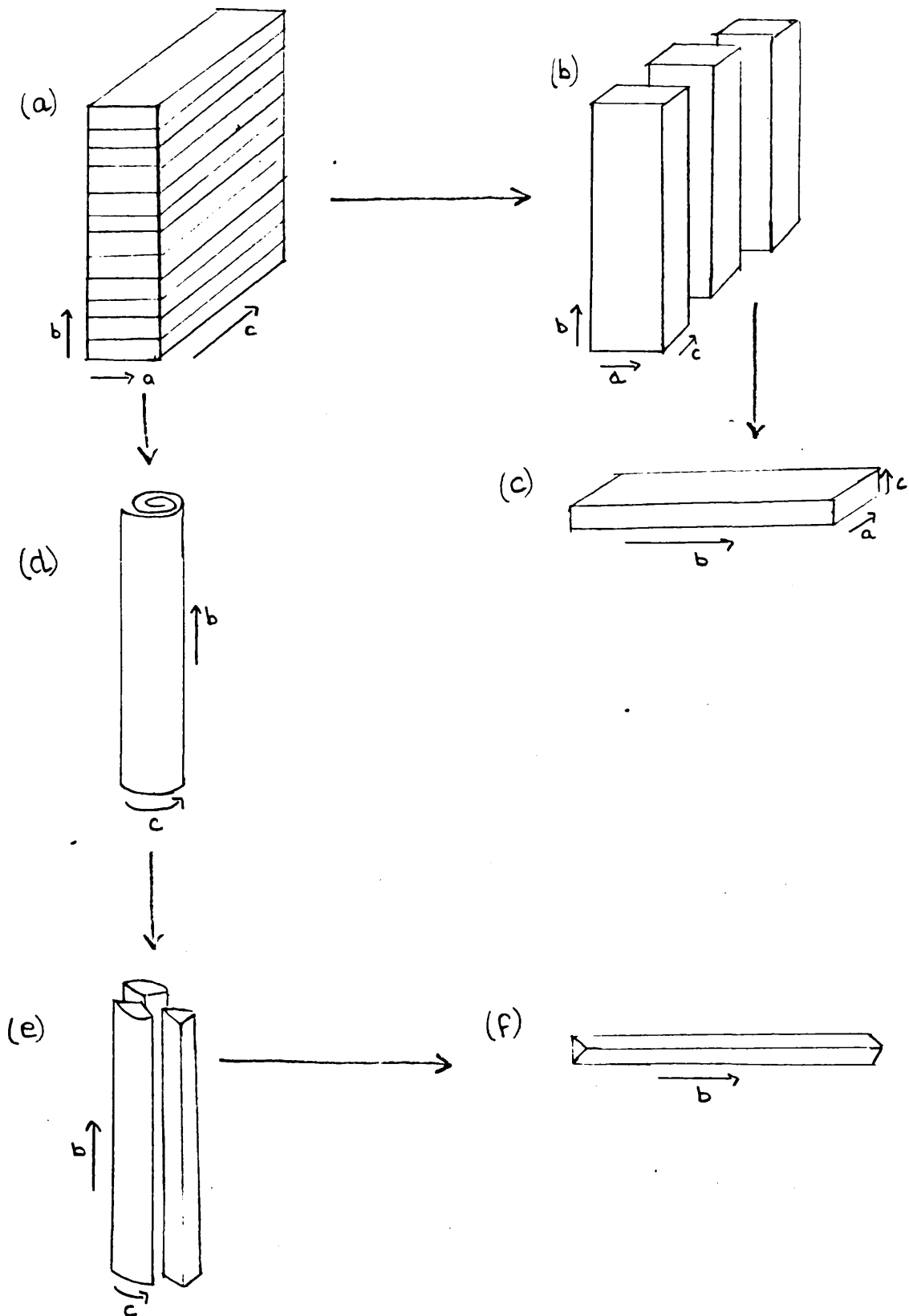


Figure 42 Mechanisms for formation of the needle crystals of Bariandite.

Conclusions from the work on the iron and vanadium systems.

The pod morphology occurs in hydrolysis of the iron(III) system. The pods of β -FeOOH are regular in length and their size is independent of the concentration of the original FeCl_3 solution. α -FeOOH with a pod morphology can be formed from the hydrolysis of $\text{Fe}_2(\text{SO}_4)_3$ solution or from the hydrolysis of 'mixed' solutions of FeCl_3 and $\text{Fe}(\text{NO}_3)_3$ where the $\text{Cl}^-/\text{Fe}^{3+}$ ratio is lower than 3/2. If the ratio is 3/2 or higher β -FeOOH is formed. The anions present in solution are important in determining the final morphology. Strongly complexing anions can block the axial positions in the low polynuclear species forcing a 2 dimensional film growth. Thin films were observed in the hydrolyses of FeCl_3 , $\text{Fe}(\text{NO}_3)_3$, $\text{Fe}_2(\text{SO}_4)_3$ and VOSO_4 solutions and the development of pods from these films was observed in the FeCl_3 and $\text{Fe}_2(\text{SO}_4)_3$ hydrolyses. The pods of β -FeOOH and α -FeOOH and the needles of Bariandite are formed by a rolling up of the thin film precursors.

Other systems.

Aluminium.

Hydrolysis of the aluminium solutions produced boehmite.

Micrographs similar to plates 23 and 24 (boehmite produced from AlCl_3 reflux) were obtained by Moscou and Van der Vlies (1959) and identified as boehmite. They obtained their precipitates by adding ammonia to $\text{Al}(\text{NO}_3)_3$ and to aluminium alum solutions and the precipitated boehmite was in the form of sheets which appeared to be made up of a network of fibrils. Brace and Matijevic (1973) prepared alumina hydrosols from solutions of the sulphate and of the nitrate, achieving optimum results with a concentration of 2×10^{-3} M. Somatoids of boehmite, formed on aging an aluminium hydroxide gel, have been reported by Souza Santos (1953), and from the reaction of $\text{NaAlSi}_3\text{O}_8$ with carbonated water at high pressures by Wyart et al (1963). Moscou and Van der Vlies observed somatoids formed on aging boehmite with ammonia but these somatoids gave a bayerite ($\text{Al}(\text{OH})_3$) diffraction pattern.

In the electron diffractions of the hydrolysis products all the spots and rings can be indexed by calculating extra spacings from the cell constants of boehmite but many of these are forbidden for the space group Amam (Ewing 1935a) to which boehmite belongs, for example $k+l = 2n+1$. Thus the 110, 130 and 150 reflections are forbidden. In plate 28 (the product from $\text{Al}(\text{NO}_3)_3$) these three reflections occur. They could be caused by the two dimensional diffraction where because of the thinness of the crystals the hkl reflections extended in the c^* direction produces a certain density of scatter at the position

of an $hk0$ reflection which is forbidden (Vainshtein 1964). Thus the 111 , 131 and 151 reflections could be producing apparent 110 , 130 and 150 reflections. The diffraction pattern also shows the typical elongation of spots due to the extreme thinness of the crystal.

In this present study a thin sheet morphology was formed by all three aluminium hydrolyses. (plates 25 and 27) However the micrographs of the $AlCl_3$ hydrolysis product (plates 23 and 24) show thickened sheets, which could be due to rolling up of the sheet, and bundles of fibrils. These two features might be called somatoids. These structures were not found in the products from $Al(NO_3)_3$ and $Al_2(SO_4)_3$ hydrolyses where the morphology was less regular. There is evidence from n.m.r. studies (Martin and Stockton 1973) that in $AlCl_3$ solutions the anion is involved in solvated structures. It has been shown (MacDonald, Butler, Owen 1973) that the hydrolysis of Al^{3+} involves three polymeric species $Al_2(OH)_2^{4+}$, $Al_3(OH)_4^{5+}$ and $Al_{14}(OH)_{34}^{8+}$ the last being a direct precursor of Boehmite. If the chloride anion became involved in these polycations the axial positions would be blocked so forcing a sheet like growth which, since the boehmite shown in plate 29 has a similar morphology to bariandite obtained after one days reflux (plate 31), would probably be formed in a similar way, that is by the rolling up of a thin film precursor which might finally produce somatoids.

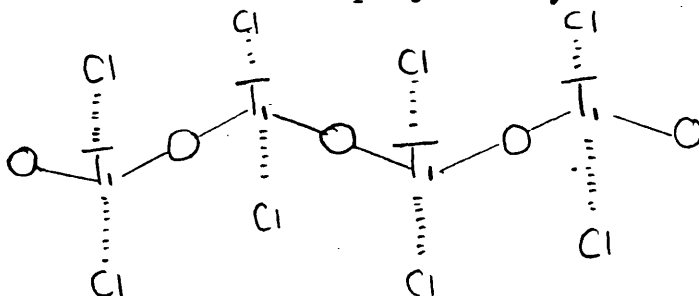
Tin

Tin compounds with octahedrally co-ordinated oxygen atoms are well known. Examples are the stannates which contain the $\text{Sn}(\text{OH})_6^{2-}$ anions and the dioxides, SnO_2 . The most common dioxide cassiterite has the rutile structure. In aqueous solution the Sn^{2+} and Sn^{4+} ions are extensively hydrolysed, the polynuclear species $\text{Sn}((\text{OH})_2\text{Sn})^{2+}$ being identified by Sillen (1959). In this work, Cassiterite, was formed from Sn^{2+} and Sn^{4+} chlorides by reflux and room temperature hydrolyses. The crystals show a chain like (plate 3) and 'sheet' (plate 2) morphology but no pod morphology was obtained. Identification was by electron diffraction. No tin oxide hydroxides were found in the ASTM index.

Titanium

TiCl_4 is similar to SnCl_4 in many ways. Both act as Lewis acids and are extensively and quickly hydrolysed in water giving the dioxide. In concentrated HCl acid chloro complexes of $(\text{TiCl}_5(\text{H}_2\text{O}))^-$ and $(\text{TiCl}_6)^{2-}$ have been observed. In $\text{TiSO}_4 \cdot \text{H}_2\text{O}$ there are chains of $(\text{TiO})_n^{2n+}$ joined in the crystal by the sulphate groups each of which is in contact with 3 metal ions with the water molecule associated with the titanium atoms so that they are approximately octahedrally co-ordinated by oxygen (Cotton and Wilkinson 1962). In sulphuric acid species such as $\text{Ti}(\text{OH})_3\text{HSO}_4$ and $\text{Ti}(\text{OH})_2\text{HSO}_4^+$ have been suggested (Cotton and Wilkinson 1962). In this present work the room temperature and reflux hydrolysis of Ti^{3+} and Ti^{4+} chlorides gave the same product. This was identified as the anatase modification of TiO_2 by electron diffraction. The crystals show a chain-like

morphology (plate 6) but no regular pods were observed. No titanium oxide hydroxides were found in the ASTM index. Since TiCl_4 behaves similarly to SnCl_4 in many ways, it might have been expected that the product from the titanium hydrolysis would have been the rutile modification of TiO_2 which has a regular octahedral co-ordination. However the product was, in all cases, anatase which has a distorted octahedral co-ordination with two short Ti--O bonds and 4 longer Ti--O bonds (figure 13 page 51). That the product has an assymetrical structure suggests assymetry in its precursors. This could have occurred because of anion involvement in the polycation, for example,



This could lead to TiO_2 with a distorted octahedral structure having 2 near oxygen neighbours and 4 oxygen neighbours further away. Anion involvement in polycation species could occur with anions with high coordinating ability such as chloride or sulphate and with metal cations with a high polarising ability. The polarising ability of a metal cation is dependent on the charge and the ionic radius of the cation. Table 31 shows the ionic and covalent radii, in Å, of Sn^{4+} and Ti^{4+} .

Table 31

Cation	Ionic radius	Covalent radius
Sn^{4+}	0.71	1.45
Ti^{4+}	0.60	1.36

The Ti^{4+} ion would have a higher polarising ability than the Sn^{4+} ion because of its smaller radius and hence would be more likely to co-ordinate anions in its polynuclear species.

Rare Earths.

The trihydroxides of Pr, Nd and Sm were formed by adding excess ammonia to solutions of their salts. $Nd(NO_3)_3$ and $NdCl_3$ gave the same product. These hydroxides show pod morphologies (plates 15, 14 and 13). Hardy, Buxton and Lloyd (1967) showed that the initial precipitates of a lanthanide hydroxide consisted of amorphous particles 30 to 60Å in diameter which, when aged in their mother liquor (8M NH_4OH) changed into crystallised sheets with a width of several thousand angstroms. When washed and aged in water the sheets changed into rods, tubes or rolled sheets. The 'pod' morphology thus seems to occur by the rolling up of sheets. A study of the aging of $Nd(OH)_3$ gels (Milligan and Dwight 1965) showed the following aging process. The initial precipitate was amorphous. After 30 minutes in water, spherical particles of diameter 30 to 50Å appeared, which aggregated into denser particles after one hour. After two and a half hours dense elongated particles were observed and after four hours rod like particles formed by the rolling of the sheets (observed earlier) were observed. After 12 hours the rods were larger and after 72 hours hexagonal platelets appeared.

Electron diffraction of the Ce precipitates of this present work identified them as CeO_2 . The diffraction rings were diffuse and the transmission image (plate 19) shows a possible pod morphology but the outline of the pods appears

to be composed of a different material indicating decomposition. The tendency for dissociation of the lanthanide hydroxides to the oxides increases with increasing cation size and will therefore be greatest for $\text{Ce}(\text{OH})_3$. The oxidation



takes place in air (Sidgwick 1950). It is possible that amorphous $\text{Ce}(\text{OH})_3$ was formed and that aging produced pods but that dissociation into CeO_2 supervened. The Gd precipitate was amorphous and no pods developed.

References

Introduction

Arnek R., Schlyter K.

Acta. Chem. Scand. 22(4) 1327 (1968)

Atkinson R. J., Posner A. M., Quirk J.P.

J. Inorg. Nucl. Chem. 30 2371—2381 (1968)

Bernal J. D., Dasgupta D. R., MacKay A. L.

Clay Min. Bull. 4 (21) 15 (1959)

Böhm J.

Z. Anorg. Allgem. Chem. 149 203 (1925)

Brace R., Matijevic E.

J. Inorg. Nucl. Chem. 35(11) 3691 (1973)

Brady G.W., Kurkjian C.R., Lyden E.F., Robin M.B., Saltman P,

Spiro T., Terzis A.

Biochemistry 7 2185 (1968)

Britz D., Nancollas G. H.

J. Inorg. Nucl. Chem. 31 3861 (1969)

Brosset C., Biedermann G., Sillen L. G.,

Acta. Chem. Scand. 8 1917 (1954)

Bye G.C., Sing K.W.S.

Soc. Chem. Industry Monograph 38 (1972)

Dasgupta D.R., MacKay A.L.

J. Phys. Soc. Japan 14 932 (1959)

Demchak R., Matijevic E.

J. Coll. Interface Sci. 31 257 (1969)

Ewing F.J. 1935 a

J. Chem Phys. 3 203 (1935)

1935 b

J. Chem. Phys. 3 420 (1935)

Feitknecht W.

4th Int. Symp. reactivity in solids 583 (1960)

Francombe M.H., Rooksby H.P.

Clay Min. Bull. 4 (1959)

Gallagher K.J.

Nature 276 1225 (1970)

Goldsztaub M.S.

O.R. Acad. Sci. 195 964 (1932)

Goodwin H.M.

Z. Phys. Chem. 21 (1896)

Graham T.

J. Chem. Soc. 15 216 (1862)

Hedström B.O.A.

Arkiv Kemi. 6 1 (1953)

Hutchison J.

Ph.D. Thesis (1970) (Univ. of Glasgow)

Jander G., Winkel A.

Z. Anorg. Allgem. Chem. 193 1-28 (1930)

Jezowska-Trzebiatowska B.

Co-ord. Chem. Rev. 3 255 (1968)

Kennedy J.T., Townsend W.P., Emmerson J.A.

J. Coll. Interface Sci. 42 589 (1973)

Kiyama M., Takada T.

Bull. Chem. Soc. Japan 46 1680 (1973)

Knight R.J., Sylva R.N.

J. Inorg. Nucl. Chem. 36(3) 591 (1974)

Kolthoff I.M., Moscovitz B.

J. Amer. Chem. Soc. 58 777 (1936)

Lamb A.L., Jaques A.G.

J. Amer. Chem. Soc. 60 967 (1938)

Lind M.D., 1967 a

J. Chem. Phys. 47(3) 990 (1967)

1967b J. Chem. Phys. 46(2) 2010 (1967)

Lutz B., Wendt H.

Ber. Bunsen Ges. Phys. Chem. 74(4) 372 (1970)

MacKay A.L.

1960a 4th. Conf. on reactivity in solids (1960)

1960b Min. Mag. 32 545 (1960)

Min. Mag. 33 270 (1962)

Matijevic E., Lindsay A.D., Kratochvill S., Jones M.E., Larson R.I.,
Cavey N.W.

J. Coll. Interface Sci. 36 273 (1971)

Matijevic E., Bell A.

Soc. Chem. Industry Monograph 38 (12) (1972)

Matijevic E., Bell A., Brace R., MacFadyen P.

J. Electrochem. Soc. 120 893 (1973)

Matijevic E., Sapijesko R.S., Melville J.B.,

J. Coll. Interface Sci. 50(3) 567 (1975)

Milligan W.O., MacAtee J.L.

J. Phys. Chem. 60 273 (1956)

Muha G.M., Vaughan P.A.

J. Chem. Phys. 33 194 (1960)

Mulay L.N., Selwood P.N.

J. Amer. Chem. Soc. 77 2693 (1955)

Posanjak E., Mervin H.E.

J. Amer. Chem. Soc. 44 1965 (1922)

Schugar H., Walling C., Jones R.B., Gray H.B.

J. Amer. Chem. Soc. 89 3712 (1967)

Schwertmann U.

Z. Anorg. Allgem. Chem. 298 337 (1959)

Shuttleworth S.G.,

J. Soc. Leather Trades Chemists 38 58 (1954)

Sillen L.G.

Quart. Rev. 13 146 (1959)

Soderquist R., Janssons S.

Acta. Chem. Scand. 20 1417 (1966)

Sommer B.A., Margerum D.W.

Inorg. Chem. 9 2517 (1970)

Spiro J.G., Allerton S.E., Renner J., Terzis A., Bils R., Saltman P.

J. Amer. Chem. Soc. 88 2721 (1966)

Sylva R.N.

Rev. Pure Applied Chem. 22 115 (1972)

Vertes A., Komor M.R., Suba M.

Ann. Univ. Sci. Budapest R.E.N. Chem. 12 79 (1971)

Watson J.H.L., Cardell R.R., Heller W.

J. Phys. Chem. 66 1757 (1962)

Weiser H.B., Milligan W.O.

J. Amer. Chem. Soc. 57 238 (1935)

Wells A.F.

Structural Inorganic Chemistry (1962)

Wendt H.

Inorg. Chem. 8 1527 (1969)

Werner A., Pfeiffer P.

Ber. 40 272 (1907)

Zyvaginsteu O.E.

Russian J. Inorg. Chem. 4 439 (1961)

Experimental

Agar A.W.,

Brit. J. Appl. Phys. 11 185 (1960)

Andrews K.W., Dyson D.J., Keown S.R.

Interpretation of Electron Diffraction Patterns . (London)
(1967)

Bassett G.A., Menter J.W., Pashley D.W.

Phil. Mag. 2 1482 (1957)

Boiko B.T., Palatnik L.S., Dervyanchenko A.S.

Dokl. Akad. Nauk. S.S.S.R. 179 316 (1967)

Bradley D.F.

Brit. J. Appl. Phys. 5 65 (1954)

Busch H.

Ann. Physik 81 974 (1926)

Cosslett V.E.

Practical Electron Microscopy. (London 1951)

Fernández-Morán H.

Proc. 6th. Int. Congr. Electron Microscopy (Kyoto) 1 13
(1966)

Glauert A.

Principles and Practice of Electron Microscope Operation
(1974)

Hanszen Z.

Adv. Opt. Electron Microscopy 4 1 (1971)

Heidenreich R. D.

Fundamentals of Transmission Electron Microscopy (1964)

Hibi T.

Proc. Int. Conf. Electron Microscopy, London (1954)

Hirsch P. B., Howie A., Nicholson R. B., Pashley D. W., Whelan M. J.

Electron Microscopy of Thin Crystals. London (1965)

Hutchison J.

Ph.D. Thesis (1970) (Univ. of Glasgow)

Johnson D. J., Crawford D.

J. Microscopy 98 (3) 313 (1973)

Komodo T.

Japan J. Appl. Phys. 3 122 (1964)

Konig H.

Z. Phys. 129 483 (1951)

Le Poole J. B.

Phillips Techn. Rundsch. 9 33 (1947)

Mihama K., Shima S., Yeuda R.

Japan. J. Appl. Phys. 13(2) 377 (1974)

Phillips R.

Brit. J. Appl. Phys. 11 504 (1960)

Rieke W.D.

Optik. 18 278 (1961)

Taylor K.A., Glasser R.M.

Rev. Sci. Inst. 44 (10) 1546 (1973)

Von Borries B., Ruska E.

Zwiss Mikroskop 56 317 (1959)

Von Dorsten A.C., Prensela H.F.

Proc. 6th. Int. Congr. Electron Microscopy (Kyoto)
1 21 (1966)

Watson J.H.L.

J. Appl. Phys. 18 153 (1947)

Whelan M.J.

J. Inst. Metals 87 392 (1959)

Results

Carbannes-Ott C.

C. R. Seance Acad. Sci. 244 2491 (1957)

Cesbron F., Vachey H.

Bull. Soc. Fr. Mineral Cristallogr. 94 49 (1971)

Gallagher K.J., Braun H.

Nature 240 13 (1972)

Garner E.V.

J. Inorg. Nucl. Chem. 21 380 (1961)

Hardy C.J., Buxton S.R., Lloyd M.A.

O.R.N.L. 4000 (1967)

La Salle M.J., Cobble J.W.

J. Phys. Chem. 59 519 (1955)

MacKenzie R.C.

Differential Thermal Analysis (1970)

Nakamoto K.

Infra-red Spectra of Inorganic and Co-ordination Compounds
(1963)

Nyquist R.A., Kagel R.O.

Infra-red Spectra of Inorganic Compounds (1971)

Watson J.H.L., Heller W., Schuster T.

European Regional Conf. on Electron Microscopy, Delft
(1960)

Discussion

Atkinson R.J., Posner A.M., Quirk J.P.

J. Inorg. Nucl. Chem. 30 2371 (1968)

Babcan J., Kristin J.

J. Thermal Analysis 3 307 (1971)

Bernal J.D., Dasgupta D.R., MacKay A.L.

Clay Min. Bull. 4 (21) 15 (1959)

Böhm J.

Z. Anorg. Allgem. Chem. 149 203 (1925)

Brace R., Matijevic E.

J. Inorg. Nucl. Chem. 35(11) 3691 (1973)

Brosset C., Biedermann G., Sillen L.A.

Acta. Chem. Scand. 8 1917 (1954)

Carbannes-Ott C.

C.R. Seance Acad. Sci. 244 2491 (1957)

Cesbron F., Vachey H.

Bull. Soc. Fr. Mineral Cristallogr. 93 235 (1970)

Ibid. 94 49 (1971)

Clearfield A.

Inorg. Chem. 3 146 (1964)

Cotton F.A., Wilkinson G.

Advanced Inorganic Chemistry (1962)

Ellis J., Giovanoli R., Stumm W.

Chimia 30 194 (1976)

Ewing F.J.

J. Chem. Phys. 3 420 (1935)

Feitknecht W., Giovanoli R., Michaelis W., Muller M.

Helv. Chem. Acta. 56(8) 2847 (1973)

Fryer J.R., Gildawie A.M., Paterson R.

Nature 252 544 (1974)

Fryer J.R., Hutchison J.L., Paterson R.

Nature 226 149 (1970)

Gallagher K.J.

Nature 226 1225 (1970)

Gallagher K.J., Braun H.

Nature 240 13 (1972)

Hardy C.J., Buxton S.R., Lloyd M.A.

O.R.N.L. 4000 (1967)

Hutchison J.

Ph.D. Thesis (1970) (Univ. of Glasgow)

Kiyama M., Takada T.

Bull. Chem. Soc. Japan 46 1680 (1973)

Knight R.J., Sylva R.N.

J. Inorg. Nucl. Chem. 36(3) 591 (1974)

MacDonald D.D., Butler P., Owen D.

J. Phys. Chem. 77 2474 (1973)

MacKay A.L.

Mineralog. Mag. 32 545 (1960)

MacKenzie R.C.

Differential Thermal Analysis (1970)

Martin J., Stockton G.

J. Magnetic Resonance 12 218 (1973)

Milligan W.O., Dwight D.W.

J. Electron Microscopy 14(4) 264 (1965)

Michell W.A.

Min. Engng. N.Y. 5 904 (1953)

Moscou L., Van der Vlies G.S.

Kolloid Z. 163 35 (1959)

Muha G.M., Vaughan P.A.

J. Chem. Phys. 33 194 (1960)

Mulay L.N., Selwood P.N.

J. Amer. Chem. Soc. 77 2693 (1955)

Nakamoto K.

Infra-red Spectra of Inorganic and Co-ordination
Compounds. (1963)

Nyquist R.A., Kagel R.O.

Infra-red Spectra of Inorganic Compounds. (1971)

Posnjak E., Merwin H.E.

J. Amer. Chem. Soc. 44 1965 (1922)

Sidgwick N.V.

Chemical Elements and their Compounds. (1950)

Sillen L.G.

Quart. Rev. 13 146 (1959)

Souza Santos H.L., Valyo-Frare A.

Kolloid Z 133 101 (1953)

Theobald F., Cesbron F.

C.R. Acad. Sci. Paris Ser.C 271 364 (1970)

Towe K.M., Bradley W.F.

J. Coll. Interface Sci. 24 384 (1967)

Vainshtein B.K.

Electron Diffraction. London (1964)

Van der Giessen A.A.

Phillips Res. Repts. Suppl. 12 (1968)

Vertes A., Komor M.R., Suba M.

Ann. Univ. Sci. Budapest R.E.N. Chem. 12 79 (1971)

Watson J.H.L., Heller W., Schuster T.

European Regional Conf. on Electron Microscopy

Delft (1960)

Weiser H.B., Milligan W.O.

J. Amer. Chem. Soc. 57 238 (1935)

Wöhler L.

Kolloid Z. 38 97 (1926)

Wyart J., Oberlin A., Tchoubar C.

C.R. Séances Acad. Sci. 256 554 (1963)